

# **Advanced Channel Estimation and Detection Techniques for MIMO and OFDM Systems**

Li Li

PhD

The University of York

Electronics

June 2013

# Abstract

Multi-input and multi-output (MIMO) and orthogonal frequency division multiplexing (OFDM) have attracted significant attention, and become promising techniques for high data rate wireless communication systems. They have been widely studied and employed for 4G systems such as WiFi, DVB-T, WiMAX and LTE-A. Hence, the performances of such systems are critical to practical applications including online gaming, files transfer and high quality video streaming *et al.*. The thesis have studied low-complexity channel estimation and detection techniques to improve the reliability of the wireless links or increase the spectral efficiency at low cost as follows.

(1) MIMO-OFDM systems over slowly varying channels. Conventional comb-type uniform pilot allocation (UPA) for MIMO-OFDM systems employed by many standards obtains reliable channel estimates in the sense that the pilots occupy the subcarriers only for channel estimation without any further benefit. To make better use of pilots for MIMO-OFDM systems to acquire an additional performance gain, a novel receiver based dynamic pilot allocation (DPA) scheme is proposed with the aid of a feedback link. The DPA inserts pilots into most faded subcarriers at expense of moderate MSE performance degradation in channel estimation.

(2) Narrow band MIMO systems. High spectral efficiency can be achieved by a large size of transmit and receive antennas, but the BER performance of conventional linear and successive interference cancellation (SIC) receivers cannot be comparable to maximum likelihood (ML) receivers. Although one alternative method (real-valued sphere decoder) can approach the performance of ML receivers with near SIC complexity at high SNR, it cannot efficiently process phase shift keying (PSK) modulation. On the other hand, the complex-valued sphere decoder can process PSK, but with complicated

enumeration. Hence, a SIC based complex-valued sphere decoder is proposed with probabilistic tree pruning. The proposed complex-valued SD can reduce the tree span and save the complexity induced by enumeration schemes. Additionally, the basic principles of complex-valued sphere decoder can be naturally extended to an instantaneous union bound estimation for ML receivers. Its complexity is significantly reduced. However, the initial radius and candidates bound for the union bound estimation have not been studied, which have significant influences on the search complexity. Hence, a channel statistics based initial radius is derived based on the Rayleigh-Ritz theorem and the probability density function (PDF) of the channel matrix. The candidates bound can also be computed by the initial radius or the updated radius to reduce the tree span as the sphere decoder does.

(3) OFDM systems over rapidly time-varying channels. Inter-carrier interference (ICI) becomes the bottleneck for the OFDM systems over rapidly time-varying channels. The complexity of equalization for such scenarios will be high if a full matrix inversion is employed in the receivers, because the number of subcarriers for existing standards is beyond several hundred. To avoid a full matrix inversion, two novel matched filter (MF) based ICI cancellation algorithms have been proposed to mitigate the dominating ICI coefficients inside the banded channel matrix. In addition, a multi-segmental iterative channel estimation technique splits one OFDM symbol into several small segments by partial fast Fourier transform (PFFT), and obtains the channel impulse response estimates for segments. One can linearly interpolate the time-varying channels between segments with low complexity. It is found that the MF based ICI cancellation algorithms, incorporating multi-segmental iterative channel estimation are robust to the time variation.

# Contents

<b>List of Figures</b>	<b>viii</b>
<b>List of Tables</b>	<b>xv</b>
<b>Acknowledgements</b>	<b>xvi</b>
<b>Declaration</b>	<b>xvii</b>
<b>1 Introduction</b>	<b>1</b>
1.1 Overview of Previous Work on MIMO and OFDM Systems . . . . .	1
1.2 Contributions . . . . .	5
1.3 Thesis Outline . . . . .	8
1.4 Notations . . . . .	9
1.5 Publication List . . . . .	10
<b>2 Fundamental Techniques</b>	<b>12</b>
2.1 Introduction . . . . .	12

2.2	Channel Modelling . . . . .	13
2.2.1	Original Reference Model . . . . .	13
2.2.2	Modified Simulation Models . . . . .	15
2.3	Introduction to OFDM . . . . .	16
2.3.1	Basic Principles of OFDM . . . . .	17
2.3.2	Cyclic-Prefix . . . . .	17
2.3.3	Inter-Carrier Interference for OFDM Systems . . . . .	20
2.4	Pilot-Based Channel Estimation for OFDM Systems over Quasi-static Channels . . . . .	21
2.4.1	Fundamental Pilot Allocation for OFDM systems . . . . .	21
2.4.2	Least-Squares Channel Estimation . . . . .	24
2.4.3	MMSE Channel Estimation . . . . .	24
2.4.4	Interpolation techniques for OFDM systems . . . . .	25
2.4.5	Decision Directed Channel Estimation . . . . .	29
2.4.6	Simulation Results . . . . .	29
2.5	Pilot-Based Channel Estimation for MIMO-OFDM Systems Over Quasi-static Channel . . . . .	32
2.5.1	Superimposed Pilot-Based Channel Estimation . . . . .	33
2.5.2	Comb-Type Channel Estimation . . . . .	36

2.5.3	STBC and SFBC based Channel Estimation . . . . .	36
2.5.4	Simulation Results . . . . .	37
2.6	Detection Techniques for MIMO Systems with Spatial Multiplexing . . . . .	42
2.6.1	MIMO System Model . . . . .	42
2.6.2	Linear ZF Detection . . . . .	43
2.6.3	Linear MMSE Detection . . . . .	44
2.6.4	SIC Detection . . . . .	44
2.6.5	ML Detection . . . . .	46
2.6.6	Sphere Decoder . . . . .	48
2.6.7	Complex-valued Sphere Decoder . . . . .	52
2.6.8	Soft Processing for MIMO Systems . . . . .	55
2.7	Extrinsic Information Transfer Chart . . . . .	59
2.7.1	Application of EXIT Charts . . . . .	60
2.8	Equalization for OFDM Systems over Doubly Selective Channels . . . . .	63
2.8.1	Banded Channel Structure and Window Techniques . . . . .	64
2.8.2	Serial Equalization and Block Equalization . . . . .	67
2.8.3	Partial Fast Fourier Transform based Equalization . . . . .	69
2.8.4	LSQR Equalization . . . . .	70
2.9	Summary . . . . .	72

<b>3</b>	<b>Dynamic Pilot Allocation with Channel Estimation in Closed-Loop MIMO-OFDM Systems</b>	<b>73</b>
3.1	Introduction . . . . .	73
3.2	MIMO-OFDM System Model with Spatial Multiplexing . . . . .	75
3.3	DFT-based Channel Estimation for MIMO-OFDM Systems . . . . .	75
3.3.1	Pilot Allocation with Multiple Transmit Antennas . . . . .	75
3.3.2	DFT-based Channel Estimation . . . . .	76
3.4	Dynamic Pilot Allocation for MIMO Receivers and MIMO Iterative Pilot Search . . . . .	78
3.4.1	Dynamic Pilot Allocation Algorithm for Linear and SIC Receivers	78
3.4.2	Dynamic Pilot Allocation for ML Receivers . . . . .	80
3.4.3	Proposed MIMO Iterative Pilot Search . . . . .	81
3.5	Limited Feedback for Dynamic Pilot Allocation . . . . .	82
3.6	Simulation Results . . . . .	85
3.7	Summary . . . . .	92
<b>4</b>	<b>Sphere Decoding Algorithms for MIMO Detection and Bound Estimation</b>	<b>94</b>
4.1	Introduction . . . . .	94
4.2	System Model . . . . .	97
4.3	Complex Sphere Decoder with Successive Interference Cancellation based Tree Pruning . . . . .	98

4.3.1	Search Strategy and Successive Interference Cancellation Tree Pruning . . . . .	98
4.3.2	Additional conditions for CCB . . . . .	101
4.4	Bound Estimation for Maximum Likelihood Detection . . . . .	102
4.4.1	System model . . . . .	102
4.4.2	Channel-Statistics Based Initial Radius . . . . .	102
4.4.3	Modified Schnorr-Euchner Enumeration . . . . .	105
4.5	List Soft Processing based Complex Sphere Decoder . . . . .	105
4.5.1	Extrinsic LLR Calculation of LSD . . . . .	107
4.5.2	Scatter List Generation . . . . .	107
4.5.3	ML based Ordering . . . . .	108
4.6	Simulation Results . . . . .	109
4.7	Summary . . . . .	120

**5 Joint Iterative Receiver Design with Multi-Segmental Channel Estimation for OFDM Systems over Rapidly Varying Channels 121**

5.1	Introduction . . . . .	122
5.2	System model . . . . .	124
5.3	Matched Filter Parallel Interference Cancellation . . . . .	126
5.4	Proposed Multi-feedback Interference Cancellation . . . . .	127

5.4.1	Problem formulation and solution . . . . .	128
5.4.2	Comparison of soft interference cancellation and MAP detection .	130
5.5	Multi-Feedback Generation Mechanism . . . . .	130
5.5.1	Gibbs sampling based generation (GSG) . . . . .	131
5.5.2	Tree search based generation (TSG) . . . . .	131
5.5.3	Further discussion on generation mechanisms . . . . .	132
5.5.4	Reduced channel matrix for multi-feedback interference cancel- lation . . . . .	134
5.6	SINR Ordering for MBMF-SIC . . . . .	137
5.7	Multi-Segmental Channel Estimation . . . . .	138
5.7.1	Least-squares based MSCE . . . . .	138
5.7.2	MSE lower bound analysis . . . . .	139
5.8	Complexity Requirements of MBMF-SIC and MSCE . . . . .	141
5.9	Simulation Results . . . . .	143
5.10	Summary . . . . .	150
<b>6</b>	<b>Conclusions and Future Work</b>	<b>152</b>
6.1	Conclusion . . . . .	152
6.2	Future Work . . . . .	155



# List of Figures

2.1	Power spectrum of baseband signals of the output of FFT at the receiver, $T_{\text{OFDM}} = 0.0625s$ . . . . .	18
2.2	The cyclic prefix of OFDM symbol . . . . .	19
2.3	Block-type pilot allocation . . . . .	22
2.4	Comb-type pilot allocation . . . . .	23
2.5	Lattice-type pilot allocation . . . . .	23
2.6	Diagram of linear interpolation using LS channel estimation for pilots ( $N_p = 8$ ) over a Multipath ( $L = 4$ ) Rayleigh fading channel with $N_s = 32$ , SNR= 30 dB . . . . .	27
2.7	Block diagram of DFT-based Interpolation . . . . .	28
2.8	Block diagram of decision directed channel estimation for OFDM systems, where $(n - 1)$ denotes the previous OFDM symbol period . . . . .	30
2.9	BER performance of frequency domain interpolation techniques over quasi-static channels with $N_s = 64$ , $L = 4$ , $N_p = 8$ , and an exponential power delay profile . . . . .	31

2.10	MSE performance of frequency domain interpolation techniques over quasi-static channels with $N_s = 64, L = 4, N_p = 8$ , and an exponential power delay profile . . . . .	31
2.11	Block diagram of a MIMO-OFDM system . . . . .	34
2.12	The superimposed pilot allocation . . . . .	34
2.13	The diagram of comb-type pilot allocation . . . . .	36
2.14	MSE performance of $2 \times 2$ MIMO-OFDM system with $N_s = 128, N_p = 16$ over frequency selective slowly varying channels ( $L = 8, f_d T_{\text{OFDM}} = 10^{-4}$ ) . . . . .	38
2.15	MSE performance of $2 \times 2$ MIMO-OFDM system with $N_s = 128, N_p = 16$ over frequency flat rapidly varying channels ( $L = 1, f_d T_{\text{OFDM}} = 10^{-2}$ ) . . . . .	38
2.16	MSE performance of $2 \times 2$ MIMO-OFDM system with $N_s = 128, N_p = 16$ frequency selective rapidly varying channel ( $L = 8, f_d T_{\text{OFDM}} = 10^{-2}$ ) . . . . .	39
2.17	BER performance of $2 \times 2$ MIMO-OFDM system with $N_s = 128, N_p = 16$ over frequency selective slowly varying channels ( $L = 8, f_d T_{\text{OFDM}} = 10^{-4}$ ) . . . . .	40
2.18	BER performance of $2 \times 2$ MIMO-OFDM system with $N_s = 128, N_p = 16$ over frequency selective slowly varying channels ( $L = 1, f_d T_{\text{OFDM}} = 10^{-2}$ ) . . . . .	41
2.19	BER performance of $2 \times 2$ MIMO-OFDM system with $N_s = 128, N_p = 16$ over frequency selective slowly varying channels ( $L = 8, f_d T_{\text{OFDM}} = 10^{-2}$ ) . . . . .	41
2.20	A $4 \times 4$ MIMO system model . . . . .	43

2.21	The BER performance of SIC detection with different ordering techniques 4 × 4 MIMO with 8PSK . . . . .	47
2.22	The BER performance of linear-MMSE, SIC and ML detection for 4 × 4 MIMO with 16QAM . . . . .	48
2.23	The tree structure of sphere decoder . . . . .	51
2.24	The number of visited nodes (branches) comparison between SQRD and MMSE-SQRD with conventional SE-SD over 4 × 4 MIMO-8PSK . . . . .	52
2.25	An example of computation coordinate bound using trigonometric func- tion for the <i>i</i> th layer and 16QAM. . . . .	53
2.26	Iterative Detection and Decoding Structure . . . . .	56
2.27	The block diagram of mutual information estimates . . . . .	61
2.28	EXIT charts of convolutional code with different rate <i>R</i> and different con- straint length <i>K</i> . . . . .	61
2.29	EXIT charts of 4 × 4-4QAM MIMO system with Max-log MAP detection and a half rate convolutional code with constraint length 3 . . . . .	62
2.30	The illustration of the banded frequency channel structure . . . . .	63
2.31	MSE performance with various windowing techniques over rapidly vary- ing channels with $f_d T_{sa} = 0.03$ , $N = 128$ , $L = 8$ . . . . .	66
2.32	BER performance with various windowing techniques over rapidly vary- ing channels with $f_d T_{sa} = 0.03$ , $N = 128$ , $L = 8$ . . . . .	67
2.33	BER performance of serial equalization and block equalization over rapidly varying channels with $f_d T_{sa} = 0.01$ , $N = 128$ , $L = 8$ . . . . .	68

3.1	Comparison of BER between MIPS and exhaustive search of DPA for $N_t = N_r = 2, N_s = 16, N_p = 4, L = 4$ . . . . .	86
3.2	Comparison of BER and MSE between DPA and UPA for $N_t = N_r = 2, N_s = 16, N_p = 4, L = 4$ . . . . .	87
3.3	Comparison of BER between DPA and UPA for $N_t = N_r = 4, N_s = 32, N_p = 4, L = 4$ . . . . .	88
3.4	Comparison of BER between different feedback bits with SVQ for $N_t = N_r = 2, N_s = 16, N_p = 4, L = 4$ at 15 dB (The pilot positions for MIPS are perfectly known to the transmitter) . . . . .	89
3.5	Comparison of BER against $f_d T_{\text{OFDM}}$ with a fixed feedback delay of 20 ms and $P_e$ between DPA and UPA for $N_t = N_r = 2, N_s = 32, N_p = 4, L = 4$ . . . . .	91
3.6	Comparison of BER between DPA and UPA with different $N_p$ for $N_t = N_r = 2, N_s = 32, L = 4$ with linear receivers . . . . .	92
4.1	Two specific examples to exclude the constellation points erroneously: (a) In Case I, the phases are bounded by $[\frac{7\pi}{8} - \frac{3\pi}{4}]$ , which is supposed to cover the constellation points between $[\frac{3\pi}{2} 2\pi]$ . But these constellation points are excluded by the CCB, because they are not inside the bound. (b) Case II has the similar problem: the constellation point $\frac{\pi}{4}$ is not in the bound $[\frac{11\pi}{4} \frac{11\pi}{6}]$ . . . . .	101
4.2	The flow chart of scatter list generation . . . . .	108
4.3	Comparison of BER and the number of visited nodes per channel use with perfect channel estimates between the proposed and other CSDs for $N_t = N_r = 8$ with 8PSK. Note that the curves of Conventional SE-CSD, Pham-CSD, PTP-CSD and proposed-CSD w/ AC are superimposed in (a). . . . .	110

4.4	Comparison of BER and the number of visited nodes per channel use with perfect channel estimates between the proposed and other CSDs for $N_t = N_r = 8$ with 16QAM. Note that the curves of Conventional SE-CSD, Pham-CSD, PTP-CSD and proposed-CSD w/ AC are superimposed in (a). . . . .	111
4.5	Comparison of BER with LS channel estimation between the proposed and other CSDs for $N_t = N_r = 8$ with 8PSK. Note that the curves of Conventional SE-CSD, Pham-CSD, PTP-CSD and proposed-CSD w/ AC are superimposed . . . . .	112
4.6	Worst case complexity of CSDs against SNR, $N_t = N_r = 8$ with 16QAM	113
4.7	The number of visited nodes against increasing dimensions $N_t = N_r$ with 16QAM at SNR= 20 dB . . . . .	113
4.8	Comparison of FLOPS between the proposed and other CSDs for $N_t = N_r = 8$ with 16QAM and 8PSK . . . . .	115
4.9	Comparison of RMSE and FLOPS between the proposed and KBFS for $N_t = N_r = 8$ with $L = [-2, 0, 2]$ (4QAM case). The number of FLOPS of the exhaustive search is more than $10^6$ . . . . .	116
4.10	Comparison of SER performances of bound estimation (proposed) and simulation results for $N_t = N_r = [4, 6, 8]$ with $L = [-2, 0, 2]$ (QPSK case)	117
4.11	EXIT chart of conventional LSD and proposed LSD with different list size at 10 dB, $N_t = N_r = 8$ with 16QAM . . . . .	117
4.12	EXIT chart of conventional LSD and proposed LSD with $L = 512$ in different SNR, $N_t = N_r = 8$ with 16QAM . . . . .	118
4.13	BER performance of conventional LSD and proposed LSD with different iterations, $N_t = N_r = 8$ with 16QAM . . . . .	118

4.14	CDF of the number of visited nodes employing different list size at 12 dB, $N_t = N_r = 8$ with 16QAM . . . . .	119
5.1	System Model of MBBMF-SIC incorporating with MSCE . . . . .	125
5.2	The matrix representations of the banded channel matrix $\mathbf{H}_D$ , the $k$ th truncated channel matrix $\mathbf{H}_k$ , and the reduced channel matrix in blue square	126
5.3	pre-processing and post-processing SINR comparison for the $b$ th feed- back with different $Q$ . $N_s = 128, f_d T_{\text{OFDM}} = 0.65$ . . . . .	137
5.4	BER performance against SNR (dB) of MF-PIC, GMBMF-SIC, OGMBMF-SIC, TMBMF-SIC, OTMBMF-SIC, MF-SIC, banded MMSE-SIC, and AMFB in the 4th iteration with $f_d T_{\text{OFDM}} = 0.65$ . . . . .	144
5.5	BER performance against the number of iterations of MF-PIC, GMBMF-SIC, OGMBMF-SIC, MF-SIC, banded MMSE-SIC, and AMFB with $f_d T_{\text{OFDM}} = 0.65$ at SNR= 12 dB . . . . .	145
5.6	BER performance against $f_d T_{\text{OFDM}}$ of MF-PIC, OGMBMF-SIC, OTMBMF-SIC, MF-SIC, and banded MMSE-SIC in the 1st iteration at SNR = 12 dB . . . . .	146
5.7	BER performance against $f_d T_{\text{OFDM}}$ of MF-PIC, OGMBMF-SIC, OTMBMF-SIC, MF-SIC, and banded MMSE-SIC in the 4th iteration at SNR= 12 dB . . . . .	147
5.8	BER performance against SNR (dB) of MF-PIC, GMBMF-SIC, OGMBMF-SIC, MF-SIC, banded MMSE-SIC, and AMFB using MSCE in the 4th iteration with $f_d T_{\text{OFDM}} = 0.65$ . . . . .	148
5.9	BER performance against $f_d T_{\text{OFDM}}$ of OGMBMF-SIC and MF-PIC using MSCE and SBCE in the 4th iteration at SNR= 16 dB . . . . .	149

5.10 BER performance against the number of multi-feedback candidates $B$	
with $f_d T_{\text{OFDM}} = 0.65$ at SNR= 12 dB . . . . .	150

# List of Tables

3.1	MIPS for the $q$ th transmit antenna . . . . .	83
3.2	SVQ for optimum pilot allocation . . . . .	85
4.1	Proposed complex sphere decoder with SIC based tree pruning . . . . .	103
4.2	Sphere Decoding Algorithm for Minimum Euclidean Distance Search . .	106
5.1	Proposed MBMF-SIC for 4QAM . . . . .	133
5.2	Complexity comparison between different interference cancellation techniques for the $p$ th iteration . . . . .	142
5.3	Complexity comparison between different channel estimation techniques for the $p$ th iteration . . . . .	143

# Acknowledgements

I would like to show my sincere gratitude to my supervisors, Prof. Alister G. Burr and Dr. Rodrigo C. de Lamare, for their support and encouragement during my Ph.D. study.

I am very grateful to my thesis advisor, Dr. Yuriy Zakharov, whose insightful discussions and suggestions have benefited me.

I would also like to thank Dr. Peng Li, Dr. Yi Wang, and Dr. JingJing Liu and other colleagues in the Communications Research Group.

This thesis is dedicated to my parents and my wife Li Si.

# Declaration

Some of the research presented in this thesis has resulted in some publications. These publications are listed at the end of Chapter 1.

All work presented in this thesis as original is so, to the best knowledge of the author. References and acknowledgements to other researchers have been given as appropriate.

# Chapter 1

## Introduction

### Contents

---

<b>1.1 Overview of Previous Work on MIMO and OFDM Systems . . . . .</b>	<b>1</b>
<b>1.2 Contributions . . . . .</b>	<b>5</b>
<b>1.3 Thesis Outline . . . . .</b>	<b>8</b>
<b>1.4 Notations . . . . .</b>	<b>9</b>
<b>1.5 Publication List . . . . .</b>	<b>10</b>

---

### 1.1 Overview of Previous Work on MIMO and OFDM Systems

Wireless communication has become one of the fastest growing industries during the last few decades. Over 2 billion users are involved and make it one of largest research and business fields [1]. With the development of mobile devices, many technical challenges have arisen such as video streaming, online-gaming and real-time video meeting. Hence, the 3rd and 4th generations of cellular systems such as WiMAX [2], LTE, and LTE-Advanced [3] have been deeply studied and deployed in many developing and developed countries. However, a higher quality of service is required for the current systems, that is, higher data rate, higher spectral efficiency and more reliable link. These features must be provided with lower cost (reduced size of equipment and less energy consumption etc.).

For instance, MIMO-OFDM has been employed in LTE-Advanced. A tradeoff between complexity and performance may be required in the sense that the suboptimal detection methods have lower complexity at the expense of poorer performance compared to ML receivers. In addition, hundreds of subcarriers have been exploited in such systems, which makes the receiver design more complicated than narrow-band MIMO systems. Also, the wireless channels results in the distortion and superposition of the transmitted signals from multiple transmit antennas. Hence, lower-complexity and more robust channel estimation and detection techniques are critical to wireless communication systems.

To obtain a higher data rate, MIMO techniques are widely used in most current wireless communication systems [2, 3]. There are three significant advantages of multi-antenna systems: (1) energy efficiency. The signal to noise ratio (SNR) is improved; (2) diversity gain. The fading effect can be compensated for the replica of signals over different uncorrelated channels; (3) multiplexing gain. The data rate can be increased by transmitting independent data streams through multiple transmit antennas. The theoretical research on MIMO was pioneered by [4], which describes that the capacity for single user communication in fading channels can significantly increases using multiple antennas. Although the theoretical analysis on the capacity of MIMO channels has been established, the more practical algorithms to achieve the capacity are still waiting for further study. Prior to the analytical work, the Bell Lab space time (BLAST) receivers have been proposed in [5] and [6]. It shows that an enhanced spectral efficiency 20 bits/Hz/s can be achieved. The advantage of multiple antennas techniques is to transmit or receive several signals carrying same information to combat with the faded channels. Hence, the fading can be beneficial in multi-antenna systems rather than detrimental in the single-antenna systems. The utilization of multi-antenna techniques has been extended in terms of space-time coding (STC) [7, 8], which achieves a higher diversity than the spatial multiplexing technique at the expense of capacity loss [9]. In other words, a fundamental tradeoff between diversity gain and multiplexing gain may exist. In [10], the diversity and multiplexing tradeoff has been well discussed to evaluate the performance for existing schemes and possibly new schemes, and it concludes that the diversity gain and multiplexing gain can be simultaneously achieved. However, the achievable data rate can be much lower than the capacity of MIMO channels, once the diversity gain is realized [9]. For space-time block codes (STBC), a general framework has been studied in [11]. Furthermore, the coding gain of STC can be further improved using space-time trellis codes

in [7, 12–14]. For spatial multiplexing, linear detection cannot realize any receive diversity, and successive interference cancellation (SIC) based receivers can only exploit coding gain [15, 16]. Hence, the approximate ML receivers (sphere decoder (SD)) have been thoroughly investigated to extract full receive diversity and achieve the optimum tradeoff between the complexity and performance. The SD is originally based on [17] to solve a Non-deterministic Polynomial-time hard (NP-hard) problem, but the authors in [18, 19] studied the SD further for MIMO channels, which can obtain near-ML performance with significant complexity reduction. In [20], the complexity of the proposed complex-valued SD is close to that of the conventional SIC receiver at high signal to noise ratio (SNR). Additionally, the expected complexity of Fincke and Pohst-SD has been studied in [21], which can be considered as an indicator for the complexity of the Schnorr and Euchner (SE)-SD. Furthermore, the authors have presented an exact performance analysis of ML detection with different modulation schemes in [22], which also give an insight into SD in bit error rate (BER).

Although the performance of SD is significantly improved, there is still a large gap between the achievable capacity of SD and the capacity of MIMO channels. Iterative detection and decoding (IDD) has attracted significant attention within the last 20 years after Turbo Codes [23] appeared, because of the near-capacity performance. In [24–27], the effectiveness of the turbo principle has been validated in different fields. The authors in [28] proposed a low complexity list sphere decoder (LSD) based IDD technique to reach the capacity of MIMO channels. The basic principles of SD can also be extended to the instantaneous union bound estimation for ML receivers, which will be discussed in Chapter 4.

OFDM as a prevailing modulation scheme has been investigated for decades and adopted in many recent wireless communication standards such as the Digital Video Broadcasting (DVB) based schemes [29, 30] and some 4G based cellular wireless communication systems [2, 3]. The OFDM systems have been first studied in [31–33], and the authors pointed out the fundamental principles. Furthermore, OFDM can provide an effective mean of converting the frequency-selective channel into multiple frequency-flat channels and eliminating the inter-symbol interference with a cyclic-prefix [34, 35]. Hence, the design of the receiver for OFDM systems over a slowly time-varying channel becomes simple. This is because the orthogonality between subcarrier will be not

destroyed if the cyclic prefix is longer than the channel impulse response [36]. To mitigate the detrimental effects caused by the channels, the channel state information (CSI) is needed for coherent detection in OFDM systems [37]. Although differential modulation techniques do not require channel estimation, it leads to lower data rates and noticeable performance loss of 3 dB compared to coherent detection [38]. Hence, the coherent detection is more preferred, and channel estimation techniques have been broadly investigated. For example, the pilot-symbol-aided channel estimation (PACE) is a most common approach used in OFDM systems. The PACE can be performed using Least Squares (LS) estimation, and then one can interpolate the channel in frequency or time domain or in both domains. Several common interpolation schemes have been well discussed in [37, 39–41]. Furthermore, adaptive filter based channel estimation for OFDM systems has been studied in [42]. Compared to single antenna OFDM systems, the PACE for MIMO-OFDM becomes more complex. This is because the signals from multiple transmit antennas are superimposed. To mitigate the effects of inter-antenna interference (IAI) for channel estimation, the following methods were proposed. The STBC and space frequency block code (SFBC) [43–45] have been employed for MIMO-OFDM channel estimation, but the channel must remain almost unchanged during several time periods or across several subcarriers. In [46, 47], a superimposed pilots based LS channel estimation for MIMO-OFDM systems has been thoroughly investigated. The correlation of received pilot signals and original pilots are used to obtain channel estimates, and the prior assumption about the channel is not needed. However equispaced pilot allocation must be employed to avoid significant mean square error (MSE) performance degradation. The authors in [48] proposed another scheme to place null subcarriers to avoid IAI, which can be easily integrated with interpolation techniques for SISO-OFDM systems. A similar scheme has been adopted by WiMAX [2]. However, these techniques are based on fixed pilot allocation (equispaced and equipower) in the absence of any prior knowledge of channels. Although the optimum MSE performance can be achieved using equispaced pilots [49–51], this pilot pattern cannot significantly improve the performance of interest such as SER and capacity. Hence, dynamic pilot allocation (DPA) for SISO-OFDM and MIMO-OFDM systems has been studied in [52–55] to insert the pilots into deep faded subcarriers at the expense of moderate MSE performance degradation. The detailed discussion of DPA will be presented in the following chapters.

The high mobility of OFDM systems is a major issue, which has been investigated in

many works. The inter-carrier interference (ICI) of OFDM systems brought by the high mobility has a detrimental effect on the channel estimation and equalization. In [56, 57], the authors exploit the banded channel matrix in the frequency domain by a time-domain window, which can maximize signal to interference plus noise ratio (SINR) or signal to interference ratio (SIR) of desired subcarriers. The ICI cancellation can be performed in a serial or block form based on the banded channel matrix. Two pre-equalizers in [58, 59] mitigate the effects of time variations to obtain an equivalent diagonal channel matrix. One has developed a partial FFT method to reduce the dimension of equalizer, and the other has formulated the pre-equalizer by minimizing ICI power beyond the diagonal. The ICI is modelled using derivatives of the channel amplitude, and iterative decision feedback equalization (DFE) is performed to obtain a single tap equalizer in frequency domain [60]. A similar idea is implemented in [61] to obtain the diagonal matrix using mean values of transmit symbols based on log-likelihood ratio (LLR) values from the channel decoder. In [62], the authors propose a MF-SIC scheme for the banded channel matrix, with iterative SIC-based single-burst channel estimation (SBCE). Another method is to approximate the symbol estimates using the sequential LSQR algorithm with selective parallel interference cancellation (PIC), which is based on the banded structure of the modified channel matrix in the time or the frequency domain [63]. Some other iterative cancellation techniques are also presented in [64, 65] employing a novel LLR criterion or a novel cancellation order. Compared to these cancellation techniques, a low-complexity maximum a posteriori probability (MAP) based detection method for mobile OFDM can be found in [66] with successively reduced search space, which can be treated as a variation of interference cancellation with a MAP criterion. In Chapter 5, two novel joint receiver designs will be presented for OFDM systems over rapidly time-varying channels to combat the high mobility using iterative detection and channel estimation.

## 1.2 Contributions

In the previous section, an overview of fundamental techniques is presented for MIMO and OFDM systems. It can be found that high spectral efficiency must be achieved with low cost algorithms. Given this principle, major contributions of this thesis are summarized as follows:

- The conventional pilot allocation in PACE for MIMO-OFDM systems is fixed, but its performance will not be improved significantly with the increasing number of pilots in fixed positions. Two similar optimized pilot allocation schemes for SISO-OFDM and Alamouti based MISO-OFDM have been proposed in [52, 53]. Additionally, these methods are only designed for linear receivers with a single-receive antenna. Hence, the optimized pilot allocation for MIMO-OFDM systems is required to be investigated. To extend the use of DPA to MIMO-OFDM systems with a feedback link, a low-complexity optimized pilot allocation search strategy namely MIMO iterative pilot search (MIPS) has been developed. The search in the space domain is implemented antenna by antenna, and the search in the frequency domain is similarly performed subcarrier by subcarrier. The SER metrics of choosing the optimum pilot allocation for different MIMO-OFDM receivers (linear, SIC, ML) have been derived based on SINR and minimum Euclidean distance, respectively. For a limited feedback channel, the feedback overhead of DPA for MIMO-OFDM systems is much higher than that for SISO-OFDM systems. Thus a stack vector quantization (SVQ) technique has been proposed to reduce the overhead of DPA for MIMO-OFDM systems. Simulation result demonstrate that DPA, with a feedback channel or a limited feedback channel, can significantly improve the BER performance at expense of moderate MSE degradation for MIMO-OFDM systems. Furthermore, a discussion is presented to validate a selection diversity realized by DPA that cannot be achieved by uniform pilot allocation (UPA).
- Although the complexity of a real-valued SD with a real-valued enumeration scheme is moderate compared to a conventional complex-valued SD, it cannot efficiently process phase shift keying modulation schemes, and must search double the number of detection layers. The complex-valued SD does not have such drawbacks. Furthermore, the conventional real-valued or complex-valued SD requires a relatively large radius to enumerate candidates first and then starts examining these enumerated branches. This procedure is very inefficient. A SIC based search strategy has been developed to reach a full branch first and then enumerate fewer possible candidates. With the aid of probabilistic tree pruning, it covers a smaller number of candidates than the conventional complex-valued SD in the sense that the candidates obtained by the enumeration is further reduced for a particular detection layer. Hence, the proposed complex-valued SD can reach the ML solution

much faster than the conventional ones.

- Compared to the conventional SD, the LSD requires more computational efforts, because more branches are involved in the search. Its complexity varies significantly with the number of transmit antenna, the order of modulation and SNR values, which are undesirable for the hardware implementation. For further reduction of complexity in LSD, the basic principles of SIC based complex-valued SD have been extended to the LSD, but the search is proceeded within several separate subtree search namely scatter list generation produced by the proposed complex-valued SD above. Additionally, the remaining branches within the radius can be filled by the ML solution in lower detection layers to construct several new full branches. These full branches can be ordered or pruned according to the full path metrics, the process of which is called ML based ordering. Hence, the list generation can be performed more efficiently than the single tree search, and this generation scheme suits pipeline implementation in hardware.
- The instantaneous union bound for ML receivers has been derived from the real-valued SD. For the conventional real-valued SD based union bound estimation, the initial radius and the candidates enumeration have not been considered. However, the initial radius and the enumeration is very important for complexity reduction. Thus a channel statistics based initial radius is obtained by the Rayleigh-Ritz theorem and the cumulative distribution function (CDF) of the channel matrix, and the lower and upper bounds of enumeration can be determined by the radius. The overall complexity of the union bound estimation is reduced by introducing the initial radius and the candidates enumeration.
- The high mobility of OFDM systems results in ICI, which degrades the performance of the receivers and places an obstacle on channel estimation. several conventional methods for such scenarios use the banded channel matrix in the frequency domain or the time domain to reduce the complexity of equalizers. However, their complexity and performance are still not satisfactory due to employing matrix inversion and residual ICI inside the band. Two proposed joint matched filter based ICI cancellation algorithms with multi-segmental channel estimation (MSCE) have been applied to OFDM systems over fast time-varying channels. Because these two algorithms are based on the matched filter with one or multiple feedback candidates for ICI cancellation, their complexity is reduced owing to no

matrix inversion required. For multi-segmental channel estimation, the received signals during one OFDM symbol periods is split into multiple segments by partial fast Fourier transform (PFFT). Hence, the channel estimation accuracy is improved by linear interpolation with multiple segments rather than one segment in single burst channel estimation.

### 1.3 Thesis Outline

The thesis is organized as follows:

- In Chapter 2, fundamentals of MIMO and OFDM systems are introduced. Firstly, the channel modelling based on Jakes' model is presented, and system models for OFDM and MIMO-OFDM systems are formulated as well as pilot based channel estimation for these two systems. Secondly, the detection methods for MIMO systems including zero-forcing (ZF) detection, minimum mean square error (MMSE) detection, SIC, and ML detection are described in detail. The extrinsic information transfer chart (EXIT) chart for iterative behaviours of detection and decoding is also presented. Finally, equalization given the banded channel matrix for OFDM systems over doubly selective channels is discussed.
- Chapter 3 presents a joint channel estimation and detection design with DPA for MIMO-OFDM systems over slowly time-varying channels. For a DFT channel estimator, the channel estimation errors variance corresponding to a particular pilot allocation is derived. This variance is used for SINR and minimum Euclidean distance calculation, which are used for finding the optimum pilot allocation. MIMO iterative pilot search (MIPS) algorithm is then proposed to reduce the complexity of the pilot allocation search. Stacked vector quantization (SVQ) is proposed to reduce the overhead of DPA for MIMO-OFDM systems with a limited feedback channel. Simulation results of DPA and UPA for MIMO-OFDM systems are illustrated to verify the SER performance improvement at the expense of MSE degradation and several feedback bits.
- In Chapter 4, an efficient complex-valued SD is proposed based on a SIC based

search strategy and probabilistic tree pruning. Additional conditions for complex SE enumeration are presented to ensure that all possible candidates are covered in the search. To extend the basic principles of SD to LSD, a scatter list generation method is proposed as well as an ML based ordering. Also, a low-complexity instantaneous union bound for ML receivers is estimated based on the real-valued SD, with a channel statistic initial radius and lower and upper bounds for enumeration. BER performance and complexity of the proposed complex-valued SD and the corresponding LSD are demonstrated, and compared with that of other complex-valued SDs. The numerical results show the advantages of the real-valued SD based instantaneous union bound over other real-valued SD based methods in terms of FLOPS and root mean square error (RMSE).

- Chapter 5 proposed two novel MF based ICI cancellation algorithms with multi-segmental iterative channel estimation. The first one, MF-PIC mitigates the ICI inside the band in one shot. The second one, a dimension reduced multi-feedback MF based SIC (MBMF-SIC) algorithm sequentially cancels the ICI inside the band with the aid of SINR ordering. Two generation schemes for multi-feedback candidates are also discussed. Simulation results demonstrate the superiority of the two MF based ICI cancellation algorithms in the complexity and the BER performance compared to other ICI cancellation algorithms.
- Conclusions are drawn and a brief discussion of future research is presented in Chapter 6.

## 1.4 Notations

$[\mathbf{A}]_{m,n}$	the element in $m$ th row and $n$ th column of the matrix $\mathbf{A}$
$\mathbf{a}_m$	the $m$ th vector
$\mathbf{A}_m$	the $m$ th matrix
$\Re$	real part
$\Im$	imaginary part
$\mathbf{I}_N$	$N \times N$ identity matrix
$()^*$	complex conjugate
$()^T, ()^H$	matrix transpose and Hermitian transpose

$\mathbb{E}$	expectation operator
$\mathbb{C}_{m \times n}$	space of complex valued matrix of size $m$ by $n$
$\mathbb{R}_{m \times n}$	space of real valued matrix of size $m$ by $n$
$\text{diag}\{\mathbf{a}\}$	a diagonal matrix whose diagonal elements are based on the elements from the vector $\mathbf{a}$
$\mathcal{D}(\mathbf{A})$	a column vector which is created from the diagonal elements of the matrix $\mathbf{A}$
$()^\dagger$	pseudo inverse
$\otimes$	Kronecker product
$\odot$	element-wise multiplication between two matrices

## 1.5 Publication List

### Journal Papers

1. L. Li, A. G. Burr and R. C. de Lamare, “Low-Complexity Multi-feedback ICI Cancellation Algorithms for OFDM Systems over Doubly Selective Channels”, *IEEE Trans. Commun.*, under preparation, 2013.
2. L. Li, R. C. de Lamare and A. G. Burr, “Dynamic Pilot Allocation with Channel Estimation in Closed-Loop MIMO-OFDM systems”, *IET Commun.*, submitted in the second round review, 2013.
3. L. Li, R. C. de Lamare and A. G. Burr, “Complex Sphere Decoding with a Modified Tree Pruning and Successive Interference Cancellation and Soft Processing”, *IET Commun.*, under preparation, 2013.

### Conference Papers

1. L. Li, R. C. de Lamare and A. G. Burr, “Dynamic Pilot Allocation Channel Estimation with Spatial Multiplexing for MIMO-OFDM Systems”, in *Proc. IEEE Veh. Technol. Conf. (VTC Spring)*, pp. 1-5, Budapest, Hungary, May 2011.

2. L. Li, R. C. de Lamare and A. G. Burr, “Low-Complexity Dynamic Pilot Allocation for Channel Estimation in MIMO-OFDM Systems with Spatial Multiplexing”, in *Proc. Wireless Conf. (EW)*, pp. 1-7, Vienna, Austria, Apr. 2011.
3. L. Li, R. C. de Lamare and A. G. Burr, “Complex Sphere Decoding with A Modified Tree Pruning and Successive Interference cancellation”, in *Proc. Int. Symp. on Wireless Commun. Syst. (ISWCS)*, pp. 226-230, Paris, France, Aug. 2012.
4. J. Liu, P. Li, L. Li, R. C. de Lamare and A. G. Burr, “Iterative QR Decomposition-Based Detection Algorithms with Multiple Feedback and Dynamic Tree Search for LDPC-Coded MIMO Systems”, *Sensor Signal Process. for Defence (SSPD)* pp. 33, London, UK, Jan. 2011.
5. Y. Wang, P. Li, L. Li, A. G. Burr and R. C. de Lamare “Irregular Code-aided Low-Complexity Three-stage Turbo Space Time Processing”, in *Proc. Int. Symp. on Wireless Commun. Syst. (ISWCS)*, pp. 604-608, Aachen, Germany, Nov. 2011.
6. L. Li, A. G. Burr and R. C. de Lamare, “Joint Iterative Receiver Design and Multi-Segmental Channel Estimation for OFDM Systems over Rapidly Time-Varying Channels”, in *Proc. IEEE Veh. Technol. Conf. (VTC Spring)*, pp. 1-5 , Dresden, Germany, Jun. 2013.

# Chapter 2

## Fundamental Techniques

### Contents

---

<b>2.1</b>	<b>Introduction</b>	<b>12</b>
<b>2.2</b>	<b>Channel Modelling</b>	<b>13</b>
<b>2.3</b>	<b>Introduction to OFDM</b>	<b>16</b>
<b>2.4</b>	<b>Pilot-Based Channel Estimation for OFDM Systems over Quasi-static Channels</b>	<b>21</b>
<b>2.5</b>	<b>Pilot-Based Channel Estimation for MIMO-OFDM Systems Over Quasi-static Channel</b>	<b>32</b>
<b>2.6</b>	<b>Detection Techniques for MIMO Systems with Spatial Multiplexing</b>	<b>42</b>
<b>2.7</b>	<b>Extrinsic Information Transfer Chart</b>	<b>59</b>
<b>2.8</b>	<b>Equalization for OFDM Systems over Doubly Selective Channels</b>	<b>63</b>
<b>2.9</b>	<b>Summary</b>	<b>72</b>

---

### 2.1 Introduction

This chapter presents and discusses fundamentals of MIMO and OFDM systems, some of which are incorporated in the following chapters for comparison or as the motivation of ideas. Firstly, we will introduce the basic concepts of OFDM and MIMO systems as well

as channel modelling. Secondly, pilot-based channel estimation techniques are discussed. Finally, the data detection for MIMO systems is covered, which can be naturally extended to other systems such as OFDM systems over time-varying channel, cooperative MIMO systems. This is because the channel matrices for these systems are similar to that of MIMO channels.

## 2.2 Channel Modelling

Channel estimation techniques for OFDM systems are primarily investigated in the following chapters. Hence, we introduce the time-varying fading channel generated by the Jakes model [67] in this section, and then discuss these models. Channel modelling has been studied for decades, and various channel models have been formulated in different ways. However, Clarke's and its simplified version (Jakes' model) were proposed and are widely used in wireless communications since the 1960s [67, 68], due to their simplicity. However, the weakness of Jakes' model is the difficulty of generating multiple uncorrelated channels [69]. Furthermore, the signals produced by Jakes' model are not wide-sense stationary [70]. Here we only discuss Jakes' model and point out some modifications made to Jakes' model in [69–72]. The improved model proposed in [72] is used for the following simulation.

### 2.2.1 Original Reference Model

Clarke's reference model considers several incoming rays with random path gains, angles and initial phases, which arrive at the mobile receiver simultaneously. The mathematical expression of Clarke's model is given by [67, 68]

$$g(t) = E_0 \sum_{n=1}^N C_n \exp(j(w_d t \cos a_n + \phi_n)), \quad (2.1)$$

where  $E_0$  is a scaling factor,  $C_n$ ,  $a_n$ ,  $\phi_n$ , for the  $n$ th propagation path, denote the random path gains, incoming angles and initial phases, and  $w_d$  is the maximum radian Doppler

frequency shift, respectively [72]. Hence, a complex form of (2.1) can be rewritten as

$$\begin{aligned}
g(t) &= g_r(t) + j g_i(t) \\
&= E_0 \sum_{n=1}^N C_n \cos(w_d t \cos a_n + \phi_n) \\
&\quad + j E_0 \sum_{n=1}^N C_n \sin(w_d t \cos a_n + \phi_n).
\end{aligned} \tag{2.2}$$

The autocorrelation and cross-correlation functions of the channel simulator in (2.2) can be given as [67]

$$\begin{aligned}
R_{g_r g_r}(\tau) &= J_0(w_d \tau) \\
R_{g_i g_i}(\tau) &= J_0(w_d \tau) \\
R_{g_r g_i}(\tau) &= 0 \\
R_{g_i g_r}(\tau) &= 0 \\
R_{gg}(\tau) &= 2J_0(w_d \tau) \\
R_{|g|^2 |g|^2} &= 4 + 4J_0^2(w_d \tau),
\end{aligned} \tag{2.3}$$

where  $R_{xx}(\tau) = \mathbb{E}\{x(t)x^*(t + \tau)\}$  and  $J_0(\cdot)$  is the 0th order Bessel function of the first kind. For normalization, let  $\sum_{n=0}^{N-1} \mathbb{E}[C_n^2] = 1$  and  $E_0 = \sqrt{2}$ . For Clarke's model, the PDF of the fading envelope  $|g|$  and the phase  $\Theta_g(t) = \arctan[g_r(t), g_i(t)]$  follow the Rayleigh and the uniform distribution, respectively. The mathematical expressions of PDF are given by

$$\begin{aligned}
f_{|g|}(x) &= x \exp\left(-\frac{x^2}{2}\right), x \geq 0 \\
f_{\Theta_g(t)} &= \frac{1}{2\pi}, \theta \in [-\pi, \pi].
\end{aligned} \tag{2.4}$$

To reduce the number of low-frequency oscillators or propagation paths  $N$  needed for the generation of (2.2), several important assumptions are made as follows [67]:

$$\begin{aligned}
C_n &= \frac{1}{\sqrt{N}} \\
a_n &= \frac{2\pi n}{N}, n = 1, 2, \dots, N \\
\phi_n &= 0, n = 1, 2, \dots, N.
\end{aligned} \tag{2.5}$$

Substituting (2.5) into (2.2), a new mathematical expression of Clarke's model after rearrangement is given by

$$\begin{aligned}
g(t) &= g_r(t) + j g_i(t) \\
&= \frac{2}{\sqrt{N}} \sum_{n=0}^M a_n \cos(w_n t) + j \frac{2}{\sqrt{N}} \sum_{n=0}^M b_n \cos(w_n t),
\end{aligned} \tag{2.6}$$

where  $N = 4M + 2$ ,  $M$  denotes the reduced number of low-frequency oscillators, and

$$\begin{aligned}
 a_n &= \begin{cases} \sqrt{2} \cos \beta_0, n = 0 \\ 2 \cos \beta_n, n = 1, 2, \dots, M \end{cases} \\
 b_n &= \begin{cases} \sqrt{2} \sin \beta_0, n = 0 \\ 2 \sin \beta_n, n = 1, 2, \dots, M \end{cases} \\
 \beta_n &= \begin{cases} \frac{\pi}{4}, n = 0 \\ \frac{\pi n}{M}, n = 1, 2, \dots, M \end{cases} \\
 w_n &= \begin{cases} w_d, n = 0 \\ w_d \cos \frac{2\pi n}{N}, n = 1, 2, \dots, M \end{cases}.
 \end{aligned} \tag{2.7}$$

From (2.6), we can observe that the number of low-frequency oscillators is reduced from  $N$  to  $M + 1$ . Note that  $N = 4M + 2$ . Hence, Jakes' model is a simplified Clark's model with fixed phase, amplitude and arrival angle for each propagation path, which lead the simulation model to be deterministic. As mentioned above, the signals produced by (2.6) are not wide-sense stationary. This is because the sums of fixed amplitude and random phase sinusoids are not ergodic. Thus the time averages may or may not be equal to the stochastic averages with these signals [70].

## 2.2.2 Modified Simulation Models

To solve the problem of generating multiple uncorrelated channels for frequency selective channels and MIMO channels, the authors in [69] proposed to use Walsh-Hadamard code-words to maintain the orthogonality between the propagation paths before the summation. In [70], random phase shifts in low frequency oscillators have been introduced to remove the non-stationary problem in Jake's model and its derivatives [67, 69, 71]. However, the random phase shifts cannot improve the mismatch between the second-order statistics of these modified models and that of the reference model in (2.3). Furthermore, the second-order statistics of the quadrature components and the envelope in the simulation models does not match that in the reference model even with infinite number of sinusoid functions [73]. To avoid these problems discussed above and generate multiple uncorrelated channels with a small number of low-frequency oscillators, an improved Jakes' model, which reintroduces the randomness to the path gain, the Doppler frequency, and the ini-

tial random phase, was proposed in [72] with good statistical properties. Here, the exact derivation and mathematical expression of the improved Jakes' model is not provided. More details can be found in [72]. The improved simulation model will be used to generate the wide-sense stationary uncorrelated scattering Rayleigh fading channels for MIMO and OFDM systems. In the following chapters, this improved simulation model will be referred to as Jakes' model for simplicity.

## 2.3 Introduction to OFDM

Orthogonal frequency division multiplexing (OFDM) is one promising multi-carrier technique adopted by many wireless communication standards. Thanks to fast Fourier transform (FFT) algorithm, OFDM becomes more popular due to its simple implementation. The basic idea of OFDM systems is to transmit symbols over multiple orthogonal subcarriers, so IFFT is performed with transmitted symbols at the transmitter, and FFT is performed with received symbols at the receiver. The basic principles and details of OFDM transmission was presented in [31–33]. Another advantage of OFDM is to convert a frequency-selective wideband channel into several frequency-flat narrow band channels. Thus the complexity of receiver for OFDM systems is much simpler than that of receivers in single-carrier systems. However, OFDM systems will be sensitive to channel variation, which induce inter-carrier interference (ICI) by destroying the orthogonality between subcarriers. The rest of the section is structured as follows. In Subsection 2.3.1, the basic principles of OFDM systems is presented. Subsection 2.3.2 discusses the insertion of cyclic-prefix (CP) to mitigate the inter-symbol interference (ISI) in OFDM systems and the system model of OFDM systems over quasi-static channels. ICI in OFDM systems over time-varying channels is formulated in Subsection 2.3.3.

### 2.3.1 Basic Principles of OFDM

Defining  $s(k)$  as the symbol transmitted over the  $k$ th subcarrier, and  $x(n)$  as the received symbol at the  $n$ th time index, the output of IFFT at the transmitter is given by

$$x(n) = \frac{1}{\sqrt{N_s}} \sum_{k=0}^{N_s-1} s(k) e^{j2\pi kn/N_s} \text{ for } n = 0, 1, \dots, N_s - 1, \quad (2.8)$$

where the quantity  $n, k$  denote the time index in an OFDM symbol period and subcarrier index, respectively, and the number of subcarriers denotes  $N_s$ . Hence, we do not introduce the multi-path channel effects and noise. Thus the received OFDM symbol at the  $n$ th time  $r(n) = x(n)$ . In the receiver, the output of FFT at the  $k$ th subcarrier is given by

$$y(k) = \frac{1}{\sqrt{N_s}} \sum_{n=0}^{N_s-1} r(n) e^{-j2\pi kn/N_s}. \quad (2.9)$$

Substituting (2.8) into (2.9), equation (2.9) after rearrangement becomes:

$$\begin{aligned} y(k) &= \frac{1}{N_s} \sum_{n=0}^{N_s-1} \sum_{q=0}^{N_s-1} s(q) e^{j2\pi qn/N_s} e^{-j2\pi kn/N_s}, N_s - 1 \\ &= \sum_{n=0}^{N_s-1} \sum_{q=0}^{N_s-1} s(q) e^{j2\pi n(q-k)/N_s} \\ &= \frac{1}{N_s} s(k) N_s + \underbrace{\sum_{q=0, q \neq k}^{N_s-1} s(q) \sum_{n=0}^{N_s-1} e^{j2\pi n(q-k)/N_s}}_0 \\ &= s(k) \text{ for } k = 0, 1, \dots, N_s. \end{aligned} \quad (2.10)$$

From (2.10), the received symbol  $y(k) = s(k)$  is not affected by the symbols from other subcarriers. To explain the orthogonality between subcarrier clearly, power spectrum of the output of FFT in (2.10) is plotted in Fig. 2.1, where  $T_{\text{OFDM}}$  denotes the period of one OFDM symbol. This plot implies that the waveforms of different subcarriers are overlapped, but for one particular subcarrier frequency, the sidelobes from other subcarriers are equal to zero. In other words, the orthogonality between subcarriers is maintained.

### 2.3.2 Cyclic-Prefix

According to the discussion in Subsection 2.3.1, the orthogonality can be maintained without the distortion brought by the multipath channels. However, it may not be true for

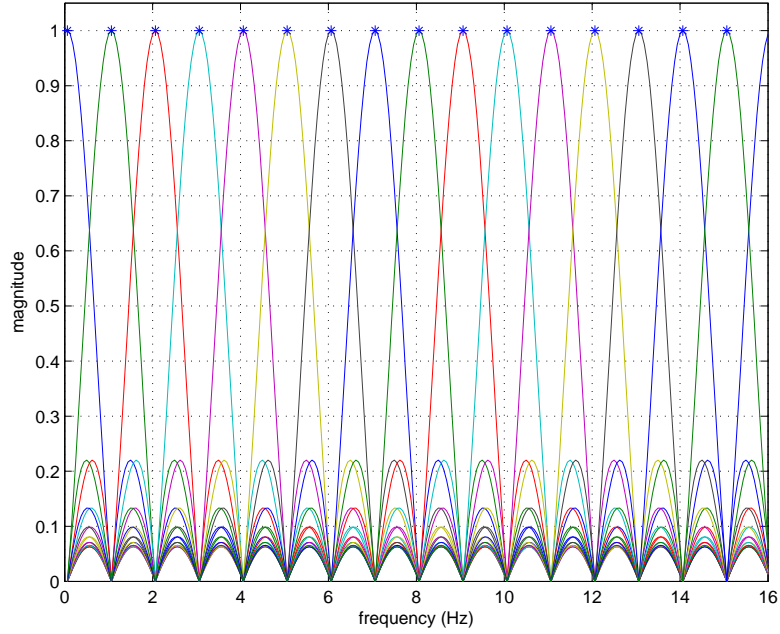


Figure 2.1: Power spectrum of baseband signals of the output of FFT at the receiver,  $T_{\text{OFDM}} = 0.0625s$

real wireless communication. In this subsection, we will discuss the effects of multi-path channels on OFDM systems. The received signal in a discrete form, with a multi-path channel and noise, can be expressed as

$$r(n) = \sum_{l=0}^{L-1} h_{ul}(n, l)x(n-l) + z(n), \quad (2.11)$$

where the quantity  $h_{ul}(n, l)$  denotes the channel impulse response for the  $n$ th time index and the  $l$ th channel path, and the quantity  $z(n)$  denotes AWGN noise at the  $n$ th time index. Additionally, the channel for each path is assumed to be quasi-static  $h_{ul}(n, l) = h_{ul(l)}$  for  $n = 0, 1, \dots, N_s - 1$ , which implies that the channel remain constant for one OFDM symbol period. From (2.11),  $x(-l) = 0$  for the first received OFDM symbol. However, it may not be true for the following received OFDM symbols, that is,  $x(-l) \neq 0$ . In other words, the signals from the previous OFDM symbols interfere with the current received OFDM symbols. Hence, Inter-symbol Inteference (ISI) exists to jeopardizes the orthogonality among subcarriers. Thus Guard interval is required to be inserted into the OFDM symbol. There are two different ways to protect the OFDM symbol from ISI. One is the zero padding (ZP) that appends zeros [74]. The other is CP [33], which copies the last several symbols  $x(n), n = N_s - L, \dots, N_s - 1$  and inserts them at the beginning

of the OFDM symbol at the transmitter as shown in Fig. 2.2. Hence, the period of OFDM symbol becomes  $N_s + L$  at least, where  $L$  denotes the number of channel paths. Hence, the ISI from the previous OFDM symbols only affect the samples in the CP, which implies that the orthogonality between subcarriers is not affected. Furthermore, perfect synchronization and channel statistical information known to receivers are assumed in the remainder of the thesis.

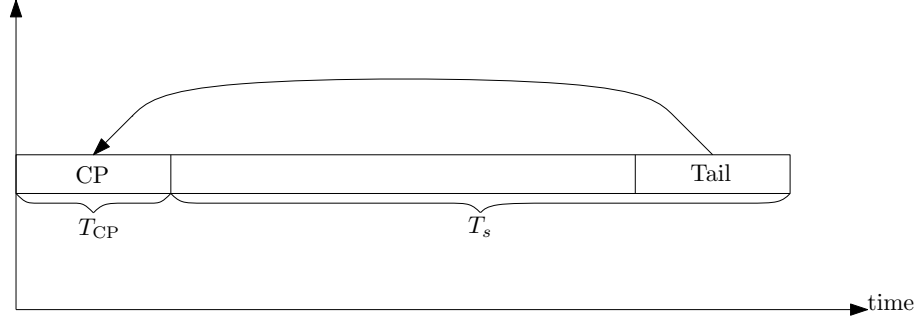


Figure 2.2: The cyclic prefix of OFDM symbol

With the use of CP, the received signal  $r(n)$  after the FFT becomes [33] :

$$\begin{aligned} y(k) &= \sum_{l=0}^{L-1} r(n) e^{-j2\pi kn/N_s} \\ &= h_{df}(k) s(k) + v(k), \end{aligned} \quad (2.12)$$

where the quantities  $h_{df}(k) = \sum_{n=0}^{N_s-1} h_{tl}(l) e^{-j2\pi kn/N_s}$ ,  $s(k)$ ,  $y(k)$ , and  $v(k)$  denote the  $k$ th subcarrier's channel frequency response, the transmitted symbol over the  $k$ th subcarrier, received symbol over the  $k$ th subcarrier, and the additive white Gaussian noise (AWGN) after the FFT for the  $k$ th subcarrier, respectively. Note that the number of channel paths equals  $L$ , so the only first  $L$  columns of discrete Fourier transform (DFT) matrix will be used in a matrix form. Defining  $\mathbf{y} = [y(0), \dots, y(k), \dots, y(N_s - 1)]^T$  as a received symbol vector,  $\mathbf{F}_L$  as a truncated  $N_s$ -point unitary DFT matrix with first  $L$  columns,  $\mathbf{h}_{tl} = [h_{tl}(0), \dots, h_{tl}(l), \dots, h_{tl}(L - 1)]^T$  as the channel impulse response during the  $i$ th OFDM symbol,  $\mathbf{s} = [s(0), \dots, s(k), \dots, s(N_s - 1)]^T$  as a transmit symbol vector, and  $\mathbf{v} = [v(0), \dots, v(k), \dots, v(N_s - 1)]^T$  as the noise vector, equation (2.12) can be rewritten in the following matrix form:

$$\mathbf{y} = \text{diag}\{\mathbf{F}_L \mathbf{h}_{tl}\} \mathbf{s} + \mathbf{v}. \quad (2.13)$$

Hence, we can use this simplified system model in (2.13), if OFDM systems inserts the CP, which is longer than the length of the multipath channel.

### 2.3.3 Inter-Carrier Interference for OFDM Systems

For quasi-static channels, the channel impulse response remains constant during one OFDM symbol period, which does not introduce any inter-carrier interference, because the orthogonality among subcarriers is perfectly maintained under the quasi-static assumption in (2.12). However, it cannot be true for the high-speed vehicular channels. In these scenarios, the channels will vary rapidly. Here, we will detail the ICI caused by the rapid varying channel in OFDM systems. We assume that the  $k$ th subcarrier is the desired one and omit the noise for simplicity, so (2.12) becomes [56]:

$$\begin{aligned}
 y(k) &= \frac{1}{N_s} \sum_{n=0}^{N_s-1} \sum_{l=0}^{L-1} \sum_{q=0}^{N_s-1} h_{tl}(n, l) s(q) e^{j2\pi(qn+ql)/N_s} e^{-j2\pi kn/N_s} \\
 &= \underbrace{h_{df}(0, k) s(k)}_{\text{desired signal}} + \underbrace{\sum_{q=0, q \neq k}^{N_s-1} h_{df}(k - q, q) s(q)}_{\text{ICI components}},
 \end{aligned} \tag{2.14}$$

where  $h_{df}(k - q, q) = \frac{1}{N_s} \sum_{n=0}^{N_s-1} \sum_{l=0}^{L-1} h_{tl}(n, l) e^{-j2\pi((k-q)n+ql)/N_s}$ , and the quantity  $h_{tl}(n, l)$  denotes the channel impulse response for the  $n$ th time index in one OFDM symbol and the  $l$ th channel path. If let  $d = k - q$  and  $k = q$ ,  $h_{df}(d, k) = \frac{1}{N_s} \sum_{n=0}^{N_s-1} \sum_{l=0}^{L-1} h_{tl}(n, l) e^{-j2\pi(dn+kl)}$ . As described in [56], the quantities in  $h_{df}(d, k)$   $d$  and  $k$  can be interpreted as ‘‘Doppler’’ index and the subcarrier index, respectively. We can also rewrite equation (2.14) in a matrix form:

$$\mathbf{y} = \mathbf{F} \mathbf{H}_{tl} \mathbf{F}^H \mathbf{s} + \mathbf{v}, \tag{2.15}$$

where

$$\mathbf{H}_{tl} = \begin{bmatrix} h_{tl}(0, 0) & 0 & \cdots & \cdots & h_{tl}(0, 2) & h_{tl}(0, 1) \\ h_{tl}(1, 1) & h_{tl}(1, 0) & \cdots & \cdots & h_{tl}(1, 3) & h_{tl}(1, 2) \\ \vdots & \vdots & \ddots & \vdots & \vdots & \vdots \\ h_{tl}(L-1, L-1) & h_{tl}(L-1, L-2) & \vdots & \ddots & 0 & 0 \\ \vdots & \vdots & \vdots & \cdots & \vdots & \vdots \\ 0 & 0 & 0 & \cdots & h_{tl}(N_s-1, 1) & h_{tl}(N_s-1, 0) \end{bmatrix}, \tag{2.16}$$

The ICI induced by the time-varying channel in (2.14) cannot be considered as noise for simplicity, because the performance of channel estimation and equalization will be significantly affected. In the following subsections, several equalization techniques will be presented to mitigate ICI via the band assumption of the channel matrix.

## 2.4 Pilot-Based Channel Estimation for OFDM Systems over Quasi-static Channels

Compared to non-coherent detection, coherent detection can achieve a higher data rate and a better performance at the price of acquiring accurate channel estimates [37]. Thus, the channel estimates become necessary. According to (2.13), the system model becomes

$$\mathbf{y} = \text{diag}\{\mathbf{F}_L \mathbf{h}_{tl}\} \mathbf{s} + \mathbf{v}. \quad (2.17)$$

Because the orthogonality between subcarriers is maintained, (2.17) can be rewritten in another form:

$$\mathbf{y} = \text{diag}\{\mathbf{s}\} \mathbf{h}_{df} + \mathbf{v}, \quad (2.18)$$

where  $\mathbf{h}_{df} = [h_{df}(0), \dots, h_{df}(k), \dots, h_{df}(N_s - 1)]^T$ , and the quantity  $h_{df}(k)$  is defined similarly to (2.12). Hence, the system model in (2.18) is used for pilot-based channel estimation in the following subsections.

### 2.4.1 Fundamental Pilot Allocation for OFDM systems

Due to the orthogonality between subcarriers in OFDM systems, different pilot allocation schemes can be adopted as in [39, 75–77]. In what follows, some fundamental pilot allocation schemes will be explained.

#### Block Type Pilot Allocation

The block type pilot allocation is to insert pilots periodically into all subcarriers in the frequency domain, so the channel frequency response for each subcarrier can be estimated [39, 75]. The diagram of block type pilot allocation is plotted as Fig. 2.3. Note that the quantity  $t_p$  denotes the time sampling period of pilot symbols, which must be much smaller than the inverse of Doppler frequency ( $f_d$ ) or coherence time. Hence, the block type pilot allocation is designed for the frequency selective channel. It may employ more pilots, if the channel variations between consecutive OFDM symbols increases.

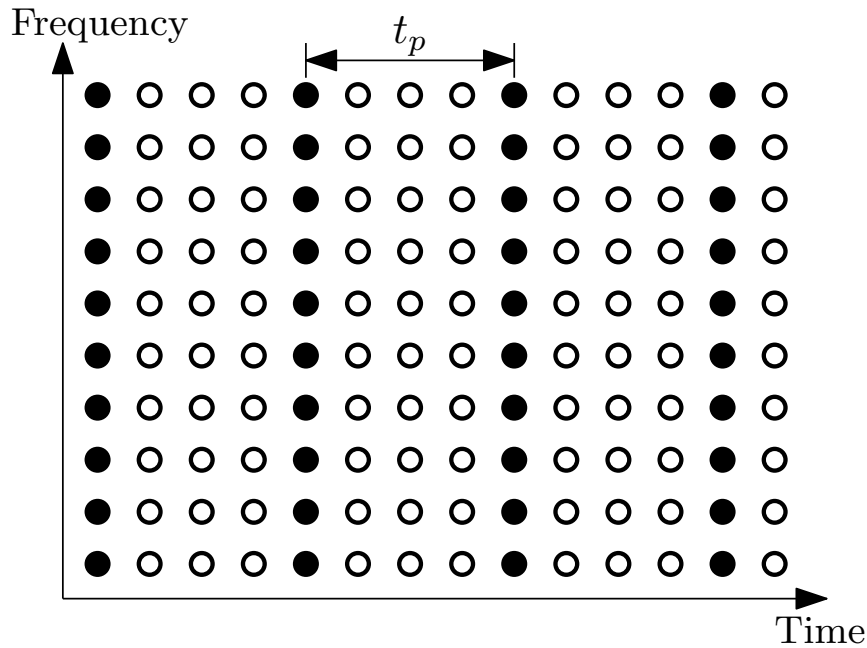


Figure 2.3: Block-type pilot allocation

### Comb-Type Pilot Allocation

The idea behind the comb-type pilot allocation is similar to the block type except that it combats the time variations of the channels between OFDM symbols. The diagram of the comb-type pilot allocation is illustrated in Fig. 2.4. The pilots are inserted in several particular subcarriers across all the time. Let  $f_p$  denote the frequency sampling period of pilot symbols, which must be much smaller than the coherence bandwidth for the reliable channel estimates.

### Lattice-Type Pilot Allocation

Compared to the above allocation schemes, the pilots are scattered over the time and the frequency domain to keep track of the frequency selectivity and time variation of the channels. Both  $t_p$  and  $f_p$  must be much smaller than the coherence time and the coherence bandwidth, respectively. The diagram of lattice-type pilot allocation is illustrated in Fig. 2.5. A better tradeoff between the overhead of pilots and performance can be achieved using lattice type compared to the other conventional pilot allocation schemes. Because it does not insert pilots across all the time compared to comb-type pilot allocation and does

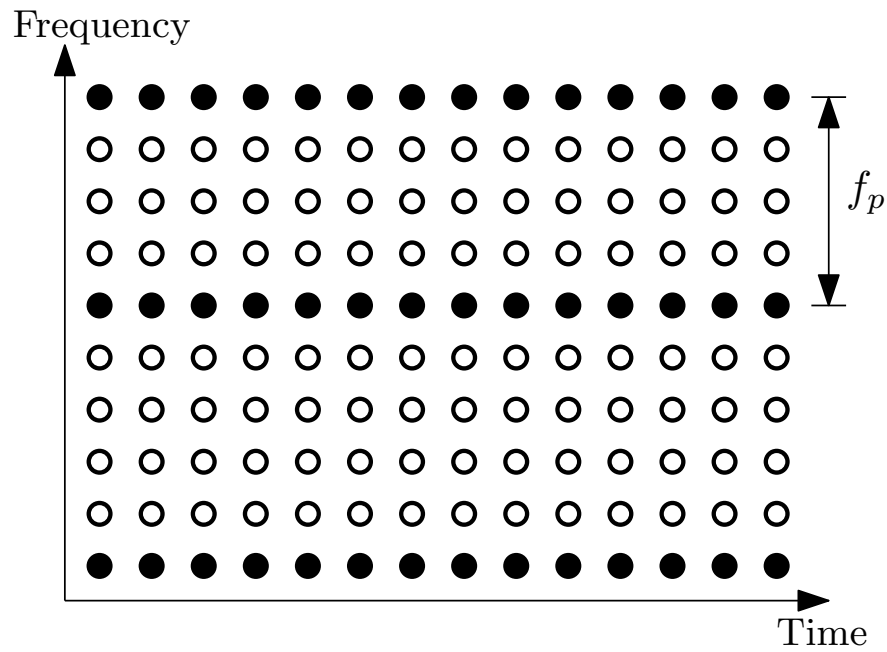


Figure 2.4: Comb-type pilot allocation

not insert pilots either in every subcarrier compared to block-type pilot allocation. Thus the lattice-type pilot allocation can estimate the less selective channels in the time and the frequency with the moderate number of pilots.

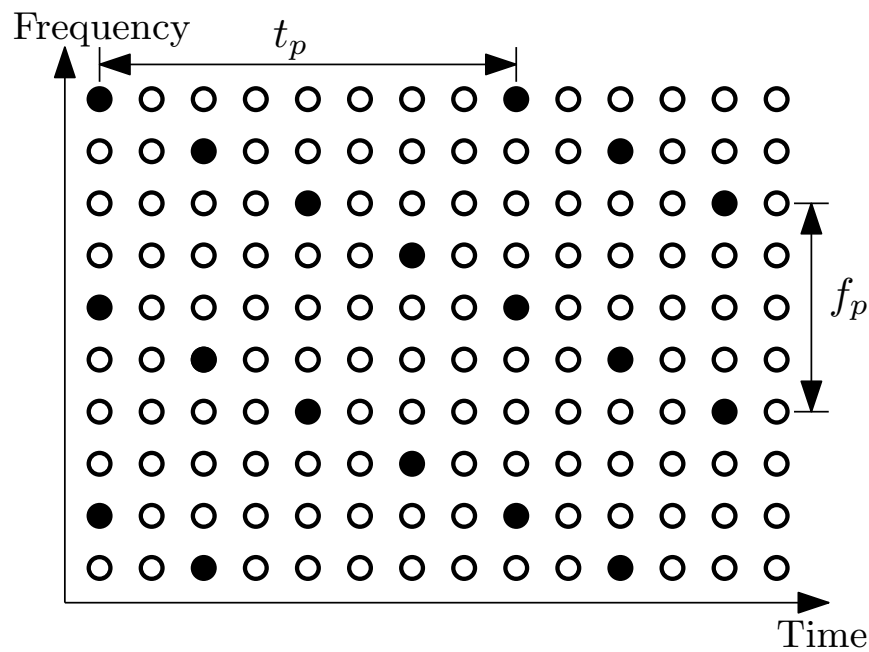


Figure 2.5: Lattice-type pilot allocation

## 2.4.2 Least-Squares Channel Estimation

According to (2.18), the solution of the LS estimation can be expressed as [78]

$$\hat{\mathbf{h}}_{df} = (\text{diag}\{\mathbf{s}\}^H \text{diag}\{\mathbf{s}\})^{-1} \text{diag}\{\mathbf{s}\}^H \mathbf{y} = \text{diag}\{\mathbf{s}\}^{-1} \mathbf{y}. \quad (2.19)$$

The MSE of LS channel estimation can be given by [78]

$$\begin{aligned} \text{MSE}_{\text{LS}} &= \mathbb{E}\{(\mathbf{h}_{df} - \hat{\mathbf{h}}_{df})^H (\mathbf{h}_{df} - \hat{\mathbf{h}}_{df})\} \\ &= \frac{\sigma_v^2}{\sigma_s^2}, \end{aligned} \quad (2.20)$$

where  $\sigma_v^2$  and  $\sigma_s^2$  denote the noise variance and the signal power, respectively. We can observe that with the reduction of  $\sigma_v^2$  the MSE performance will be consistently improved. But it may suffer noise enhancement, that is, the signal power  $\sigma_s^2$  is too small in the deep faded channels. Hence, the MSE performance of LS channel estimation will be significantly degraded.

## 2.4.3 MMSE Channel Estimation

According to (2.19) and [79], the MMSE estimate using the rough channel estimate  $\hat{\mathbf{h}}_{df}$  obtained by LS channel estimation is given by  $\tilde{\mathbf{h}}_{df} = \mathbf{W}\hat{\mathbf{h}}_{df}$ , where the weight matrix  $\mathbf{W}$  denotes the MMSE filter. The MMSE filter can be represented by [79]

$$\mathbf{W} = \mathbf{R}_{\mathbf{h}_{df}\hat{\mathbf{h}}_{df}} \mathbf{R}_{\hat{\mathbf{h}}_{df}\hat{\mathbf{h}}_{df}}^{-1} \quad (2.21)$$

where the matrices  $\mathbf{R}_{\mathbf{h}_{df}\hat{\mathbf{h}}_{df}} = \mathbb{E}\{\mathbf{h}_{df}\hat{\mathbf{h}}_{df}^H\}$  and  $\mathbf{R}_{\hat{\mathbf{h}}_{df}\hat{\mathbf{h}}_{df}} = \mathbb{E}\{\hat{\mathbf{h}}_{df}\hat{\mathbf{h}}_{df}^H\}$  denote the cross-correlation matrix between the real channel and the LS channel estimate in the frequency domain and the corresponding autocorrelation matrix. The MMSE channel estimate is given by

$$\tilde{\mathbf{h}}_{df} = \mathbf{W}\hat{\mathbf{h}}_{df} = \mathbf{R}_{\mathbf{h}_{df}\hat{\mathbf{h}}_{df}} \mathbf{R}_{\hat{\mathbf{h}}_{df}\hat{\mathbf{h}}_{df}}^{-1} \hat{\mathbf{h}}_{df} = \mathbf{R}_{\mathbf{h}_{df}\hat{\mathbf{h}}_{df}} (\mathbf{R}_{\mathbf{h}_{df}\hat{\mathbf{h}}_{df}} + \frac{\sigma_v^2}{\sigma_s^2} \mathbf{I})^{-1} \hat{\mathbf{h}}_{df} \quad (2.22)$$

Additionally, with the use of typical wide-sense stationary uncorrelated scattering model and white Gaussian noise assumption, the elements of  $\mathbf{R}_{\mathbf{h}_{df}\hat{\mathbf{h}}_{df}}$  and  $\mathbf{R}_{\hat{\mathbf{h}}_{df}\hat{\mathbf{h}}_{df}}$  can be expressed as [37]

$$\mathbb{E}\{h_{df}(n, k)\hat{h}_{df}^*(n', k')\} = \mathbb{E}\{h_{df}(n, k)h_{df}^*(n', k')\} = r_f(k - k')r_t(n - n'), \quad (2.23)$$

where  $k$  and  $k'$  denote two different subcarriers' indices, and  $n$  and  $n'$  denote time indices. Note that  $\hat{h}_{df}(n, k) = h_{df}(n, k) + v(n, k)/s(n, k)$  according to (2.19) and  $\mathbb{E}\{h_{df}(n, k)(v(n', k')/s(n', k'))^*\} = 0$ , so the cross-correlation between  $h_{df}(n, k)$  and  $h_{df}(n', k')$  can be simplified as

$$\begin{aligned}\mathbb{E}\{h_{df}(n, k)\hat{h}_{df}^*(n', k')\} &= \mathbb{E}\{h_{df}(n, k)(h_{df}^*(n', k') + v^*(n', k')/s^*(n', k'))\} \\ &= \mathbb{E}\{h_{df}(n, k)h_{df}^*(n', k')\} + \mathbb{E}\{h_{df}(n, k)(v(n', k')/s(n', k'))^*\} \\ &= \mathbb{E}\{h_{df}(n, k)h_{df}^*(n', k')\}\end{aligned}\tag{2.24}$$

For an exponential power delay profile, the mathematical expression of the frequency-domain correlation is given by [77]

$$r_{\Delta f}(k) = \frac{1}{1 + j2\pi\tau_{\max}\Delta f},\tag{2.25}$$

where  $\Delta f = (k - k')/N_s$  is the spacing between two subcarriers, and  $\tau_{\max}$  denotes the root mean square delay spread. For a uniform power delay profile, the frequency correlation can be calculated by [37]

$$r_f(\Delta f) = \sum_{l=0}^{L-1} \sigma_l^2 e^{-j2\pi\Delta f l}\tag{2.26}$$

where  $\sigma_l^2$  denotes the average power of the  $l$ th path. Referring to Jakes' model, the time correlation for the fading channel is described by

$$r_t(\Delta t) = J_0(2\pi f_d \Delta t),\tag{2.27}$$

where  $f_d$  denotes the maximum Doppler frequency, and  $\Delta t = (n - n')(N_s + L)$ . Note that we assume the length of CP equals the length of multipath. The function  $J_0(\cdot)$  is the 0th-order Bessel function of the first kind and  $r_f(0) = r_t(0) = 1$ .

#### 2.4.4 Interpolation techniques for OFDM systems

According to the pilot allocation schemes discussed above, the pilots will be inserted in the time or frequency domain to estimate the channels for a particular time instant or subcarriers. However, the channels for data symbols are unknown to the receiver except the pilot channel estimates. The interpolation techniques are needed to estimate the channels between subcarriers or time slots. The interpolation techniques for the time domain are

similar to that for the frequency domain, so we will only discuss the interpolation techniques in the frequency domain. The interpolation can be naturally extended to the time domain with straightforward modifications. The interpolation is performed based on the channel estimates obtained by LS or MMSE channel estimation as previously described.

### Linear Interpolation

Linear interpolation is a simple method to outperform piecewise constant interpolation [80], which estimates the channels between two pilots with the aid of linear approximation. The optimal number of pilots for a given BER can be determined in advance for OFDM systems with numerical evaluation as in [81]. According to (2.13), the channel estimate of the  $d$ th subcarrier using linear interpolation between the  $p$ th and  $(p+1)$ th pilot subcarriers is given by

$$\begin{aligned}\hat{h}_{df}(d) &= \hat{h}_{df}\left(p\frac{N_s}{N_p} + d\right) \quad 0 \leq d < \frac{N_s}{N_p} - 1 \\ &= \frac{(\hat{h}_{df}(p+1) - \hat{h}_{df}(p))d}{N_s/N_p} + \hat{h}_{df}(p),\end{aligned}\tag{2.28}$$

where  $\hat{h}_{df}(p)$  denotes the channel estimate of the  $p$ th pilot obtained by LS or MMSE estimation, and the quantity  $d$  denotes the desired subcarrier index between the  $p$ th and the  $(p+1)$ th pilot. Fig. 2.6 shows a diagram of linear interpolation in the frequency domain.

### Second-order Interpolation

For second-order interpolation, the MSE performance will be better than that of the linear interpolation with complexity increase, and the idea behind it is similar to the linear interpolation except that it employs a second-order approximation. Hence, a similar mathematical expression is defined as [75]

$$\begin{aligned}\hat{h}_{df}(d) &= \hat{h}_{df}\left(p\frac{N_s}{N_p} + d\right) \quad 0 \leq d < \frac{N_s}{N_p} \\ &= c_1\hat{h}_{df}(p-1) + c_0\hat{h}_{df}(p) + c_{-1}\hat{h}_{df}(p+1),\end{aligned}\tag{2.29}$$

where  $c_1 = \frac{\alpha(\alpha-1)}{2}$ ,  $c_0 = -(\alpha-1)(\alpha+1)$  and  $c_{-1} = \frac{\alpha(\alpha+1)}{2}$ ,  $\alpha = \frac{d}{N_s}$ , and the quantity  $d$  denotes the desired subcarrier index between the  $p$ th and the  $(p+1)$ th pilot as (2.28).

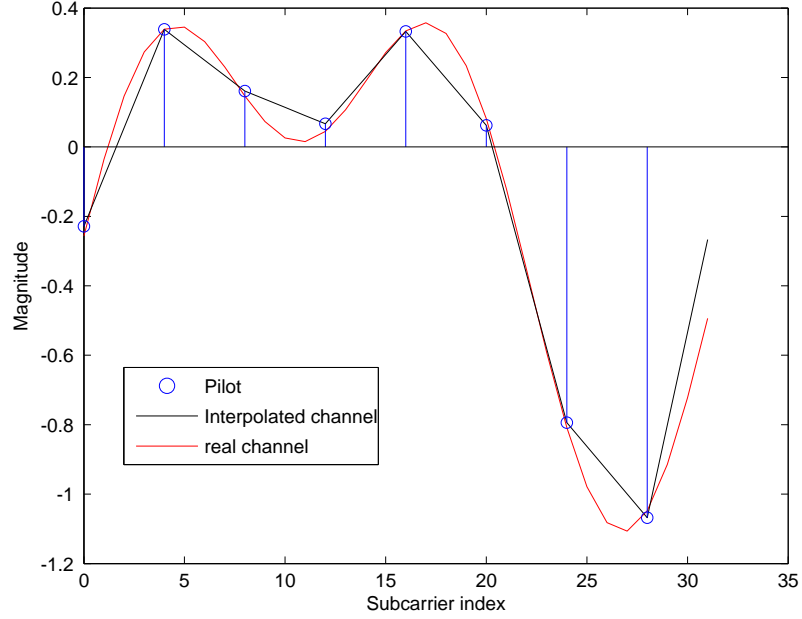


Figure 2.6: Diagram of linear interpolation using LS channel estimation for pilots ( $N_p = 8$ ) over a Multipath ( $L = 4$ ) Rayleigh fading channel with  $N_s = 32$ , SNR= 30 dB

### DFT-based Interpolation

The DFT-based interpolation technique is the output of the Fourier transform of the channel impulse response, which is clearly illustrated by a block diagram in Fig. 2.7. The DFT-based interpolation effectively removes the effects of noise outside the maximum channel delay spread or the length of multipath channel  $L$ , where  $h_{tl}(l)$  denotes the channel impulse response for the  $l$ th path. The implementation of the DFT-based interpolation is also straightforward compared to the linear or second-order interpolation, but the length of multipath channel must be known to the receiver. Symbol 1 is used for pilots in the following derivation. Referring to (2.18), the system model based on pilot subcarriers can be rewritten as

$$\begin{aligned} \mathbf{y}^{\text{pilot}} &= \text{diag}\{\mathbf{Xs}\} \underbrace{\mathbf{F}_L \mathbf{h}_{tl}}_{\mathbf{h}_{df}} + \mathbf{Xv} \\ &= \mathbf{X} \mathbf{F}_L \mathbf{h}_{tl} + \mathbf{Xv}, \end{aligned} \quad (2.30)$$

where  $\mathbf{y}^{\text{pilot}} = \mathbf{Xy}$ , and  $\mathbf{X}$  denotes a particular pilot allocation matrix, which is a diagonal matrix with zero diagonal elements for data subcarrier and 1s for pilots as follows. So only pilot subcarriers will be extracted, and zeros are allocated to the data subcarriers.

The symbol vector  $s$  used in the previous equations can be omitted.

$$\mathbf{X} = \begin{bmatrix} 1 & 0 & \dots & 0 \\ 0 & 0 & \dots & \vdots \\ \vdots & \vdots & \ddots & \vdots \\ 0 & 0 & \dots & 1 \end{bmatrix} \quad (2.31)$$

Using LS channel estimation in (2.19), the channel frequency responses corresponding to pilot subcarrier can be obtained by

$$\hat{\mathbf{h}}_{df}^{\text{pilot}} = \mathbf{X}^{-1} \mathbf{y}^{\text{pilot}}, \quad (2.32)$$

where  $\hat{\mathbf{h}}_{df}^{\text{pilot}} = [\hat{h}_{df}(0), 0, \dots, \hat{h}_{df}(p), 0, \dots, \hat{h}_{df}(N_p - 1)]^T$ . Thus, the estimate of the channel impulse response can be computed using IFFT:

$$\hat{\mathbf{h}}_{tl} = \mathbf{F}^H \hat{\mathbf{h}}_{df}^{\text{pilot}}. \quad (2.33)$$

If the length of multipath is known to the receiver, the vector  $\hat{\mathbf{h}}_{tl}$  will be truncated, that is,  $\hat{\mathbf{h}}_{tl} = [\hat{h}_{tl}(0), \dots, \hat{h}_{tl}(l), \dots, \hat{h}_{tl}(L - 1)]^T$ . So the channel estimate after FFT in the frequency domain becomes

$$\tilde{\mathbf{h}}_{df} = \mathbf{F} \hat{\mathbf{h}}_{tl}. \quad (2.34)$$

From (2.33) and (2.34), the DFT based interpolation technique only requires FFT and IFFT computation as well as the length of multipath, so it is a very common approach used in channel estimation for OFDM systems.

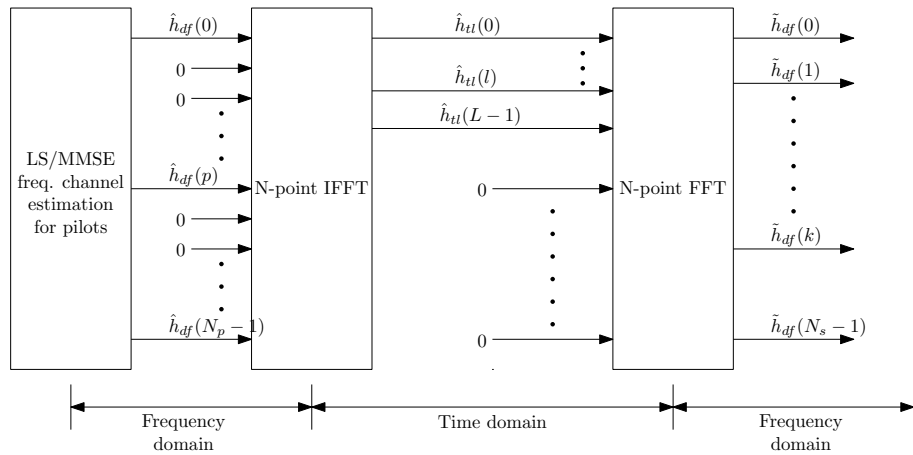


Figure 2.7: Block diagram of DFT-based Interpolation

## MMSE Interpolation

Compared to other interpolation techniques, MMSE interpolation may be the most effective way to estimate the channels between pilots with the aid of statistical information on the channels such as the channel correlation and SNR, as well as additional computation of the matrix inversion. However, it can achieve an excellent performance as compared to linear, second-order and DFT-based interpolation [51, 75]. Modifying (2.22), the MMSE interpolation follows as [37, 40, 41]

$$\tilde{\mathbf{h}}_{df} = \mathbf{R}_{\mathbf{h}_{df}} \hat{\mathbf{h}}_{df}^{\text{pilot}} (\mathbf{R}_{\mathbf{h}_{df}^{\text{pilot}}} \mathbf{h}_{df}^{\text{pilot}} + \frac{\sigma_v^2}{\sigma_s^2} \mathbf{X} \mathbf{I}_{N_s})^{-1} \hat{\mathbf{h}}_{df}^{\text{pilot}}, \quad (2.35)$$

where

$$\begin{aligned} \mathbf{R}_{\mathbf{h}_{df}^{\text{pilot}}} \mathbf{h}_{df}^{\text{pilot}} &= \mathbb{E}\{\mathbf{X} \mathbf{h}_{df} \mathbf{h}_{df}^H \mathbf{X}^H\} = \mathbf{X} \mathbb{E}\{\mathbf{h}_{df} \mathbf{h}_{df}^H\} \mathbf{X}^H = \mathbf{X} \mathbf{R}_{\mathbf{h}_{df}} \mathbf{h}_{df} \mathbf{X}^H \\ \mathbf{R}_{\mathbf{h}_{df}} \hat{\mathbf{h}}_{df}^{\text{pilot}} &= \mathbb{E}\{\mathbf{h}_{df} \hat{\mathbf{h}}_{df}^H \mathbf{X}^H\} = \mathbf{X} \mathbb{E}\{\mathbf{h}_{df} \hat{\mathbf{h}}_{df}^H\} = \mathbf{X} \mathbf{R}_{\mathbf{h}_{df}} \hat{\mathbf{h}}_{df}. \end{aligned} \quad (2.36)$$

According to (2.23) and (2.25), the autocorrelation matrix in (2.36) can be obtained for the exponential power delay profile. The autocorrelation function for other power delay profile can be found in [37].

## 2.4.5 Decision Directed Channel Estimation

Another channel estimation method is decision directed channel estimation [82], which employs the training sequences for the initial channel estimation, and then uses the detected symbols using the previous channel estimate in the  $(n-1)$ th OFDM symbol period to estimate the  $n$ th channel estimate. This method can achieve very high data rate at the expense of introducing an additional processing delay. The block diagram of decision directed channel estimation is illustrated in Fig. 2.8. We do not detail further on this method, which is easily integrated with LS or MMSE channel estimation.

## 2.4.6 Simulation Results

For the simulations, we consider an uncoded OFDM system with the number of sub-carrier  $N_s = 64$ , and the number of pilots  $N_p = 8$  (uniformly placed). The signal is

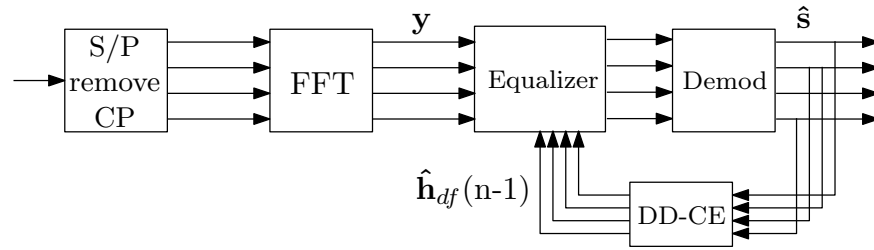


Figure 2.8: Block diagram of decision directed channel estimation for OFDM systems, where  $(n - 1)$  denotes the previous OFDM symbol period

modulated by QPSK. The channel is generated using Jakes' model with a normalized Doppler frequency  $f_d T_{\text{OFDM}} = 10^{-4}$ , the length of which is  $L = 4$  with an exponential power delay profile suggested by [83]. Furthermore, the channel taps for different delays are independent from each other. The BER and MSE performance for different frequency domain interpolation techniques are illustrated in Fig. 2.9 and 2.10 including linear interpolation, second-order interpolation, DFT-based interpolation, MMSE interpolation and decision directed channel estimation [39, 75, 82]. The MMSE detector is employed at the receiver, and the channel frequency responses of pilot subcarriers are estimated by LS estimation. The decision directed channel estimation send pilots across subcarriers in every 8 OFDM symbols. Although decision directed channel estimation has an excellent performance compared to other interpolation techniques, it introduce an additional processing delay in OFDM systems, and is relatively sensitive to channel variations between OFDM symbols. We can also observe that the MMSE interpolation outperforms other techniques in the BER and MSE performance except decision directed channel estimation, but it requires statistical information on channels such as frequency correlation and SNR, and matrix inversions must be performed for each OFDM symbol. The performance of DFT channel estimation is worse than that of MMSE with 4 dB loss in the MSE performance, but these two channel estimators perform almost identically in the BER performance. Furthermore, the DFT channel estimation only requires the information on the length of multipath channel and implementation of FFT and IFFT. Other techniques including piecewise constant, linear and second-order interpolation experience error floors in BER and MSE, respectively. The error floors of BER are caused by the unreliable channel estimates over non-pilot subcarriers acquired by these interpolation techniques. Hence, the DFT interpolation may achieve an attractive tradeoff between complexity and performance.

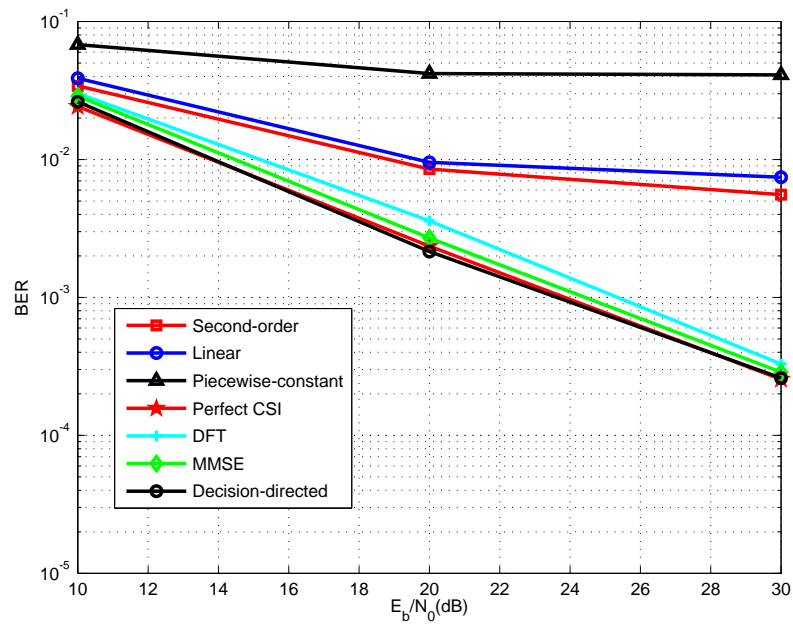


Figure 2.9: BER performance of frequency domain interpolation techniques over quasi-static channels with  $N_s = 64$ ,  $L = 4$ ,  $N_p = 8$ , and an exponential power delay profile

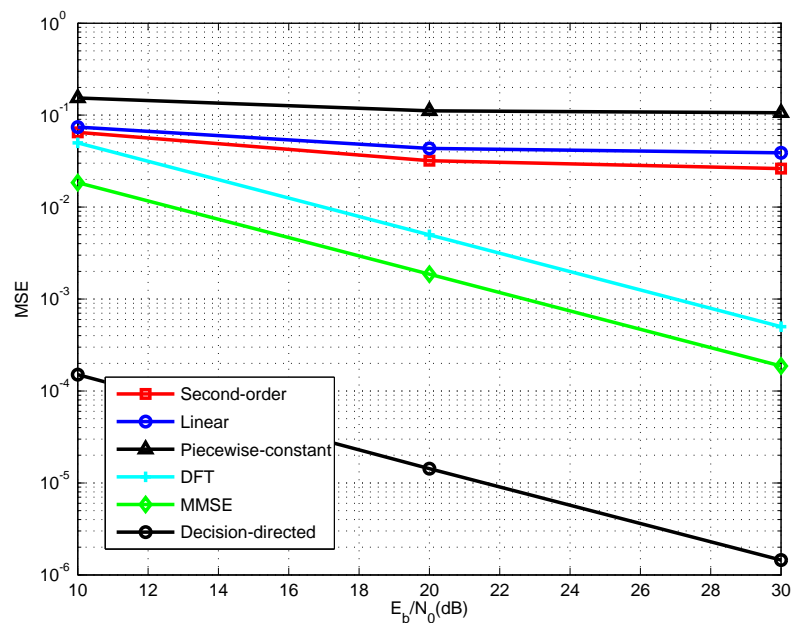


Figure 2.10: MSE performance of frequency domain interpolation techniques over quasi-static channels with  $N_s = 64$ ,  $L = 4$ ,  $N_p = 8$ , and an exponential power delay profile

## 2.5 Pilot-Based Channel Estimation for MIMO-OFDM Systems Over Quasi-static Channel

Due to the difficulty of allocating pilots for MIMO-OFDM channel estimation compared to single transmit antenna, the techniques used in SISO-OFDM cannot be simply extended to the MIMO case. Note that the superposition of signals from multiple transmit antennas makes decoupling pilot signals difficult. To eliminate the effects of inter-antenna interference, we discuss three different schemes in this subsection. Firstly, superimposed pilot allocation was investigated to exploit the correlation between pilot signals and received signals to estimate the channel over pilot subcarriers, but the pilots must be equispaced [46, 47] across the subcarriers to maintain an acceptable MSE performance. This is because the MSE is minimized with phase-shift orthogonal pilots from different transmit antennas [84]. Additionally, the transmit antenna sends a pilot at one subcarrier, and the others remain silent (null subcarrier), which is similar to the comb-type pilot allocation [48]. Finally, STBC or SFBC is also employed to implement the channel estimation for comparison.

We consider an uncoded spatial multiplexing MIMO-OFDM system with  $N_s$  subcarriers,  $N_t$  transmit and  $N_r$  receive antennas, where  $N_t \leq N_r$ , as shown in Fig. 2.11. In Fig. 2.11, the modulated symbols from the modulators (MOD) and pilots are inserted into data subcarriers and pilot subcarriers via pilot allocation. The output of pilot allocation is then passed through IFFT and appended with CP for transmission. At the receiver, the CP is removed and the truncated received signals without CP are then passed through FFT. The pilots are used for channel estimation (CE), and the detection is performed with the estimated channels. The transmitted symbols are recovered through the demodulators (DEMODO) with the output of detection. The received signals are organized in a  $N_r N_s \times 1$  vector  $\mathbf{y} = [\mathbf{y}_1, \dots, \mathbf{y}_i, \dots, \mathbf{y}_{N_r}]^T$  expressed by

$$\mathbf{y} = \mathbf{H}_{df} \mathbf{s} + \mathbf{v}, \quad (2.37)$$

where  $\mathbf{H}_{df}$  is a  $N_r N_s \times N_t N_s$  matrix:

$$\mathbf{H}_{df} = \begin{bmatrix} \mathbf{H}_{df}^{11} & \mathbf{H}_{df}^{21} & \dots & \mathbf{H}_{df}^{N_t 1} \\ \mathbf{H}_{df}^{12} & \mathbf{H}_{df}^{22} & \dots & \vdots \\ \vdots & \vdots & \mathbf{H}_{df}^{ij} & \vdots \\ \vdots & \vdots & \ddots & \vdots \\ \mathbf{H}_{df}^{1N_r} & \mathbf{H}_{df}^{2N_r} & \dots & \mathbf{H}_{df}^{N_t N_r} \end{bmatrix}. \quad (2.38)$$

The matrix  $\mathbf{H}_{df}^{ij}$  is a  $N_s \times N_s$  diagonal matrix in  $\mathbf{H}_{df}$  that represents the frequency selective channel between the  $i$ th transmit antenna and the  $j$ th receive antenna, so the channel frequency response similar to (2.13) is given as

$$\begin{aligned} \mathbf{H}_{df}^{ij} &= \text{diag}\{\mathbf{F}_L \mathbf{h}_{tl}^{ij}\} = \text{diag}\{\mathbf{h}_{df}^{ij}\} \\ i &= 1, 2, \dots, N_t, \quad j = 1, 2, \dots, N_r, \end{aligned} \quad (2.39)$$

where  $\text{diag}\{\}$  represents a diagonal matrix constructed by the corresponding vector. The vector  $\mathbf{h}_{tl}^{ij}$  denotes the length  $L$  channel impulse response vector  $\mathbf{h}_{tl}^{ij} = [h_{tl}^{ij}(0), h_{tl}^{ij}(1), \dots, h_{tl}^{ij}(L-1)]^T$  between the  $i$ th transmit antenna and the  $j$ th receive antenna, which is modelled as a tapped delay line. Each entry in the vector can be modelled as an independent identically distributed (i.i.d.) complex Gaussian random variable with  $\mathcal{CN}(0, \sigma_{h_{tl}^{ij}(l)}^2)$ . Additionally, the channel is assumed to experience quasi-static fading, which implies that the channel is constant during one OFDM symbol and varies OFDM symbol by OFDM symbol based on Jakes' model. The power delay profile for any transmit and receive antenna pair is the same. Given the prior assumptions, the correlation matrix can be represented as  $\mathbf{R}_c = \mathbf{F}_L \mathbb{E}\{\mathbf{h}_{tl}^{ij} \mathbf{h}_{tl}^{ijH}\} \mathbf{F}_L$ . Hence, the  $k$ th subcarrier's channel frequency response  $h_{df}^{ij}(k)$  can be also modelled as  $\mathcal{CN}(0, \sigma_{h_{df}^{ij}(k)}^2)$ , where  $\sigma_{h_{df}^{ij}(k)}^2 = \sum_{l=0}^{L-1} \sigma_{h_{tl}^{ij}(l)}^2 = 1$ . The matrix  $\mathbf{F}_L$  is the first  $L$  columns of the  $N_s \times N_s$  DFT matrix.

## 2.5.1 Superimposed Pilot-Based Channel Estimation

Superimposed Pilot-Based Channel Estimation is not a straightforward approach compared to the following two schemes, which is inflexible in the pilot allocation and difficult to extend to the arbitrary number of transmit antennas. But it can save the subcarriers occupied by the pilots as depicted in Fig. 2.12. In other words, this method estimates

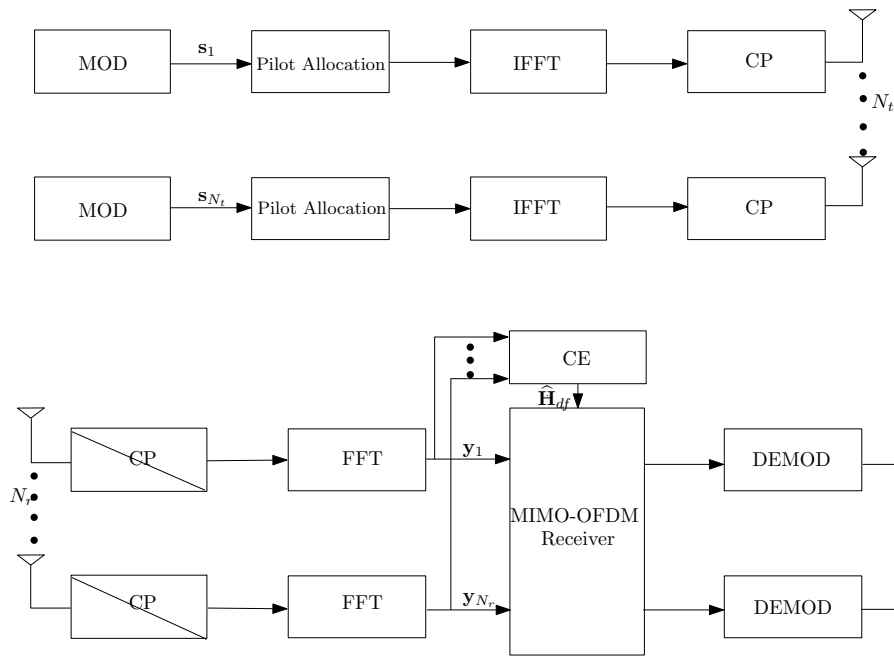


Figure 2.11: Block diagram of a MIMO-OFDM system

the MIMO-OFDM channel without employing additional pilots in the frequency domain, which improves the spectral efficiency. The simplified version can be found in [47]. The extension to more transmit antenna has been discussed in [85]. Equation (2.39) can be

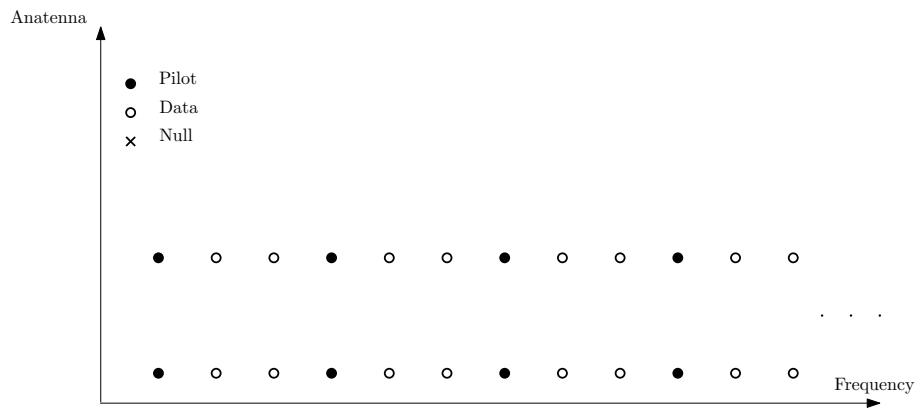


Figure 2.12: The superimposed pilot allocation

rewritten in a discrete form as

$$h_{df}^{ij}(k) = \sum_{l=0}^{L-1} h_{dl}^{ij}(l) W_{N_s}^{k,l}, \quad (2.40)$$

where  $W_{N_s}^{k,l} = e^{-j2\pi kl/N_s}$ . We only consider the two transmit antenna case for simplicity. Thus, the received signal of the  $k$ th subcarrier for one particular receive antenna can be

expressed as

$$y_j(k) = \sum_{i=1}^2 h_{df}^{ij}(k) s_i(k) + v_j(k). \quad (2.41)$$

Substituting (2.40) into (2.41), equation (2.41) can be rewritten in a matrix form:

$$\begin{aligned} \mathbf{y}_j &= \sum_{i=1}^2 \mathbf{X}_i \mathbf{F}_L \mathbf{h}_{tl}^{ij} + \mathbf{v}_j \\ &= [\mathbf{X}_1 \mathbf{F}_L \quad \mathbf{X}_2 \mathbf{F}_L] \begin{bmatrix} \mathbf{h}_{tl}^{1j} \\ \mathbf{h}_{tl}^{2j} \end{bmatrix} + \mathbf{v}_j \\ &= \mathbf{A} \mathbf{h}_{tl}^j + \mathbf{v}_j \end{aligned} \quad (2.42)$$

where the matrix  $\mathbf{X}_i$  denotes the diagonal matrix only containing pilot symbols in its diagonal elements, the rest of which are zeros,  $\mathbf{A} = [\mathbf{X}_1 \mathbf{F}_L, \mathbf{X}_2 \mathbf{F}_L]$ , and  $\mathbf{h}_{tl}^j = [\mathbf{h}_{tl}^{1jT}, \mathbf{h}_{tl}^{2jT}]^T$ . The MSE cost function is required to be minimized:

$$\mathcal{J}(\mathbf{h}_{tl}^j) = \|\mathbf{y}_j - \mathbf{A} \mathbf{h}_{tl}^j\|^2. \quad (2.43)$$

Hence, the channel impulse response estimates  $\hat{\mathbf{h}}_{tl}^j$  can be obtained by LS estimation. That is

$$\hat{\mathbf{h}}_{tl}^j = \mathbf{A}^\dagger \mathbf{y}_j, \quad (2.44)$$

where  $(\cdot)^\dagger$  denotes the pseudo-inverse of a matrix. The advantages of this superimposed pilots based channel estimation is high spectral efficiency, low complexity (the pseudo-inverse of  $\mathbf{A}^\dagger$  can be pre-computed.), and no priori knowledge about channels and noise required. However, the pilot symbols should satisfy the following condition [85]:

$$\mathbf{F}_L^H \mathbf{X}_i \mathbf{X}_{i'} \mathbf{F}_L^H = \begin{cases} \mathbf{0}_{L \times L}, & i \neq i' \\ c \mathbf{I}_{L \times L}, & i = i' \end{cases} \quad (2.45)$$

where  $c$  is a constant, and the quantity  $i$  and  $i'$  denote the  $i$ th transmit antenna and the  $i'$ th transmit antenna, respectively. According to (2.42), the matrix size of  $\mathbf{A}$  increases with the number of transmit antenna. Furthermore, if we assume pilots for any transmit antenna are all ones for simplicity, the pilots must be uniformly placed. Otherwise, the condition in (2.45) cannot be satisfied. In other words, the pilot symbols must be re-designed for different pilot patterns. The optimum pilots designs for MIMO-OFDM systems have been discussed in [47, 84–86]. However, the superimposed pilot allocation can improve spectral efficiency, because the pilots can be inserted into the same subcarriers for different transmit antennas.

## 2.5.2 Comb-Type Channel Estimation

The comb-type channel estimation for MIMO-OFDM systems is similar to these techniques employed in a single antenna scenario, due to the comb structure in the frequency and space domain. The diagram of such pilot allocation is illustrated in Fig. 2.13, which effectively eliminates the effects of inter-antenna interference using additional null subcarriers. Hence, these advanced techniques discussed in Section 2.4 can be naturally extended to MIMO-OFDM systems, because the pilot pattern for each pair of transmit and receive antenna is similar to that of SISO-OFDM systems. Furthermore, the positions of pilots can be readily placed in the frequency and space domain compared to superimposed pilot allocation. In other words, the number of degrees of freedom are significantly greater, so the frequency diversity may be exploited for data subcarriers. However, the comb-type channel estimation over very frequency selective channels requires more pilots in the sense that the more null subcarrier are employed, which reduces the spectral efficiency.

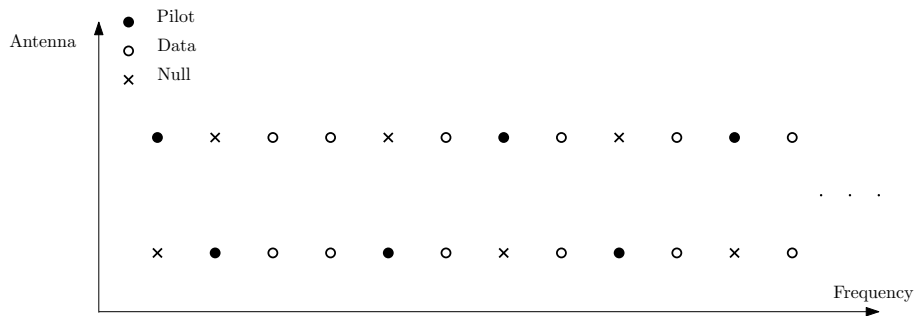


Figure 2.13: The diagram of comb-type pilot allocation

## 2.5.3 STBC and SFBC based Channel Estimation

STBC and SFBC can be used in the channel estimation for MIMO-OFDM systems with the assumption that the channels remain constant in the time or frequency domain during several OFDM symbols. The STBC and SFBC schemes discussed in this subsection are based on Alamouti scheme [8]. The  $2 \times 2$  MIMO-OFDM example is provided to illustrate the idea. The STBC based channel estimation for the  $k$ th subcarrier of  $j$ th receive antenna

at the  $n$ th and the  $(n + 1)$ th time index can be expressed as

$$\begin{pmatrix} y_j(n, k) \\ y_j(n + 1, k) \end{pmatrix} = \begin{pmatrix} s_1(n, k) & s_2(n + 1, k) \\ s_2^*(n + 1, k) & -s_1^*(n + 1, k) \end{pmatrix} \begin{pmatrix} h_{df}^{1j}(n, k) \\ h_{df}^{2j}(n, k) \end{pmatrix} + \begin{pmatrix} v_j(n, k) \\ v_j(n + 1, k) \end{pmatrix}, \quad (2.46)$$

where  $j = 1, 2$ . Note that the channels in two OFDM symbols are assumed to be constant in (2.46). In a matrix form, equation (2.46) can be rewritten as

$$\mathbf{y}_j(k) = \mathbf{S}(k)\mathbf{h}_{df}^j(k) + \mathbf{v}_j(k), \quad (2.47)$$

where  $s_i(n, k) = s_i(n + 1, k)$ ,  $i = 1, 2$ . Hence, the channel frequency response for the  $k$ th subcarrier at the  $n$ th and  $(n + 1)$ th time slot can be estimated using LS estimation by

$$\hat{\mathbf{h}}_{df}^j(k) = \mathbf{S}^{-1}(k)\mathbf{y}_j(k). \quad (2.48)$$

For SFBC,

$$\begin{pmatrix} y_j(n, k) \\ y_j(n, k + 1) \end{pmatrix} = \begin{pmatrix} s_1(n, k) & s_2(n, k) \\ s_2^*(n, k + 1) & -s_1^*(n, k + 1) \end{pmatrix} \begin{pmatrix} h_{df}^{1j}(n, k) \\ h_{df}^{2j}(n, k + 1) \end{pmatrix} + \begin{pmatrix} v_j(n, k) \\ v_j(n, k + 1) \end{pmatrix}, \quad (2.49)$$

and

$$\mathbf{y}_j(n) = \mathbf{S}(n)\mathbf{h}_{df}^j(n) + \mathbf{v}_j(n), \quad (2.50)$$

where  $s_i(n, k) = s_i(n, k + 1)$ ,  $i = 1, 2$ . The channel estimation for SFBC is omitted due to the similarity to that for STBC. Note that STBC and SFBC based channel estimation can be naturally extended to more transmit and receive antennas scenarios, which requires that the channel remains constant during more OFDM symbols or across a large number of subcarriers. The assumption may not be practical in some scenarios, and the performance will be significantly affected if the channels becomes more selective.

## 2.5.4 Simulation Results

In the simulations, we choose a  $2 \times 2$  MIMO-OFDM system with  $N_s = 128$  subcarriers and  $N_p = 16$  pilots for each transmit antenna. For comb-type channel estimation, we employ 8 pilots and 8 null subcarriers for fair comparison. The channel length is  $L = 8$  with normalized Doppler frequency  $f_d T_{\text{OFDM}}$  according to Jakes' model. The MSE

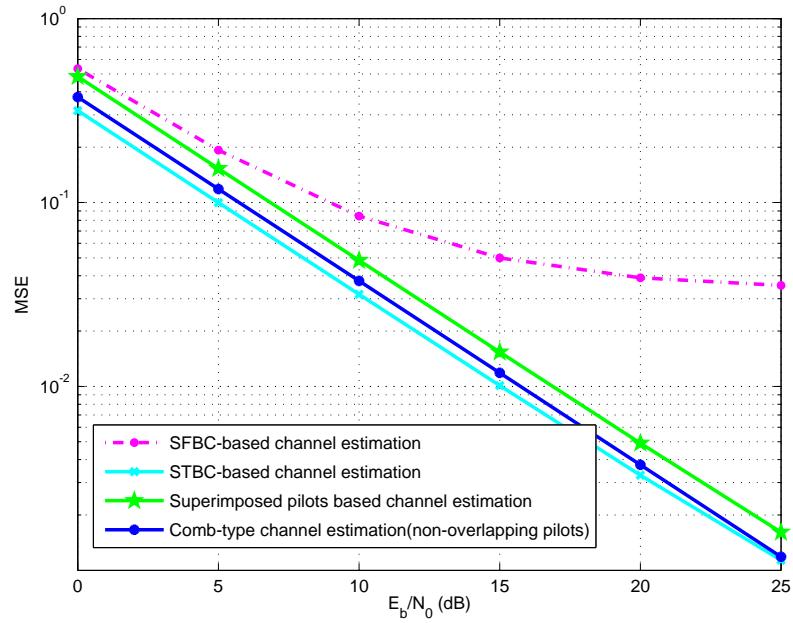


Figure 2.14: MSE performance of  $2 \times 2$  MIMO-OFDM system with  $N_s = 128$ ,  $N_p = 16$  over frequency selective slowly varying channels ( $L = 8$ ,  $f_d T_{\text{OFDM}} = 10^{-4}$ )

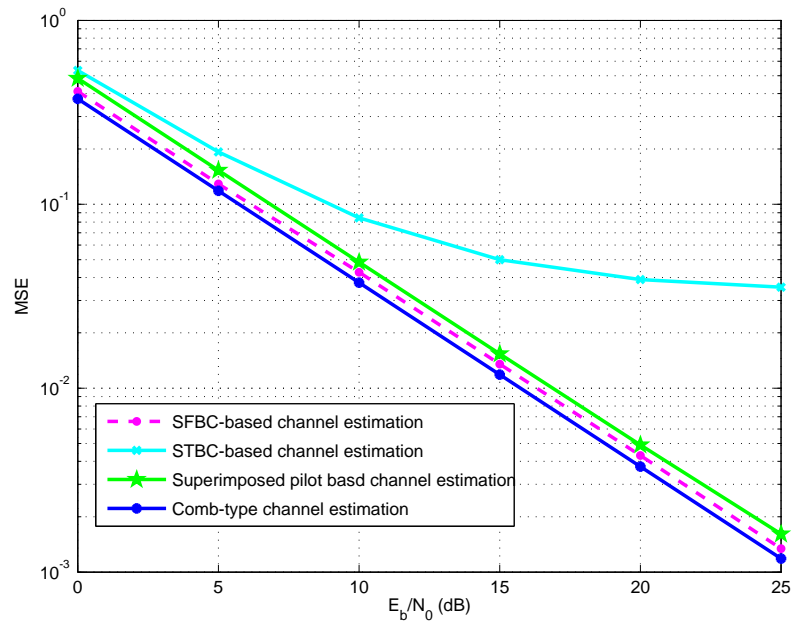


Figure 2.15: MSE performance of  $2 \times 2$  MIMO-OFDM system with  $N_s = 128$ ,  $N_p = 16$  over frequency flat rapidly varying channels ( $L = 1$ ,  $f_d T_{\text{OFDM}} = 10^{-2}$ )

performance is provided to illustrate the advantages of these techniques. MMSE interpolation is employed for channel estimation between pilots. In Figs. 2.14 and 2.15, the

MSE performance is plotted over time and frequency selective channels. We can observe that superimposed pilot based channel estimation and comb-type channel estimation can work in these scenarios. However, STBC can only work in the slowly varying channel scenario, and the error floor becomes more obvious with a normalized Doppler frequency  $f_d T_{\text{OFDM}} = 10^{-2}$  in Fig. 2.15. Compared to STBC, SFBC can work in frequency flat channels with a higher Doppler frequency  $f_d T_{\text{OFDM}} = 10^{-2}$ . Both STBC and SFBC must follow the channel invariance assumption, so it may not be a good option for general scenarios. In Fig. 2.16, the MSE performance over a frequency selective rapidly varying

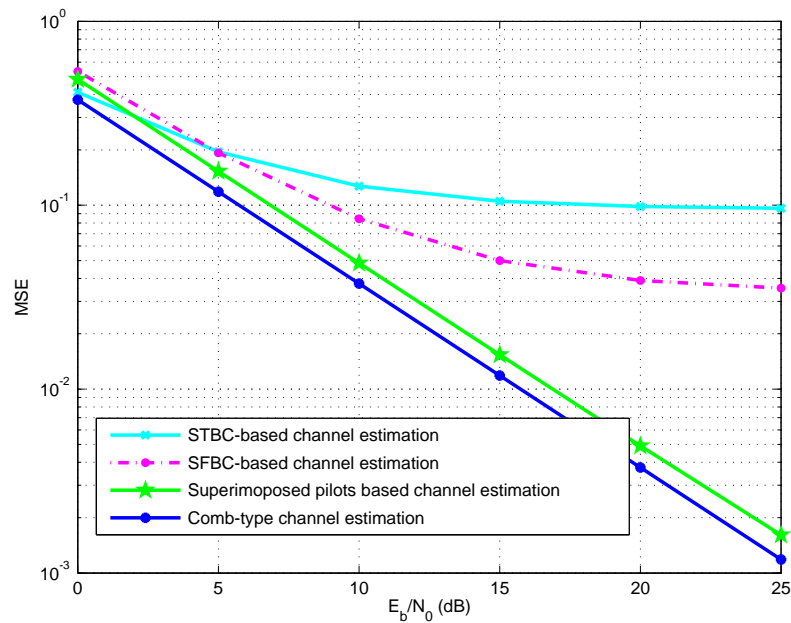


Figure 2.16: MSE performance of  $2 \times 2$  MIMO-OFDM system with  $N_s = 128$ ,  $N_p = 16$  frequency selective rapidly varying channel ( $L = 8, f_d T_{\text{OFDM}} = 10^{-2}$ )

channel is depicted. Both STBC and SFBC encounter error floors, and comb-type and superimposed pilot based channel estimation outperform them significantly. Furthermore, comb-type channel estimation work better than superimposed pilot based channel estimation with the same number of pilots, which implies they have the same number of data subcarriers.

Figs. 2.17, 2.18 and 2.19 plot the BER performance of MMSE detection with different MIMO-OFDM channel estimation techniques. The BER performance of STBC or SFBC based channel estimation can only work in the scenarios, which are not very selective in the time domain ( $f_d T_{\text{OFDM}} = 10^{-4}$ ) or the frequency domain ( $L = 1$ ). The curves

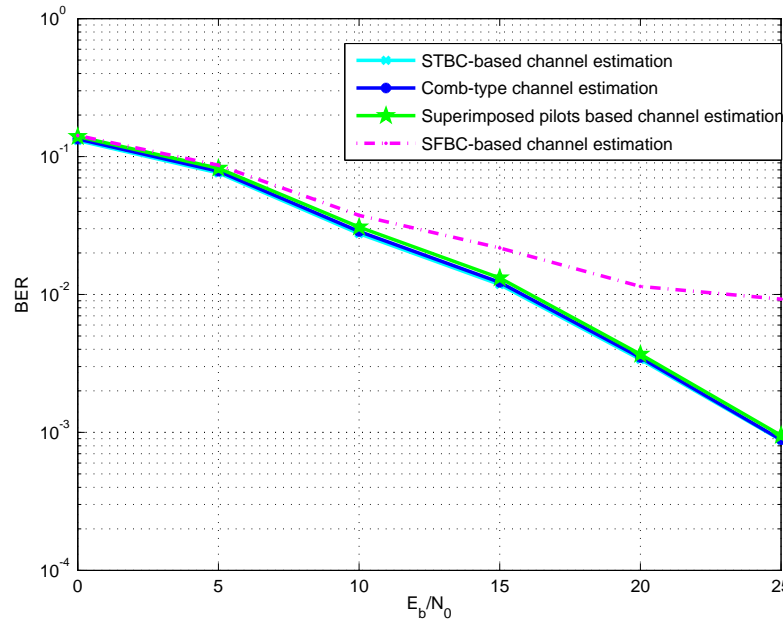


Figure 2.17: BER performance of  $2 \times 2$  MIMO-OFDM system with  $N_s = 128$ ,  $N_p = 16$  over frequency selective slowly varying channels ( $L = 8$ ,  $f_d T_{\text{OFDM}} = 10^{-4}$ )

of BER performance for STBC and SFBC based channel estimation almost agree with the curves of MSE performance. However, superimposed pilots based channel estimation and comb-type channel estimation is more robust to the selectivity of channels. In other words, the BER performance of these two techniques is promising over different channels. As discussed above, superimposed pilots based channel estimation requires re-design of pilot symbols for different transmit antennas and different subcarriers. Hence, the pilot patterns of superimposed channel estimation is not flexible compared to that of comb-type channel estimation. The BER performance of comb-type channel estimation is slightly better than that of superimposed one. We employ the comb-type channel estimation in Chapter 3 to design the dynamic pilot allocation.

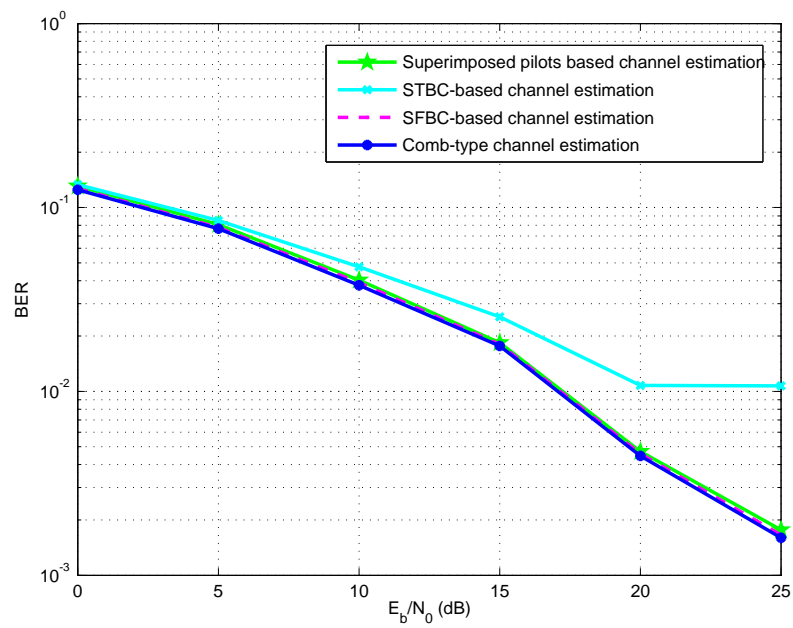


Figure 2.18: BER performance of  $2 \times 2$  MIMO-OFDM system with  $N_s = 128$ ,  $N_p = 16$  over frequency selective slowly varying channels ( $L = 1$ ,  $f_d T_{\text{OFDM}} = 10^{-2}$ )

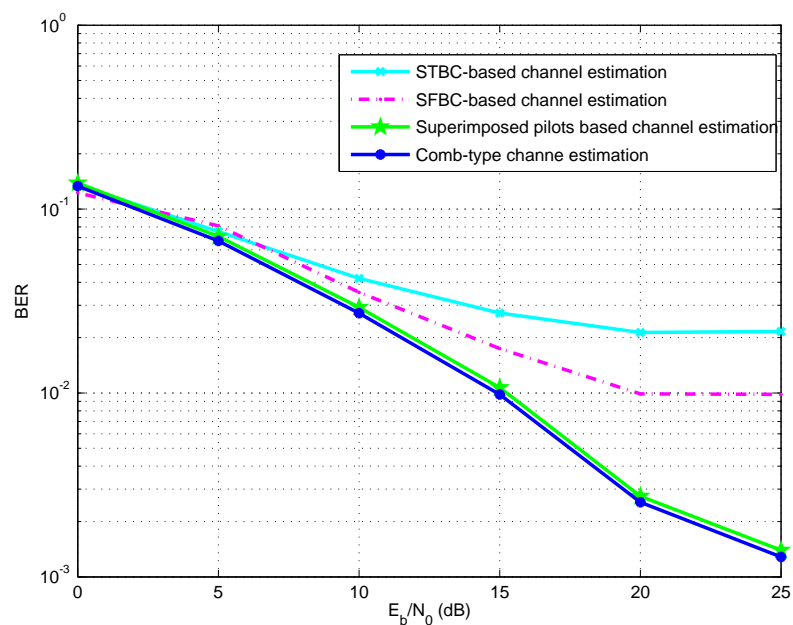


Figure 2.19: BER performance of  $2 \times 2$  MIMO-OFDM system with  $N_s = 128$ ,  $N_p = 16$  over frequency selective slowly varying channels ( $L = 8$ ,  $f_d T_{\text{OFDM}} = 10^{-2}$ )

## 2.6 Detection Techniques for MIMO Systems with Spatial Multiplexing

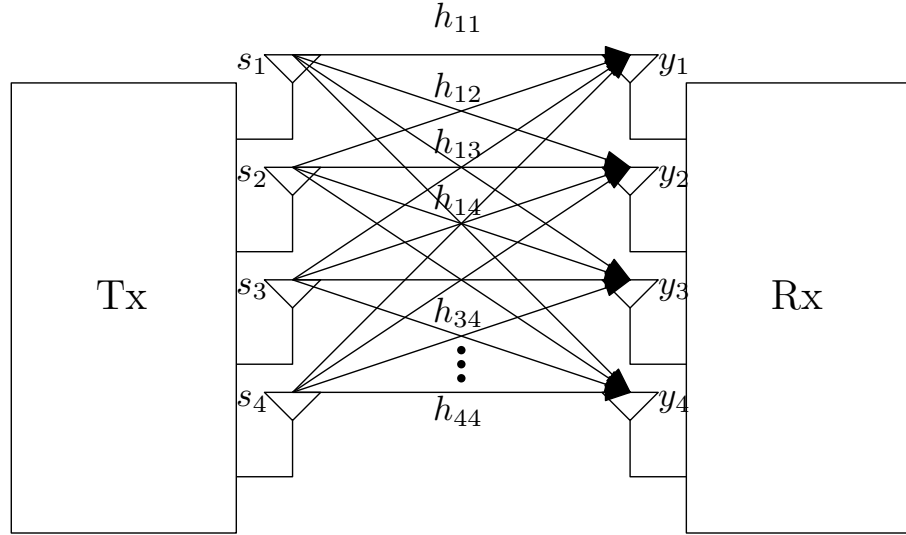
Multi-antenna systems have been investigated for several decades, and is one promising technique to significantly improve the spectral efficiency and the reliability. Multiple antennas have been adopted by several current wireless communication standards such as WiMAX, LTE and LTE-A [2, 3], and successfully deployed in some countries for broadband wireless access. In this subsection, MIMO with spatial multiplexing configuration has been discussed including several conventional detection algorithms and iterative processing. Spatial multiplexing techniques can substantially maximize the data rate by sending multiple independent data streams simultaneously through multiple transmit antennas. The capacity of MIMO channels may be achieved using Spatial multiplexing. The details about the capacity of MIMO channels can be found in [4].

### 2.6.1 MIMO System Model

The block diagram of a MIMO system with  $N_t = 4$  transmit antennas and  $N_r = 4$  receive antennas has been depicted in Fig. 2.20. The channels between transmit and receive antennas are assumed to be independent frequency flat fading. The channel can be represented by  $\mathbf{H} \in \mathbb{C}_{N_t \times N_r}$ . Defining the transmit symbol vector  $\mathbf{s} = [s_1 \dots s_i \dots s_{N_t}]^T \in \mathbb{C}_{N_t \times 1}$ , the received signal  $\mathbf{y} = [y_1 \dots y_j \dots y_{N_r}]^T$ , and the AWGN noise vector  $\mathbf{v} = [v_1 \dots v_j \dots v_{N_r}]^T$ , the system model can be written as

$$\mathbf{y} = \mathbf{H}\mathbf{s} + \mathbf{v}, \quad (2.51)$$

where  $\mathbb{E}\{\mathbf{s}\mathbf{s}^H\} = \sigma_s^2 \mathbf{I}_{N_t \times N_t}$ . Note that each element in the AWGN noise vector is assumed to be a zero-mean circular symmetric complex Gaussian variable, which implies that the phase rotation of  $\mathbf{v}$  will not affect its statistical properties, and  $\mathbb{E}\{\mathbf{v}\mathbf{v}^H\} = \sigma_v^2 \mathbf{I}_{N_r \times N_r}$ .

Figure 2.20: A  $4 \times 4$  MIMO system model

## 2.6.2 Linear ZF Detection

Linear ZF detection is a common approach in MIMO detection, due to the simplicity of implementation without any a priori knowledge of noise statistics as compared to MMSE detection. The mathematical expression of ZF filter is given by

$$\mathbf{W}_{\text{ZF}} = (\mathbf{H}^H \mathbf{H})^{-1} \mathbf{H}^H \quad (2.52)$$

Thus the symbol estimate of ZF detection can be written as

$$\hat{\mathbf{s}}_{\text{ZF}} = \mathbf{W}_{\text{ZF}} \mathbf{y} = \mathbf{s} + (\mathbf{H}^H \mathbf{H})^{-1} \mathbf{H}^H \mathbf{v} = \mathbf{s} + \tilde{\mathbf{v}}_{\text{ZF}}. \quad (2.53)$$

From (2.53), we can observe that the performance of ZF detection is mainly affected by  $\tilde{\mathbf{v}}_{\text{ZF}} = (\mathbf{H}^H \mathbf{H})^{-1} \mathbf{H}^H \mathbf{v}$ . Using SVD, the post-detection noise power can be decomposed as [78]

$$\mathbb{E}\{\|\tilde{\mathbf{v}}_{\text{ZF}}\|^2\} = \sum_{i=1}^{N_t} \frac{\sigma_v^2}{\sigma_{s,i}^2}, \quad (2.54)$$

where the quantity  $\sigma_{s,i}^2$  denotes the equivalent signal power of the  $i$ th transmit antenna at the receiver. The noise enhancement effect will be enlarged if  $\sigma_{s,i}^2$  becomes small, which implies that the signals from the  $i$ th transmit antenna experience the null channel. In other words, the  $i$ th singular value of  $\mathbf{H}$  is close to zero. In the following subsection, the MMSE detection will be presented, and the noise enhancement will be reduced by introducing statistical information of the noise.

### 2.6.3 Linear MMSE Detection

Linear MMSE detection is based on the minimum mean square error criterion, which maximizes the SINR after detection. The linear MMSE filter is given by

$$\mathbf{W}_{\text{MMSE}} = (\mathbf{H}^H \mathbf{H} + \sigma_v^2 \mathbf{I}_{N_r})^{-1} \mathbf{H}^H. \quad (2.55)$$

Hence, the output of linear MMSE detection can be evaluated as

$$\hat{\mathbf{s}}_{\text{MMSE}} = \mathbf{W}_{\text{MMSE}} \mathbf{y} = (\mathbf{H}^H \mathbf{H} + \sigma_v^2 \mathbf{I}_{N_r})^{-1} \mathbf{H}^H \mathbf{y} = \tilde{\mathbf{s}} + (\mathbf{H}^H \mathbf{H} + \sigma_v^2 \mathbf{I}_N)^{-1} \mathbf{H}^H \mathbf{v} = \tilde{\mathbf{s}} + \tilde{\mathbf{v}}_{\text{MMSE}}. \quad (2.56)$$

Similar to ZF detection using SVD, the post-detection noise power can be expressed as [78]

$$\mathbb{E}\{\|\tilde{\mathbf{v}}_{\text{MMSE}}\|^2\} = \sum_{i=1}^{N_t} \frac{\sigma_v^2 \sigma_{s,i}^2}{(\sigma_v^2 + \sigma_{s,i}^2)}. \quad (2.57)$$

From (2.57), the noise enhancement is significantly reduced. If the equivalent signal power  $\sigma_{s,i}^2$  becomes small, the mean square error  $\mathbb{E}\{\|\tilde{\mathbf{v}}_{\text{MMSE}}\|^2\}$  will be close to zero. Hence, the noise enhancement in MMSE filter is less critical compared to that in ZF filter.

### 2.6.4 SIC Detection

Successive interference cancellation is a suboptimal non-linear method compared to ML detection, but the performance is much better than the linear counterparts such as ZF and MMSE detection. The main idea is to detect the data stream of each transmit antenna after mitigation of previously detected data streams [6]. The order of cancellation can be determined by different criteria including SINR, SNR and channel norm based ordering. Although the order of cancellation cannot improve the diversity order of SIC detection, which is lower bounded by  $N_r - N_t + 1$ , but the performance gain can be acquired due to coding gain [15, 16]. It can achieve an attractive tradeoff between complexity and performance. The conventional SIC is given by

$$\mathbf{y}_k = \mathbf{y} - \sum_{j=1}^{k-1} \mathbf{h}_j \hat{s}_j, \quad (2.58)$$

where  $\mathbf{y}_k$  denotes the received signals after the  $k - 1$ th cancellation, and  $\mathbf{h}_j$  denotes the  $j$ th column vector of  $\mathbf{H}$  after ordering. Note that the subscript  $k$  denotes the  $k$ th cancellation

order rather than the notation of the  $k$ th transmit antenna. For the  $k$ th data stream, the MMSE detection must be re-designed based on the remaining interference. The MMSE detection for the  $k$ th data stream can be written as

$$\mathbf{W}_k = (\mathbf{H}_{\bar{k}}^H \mathbf{H}_{\bar{k}} + \sigma_v^2 \mathbf{I}_{N_r})^{-1} \mathbf{H}_{\bar{k}}^H, \quad (2.59)$$

where the quantity  $\mathbf{H}_{\bar{k}}$  denotes the remaining column vectors of  $\mathbf{H}$  after the  $(k - 1)$ th cancellation. Hence, the estimated symbol for the  $k$ th ordered transmit antenna is given by

$$\hat{s}_k = \mathbf{w}_k \mathbf{y}_k, \quad (2.60)$$

where the vector  $\mathbf{w}_k$  denotes the  $k$ th row vector of MMSE matrix in (2.59). Note that the quantity  $\hat{s}_k$  can not only be used for hard-decision cancellation, but also for log-likelihood ratio (LLR) computation for soft cancellation [87]. However, the quantity  $\hat{s}_k$  may not be estimated correctly in some cases, which means  $\hat{s}_k \neq s_k$ . It will have a detrimental effect on SIC detection namely error propagation [88, 89]. The detection ordering is an effective way to reduce the error propagation, and ensures that the symbols with the highest power are detected first. There are three different ordering techniques discussed as follows

### SINR Ordering

The cancellation order can be obtained according to the post-detection signal to interference plus noise ratio (SINR). The  $k$ th post-detection SINR can be evaluated as

$$\gamma_k = \frac{\sigma_s^2 |\mathbf{w}_k \mathbf{h}_k|^2}{\sigma_s^2 \sum_{j \neq [1, k-1]} |\mathbf{w}_k \mathbf{h}_j| + \sigma_v^2 \|\mathbf{w}_k\|^2}, \quad (2.61)$$

where the quantity  $\gamma_k$  denotes the SINR, and the vector  $\mathbf{h}_k$  denotes the  $k$ th column vector of  $\mathbf{H}$ . The MMSE criterion can maximize the post-detection SINR. Hence, we choose a particular transmit antenna corresponding to the highest SINR for detection from the remaining undetected transmit antennas  $j$ , which implies that the ordering process will be performed before each detection until all transmit antennas are detected.

### SNR Ordering

For SNR ordering, the interference term is omitted for simplicity. The mathematical expression of SNR  $\gamma'_k$  can be written as

$$\gamma'_k = \frac{\sigma_s^2}{\sigma_v^2 \|\mathbf{w}_k\|^2} \quad (2.62)$$

The process of ordering can be performed similarly to the SINR ordering without the interference term.

### Channel Norm based Ordering

The SINR ordering can improve the performance of SIC detection at the expense of complex implementation. It may be impractical for MIMO systems with a large number of transmit and receive antenna pairs. The channel norm based ordering only considers the power of channels experienced by the transmit antennas instead of exploiting the SINR or SNR. Thus the complexity of such ordering becomes moderate even for massive MIMO systems at the price of performance degradation. The ordering process can be performed as  $\max_{j=[k, N_t]} \|\mathbf{h}_j\|$ . Simply speaking, the process of channel norm ordering is to choose the transmit antenna with maximum channel norm from the remaining transmit antennas for detection. Fig. 2.21 plots the BER performance with different ordering techniques. The channel norm ordering has the poorest performance among these ordering techniques. The SINR ordering outperform the SNR ordering in the case of  $4 \times 4$  MIMO system with 8PSK modulation. We also plot the MMSE detection as a reference to illustrate that the SIC receiver works much better than the MMSE counterpart.

### 2.6.5 ML Detection

Maximum likelihood (ML) detection [90] is the optimum approach to detect the symbols from multiple transmit antennas without iterative processing. In other words, ML detection can be considered as MAP detection without the aid of a priori information. Defining  $\mathbb{C}$  as a set of constellation points, and  $N_t$  as the number of transmit antennas, the ML

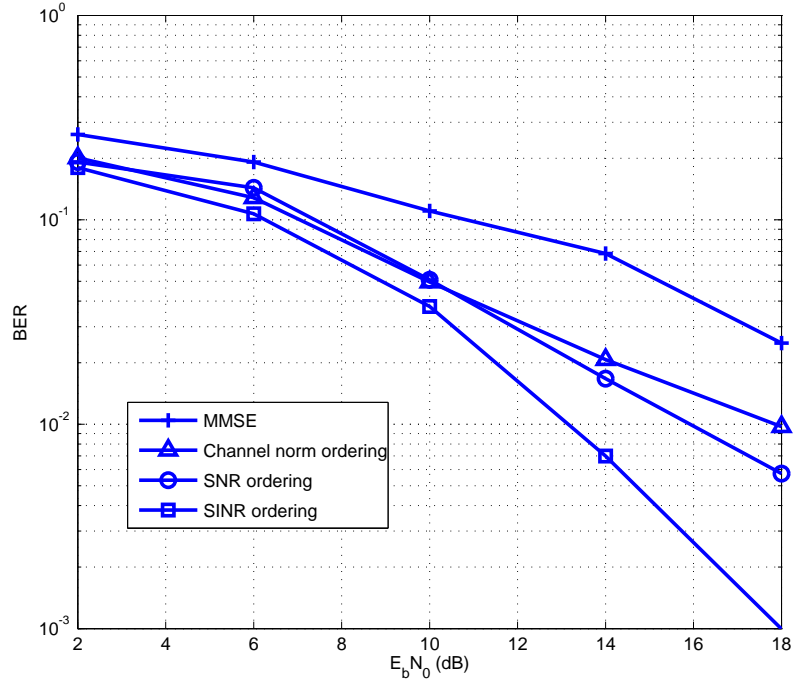


Figure 2.21: The BER performance of SIC detection with different ordering techniques  $4 \times 4$  MIMO with 8PSK

metric can be expressed as

$$\hat{\mathbf{s}}_{\text{ML}} = \underset{\mathbf{s} \in \mathbb{C}^{N_t}}{\text{argmin}} \|\mathbf{y} - \mathbf{H}\mathbf{s}\|^2. \quad (2.63)$$

where the quantity  $\mathbb{C}^{N_t}$  denotes all combinations of transmit symbols. The ML criterion calculates all combinations of transmit symbols, and chooses one particular combination with the minimum Euclidean distance. Because the ML metric in (2.63) will test every possible constellation point combination, its complexity will increase exponentially with the number of transmit antennas. Hence, the application of ML detection will be prohibitive for high order modulation and a large number of transmit and receive antennas. However, the performance of ML detection, with  $4 \times 4$ -MIMO and 16QAM modulation, is much better than that of the linear and SIC detection as plotted in Fig. 2.22. The uncorrelated Rayleigh fading channels are used in the simulation. Additionally, MMSE filter obtains initial symbol estimates for SIC detection. In the next subsection, an alternative method sphere decoder is discussed, because of the much lower complexity and near-ML performance.

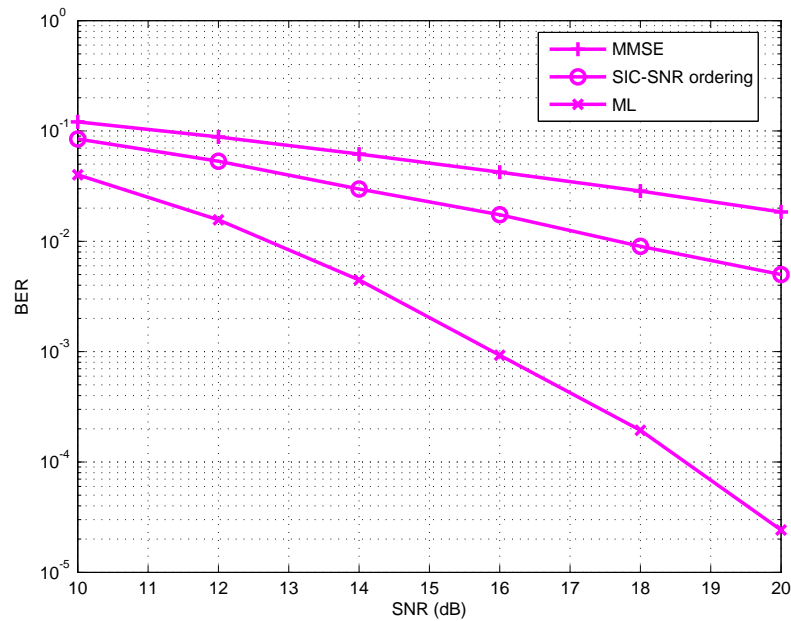


Figure 2.22: The BER performance of linear-MMSE, SIC and ML detection for  $4 \times 4$  MIMO with 16QAM

## 2.6.6 Sphere Decoder

The sphere decoder (SD) [18] is one of the most promising detection methods to reach a near-ML performance with much less implementation complexity. The idea behind it is to reduce the number of possible combinations of constellation points tested by the ML metric using a radius in the lattice. There are several different ways of implementing such ideas. In general, The SDs can be categorised into two main groups according to the representation of the system model: real-valued SD, and complex-valued SD. However, there are no significant differences between these two types of SDs except the pre-processing techniques and enumeration. In this subsection, we briefly discuss the main idea of SDs in terms of real-valued SD and complex-valued SD. Furthermore, the search strategy can also be considered as one of the very fundamental principles to categorize them into depth-first search (DFS) SD and breadth-first search (BFS) SD. In each category, various SDs have been discussed and investigated such as Schnorr-Echnner (SE) enumeration based SD, sequential Fano decoders, Fincke and Pohst (FP) based SD and the M-algorithm [17, 19, 91–93]. Additionally, some hybrid methods employing SIC and parallel interference cancellation (PIC) can also be considered as a variation of the sphere

decoder. *e.g.*, fixed complexity sphere decoder [94,95].

### Basic ideas

For simplicity, the SD is constructed in a real-valued form:

$$\bar{\mathbf{y}} = \bar{\mathbf{H}}\bar{\mathbf{s}} + \bar{\mathbf{v}}, \quad (2.64)$$

where

$$\bar{\mathbf{y}} = \begin{bmatrix} \Re(\mathbf{y}) \\ \Im(\mathbf{y}) \end{bmatrix} \quad \bar{\mathbf{s}} = \begin{bmatrix} \Re(\mathbf{s}) \\ \Im(\mathbf{s}) \end{bmatrix} \quad \bar{\mathbf{v}} = \begin{bmatrix} \Re(\mathbf{v}) \\ \Im(\mathbf{v}) \end{bmatrix}, \quad (2.65)$$

and

$$\bar{\mathbf{H}} = \begin{bmatrix} \Re(\mathbf{H}) & -\Im(\mathbf{H}) \\ -\Im(\mathbf{H}) & \Re(\mathbf{H}) \end{bmatrix} \in \mathbb{R}_{2N_r \times 2N_t}. \quad (2.66)$$

Using a similar metric as ML detection in (2.63), the following equivalence is exploited as

$$\underset{\bar{\mathbf{s}}}{\operatorname{argmin}} \|\bar{\mathbf{y}} - \bar{\mathbf{H}}\bar{\mathbf{s}}\|^2 = \underset{\bar{\mathbf{s}}}{\operatorname{argmin}} (\bar{\mathbf{s}} - \hat{\bar{\mathbf{s}}})^T \bar{\mathbf{H}}^T \bar{\mathbf{H}} (\bar{\mathbf{s}} - \hat{\bar{\mathbf{s}}}) \quad (2.67)$$

where  $\hat{\bar{\mathbf{s}}}$  denotes the LS solution of (2.64). Using a QR decomposition of  $\bar{\mathbf{H}}$ , (2.67) is constrained by a sphere radius, which is expressed by

$$(\bar{\mathbf{s}} - \hat{\bar{\mathbf{s}}})^T \bar{\mathbf{H}}^T \bar{\mathbf{H}} (\bar{\mathbf{s}} - \hat{\bar{\mathbf{s}}}) = (\bar{\mathbf{s}} - \hat{\bar{\mathbf{s}}})^T \bar{\mathbf{R}}^T \bar{\mathbf{R}} (\bar{\mathbf{s}} - \hat{\bar{\mathbf{s}}}) = \|\bar{\mathbf{R}}(\bar{\mathbf{s}} - \hat{\bar{\mathbf{s}}})\|^2 \leq r_{\text{SD}}^2, \quad (2.68)$$

where  $\bar{\mathbf{R}}$  denotes an upper triangular matrix. Note that the complexity of SD is significantly affected by the radius  $r_{\text{SD}}^2$ , which can be determined by the distribution of the noise  $\bar{\mathbf{v}}$  or the Euclidean distance obtained by the current best candidate transmit vector. The method discussed above employs a LS solution to define the SD metric, but an additional complexity will be involved with a matrix inversion. Hence, the system model can be re-defined as

$$\bar{\mathbf{y}} = \bar{\mathbf{H}}\bar{\mathbf{s}} + \bar{\mathbf{v}} \quad (2.69)$$

$$\bar{\mathbf{Q}}^H \bar{\mathbf{y}} = \bar{\mathbf{Q}}^H \bar{\mathbf{Q}} \bar{\mathbf{R}} \bar{\mathbf{s}} + \bar{\mathbf{Q}}^H \bar{\mathbf{v}} \quad (2.70)$$

$$\tilde{\mathbf{y}} = \bar{\mathbf{R}}\bar{\mathbf{s}} + \tilde{\mathbf{v}} \quad (2.71)$$

The problem of finding the candidate transmit vector corresponding to the minimum Euclidean distance can be reformulated as a tree search problem as illustrated in Fig. 2.23.

Each arrow represents a constellation point, and the dashed ones correspond to the discarded constellation points, the partial Euclidean distances or partial weights of which are beyond the radius  $r_{\text{SD}}^2$ . The mathematical expression of SD is given by

$$\hat{\mathbf{s}}_{\text{SD}} = \underset{\mathbf{s}}{\operatorname{argmin}} \|\tilde{\mathbf{y}} - \bar{\mathbf{R}}\mathbf{s}\|^2 = \underset{\mathbf{s}}{\operatorname{argmin}} \left| \sum_{i=1}^{N_t} \tilde{y}_i - \bar{r}_{i,i}\bar{s}_i - \sum_{j=1}^{i-1} \bar{r}_{i,j}\bar{s}_j \right|^2, \quad (2.72)$$

where  $\bar{r}_{i,j}$  denotes the  $(N_t - i + 1, N_t - j + 1)$ th element of  $\bar{\mathbf{R}}$ . Based on the tree structure, different search strategies can be employed for SD. The various ways of performing the search strategy will be presented:

1. Depth-first search [17, 19, 91]: The DFS corresponds to searching down the branch in Fig. 2.23 to reach the bottom first, and the search proceeds upward and downward until all available branches within the radius are accessed. Note that the current optimum branch accessed by DFS may be replaced by the new branches with a lower cost. In other words, the branches accessed by DFS are also discarded simultaneously once the new better branches are obtained. The metric of choosing the branch is based on the minimum cost at each detection layer. The complexity of DFS will converge to that of the decision feedback equalizer (DFE) at high SNR values, if the ML solution is identical to the DFE in the initial search. Because no branch has lower cost than that of the ML solution, the search will be completed much faster than other cases. For example, the ML solution is not obtained in the initial search. However, the complexity of DFS at low SNR values will be significantly increased due to a large number of suboptimal branches which are required to be pruned. Since the number of branches accessed by DFS is varying, the complexity of DFS does not remain constant.
2. Breadth-first search strategy [93]: The BFS will search all available branches downward simultaneously in each layer, if the available branches are inside the radius. Additionally, several best branches with lower costs will be reserved, and then these reserved branches will be extended to the next layer accordingly. The search process is repeated until the bottom layer is reached. In Fig. 2.23, the 4th layer is the bottom layer. Unlike DFS, the search of BFS will not proceed upward, because all available branches inside the radius in each layer have been tested in BFS. Thus the complexity of BFS is relatively constant compared to DFS only keeping a fixed

number of branches tested in each layer, and it is also insensitive to the SNR values. The BFS can be performed with fixed complexity, which is suitable for pipeline implementation. Other search strategies such as Best-first search [96] will not be discussed further, because they are similar to BFS. The idea behind it is to reserve a sorted list of branches and search down the best branches even if they are not in the same layer, so it requires much more memory to keep such sorted lists, and order them for new added best branches.

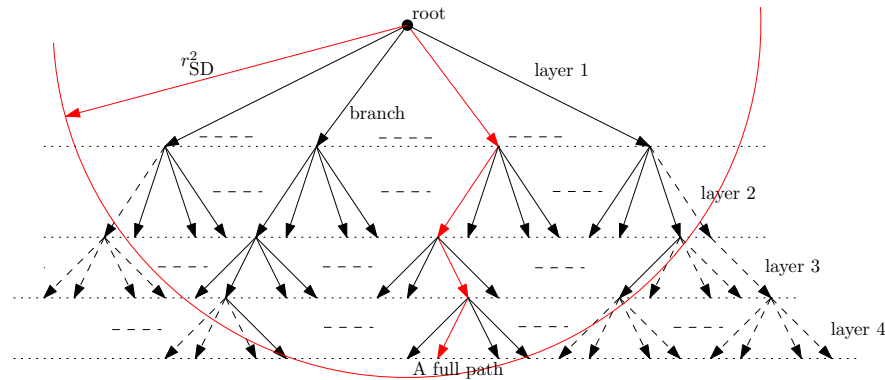


Figure 2.23: The tree structure of sphere decoder

### Channel Matrix Preprocessing

SD requires QR decomposition of the channel matrix to construct a tree structure, so QR decomposition can be considered as a preprocessing technique. The advanced preprocessing technique can achieve a significant complexity reduction with negligible performance loss. The preprocessing techniques based on the receive signals  $\mathbf{y}$  have been well discussed [97, 98], but they must be implemented for each symbol. Hence, the sorted QR decomposition (SQRD) only based on  $\mathbf{H}$  has been presented in [99]. The column based sorted version is similar to channel norm ordering, and the QR decomposition is performed on the basis of ordered  $\mathbf{H}$ , *i.e.*,  $\mathbf{HP} = \mathbf{QR}$ , where  $\mathbf{P}$  is a permutation matrix corresponding to the channel norm ordering. Simplified sorted QR decomposition (SQRD) has been proposed in [100]. A more complicated SQRD based on  $\mathbf{H}$  was proposed in [101] to further reduce the complexity of search in SDs at the expense of a negligible performance loss, which can be referred to as MMSE-SQRD. The mathematical

expression of MMSE-SQRD is given by

$$\begin{bmatrix} \mathbf{H} \\ \alpha \mathbf{I}_{N_t \times N_t} \end{bmatrix} \mathbf{P} = \begin{bmatrix} \mathbf{Q}_1 & \mathbf{Q}_2 \\ \mathbf{Q}_3 & \mathbf{Q}_4 \end{bmatrix} \begin{bmatrix} \tilde{\mathbf{R}} \\ \mathbf{0}_{N_r \times N_t} \end{bmatrix} \quad (2.73)$$

where  $\alpha$  denotes  $\frac{\sigma_n}{\sigma_s}$ . Thus (2.69) becomes

$$\hat{\mathbf{y}} = \tilde{\mathbf{R}}\tilde{\mathbf{s}} + \hat{\mathbf{v}}, \quad (2.74)$$

where  $\hat{\mathbf{y}} = \mathbf{Q}_1^H \bar{\mathbf{y}}$ ,  $\tilde{\mathbf{s}} = \mathbf{P}^T \bar{\mathbf{s}}$ ,  $\hat{\mathbf{v}} = -\alpha \mathbf{Q}_3^H \bar{\mathbf{s}} + \mathbf{Q}_3^H \bar{\mathbf{v}}$ . Note that the detection ordering brought by the permutation matrix  $\mathbf{P}$  is required to be reversed after the detection. We plotted the curves of the number of visited nodes or branches against SNR using SQRD and MMSE-SQRD. MMSE-SQRD can save significant computational efforts compared to SQRD, so MMSE-SQRD is employed for SDs in Chapter 4.

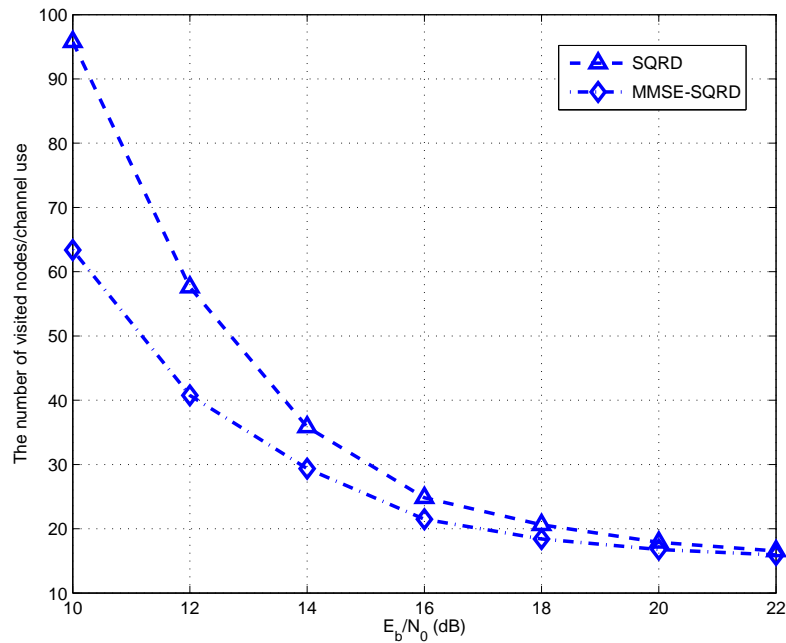


Figure 2.24: The number of visited nodes (branches) comparison between SQRD and MMSE-SQRD with conventional SE-SD over  $4 \times 4$  MIMO-8PSK

## 2.6.7 Complex-valued Sphere Decoder

In the previous subsections, the basic ideas of SD has been reviewed. The system model for the real-valued SD (2.74) can be naturally extended to the complex-valued SD by

replacing the real-valued elements in the matrices and vectors by the complex-valued elements. That can be rewritten as

$$\mathbf{z} = \mathbf{R}\mathbf{s} + \mathbf{v} \quad (2.75)$$

where  $\mathbf{z} \in \mathbb{C}_{N_r \times 1}$ ,  $\mathbf{s} \in \mathbb{C}_{N_t \times 1}$ ,  $\mathbf{v} \in \mathbb{C}_{N_r \times 1}$ , and  $\mathbf{R} \in \mathbb{C}_{N_r \times N_t}$  denotes a complex upper triangular matrix, where  $r_{i,j}$  locates in the  $(N_t - i + 1)$ th row and the  $(N_t - j + 1)$ th column of the matrix  $\mathbf{R}$ . The main difference between the real-valued SD and the complex-valued SD is the enumeration scheme, which is used to find the candidates for each detection layer. For real-valued SD, the search is only performed in the real domain rather than the complex domain. Hence, it is simpler than that of complex-valued SD. This sub-

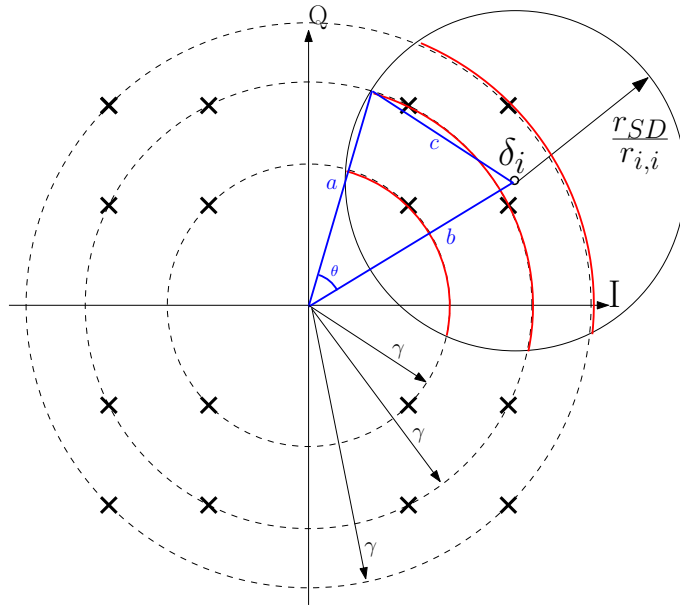


Figure 2.25: An example of computation coordinate bound using trigonometric function for the  $i$ th layer and 16QAM.

section demonstrates a complex-valued enumeration namely computation of coordinate bound (CCB) or complex SE enumeration. This bound was first proposed in [28], and an improved version was presented in [102], which separates the constellation points into groups located on one or multiple concentric rings and computes the phase bound based on the current sphere radius and previously detected symbols  $\hat{s}_k$  and  $r_{i,k}$ . In this case, these constellation points can be tested according to the bound in (2.78) to determine whether they are in the circle of NC points. The constellation points  $s_i^m = \gamma e^{j\theta_m}$  can be represented in polar coordinates, where the quantity  $s_i^m$  denotes the  $m$ th candidate constellation point at layer  $i$ , and  $0 \leq \theta_m < 2\pi$ . Note that the quantity  $\gamma$  will be different

in different concentric rings as shown in Fig. 2.25. This figure illustrates that the phase bound of the constellation points for one particular concentric ring can be determined by the sphere radius. The red curves correspond to the phase bounds of concentric rings. According to (2.72) and (2.75), the null-cancelling point for the  $i$ th layer can be defined as

$$\delta_i = \left( z_i - \sum_{k=1}^{i-1} r_{i,k} \hat{s}_k \right) / r_{i,i}. \quad (2.76)$$

With the aid of trigonometric function, we thus calculate the phase bound of  $\theta_m$  as Fig. 2.25

$$\cos(\theta_m - \theta_{\delta_i}) = \frac{1}{2\gamma|\delta_i|} \left( \gamma^2 + |\delta_i|^2 - \frac{r_{SD}^2}{r_{i,i}^2} \right) = \psi \quad (2.77)$$

where  $r_{SD}$  denotes the sphere radius. In Fig. 2.25, a specific example of CCB has been presented. If the previous detected symbols  $\hat{s}_k$  are perfect, the equivalent sphere radius  $\frac{r_{SD}}{r_{i,i}}$  can be used to compute the phase bound (red curves) with the trigonometric function  $\cos \theta = \frac{a^2+b^2-c^2}{2ab}$ , where  $a = \gamma$ ,  $b = |\delta_i|$ , and  $c = \frac{r_{SD}}{r_{i,i}}$ . The vector with possible candidates  $\tilde{s}_i$  in layer  $i$  for a given concentric ring can be categorized as

$$\tilde{s}_i = \begin{cases} \emptyset, \psi > 1, \\ s_i^m, m = 1, 2, \dots, M, \text{ and } \psi < -1 \\ s_i^m, \theta_m \in [\theta_{\delta_i} - \arccos(\psi), \theta_{\delta_i} + \arccos(\psi)], \\ \text{and } -1 \leq \psi \leq 1, \end{cases} \quad (2.78)$$

where  $0 \leq \arccos(\psi) \leq \pi$ . From (2.78), no constellation points in one concentric ring will be included for the candidates if  $\psi > 1$ , which implies that the phase bound is too small to cover any constellation points except  $\delta_i$ . For  $\psi < -1$ , the corresponding phase bound  $[\theta_{\delta_i} - \pi, \theta_{\delta_i} + \pi]$  to include all constellation. For  $-1 \leq \psi \leq 1$ , only the constellation points inside the bound can be used for the search. However, the phase bound described above may eliminate some candidates, which should be included in the search. This is because the phases of the constellation points are between 0 and  $2\pi$ , and the corresponding phase bound may not locate within  $[0, 2\pi]$ . Thus the mismatch between the phases of constellation points and the phase bound must be fixed to avoid missing candidates.

## 2.6.8 Soft Processing for MIMO Systems

The detection algorithms discussed above are all based on the hard decision, the output of which can also be used for the channel decoder with significant performance loss. To compensate the performance loss, the soft LLRs given receive signals  $\mathbf{y}$  are required.

### Linear Detection and Soft Interference Cancellation

For simplicity, we use BPSK as the modulation scheme to present the idea of linear detection and soft interference cancellation. The same principle can be extended to other modulation schemes accordingly as described in [103]. Further details on soft interference cancellation can be found in [87, 104]. Defining  $\mathbf{H}_{\bar{m}}$  as the channel matrix omitting the  $m$  column vector,  $\hat{\mathbf{s}}_{\bar{m}}$  as the estimated soft symbol vector omitting the  $m$ th symbol, and  $\tilde{\mathbf{s}}_{\bar{m}} = \mathbf{s}_{\bar{m}} - \hat{\mathbf{s}}_{\bar{m}}$  as the residual symbol vector, the output of MMSE detection for the  $m$ th transmit antenna can be found as

$$\begin{aligned} z_m &= \mathbf{w}_m(\mathbf{y} - \mathbf{H}_{\bar{m}}\hat{\mathbf{s}}_{\bar{m}}) = \mathbf{w}_m(\mathbf{h}_m s_m + \mathbf{H}_{\bar{m}}\tilde{\mathbf{s}}_{\bar{m}} + \mathbf{v}) \\ &= \mu_m s_m + \eta_m, \end{aligned} \quad (2.79)$$

where  $\mu_m = \mathbf{w}_m \mathbf{h}_m$ ,  $\eta_m = \mathbf{w}_m(\mathbf{H}_{\bar{m}}\tilde{\mathbf{s}}_{\bar{m}} + \mathbf{v})$ , and  $\mathbf{w}_m$  denotes the  $m$ th row vector of the MMSE matrix. For the interference cancellation case, the vector  $\mathbf{w}_m$  is required to be re-calculated after each soft interference cancellation, which is similar to the hard interference cancellation. Accordingly, the definition of LLR for the  $m$ th transmit antenna symbol is given by

$$\mathbf{L}(s_m) = \ln \frac{\Pr(s_m = +1|z_m)}{\Pr(s_m = -1|z_m)} \quad (2.80)$$

$$= \ln \frac{\Pr(z_m|s_m = +1)\Pr(s_m = +1)}{\Pr(z_m|s_m = -1)\Pr(s_m = -1)} \quad (2.81)$$

$$= \ln \frac{\exp(-\frac{1}{\sigma_{\eta_m}^2}(|z_m - \mu_m s_m^+|^2))}{\exp(-\frac{1}{\sigma_{\eta_m}^2}(|z_m - \mu_m s_m^-|^2))} + \mathbf{L}_a(s_m) \quad (2.82)$$

$$= \frac{1}{\sigma_{\eta_m}^2}(|z_m - \mu_m s_m^-|^2 - |z_m - \mu_m s_m^+|^2) + \mathbf{L}_a(s_m) \quad (2.83)$$

where  $\mathbf{L}_a(s_m)$  denotes the a priori LLR for  $s_m$ , and  $\sigma_{\eta_m}^2 = \mathbf{w}_m(\mathbf{H}_{\bar{m}}\mathbb{E}\{\tilde{\mathbf{s}}\tilde{\mathbf{s}}^H\}\mathbf{H}_{\bar{m}}^H + \sigma_n^2\mathbf{I})\mathbf{w}_m^H$  and  $\Pr(z_m|s_m = +1) = \frac{1}{\pi\sigma_{\eta_m}^2} \exp(-\frac{1}{\sigma_{\eta_m}^2}|z_m - \mu_m s_m^+|^2)$ . Note that if we omit the term

$\mathbf{H}_{\bar{m}}\hat{\mathbf{s}}_{\bar{m}}$  and let  $\eta_m = \mathbf{w}_m(\mathbf{H}_{\bar{m}}\mathbf{s}_{\bar{m}} + \mathbf{v})$  in (2.79), the procedure described above will reduce to the conventional MMSE detection without soft interference cancellation. The soft symbols  $\hat{\mathbf{s}}$  can be obtained by

$$\begin{aligned}\hat{s}_m &= \sum_{+1,-1} s_m \Pr(s_m|z_m) \\ &= \Pr(s_m = +1|z_m) - \Pr(s_m = -1|z_m) \\ &= \frac{\exp(\mathbf{L}(s_m))}{\exp(\mathbf{L}(s_m)) + 1} - \frac{1}{\exp(\mathbf{L}(s_m)) + 1} \\ &= \tanh\left(\frac{\mathbf{L}(s_m)}{2}\right),\end{aligned}\tag{2.84}$$

where  $\mathbf{L}_{e_1}(s_m) = \mathbf{L}(s_m) - \mathbf{L}_a(s_m)$  denotes extrinsic LLR.

### MAP Detection

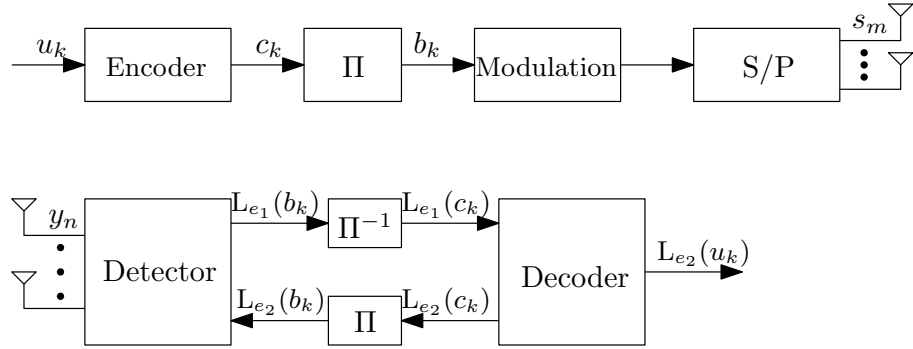


Figure 2.26: Iterative Detection and Decoding Structure

Maximum a priori probability detection, which considers the probability of all combinations of all bits, is an optimum detection method for MIMO systems. Hence, the complexity of MAP detection will increase with the number of transmit antennas and the order of modulation schemes. We review the conventional MAP detection in this subsection, the idea of which can be employed for the list sphere decoder in the later section. The block diagram for iterative detection and decoding (IDD) is illustrated in Fig. 2.26. As discussed above, the definition of LLR with extrinsic LLR  $\mathbf{L}_{e_2}(\mathbf{b}_{\bar{k}})$  without the desired  $k$ th bit from the channel decoder can be written by modifying (2.80):

$$\mathbf{L}(b_k) = \ln \frac{\Pr(b_k = +1|\mathbf{y}, \mathbf{L}_{e_2}(\mathbf{b}_{\bar{k}}))}{\Pr(b_k = -1|\mathbf{y}, \mathbf{L}_{e_2}(\mathbf{b}_{\bar{k}}))},\tag{2.85}$$

where

$$\Pr(b_k = +1 | \mathbf{y}, \mathbf{L}_{e_2}(\mathbf{b}_{\bar{k}})) \quad (2.86)$$

$$= \sum_{i=1}^{|\mathcal{C}|^M} \Pr(b_k = +1, \mathbf{b}_{\bar{k}}^{(i)} | \mathbf{y}, \mathbf{L}_{e_2}(\mathbf{b}_{\bar{k}})) \quad (2.87)$$

$$= \sum_{i=1}^{|\mathcal{C}|^M} \Pr(b_k = +1 | \mathbf{b}_{\bar{k}}^{(i)}, \mathbf{y}, \mathbf{L}_{e_2}(\mathbf{b}_{\bar{k}})) \Pr(\mathbf{b}_{\bar{k}}^{(i)} | \mathbf{y}, \mathbf{L}_{e_2}(\mathbf{b}_{\bar{k}})). \quad (2.88)$$

and the quantity  $\mathbf{b}_{\bar{k}}^{(i)}$  corresponds to the  $i$ th particular bit combination neglecting the desired  $k$ th bit. Using Bayes' rules, the first term in (2.88) can be written as

$$\begin{aligned} & \Pr(b_k = +1 | \mathbf{y}, \mathbf{b}_{\bar{k}}^{(i)}, \mathbf{L}_{e_2}(\mathbf{b}_{\bar{k}})) \\ &= \frac{\Pr(\mathbf{y} | b_k = +1, \mathbf{b}_{\bar{k}}^{(i)}, \mathbf{L}_{e_2}(\mathbf{b}_{\bar{k}})) \Pr(b_k = +1)}{\Pr(b_k = +1) \Pr(\mathbf{y} | \mathbf{b}_{\bar{k}}^{(i)}, b_k = +1, \mathbf{L}_{e_2}(\mathbf{b}_{\bar{k}})) + \Pr(b_k = -1) \Pr(\mathbf{y} | \mathbf{b}_{\bar{k}}^{(i)}, b_k = -1, \mathbf{L}_{e_2}(\mathbf{b}_{\bar{k}}))} \\ &= \frac{\Pr(\mathbf{y} | b_k = +1, \mathbf{b}_{\bar{k}}^{(i)}, \mathbf{L}_{e_2}(\mathbf{b}_{\bar{k}})) \Pr(b_k = +1)}{\Pr(\mathbf{y} | \mathbf{b}_{\bar{k}}^{(i)}, \mathbf{L}_{e_2}(\mathbf{b}_{\bar{k}}))} \end{aligned} \quad (2.89)$$

Accordingly, the second term in (2.88) becomes:

$$\Pr(\mathbf{b}_{\bar{k}}^{(i)} | \mathbf{y}, \mathbf{L}_{e_2}(\mathbf{b}_{\bar{k}})) = \frac{\Pr(\mathbf{y} | \mathbf{b}_{\bar{k}}^{(i)}, \mathbf{L}_{e_2}(\mathbf{b}_{\bar{k}})) \Pr(\mathbf{b}_{\bar{k}}^{(i)})}{\sum_{i=1}^{|\mathcal{C}|^M} \Pr(\mathbf{b}_{\bar{k}}^{(i)}) \Pr(\mathbf{y} | \mathbf{b}_{\bar{k}}^{(i)}, \mathbf{L}_{e_2}(\mathbf{b}_{\bar{k}}))} \quad (2.90)$$

$$= \frac{\Pr(\mathbf{y} | \mathbf{b}_{\bar{k}}^{(i)}, \mathbf{L}_{e_2}(\mathbf{b}_{\bar{k}})) \Pr(\mathbf{b}_{\bar{k}}^{(i)})}{\Pr(\mathbf{y} | \mathbf{L}_{e_2}(\mathbf{b}_{\bar{k}}))} \quad (2.91)$$

Hence, the conditional probability given  $\mathbf{y}$  and  $\mathbf{L}_{e_2}(\mathbf{b}_{\bar{k}})$  in (2.86) can be expressed as

$$\begin{aligned} & \Pr(b_k = +1 | \mathbf{y}, \mathbf{L}_{e_2}(\mathbf{b}_{\bar{k}})) \\ &= \sum_{i=1}^{|\mathcal{C}|^M} \frac{\Pr(\mathbf{y} | b_k = +1, \mathbf{b}_{\bar{k}}^{(i)}, \mathbf{L}_{e_2}(\mathbf{b}_{\bar{k}})) \Pr(b_k = +1)}{\Pr(\mathbf{y} | \mathbf{b}_{\bar{k}}^{(i)}, \mathbf{L}_{e_2}(\mathbf{b}_{\bar{k}}))} \cdot \frac{\Pr(\mathbf{y} | \mathbf{b}_{\bar{k}}^{(i)}, \mathbf{L}_{e_2}(\mathbf{b}_{\bar{k}})) \Pr(\mathbf{b}_{\bar{k}}^{(i)})}{\Pr(\mathbf{y} | \mathbf{L}_{e_2}(\mathbf{b}_{\bar{k}}))} \end{aligned} \quad (2.92)$$

The probability for  $b_k = -1$  can also be obtained similarly, so the LLR in (2.85) is given by

$$\mathbf{L}(b_k) = \ln \underbrace{\frac{\sum_{i=1}^{|\mathcal{C}|^M} \Pr(\mathbf{y} | b_k = +1, \mathbf{b}_{\bar{k}}^{(i)}, \mathbf{L}_{e_2}(\mathbf{b}_{\bar{k}})) \Pr(\mathbf{b}_{\bar{k}}^{(i)})}{\sum_{i=1}^{|\mathcal{C}|^M} \Pr(\mathbf{y} | b_k = -1, \mathbf{b}_{\bar{k}}^{(i)}, \mathbf{L}_{e_2}(\mathbf{b}_{\bar{k}})) \Pr(\mathbf{b}_{\bar{k}}^{(i)})}}_{\mathbf{L}_{e_1}(b_k)} + \ln \underbrace{\frac{\Pr(b_k = +1)}{\Pr(b_k = -1)}}_{\mathbf{L}_{e_2}(b_k)}, \quad (2.93)$$

where  $\mathbf{L}_{e_1}(b_k)$  and  $\mathbf{L}_{e_2}(b_k)$  denote the extrinsic LLR from the MAP detection and channel decoder, respectively. Note that  $\mathbf{L}_{e_2}(b_k) = \mathbf{L}_{a_1}(b_k)$ . For non-iterative MAP detection, the

term  $\Pr(\mathbf{b}_k^{(i)})$  is unknown, and every bit in  $\mathbf{b}_k^{(i)}$  is assumed to be equally probable. So (2.93) can be reduced to an ML solution. Because we assume the channel is zero-mean circular symmetric complex Gaussian, the probability  $\Pr(\mathbf{y}|b_k = +1, \mathbf{b}_{\bar{k}}^{(i)}, \mathbf{L}_{e_2}(\mathbf{b}_{\bar{k}}))\Pr(\mathbf{b}_{\bar{k}}^{(i)})$  can be computed as

$$\Pr(\mathbf{y}|b_k = +1, \mathbf{b}_{\bar{k}}^{(i)}, \mathbf{L}_{e_2}(\mathbf{b}_{\bar{k}}))\Pr(\mathbf{b}_{\bar{k}}^{(i)}) = \frac{1}{(\pi\sigma_n^2)^M} e^{-\|\mathbf{y} - \mathbf{H}\mathbf{s}_{k+}^{(i)}\|^2/\sigma_n^2 + \ln(\Pr(\mathbf{b}_{\bar{k}}^{(i)}))} \quad (2.94)$$

Let  $\xi_{k+} = -\|\mathbf{y} - \mathbf{H}\mathbf{s}_{k+}^{(i)}\|^2/\sigma_n^2 + \ln(\Pr(\mathbf{b}_{\bar{k}}^{(i)}))$  and  $\mathbf{s}_{k+}^{(i)}$  denote a symbol vector corresponding to the  $i$ th bit combination with the  $k$ th bit  $+1$ , we therefore can reformulate  $\mathbf{L}_{e_1}(b_k)$  in (2.85) as

$$\mathbf{L}_{e_1}(b_k) = \ln\left(\sum_{i=1}^{|\mathbb{C}|^M} e^{\xi_{k+}^{(i)}}\right) - \ln\left(\sum_{i=1}^{|\mathbb{C}|^M} e^{\xi_{k-}^{(i)}}\right). \quad (2.95)$$

With the Max-log approximation, (2.95) becomes

$$\mathbf{L}_{e_1}(b_k) \approx \max_i \xi_{k+}^{(i)} - \max_i \xi_{k-}^{(i)}. \quad (2.96)$$

Note that the computation of  $\Pr(\mathbf{b}_{\bar{k}}^{(i)})$  can be simplified further with logarithm computation. It is then easily found that

$$\Pr(\mathbf{b}_{\bar{k}}^{(i)}) = \prod_{k' \neq k, k'=1}^{|\mathbb{C}|^M} \Pr(b_{k'} = b_{k'}^{(i)}), \quad (2.97)$$

where  $\Pr(b_{k'} = \pm 1) = \frac{e^{\pm \mathbf{L}_{e_2}(b_{k'})}}{1 + e^{\pm \mathbf{L}_{e_2}(b_{k'})}} = \frac{e^{-\mathbf{L}_{e_2}(b_{k'})}}{1 + e^{-\mathbf{L}_{e_2}(b_{k'})}} e^{\mathbf{L}_{e_2}(b_{k'})b_{k'}/2} = A_{k'} e^{\mathbf{L}_{e_2}(b_{k'})b_{k'}/2}$ .

Thus,

$$\begin{aligned} \ln(\Pr(\mathbf{b}_{\bar{k}}^{(i)})) &= \ln\left(\prod_{k' \neq k, k'=1}^{|\mathbb{C}|^M} A_{k'} e^{\mathbf{L}_{e_2}(b_{k'})b_{k'}/2}\right) = \ln\left(\prod_{k' \neq k, k'=1}^{|\mathbb{C}|^M} A_{k'} e^{\sum_{k' \neq k, k'=1}^{|\mathbb{C}|^M} \mathbf{L}_{e_2}(b_{k'})b_{k'}/2}\right) \\ &= \ln\left(\prod_{k' \neq k, k'=1}^{|\mathbb{C}|^M} A_{k'}\right) + \ln\left(e^{\sum_{k' \neq k, k'=1}^{|\mathbb{C}|^M} \mathbf{L}_{e_2}(b_{k'})b_{k'}/2}\right) \approx \frac{1}{2} \sum_{k' \neq k, k'=1}^{|\mathbb{C}|^M} \mathbf{L}_{e_2}(b_{k'})b_{k'}. \end{aligned} \quad (2.98)$$

We can observe that MAP detection will test  $|\mathbb{C}|^M$  bit combinations even with the Max-log approximation, so it is quite prohibitive in practice. The complexity of MAP detection will increase with the number of transmit antennas  $M$  and order of modulation  $|\mathbb{C}|$  as shown in (2.97) and (2.98).

## List Sphere Decoder

In the previous subsections, we have reviewed an optimum detection method, *i.e.*, the MAP detector for MIMO systems, which has exponentially increasing complexity. In most cases, applications of such optimum detection methods may be quite constrained by the size of the system. Hence, a near-optimum method will be discussed in this subsection, namely, the list sphere decoder (LSD), the idea of which is very similar to the conventional SD, but that generates a list of possible candidates based on the Euclidean distance for MAP detection rather than only one output. From (2.97) and (2.98), all  $\mathbf{s}_{k+/-}^{(i)}$  and  $\mathbf{b}_k^{(i)}$ ,  $\forall i$  will be calculated. In LSD, only the  $L$  most significant candidates having relatively smaller Euclidean distance will be calculated. Thus the mathematical expression becomes

$$\begin{aligned} L_{e_1}(b_k) &= \ln\left(\sum_{l=1}^L e^{\xi_{k+}^{(l)}}\right) - \ln\left(\sum_{l=1}^L e^{\xi_{k-}^{(l)}}\right) \\ &\approx \max_l \xi_{k+}^{(l)} - \max_l \xi_{k-}^{(l)} \end{aligned} \quad (2.99)$$

Because the size of the list is much smaller than the number of all possible bit combinations, one of the terms  $\xi_{k+}^{(l)}$  or  $\xi_{k-}^{(l)}$  in (2.99) may be missing. In other words, the candidate symbol vectors in the list do not cover all probabilities for the particular  $k$ th bit, which equals  $+1$  or  $-1$ . No LLR can be computed for this particular bit. In [28], this kind of problem was fixed by introducing the ML solution with a given LLR magnitude (*e.g.* 8), so it becomes the ML solution for this particular bit. However, it will suffer a noticeable performance loss. Other techniques in [105, 106] have been discussed to alleviate the negative effects brought by the LSD.

## 2.7 Extrinsic Information Transfer Chart

The extrinsic information transfer chart was examined in [107], and a tutorial of this analysis tool for iterative techniques has been presented in [108]. For iterative techniques, the two decoders or one detector and one decoder exchange their extrinsic information between each other to improve the reliability of the transmitted information. However, this iterative process consisting of two decoding components with extrinsic information

exchange is not easy to analyse. The EXIT chart can provide an indicator of the performance and the iterative behaviour of the extrinsic information, so the design of channel coding and detection using iterative process can be visualized with the EXIT chart. According to [108], the mutual information described above can be evaluated by

$$\begin{aligned}
 I(L; x) &= 1 - \int_{-\infty}^{+\infty} \Pr(L|x = +1) \log_2(1 + e^{-L}) dL \\
 &= 1 - \mathbb{E}\{\log_2(1 + e^{-L})\} \\
 &\approx 1 - \frac{1}{N} \sum_{n=1}^N \log_2(1 + e^{-x_n L_n}),
 \end{aligned} \tag{2.100}$$

where  $L_n$  denotes the LLR of a given  $n$  sample,  $x_n$  denotes  $\pm 1$ . Due to the ergodicity, an accurate estimate of the mutual information can be evaluated with a large number  $N$  of  $x_n$  even for non-Gaussian and unknown distribution. It will be very useful for IDD in MIMO systems, because the distribution of the MIMO detector output may not be Gaussian. In addition, a large interleaver is required to guarantee the statistical independence between information bits. The block diagram of the mutual information estimates  $I(L_{e_1}; x)$  and  $I(L_{a_1}; x)$  of the MIMO detector is plotted in Fig. 2.27. Note that we omit the modulation block, and use the notation  $L_{a_1}$  as the a priori input of the MIMO detector, which is interchangeable for the extrinsic output  $L_{e_2}$  of the channel decoder. Furthermore, the quantity  $\sigma_a^2$  can be computed by  $J^{-1}(I(L_{a_d}; x))$  in the Appendix of [109], where  $L_{a_d}$  denotes the desired mutual information for  $I(L_{a_1}; x)$ .

### 2.7.1 Application of EXIT Charts

In this subsection, Several EXIT charts of detectors and decoders have been plotted. Denoting  $I_e$  and  $I_a$  as the mutual information of extrinsic information and a priori information, respectively, the subscripts 1 and 2 denote the detector and the decoder. In Fig. 2.28, the EXIT chart of the convolutional code with different constraint length  $K$  and coding rate  $R$  is plotted. We can observe that the convolutional code with lower rate has relatively flat curves, which implies that the quantity  $I_{e_2}$  can reach 1 (the right end of the EXIT chart) with moderate increase of  $I_{a_2}$ , but with more parity bits. In other words, the performance of lower rate convolutional code will be better than the higher rate counterparts at the expense of transmission efficiency. The constraint length can only change the shapes of the curves, the area under which may not be affected. Hence, the capacity achieved

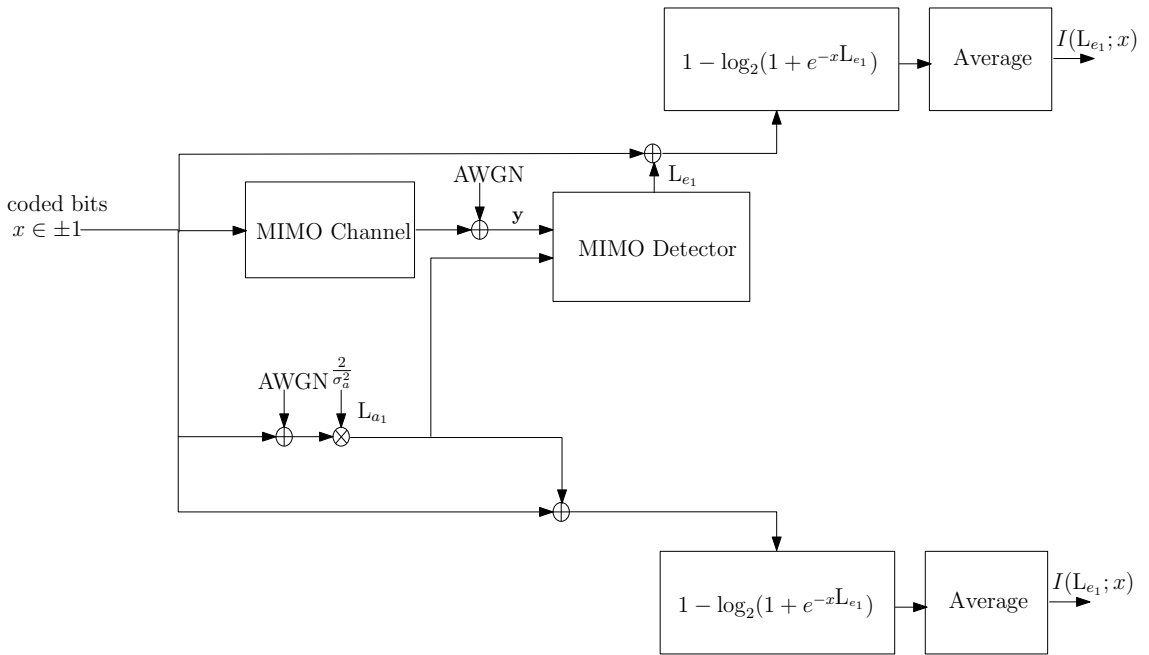


Figure 2.27: The block diagram of mutual information estimates

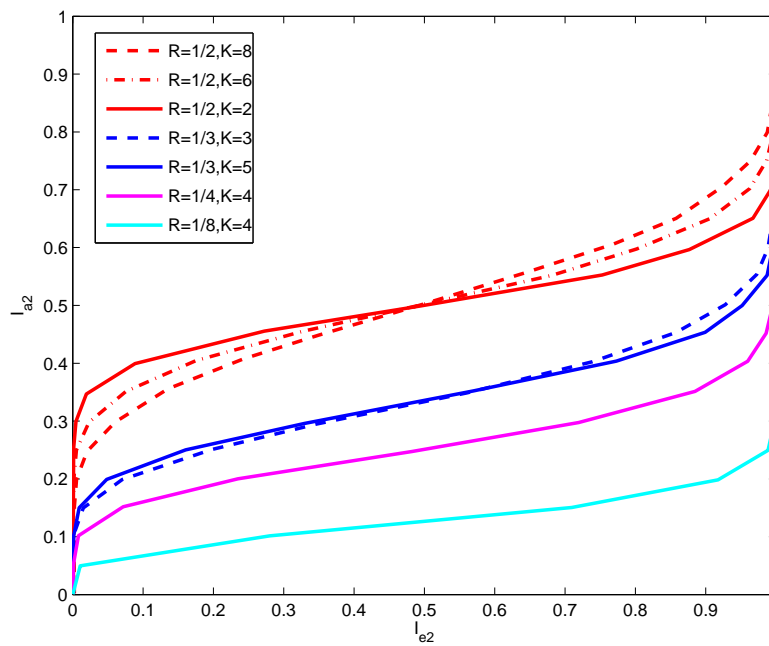


Figure 2.28: EXIT charts of convolutional code with different rate  $R$  and different constraint length  $K$ .

with such convolutional codes using the other decoding component will be the same, because the areas of the tunnel between two decoding components are the same. The area property of EXIT chart is well discussed in [109]. The area property can be considered

as one particular representation of Shannon's capacity theorem. Additionally, Fig. 2.29 illustrates an EXIT chart of  $4 \times 4$ -4QAM spatial multiplexing MIMO system with IDD at the receiver, and the exchange of soft information between two decoding components (Max-log-MAP and half rate convolutional code with constraint length 3) is illustrated by the trajectory. This mechanism is very similar to the turbo engine. Two components take extrinsic information from the other component as a priori information. If two curves of two decoding components intersect, the high error probability will appear. According to the EXIT chart, several possible improvements of decoding components may be made to reduce the error probability such as reshaping the curves of decoding components. The most straightforward method is increasing the SNR in Fig. 2.29. Also, by introducing a lower rate outer code or more powerful code (turbo code or LDPC code), the curves will become relatively flat, so the intersection can be removed at this particular SNR value. Another common approach is to reshape the curves of the inner code. In Fig. 2.29, the curve of Max-log MAP (inner code) can be reshaped using another rate one precoder as discussed in [110]. Thus the EXIT chart is a reliable analysis tool to evaluate the performance of IDD, and visualize iterative behaviours of different channel codes for code design.

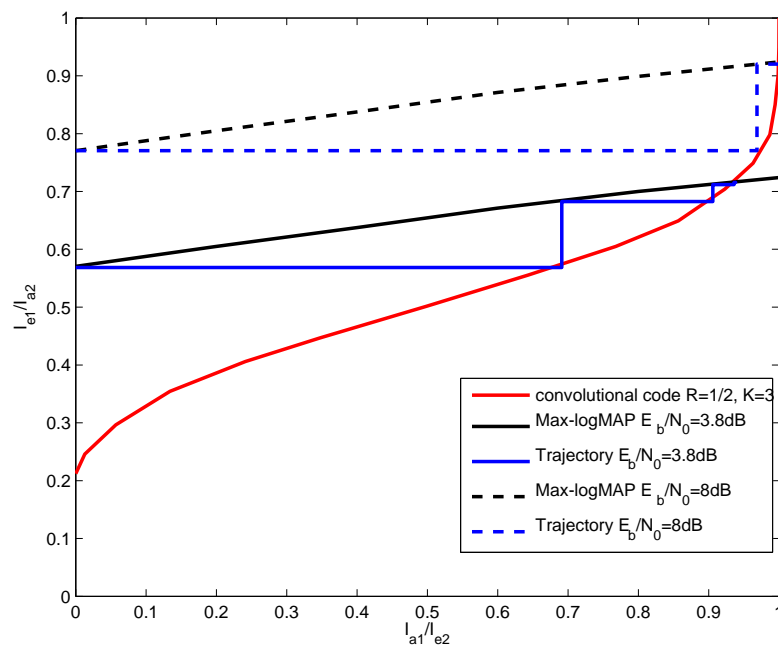


Figure 2.29: EXIT charts of  $4 \times 4$ -4QAM MIMO system with Max-log MAP detection and a half rate convolutional code with constraint length 3

## 2.8 Equalization for OFDM Systems over Doubly Selective Channels

For rapidly time-varying channels, the orthogonality between subcarriers in OFDM systems will be destroyed, which makes the signals from the neighbour subcarriers interfere with the signals of the desired subcarrier namely inter-carrier interference (ICI). In our thesis, we only consider the ICI caused by the rapidly varying channel. In Subsection 2.3.3, ICI has been discussed in a mathematical derivation. In the following, we will review some existing techniques to combat ICI with dimension reduced processing, and compare some of them in BER performance and implementation complexity. As described in (2.15), the system model can be represented in a simple form as

$$\mathbf{y} = \mathbf{H}_{df} \mathbf{s} + \mathbf{v}. \quad (2.101)$$

where  $\mathbf{H}_{df} = \mathbf{F} \mathbf{H}_{tl} \mathbf{F}^H$ .  $[\mathbf{H}_{df}]_{d,k} = h_{df}(d - k, k) = \frac{1}{N} \sum_{n=0}^{N-1} \sum_{l=0}^{L-1} h(n, l) e^{-j \frac{2\pi}{N} (lk + (d-k)n)}$ .

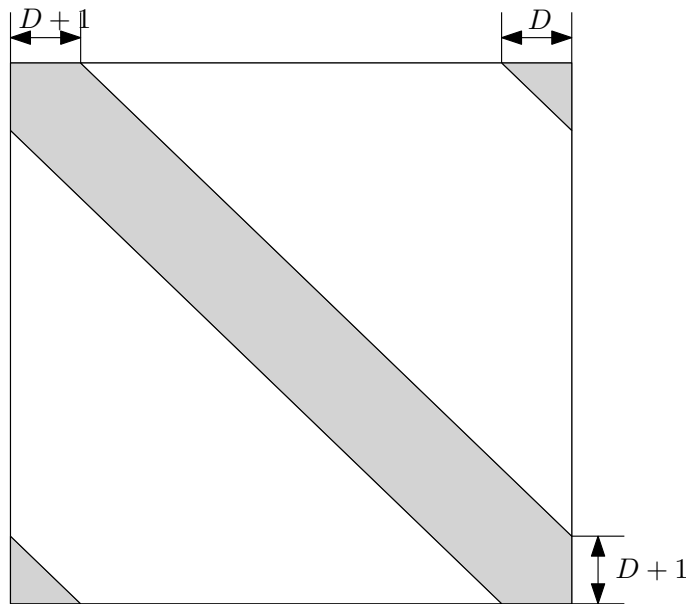


Figure 2.30: The illustration of the banded frequency channel structure

### 2.8.1 Banded Channel Structure and Window Techniques

The banded channel structure assumption has been considered as one of the most effective approaches to reduce the complexity of equalization for OFDM systems over rapidly varying channels. Based on this assumption, the signal of the desired subcarrier is only affected by several neighbour subcarriers, because the power of signals outside the band is significantly lower than the signals inside the band. The equivalent banded frequency channel matrix is plotted as Fig. 2.30. The shaded area represents the desired subcarriers, and the subcarriers inside the shaded area will be employed for detection. Basically, the banded structure is an approximation to the original frequency channel matrix, so the banded structure can be obtained by several window techniques described in [56, 57] such as Hamming window, Blackman window, and the rectangular window. Here we review one optimum window technique, which maximizes the signal power inside the band against the interference power outside the band. For simplicity, we denote the original frequency channel matrix as  $\mathbf{H}_{df}$ , the time channel matrix as  $\mathbf{H}_{tl}$ , and  $\mathbf{F}$  as the DFT matrix, respectively. The notations  $\|\cdot\|_F$  and  $\|\cdot\|_2$  return the Frobenius norm and the 2-norm of the matrix. Furthermore,  $\text{vec}(\cdot)$  corresponds to a conversion from a matrix to a vector, and  $\otimes$  is Kronecker product. According to the well-known property below [111],

$$\begin{aligned}\|\mathbf{A}\|_F &= \|\text{vec}(\mathbf{A})\|_2, \\ \text{vec}(\mathbf{AXB}) &= (\mathbf{B}^T \otimes \mathbf{A})\text{vec}(\mathbf{X}),\end{aligned}\tag{2.102}$$

The matrices  $\mathcal{C}(\beta)$  and  $\text{diag}(\mathbf{b})$  denote the window in the frequency domain and the time domain. Note that  $\text{diag}(\mathbf{b})$  is a diagonal matrix based on  $\mathbf{b}$ . Using the property in (2.102), the desired signal power (the power of the elements in the shaded area in Fig. 2.30) inside the band can be rewritten in another form as follows:

$$\begin{aligned}\|\mathbf{P}_D \mathcal{C}(\beta) \mathbf{H}_{df}\|_F^2 &= \|\text{vec}(\underbrace{\mathbf{P}_D \mathbf{F}}_{\mathbf{F}_D} \underbrace{\text{diag}(\mathbf{b})}_{\mathbf{B}} \underbrace{\mathbf{F}^H \mathbf{F} \mathbf{H}_{tl} \mathbf{F}^H}_{\tilde{\mathbf{H}}})\|_2^2 \\ &= \|\tilde{\mathbf{H}}^T \otimes \mathbf{F}_D \text{vec}(\mathbf{B})\|_2^2,\end{aligned}\tag{2.103}$$

where  $\mathbf{P}_D$  is the shading matrix to obtain the desired subcarriers inside the band with the size of  $2D + 1$  as plotted in Fig. 2.30, and  $\mathbf{F}_D = \mathbf{P}_D \mathbf{F}$ .

$$\mathbf{P}_D = \begin{bmatrix} \mathbf{I}_{D+1} & \mathbf{0} & \mathbf{0} \\ \mathbf{0} & \mathbf{0} & \mathbf{0} \\ \mathbf{0} & \mathbf{0} & \mathbf{I}_D \end{bmatrix},\tag{2.104}$$

As we know in (2.103), the diagonal matrix  $\mathbf{B}$  mainly contains zeros. Hence, the Kronecker product can be simplified as

$$\tilde{\mathbf{H}}^T \otimes \mathbf{F}_D \text{vec}(\mathbf{B}) = \begin{bmatrix} \mathbf{F}_D \odot \tilde{\mathbf{H}}_1 \mathbf{b} \\ \mathbf{F}_D \odot \tilde{\mathbf{H}}_2 \mathbf{b} \\ \vdots \\ \mathbf{F}_D \odot \tilde{\mathbf{H}}_N \mathbf{b} \end{bmatrix} \quad (2.105)$$

where the operation  $\odot$  denotes the element-wise multiplication between two matrix.  $\tilde{\mathbf{h}}_k = [h(0, k) \dots h(n, k) \dots h(N_s - 1, k)]^T$ , and  $\tilde{\mathbf{H}}_k = \underbrace{[\tilde{\mathbf{h}}_k, \dots, \tilde{\mathbf{h}}_k]^{2D+1}}_{2D+1}$ , and  $h(n, k) = \sum_{l=0}^{L-1} h_{tl}(n, l) e^{-j \frac{2\pi}{N}(l+n)k}$ . Hence, the time-domain window vector  $\mathbf{b}$  for the  $k$ th subcarrier can be represented as

$$\begin{aligned} \|\mathbf{F}_D \odot \tilde{\mathbf{H}}_k \mathbf{b}\|_2^2 &= \mathbf{b}^H (\mathbf{F}_D \odot \tilde{\mathbf{H}}_k)^H (\mathbf{F}_D \odot \tilde{\mathbf{H}}_k) \mathbf{b} \\ &= \sum_{m,n} b_m b_n \sum_{\|d\| \leq D} \left( \sum_{q=0}^{L-1} h(n, q) e^{-j \frac{2\pi}{N} qk} \right) \\ &\quad \cdot \left( \sum_{p=0}^{L-1} h(m, p) e^{-j \frac{2\pi}{N} pk} \right)^* e^{-j \frac{2\pi}{N} dn} (e^{-j \frac{2\pi}{N} dm})^*, \end{aligned} \quad (2.106)$$

where the quantity  $d$  denote the subcarrier index inside the shading area, the quantities  $m$  and  $n$  denote the time indices in one OFDM symbol, and the quantities  $p$  and  $q$  denote the path indices. If we assume the channels of different paths are uncorrelated ( $\mathbb{E}\{h_{tl}(n, p)h_{tl}^*(m, q)\} = 0$ ), the equation (2.106) can be simplified as [56, 57]

$$\begin{aligned} \|\mathbf{F}_D \odot \tilde{\mathbf{H}}_k \mathbf{b}\|_2^2 &= \sum_{m,n} b_n b_m^* \sum_{\|d\| \leq D} \left( \sum_{q=0}^{L-1} h(n, q) e^{-j \frac{2\pi}{N} qk} \right) \\ &\quad \left( \sum_{p=0}^{L-1} h(m, p) e^{-j \frac{2\pi}{N} pk} \right)^* \cdot e^{-j \frac{2\pi}{N} (n-m)d} \\ &= \sum_{m,n} b_n b_m^* \sum_{\|d\| \leq D} \sum_{l=0}^{L-1} h(n, l) h^*(m, l) \cdot e^{-j \frac{2\pi}{N} (n-m)d} \\ &= \mathbf{b}^H (\mathbf{A} \odot \tilde{\mathbf{R}}) \mathbf{b}. \end{aligned} \quad (2.107)$$

where  $[\mathbf{A}]_{m,n} = \frac{\sin(\frac{\pi}{N_s}(2D+1)(n-m))}{N_s \sin(\frac{\pi}{N_s}(n-m))}$ , and  $\tilde{\mathbf{R}} = \mathbb{E}\{\mathbf{h}_{tl}(l)\mathbf{h}_{tl}^H(l)\}$  denotes the autocorrelation matrix of the channels. Note that  $\mathbf{h}_{tl}(p) = [h_{tl}(0, l), \dots, h_{tl}(n, l), \dots, h_{tl}(N_s - 1, l)]^T$ . Equation (2.107) is similar to the problem

formulation in [56,57], which is the maximization of the desired signal power. Hence, the problem becomes the maximization of  $\mathbf{b}^H(\mathbf{A} \odot \tilde{\mathbf{R}})\mathbf{b}$  using the optimum  $\mathbf{b}$ . Furthermore, equation (2.107) to find the optimum window  $\mathbf{b}$  for different subcarriers are the same. Thus, the optimum time domain window  $\mathbf{b}$  can be obtained using eigen-decomposition in one shot. However, this optimum window design requires channel statistical information such as channel autocorrelation matrix for each independent channel path, Doppler frequencies. Furthermore, performance degradation may occur if the channel autocorrelation function is not matched to the prior assumption. Although the window techniques can only partially reduce the error floor of OFDM systems employing the banded structure, it can be easily integrated with any OFDM systems. Fig. 2.31 and Fig. 2.32 illustrate several MSE and BER curves employing different windows with serial linear equalization discussed in Subsection 2.8.2. The performance of the eigenfilter or eigen-decomposition based window is apparently better than others in MSE performance and BER performance, where the quantity  $T_{sa}$  denotes the sample period.

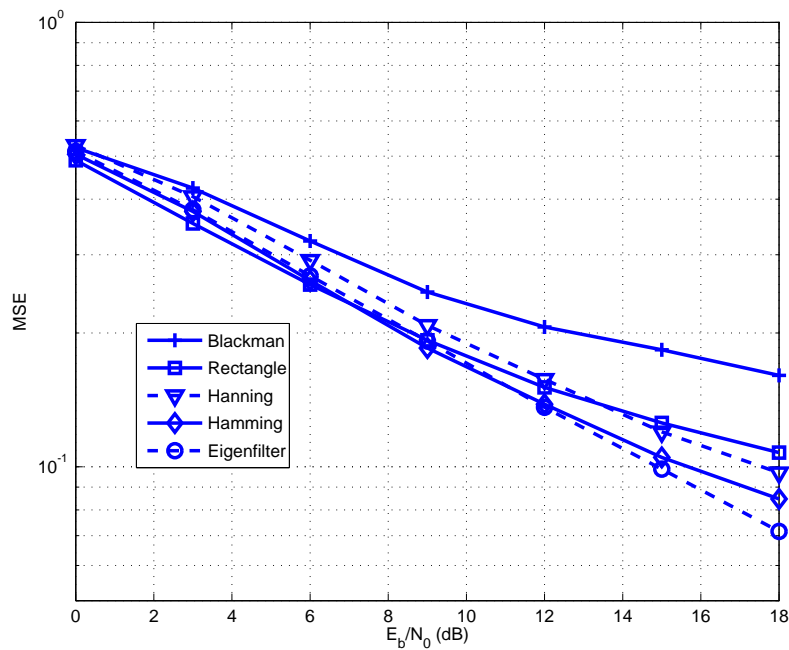


Figure 2.31: MSE performance with various windowing techniques over rapidly varying channels with  $f_d T_{sa} = 0.03$ ,  $N = 128$ ,  $L = 8$

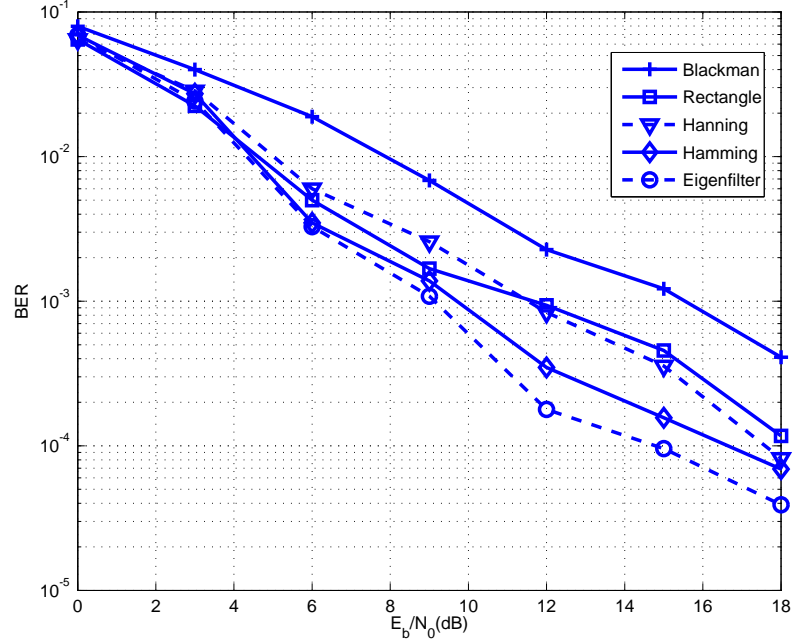


Figure 2.32: BER performance with various windowing techniques over rapidly varying channels with  $f_d T_{sa} = 0.03$ ,  $N = 128$ ,  $L = 8$

## 2.8.2 Serial Equalization and Block Equalization

With the use of the banded channel matrix, two different linear equalization methods have been proposed in [56, 57, 112]. The one in [56] performs MMSE filtering subcarrier by subcarrier, and the other one in [57, 112] uses  $\text{LDL}^H$  factorization to process the entire OFDM symbol in one shot. The serial equalization for OFDM systems is similar to MMSE detection with soft interference cancellation for MIMO systems discussed in Subsection 2.6.8, so we only present the block equalization, and compare the performance with a serial version. The steps of implementing block equalization follows as [112]

1. Fix the band size  $D$  and construct the banded matrix  $\mathbf{B} = \mathcal{C}(\beta)\mathbf{H}_{df}$ ;
2.  $\mathbf{M} = \mathbf{B}\mathbf{B}^H + \frac{\sigma_n^2}{\sigma_s^2}\mathbf{I}_{N_s}$ . Note that the size of the main diagonal band in  $\mathbf{M}$  becomes wider  $4D + 1$  due to the autocorrelation calculation  $\mathbf{B}\mathbf{B}^H$ ;
3. Obtain  $\mathbf{M}^{-1}$  by  $\text{LDL}^H$  factorization. Let  $\text{LDL}^H = \mathbf{M}$ . Assume  $\mathbf{M}^{-1}\mathbf{y} = \mathbf{d}$ . Solve  $\mathbf{y} = \mathbf{M}\mathbf{d}$  for  $\mathbf{d}$  by  $\mathbf{y} = \underbrace{\mathbf{L}\mathbf{D}\mathbf{L}^H}_{\mathbf{f}}\mathbf{d}$ ,  $\underbrace{\mathbf{D}\mathbf{L}^H}_{\mathbf{g}}\mathbf{d} = \mathbf{f}$ ,  $\mathbf{L}^H\mathbf{d} = \mathbf{g}$ , and finally obtain  $\mathbf{d}$ ;

4. Calculate symbol estimates  $\hat{s}$  in (2.101) by  $\mathbf{B}^H \mathbf{d}$ .

Note that due to replacement of serial matrix inversions by  $\mathbf{LDL}^H$  factorization, the complexity of the method described above is  $\mathcal{O}(DN_s^2)$  compared to  $(28D^2 + 24D + 5)N_s$  complex operations for serial equalization, which is 1.75 and 2.5 times smaller than serial equalization for the case of  $D = 2$  and  $D = 4$ . It implies that the block equalization is more efficient in a quite wide range of the normalized Doppler frequency  $f_d T_{\text{OFDM}}$ . In Fig. 2.33, we compare the BER performance of block equalization with serial equalization with the size of  $D = \lceil f_d T_{\text{OFDM}} \rceil + 1$ . The performance of the block version is slightly better than the serial one. Thus, the banded assumption is promising to reduce the complexity of equalization for OFDM systems over rapidly varying channels, and maintain an acceptable performance. We will investigate further the banded structure for equalization and interference cancellation in Chapter 5.

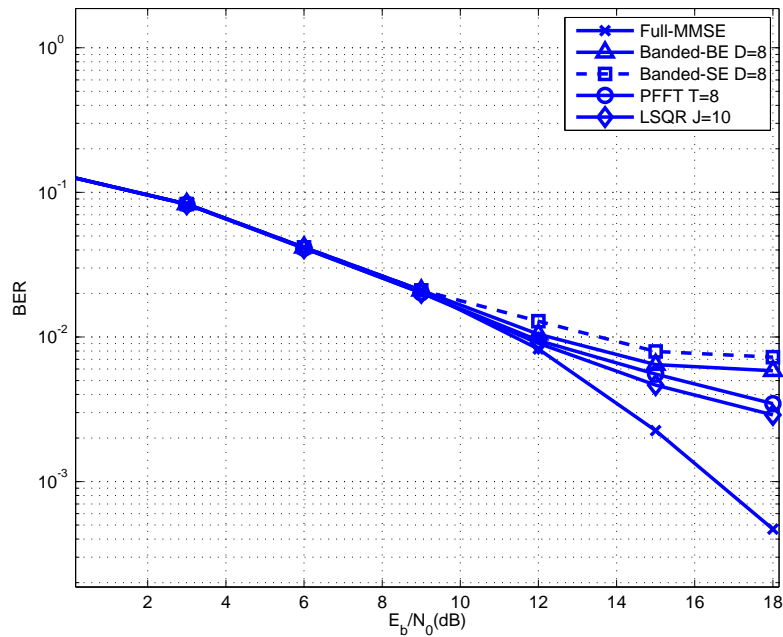


Figure 2.33: BER performance of serial equalization and block equalization over rapidly varying channels with  $f_d T_{sa} = 0.01$ ,  $N = 128$ ,  $L = 8$

### 2.8.3 Partial Fast Fourier Transform based Equalization

As mentioned above, another dimension reduced processing namely partial fast Fourier transform (PFFT) is discussed. The main idea is splitting one OFDM symbol into several segments, and the channel in each segment is assumed to remain unchanged. At the receiver side, the received signals pass through several partial FFTs. Unlike the conventional FFT, the dimension of the received signal from the partial FFT is significantly reduced from  $N_s$  to  $T$ . Hence, the complexity of filter design becomes moderate. For PFFT, we split the received signals of the time domain into  $T$  segments, and each has  $M$  samples. The output of PFFT for the  $t$ th segment can be rewritten in the following form:

$$\begin{aligned}
 y_d(t) &= \frac{1}{\sqrt{N_s}} \sum_{n=(t-1)M}^{tM-1} r(n) e^{-j \frac{2\pi}{N_s} dn} \\
 &= \frac{1}{N_s} \sum_{n=(t-1)M}^{tM-1} \underbrace{\sum_{l=0}^{L-1} h_{tl}(n, l) e^{-j \frac{2\pi}{N_s} kl}}_{h_{df}(n, k)} \\
 &\quad \cdot \sum_{k=0}^{N_s-1} s_k e^{-j \frac{2\pi}{N_s} nk} e^{-j \frac{2\pi}{N_s} nd} \\
 &= \frac{1}{N_s} \sum_{k=0}^{N_s-1} s_k \sum_{n=(t-1)M}^{tM-1} h_{df}(n, k) e^{-j \frac{2\pi}{N_s} n(d-k)},
 \end{aligned} \tag{2.108}$$

where the quantity  $h_{df}(n, k)$  denotes the channel frequency response for the  $k$ th subcarrier at time index  $n$ , and the desired subcarrier is denoted by  $d$ . We assume that the channel remains constant during segment  $t$ , so (2.108) can be simplified as [58]

$$\begin{aligned}
 y_d(t) &= \sum_{k=0}^{N_s-1} s_k h_{df}(t, k) \underbrace{\left( \frac{1}{N_s} \sum_{n=(t-1)N_t}^{tN_t-1} e^{-j \frac{2\pi}{N_s} n(d-k)} \right)}_{\delta_{d-k}(t)} \\
 &= \sum_{k=0}^{N_s-1} s_k h_{df}(t, k) \delta_{d-k}(t),
 \end{aligned} \tag{2.109}$$

where  $h_{df}(n, k) = h_{df}(t, k)$ ,  $n = (t-1)M, (t-1)M+1, \dots, tM-1$ , and

$$\delta_{d-k}(t) = \frac{1}{N_t} e^{j2\pi(d-k)\frac{2t-1}{2N_t}} \text{sinc}\left(\frac{\pi(d-k)}{N_t}\right), \tag{2.110}$$

where  $\text{sinc}(\cdot)$  denotes the sinc function. By defining  $\mathbf{y}_d = [y_d(0) \dots y_d(T-1)]^T$ ,  $\mathbf{h}_{df}(k) = [h_{df}(0, k) \dots h_{df}(T-1, k)]^T$ , we have

$$\mathbf{y}_d = \sum_{k=1}^{N_s} \text{diag}(\mathbf{h}_{df}(k)) \mathbf{z}_{d-k} s_k + \mathbf{v}_d, \quad (2.111)$$

where the vector  $\mathbf{z}_k = [\delta_k(0) \delta_k(1) \dots \delta_k(T-1)]^T$ ,  $\mathbb{E}\{z_k(t) z_{k'}^*(t')\} = \frac{\sigma_n^2}{T} e^{-j\pi(k-k')(2t-1)/T} \text{sinc}(\frac{\pi(k-k')}{2T})$ , if  $t = t'$ . For the  $d$ th subcarrier, the MMSE filter for PFFT can be given as

$$\mathbf{w}_d = \mathbf{R}_{\mathbf{y}_d \mathbf{y}_d}^{-1} \text{diag}(\mathbf{h}_{df}(d)) \mathbf{z}_0, \quad (2.112)$$

and the symbol estimate is evaluated by

$$\hat{s}_d = \mathbf{w}_d^H \mathbf{y}_d. \quad (2.113)$$

The filter design for PFFT is simple compared to the full matrix inversion, but the complexity  $\mathcal{O}(N_s T^3)$  is not as low as the previous methods (serial and block equalization for general scenarios). However, PFFT does not employ any other preprocessing before equalization, and only splits one OFDM symbol into several segments using partial FFT, so the structure of the OFDM system is similar to the conventional one. Furthermore, the authors extended the idea to the distorted underwater acoustic channel with further reduced complexity, and also to adaptive filtering in [58]. The PFFT based MMSE filter is promising with an appropriate number of segments  $T$ , and has a relatively low error floor in Fig. 2.33.

## 2.8.4 LSQR Equalization

In [113], an iterative method for solving sparse least squares problems has been well investigated, and several works based on LSQR algorithm for ICI equalization have been proposed in [63, 114]. Because of the sparsity property (banded assumption for the channel matrix as Fig. 2.30), the LSQR algorithm can be performed with low complexity to obtain the symbol estimates. In this subsection, the basic idea of the LSQR algorithm for ICI equalization has been presented to broaden our view on equalization for OFDM systems. As described in [114], the symbol estimates can be evaluated by  $\arg\min_{\mathbf{s} \in \mathbb{C}^{N_s}} \|\mathbf{y} - \mathbf{H}_{df} \mathbf{s}\|$ , which is equivalent to solving the equation  $\mathbf{H}_{df}^H \mathbf{H}_{df} \mathbf{s}^i = \mathbf{H}_{df}^H \mathbf{y}$ . Hence, an approximate solution  $\hat{\mathbf{s}}^i$  for the above equation can be obtained by the following steps:

1. Initialization:  $\alpha_1 = \|\mathbf{H}_{df}^H \mathbf{y}\|$ ,  $\beta_1 = \|\mathbf{y}\|$ ,  $\mathbf{u}_1 = \frac{\mathbf{y}}{\beta_1}$ ,  $\mathbf{v}_1 = \frac{\mathbf{H}_{df}^H \mathbf{y}}{\alpha_1}$
2. Recursion: for  $j = 1, 2, \dots$ ,

$$\begin{aligned}\alpha_{j+1} &= \|\mathbf{H}_{df}^H \mathbf{u}_j - \beta_j \mathbf{v}_j\| \\ \beta_{j+1} &= \|\mathbf{H}_{df}^H \mathbf{v}_j - \alpha_j \mathbf{u}_j\| \\ \mathbf{u}_{j+1} &= \frac{1}{\beta_{j+1}} (\mathbf{H}_{df}^H \mathbf{v}_j - \alpha_j \mathbf{u}_j) \\ \mathbf{v}_{j+1} &= \frac{1}{\alpha_{j+1}} (\mathbf{H}_{df}^H \mathbf{u}_j - \beta_j \mathbf{v}_j)\end{aligned}$$

3. Solve  $\text{argmin}_{\mathbf{w}} \|\mathbf{B}_j \mathbf{w} - \beta_1 \mathbf{e}_1\|$  by QR decomposition, where  $\mathbf{B}_j$  denotes a bidiagonal matrix having  $[\alpha_1 \dots \alpha_j]$  as the main diagonal elements, and  $[\beta_2 \dots \beta_{j+1}]$  as first subdiagonal elements, and  $\mathbf{e}_1 = [1 \ 0 \ \dots \ 0]^T$ .
4. Obtain an approximate solution after  $j$ th iterations:  $\hat{\mathbf{s}}_j = [\mathbf{v}_1 \ \dots \ \mathbf{v}_j] \mathbf{w}_j$ .

Hence, the LSQR algorithm for ICI equalization may be split into two blocks: (1) projection vector  $\mathbf{v}_j$  construction in step 1 and 2; (2) dimension reduced filter design  $\mathbf{w}_j$ . After the  $j$ th iteration, the symbol estimates  $\hat{\mathbf{s}}_j$  over the  $j$ th Krylov subspace can be extracted by the vector  $\mathbf{w}_j$ . Its popularity is due to the low complexity  $\mathcal{O}(N_s(2D+1)J)$ , numerical stability, and inherent regularization achieved by early termination of the iterative process. However, the output of LSQR cannot be readily converted to LLR due to its recursive nature, so its application to iterative detection and decoding is constrained. Furthermore, the effects brought by ICI can be partially removed, and it can achieve a good performance as compared to other techniques discussed above. Because of regularization, the number of iterations  $J = 10$  is relatively small in Fig. 2.33. We can observe that the BER performance of the LSQR algorithm is slightly better than other approaches. Although the processing dimension is reduced, the QR decomposition is still required in step 3, and the optimum number of iterations is unknown. In other words, the complexity of the LSQR algorithm is variable, which may not be suitable for hardware implementation.

## 2.9 Summary

In this chapter, we have reviewed some fundamentals of MIMO and OFDM systems. The quasi-static channel estimation for OFDM and MIMO-OFDM systems has been investigated, and we found that the comb-type pilot allocation for MIMO-OFDM may be a good candidate for the dynamic pilot allocation in Chapter 3, and the optimum MSE can be achieved using the MMSE criterion with uniform pilot allocation in the time or frequency domain. Furthermore, the detection methods for MIMO systems have been presented. The complexity of the optimum detection method (ML or MAP) is too high to implement. Its alternatives such as sphere decoder (SD) and list sphere decoder (LSD) still have room for further complexity reduction. Hence, the main target of MIMO detection is achieving the optimum performance with moderate implementation complexity. In Chapter 4, a novel complex-valued SD will be discussed to further reduce the complexity and maintain the diversity of the ML receiver. Besides, equalization for ICI has been reviewed in detail. The core of such equalization is based on dimension reduced processing including window techniques, partial FFT and LSQR algorithm. Many studies have been presented in this field, but the removal of error floors, complexity reduction of equalization, and a better banded assumption are worthy to investigate.

# Chapter 3

## Dynamic Pilot Allocation with Channel Estimation in Closed-Loop MIMO-OFDM Systems

### Contents

---

<b>3.1 Introduction . . . . .</b>	<b>73</b>
<b>3.2 MIMO-OFDM System Model with Spatial Multiplexing . . . . .</b>	<b>75</b>
<b>3.3 DFT-based Channel Estimation for MIMO-OFDM Systems . . . . .</b>	<b>75</b>
<b>3.4 Dynamic Pilot Allocation for MIMO Receivers and MIMO Iterative Pilot Search . . . . .</b>	<b>78</b>
<b>3.5 Limited Feedback for Dynamic Pilot Allocation . . . . .</b>	<b>82</b>
<b>3.6 Simulation Results . . . . .</b>	<b>85</b>
<b>3.7 Summary . . . . .</b>	<b>92</b>

---

### 3.1 Introduction

MIMO-OFDM has been adopted by many current wireless communication standards for broadband wireless data transmission. The capacity of such systems is maximized by

means of spatial multiplexing [5], and the inter-symbol interference caused by frequency selective channels can be eliminated with a cyclic prefix (CP) [80]. However, coherent receiver design requires accurate channel state information (CSI) to achieve a comparable symbol error rate (SER) performance to that with perfect CSI [115]. Pilot-symbol-aided channel estimation (PACE) is the most common approach exploited in OFDM systems. For MIMO-OFDM, the pilot allocation is more complicated than for single-input single-output (SISO)-OFDM, because of the superposition of signals from multiple transmit antennas. A number of methods have been proposed to estimate the channel in the presence of inter-antenna interference. A superimposed pilot based channel estimation technique [46], which is based on correlation of received pilot signals and original pilots to obtain channel estimates, does not require the channel to remain constant in time or frequency compared to STBC and SFBC discussed in Chapter 2. However, the pilots must be equispaced (uniform pilot allocation (UPA)), and follow the particular conditions [47, 84–86]. Alternatively, the transmit antenna sends its pilot over one tone, and the others remain silent at this subcarrier, which is similar to WiMAX’s pilot scheme and can be easily integrated with the conventional OFDM DFT-based channel estimation [48]. However, the techniques described above are normally designed for uniform pilot allocation (UPA), without any prior knowledge of the channels. Furthermore, these channel estimators often concentrate on the mean square error (MSE) minimization of channel estimates rather than SER optimization. Although the minimum MSE can be achieved using UPA [49, 50], MSE optimization is not equivalent to SER optimization. It has been shown that the BER performance can be substantially improved through DPA or iterative pilot search based DPA for SISO-OFDM and Alamouti- $2 \times 1$ -OFDM systems [52, 53].

In this chapter, we develop a dynamic pilot allocation (DPA) algorithm for MIMO-OFDM systems with spatial multiplexing. The main idea behind DPA is to allocate the pilots to appropriate subcarriers for arbitrary numbers of transmit and receive antennas. The contributions of this chapter can be summarised as follows. (1) A DPA algorithm for different MIMO-OFDM receivers (linear, SIC, ML) is presented, and a low complexity error approximation technique is applied to DPA for ML receivers; (2) A reduced complexity DPA with MIPS is presented; (3) A SVQ scheme for DPA is proposed to reduce the feedback overhead and the number of search trials, and the SVQ scheme is robust to the delays and errors of the feedback channels; (4) A simulation study of the proposed and existing algorithms for UPA and DPA.

This chapter is organized as follows. Section 3.2 describes the MIMO-OFDM system model with spatial multiplexing and the feedback channels. Section 3.3 describes a pilot allocation framework and formulates a DFT-based channel estimation scheme. The derivation of a DPA algorithm for linear, SIC, and ML receivers is then discussed, as well as the MIPS algorithm in Section 3.4. Section 3.5 presents the SVQ scheme. The simulation results are provided in Section 3.6, and Section 3.7 draws a summary.

## 3.2 MIMO-OFDM System Model with Spatial Multiplexing

In Subsection 2.5, the system model for MIMO-OFDM has been described in details. Furthermore, the DPA algorithm require a feedback channel to convey the pilot allocation indices. This typically introduces a delay of some OFDM symbol periods (eg. 20 OFDM symbols) [116]. In other words, the pilot allocation indices sent by the receiver may be mismatch to the current channels.

## 3.3 DFT-based Channel Estimation for MIMO-OFDM Systems

In this section, the DFT-based channel estimation and pilot allocation for MIMO-OFDM are discussed, and channel estimation errors for particular pilot patterns have been derived for the following optimization metrics.

### 3.3.1 Pilot Allocation with Multiple Transmit Antennas

We consider a  $N_t \times N_r$  MIMO scenario here, and a comb-type pilot pattern is utilized for each antenna. The uniform pilot allocation (UPA) is depicted in Fig. 2.4. If a pilot is allocated at the  $k$ th subcarrier for one antenna no other antenna allocates a pilot or data

in this subcarrier [48]. Hence, inter-antenna interference can be avoided for channel estimation due to the null subcarrier assigned by other transmit antennas, and pilots can be inserted into any subcarriers except occupied ones. This principle can be also applied to a scenario with arbitrary numbers of transmit antennas except requiring more null subcarriers for transmit antennas. The  $i$ th transmit antenna pilot pattern can be represented by a  $N_s \times N_s$  diagonal matrix  $\mathbf{P}_i$  in which 1s denote the pilot subcarriers, and zeros are used for data or null subcarriers.

$$\mathbf{P}_i = \begin{bmatrix} 1 & 0 & \dots & 0 \\ 0 & 0 & \dots & \vdots \\ \vdots & \vdots & \ddots & \vdots \\ 0 & 0 & \dots & 1 \end{bmatrix} \quad i = 1, 2, \dots, N_t, \quad (3.1)$$

where  $\mathbf{P}_i \in \mathcal{P}$ ,  $\|\mathcal{P}\| = \begin{pmatrix} N_s - (i-1)N_p \\ N_p \end{pmatrix}$ ,  $tr\{\mathbf{P}_i\} = N_p$ ,  $\forall i$ , and  $\mathcal{P}$  denotes the set of all possible combinations of pilot allocation. The matrix in (3.1) represents one particular example of a pilot allocation matrix for the  $i$ th antenna.

### 3.3.2 DFT-based Channel Estimation

Since the pilot subcarriers for the  $i$ th transmit antenna are interference free, we use 1 as the pilot symbols in the pilot allocation matrix  $\mathbf{P}_i$  to obtain the channel in the frequency domain  $\widehat{\mathbf{H}}_{df}^{ij}$  between the  $i$ th transmit antenna and the  $j$ th receive antenna. The received pilot signals for the  $j$ th receive antenna can be described as

$$\mathbf{r}_j^{(\text{pilot})} = \mathbf{P}_i \mathbf{F}_L \mathbf{h}_{tl}^{ij} + \mathbf{P}_i \mathbf{v}_j, \quad (3.2)$$

where  $\mathbf{r}_j^{(\text{pilot})} = \mathbf{P}_i \mathbf{r}_j$ , and  $\mathbf{r}_j$  and  $\mathbf{v}_j$  denote the received signals and noise for the  $j$ th receive antenna, respectively. The CIR can be computed using LS estimation [78], and the channel frequency response (CFR) estimates can be obtained by transformation of the CIR:

$$\begin{aligned} \widehat{\mathbf{h}}_{tl}^{ij} &= (\mathbf{P}_i \mathbf{F}_L)^\dagger \mathbf{r}_j^{(\text{pilot})} = (\mathbf{F}_L^H \mathbf{P}_i \mathbf{F}_L)^{-1} \mathbf{F}_L^H \mathbf{P}_i \mathbf{r}_j^{(\text{pilot})}, \\ \widehat{\mathbf{H}}_{df}^{ij} &= \text{diag}(\mathbf{F}_L (\mathbf{F}_L^H \mathbf{P}_i \mathbf{F}_L)^{-1} \mathbf{F}_L^H \mathbf{P}_i \mathbf{r}_j^{(\text{pilot})}), \end{aligned} \quad (3.3)$$

where  $L \leq N_p$ . After some manipulation with  $\mathbf{r}_j^{(\text{pilot})}$ , we obtain a mathematical expression for the CFR estimates by substituting (3.2) into (3.3)

$$\widehat{\mathbf{H}}_{df}^{ij} = \mathbf{H}_{df}^{ij} + \text{diag}(\mathbf{F}_L(\mathbf{F}_L^H \mathbf{P}_i \mathbf{F}_L)^{-1} \mathbf{F}_L^H \mathbf{P}_i \mathbf{v}_j) = \mathbf{H}_{df}^{ij} + \boldsymbol{\Omega}_{ij}, \quad (3.4)$$

where  $\boldsymbol{\Omega}_{ij}$  denotes the channel estimation errors between the  $i$ th transmit antenna and the  $j$ th receive antenna. Hence, the covariance matrix of  $\widehat{\mathbf{H}}_{df}^{ij}$  can be represented as

$$\begin{aligned} \mathbb{E}\{\widehat{\mathbf{H}}_{df}^{ij} \widehat{\mathbf{H}}_{df}^{ijH}\} &= \mathbb{E}\{\mathbf{H}_{df}^{ij} \mathbf{H}_{df}^{ijH}\} + \mathbb{E}\{\boldsymbol{\Omega}_{ij} \boldsymbol{\Omega}_{ij}^H\} = \mathbb{E}\{\mathbf{H}_{df}^{ij} \mathbf{H}_{df}^{ijH}\} + \sigma_v^2 \text{diag}(\mathbf{F}_L(\mathbf{F}_L^H \mathbf{P}_i \mathbf{F}_L)^{-1} \mathbf{F}_L^H) \\ &= \mathbf{I}_{N_s} + \sigma_v^2 \boldsymbol{\Xi}_{ij}, \end{aligned} \quad (3.5)$$

where  $\boldsymbol{\Xi}_{ij}$  denotes the covariance matrix of the channel estimation errors, which is determined by one particular pilot allocation matrix  $\mathbf{P}_i$ . Based on (3.4) and (3.5), the actual channel  $\mathbf{H}_{df}^{ij}$  can be approximated by the estimated channel  $\widehat{\mathbf{H}}_{df}^{ij}$  as [117]

$$\mathbf{H}_{df}^{ij} = (\mathbf{I}_{N_s} + \mathbb{E}\{\boldsymbol{\Omega}_{ij} \boldsymbol{\Omega}_{ij}^H\})^{-1} \widehat{\mathbf{H}}_{df}^{ij} - \widetilde{\boldsymbol{\Omega}}_{ij} = (\mathbf{I}_{N_s} + \sigma_v^2 \boldsymbol{\Xi}_{ij})^{-1} \widehat{\mathbf{H}}_{df}^{ij} - \widetilde{\boldsymbol{\Omega}}_{ij}, \quad (3.6)$$

In order to obtain the covariance matrix of  $\widetilde{\boldsymbol{\Omega}}_{ij}$ , equation (3.4) can be transformed as follows. Substituting (3.6) into (3.4), the expression becomes

$$\boldsymbol{\Omega}_{ij} - \widetilde{\boldsymbol{\Omega}}_{ij} = (\mathbf{I}_{N_s} + \sigma_v^2 \boldsymbol{\Xi}_{ij})^{-1} \sigma_v^2 \boldsymbol{\Xi}_{ij} \widehat{\mathbf{H}}_{df}^{ij}, \quad (3.7)$$

so

$$\widetilde{\boldsymbol{\Omega}}_{ij} = \boldsymbol{\Omega}_{ij} - (\mathbf{I}_{N_s} + \sigma_v^2 \boldsymbol{\Xi}_{ij})^{-1} \sigma_v^2 \boldsymbol{\Xi}_{ij} \widehat{\mathbf{H}}_{df}^{ij}. \quad (3.8)$$

It can be found that  $\mathbb{E}\{\widetilde{\boldsymbol{\Omega}}_{ij}\} = 0$ , and the covariance matrix of  $\widetilde{\boldsymbol{\Omega}}_{ij}$  is given by

$$\begin{aligned} \mathbb{E}\{\widetilde{\boldsymbol{\Omega}}_{ij} \widetilde{\boldsymbol{\Omega}}_{ij}^H\} &= \sigma_v^2 \boldsymbol{\Xi}_{ij} - 2(\mathbf{I}_{N_s} + \sigma_v^2 \boldsymbol{\Xi}_{ij})^{-1} \sigma_v^2 \boldsymbol{\Xi}_{ij} \sigma_v^2 \boldsymbol{\Xi}_{ij}^H + (\mathbf{I}_{N_s} + \sigma_v^2 \boldsymbol{\Xi}_{ij})^{-1} \sigma_v^2 \boldsymbol{\Xi}_{ij} \sigma_v^2 \boldsymbol{\Xi}_{ij}^H \\ &= (\mathbf{I}_{N_s} + \sigma_v^2 \boldsymbol{\Xi}_{ij})^{-1} \sigma_v^2 \boldsymbol{\Xi}_{ij}. \end{aligned} \quad (3.9)$$

From (3.6), the actual channel can be approximated by the estimated channel, which corresponds to one particular pilot pattern. In the following section, equation (3.6) will be used to calculate the SINR or MSE and the corresponding SER estimates, which correspond to different pilot patterns. Then, the optimum pilot pattern can be chosen based on the SER estimates.

### 3.4 Dynamic Pilot Allocation for MIMO Receivers and MIMO Iterative Pilot Search

In this section, we derive DPA using (3.6) for different receivers with BPSK modulation. The same strategy can also be extended to other receiver techniques such as [64] with other modulation schemes.

#### 3.4.1 Dynamic Pilot Allocation Algorithm for Linear and SIC Receivers

For linear and SIC receivers, the SINR is used for the SER estimates. Due to channel estimation errors, inter-antenna interference and noise, the expression of the detected symbols for the  $q$ th desired transmit antenna is obtained by substituting (3.6) into the system model described in Subsection (2.5):

$$\begin{aligned}
 \widehat{\mathbf{s}}_q = & \widehat{\mathbf{W}}_{\text{linear}}^q \mathbf{y} = \underbrace{\widehat{\mathbf{W}}_{\text{linear}}^q (\mathbf{I}_{N_r N_s} + \sigma_v^2 \boldsymbol{\Xi}_q)^{-1} \widehat{\mathbf{H}}_{df}^q \mathbf{s}_q}_{\text{signals}} - \underbrace{\widehat{\mathbf{W}}_{\text{linear}}^q \widetilde{\boldsymbol{\Omega}}_q \mathbf{s}_q}_{\text{channel estimation error}} \\
 & - \underbrace{\widehat{\mathbf{W}}_{\text{linear}}^q \sum_{i=1}^{d-1} (\mathbf{I}_{N_r N_s} + \sigma_v^2 \boldsymbol{\Xi}_i)^{-1} \sigma_v^2 \boldsymbol{\Xi}_i \widehat{\mathbf{H}}_{df}^i \widehat{\mathbf{s}}_i}_{\text{residual interference}} \\
 & + \underbrace{\widehat{\mathbf{W}}_{\text{linear}}^q \sum_{\substack{i=d \\ i \neq q}}^{N_t} (\mathbf{I}_{N_r N_s} + \sigma_v^2 \boldsymbol{\Xi}_i)^{-1} \widehat{\mathbf{H}}_{df}^i \mathbf{s}_i}_{\text{inter-antenna interference}} - \underbrace{\widehat{\mathbf{W}}_{\text{linear}}^q \sum_{\substack{i=1 \\ i \neq q}}^{N_t} \widetilde{\boldsymbol{\Omega}}_i \mathbf{s}_i}_{\text{channel estimation error}} + \underbrace{\widehat{\mathbf{W}}_{\text{linear}}^q \mathbf{v}}_{\text{noise}}, \quad q = 1, \dots, N_t
 \end{aligned} \tag{3.10}$$

where  $\widehat{\mathbf{H}}_{df}^i = [\widehat{\mathbf{H}}_{df}^{i1} \dots \widehat{\mathbf{H}}_{df}^{ij} \dots \widehat{\mathbf{H}}_{df}^{iN_r}]^T$ ,  $\boldsymbol{\Xi}_i = \text{diag}\{\boldsymbol{\Xi}_{i1} \dots \boldsymbol{\Xi}_{ij} \dots \boldsymbol{\Xi}_{iN_r}\}$ ,  $\widetilde{\boldsymbol{\Omega}}_i = [\widetilde{\boldsymbol{\Omega}}_{i1} \dots \widetilde{\boldsymbol{\Omega}}_{ij} \dots \widetilde{\boldsymbol{\Omega}}_{iN_r}]^T$ , and the MMSE filter for the  $q$ th transmit antenna given on the channel estimates in (3.3) can be given by

$$\widehat{\mathbf{W}}_{\text{linear}}^q = (\widehat{\mathbf{H}}_{df}^{qH} \widehat{\mathbf{H}}_{df}^q + \sum_{\substack{i=d \\ i \neq q}}^{N_t} \widehat{\mathbf{H}}_{df}^{iH} \widehat{\mathbf{H}}_{df}^i + \sigma_v^2 \mathbf{I}_{N_s})^{-1} \widehat{\mathbf{H}}_{df}^{qH}. \tag{3.11}$$

Note that the value of  $d$  distinguishes the mathematical expressions of the linear receiver ( $d = 1$ ) and the SIC receiver ( $d = q$ ). Let  $(\mathbf{I}_{N_r N_s} + N_0 \boldsymbol{\Xi}_i)^{-1} = \boldsymbol{\Lambda}_i$  and

$(\mathbf{I}_{N_r N_s} + N_0 \mathbf{\Xi}_i)^{-1} \sigma_v^2 \mathbf{\Xi}_i = \tilde{\Lambda}_i$ . Hence, the signal power  $\gamma_S^q$  for the  $q$ th transmit antenna can be calculated according to (3.10), which is

$$\gamma_S^q = \mathcal{D}(\widehat{\mathbf{W}}_{\text{linear}}^q \Lambda_q \widehat{\mathbf{H}}_{df}^q \widehat{\mathbf{H}}_{df}^{qH} \Lambda_q^H \widehat{\mathbf{W}}_{\text{linear}}^{qH}), \quad (3.12)$$

where  $\mathcal{D}()$  denotes the operation which extracts the diagonal elements of a matrix. Hence,  $\boldsymbol{\gamma}_S^q = [\gamma_S^q(0), \dots, \gamma_S^q(k), \dots, \gamma_S^q(N_s - 1)]^T$ . Similarly, the interference power for the  $q$ th transmit antenna can be approximated by

$$\boldsymbol{\gamma}_I^q = \mathcal{D}\left(\sum_{i=1}^{d-1} \widehat{\mathbf{W}}_{\text{linear}}^q \tilde{\Lambda}_i \widehat{\mathbf{H}}_{df}^i \widehat{\mathbf{H}}_{df}^{iH} \tilde{\Lambda}_i^H \widehat{\mathbf{W}}_{\text{linear}}^{qH} + \sum_{\substack{i=d \\ i \neq q}}^{N_t} \widehat{\mathbf{W}}_{\text{linear}}^q \Lambda_i \widehat{\mathbf{H}}_{df}^q \widehat{\mathbf{H}}_{df}^{iH} \Lambda_i^H \widehat{\mathbf{W}}_{\text{linear}}^{qH}\right). \quad (3.13)$$

Similar to  $\boldsymbol{\gamma}_S^q$ ,  $\boldsymbol{\gamma}_I^q = [\gamma_I^q(0), \dots, \gamma_I^q(k), \dots, \gamma_I^q(N_s - 1)]^T$ . Accordingly, the power of noise plus channel estimation errors can be given as

$$\boldsymbol{\gamma}_N^q = \mathcal{D}\left(\sum_{i=1}^{N_t} \widehat{\mathbf{W}}_{\text{linear}}^q \tilde{\Lambda}_i \widehat{\mathbf{W}}_{\text{linear}}^{qH} + \sigma_v^2 \widehat{\mathbf{W}}_{\text{linear}}^q \widehat{\mathbf{W}}_{\text{linear}}^q\right), \quad (3.14)$$

where  $\boldsymbol{\gamma}_N^q = [\gamma_N^q(0), \dots, \gamma_N^q(k), \dots, \gamma_N^q(N_s - 1)]^T$ . Hence, the SINR for the  $k$ th subcarrier can be written as

$$\text{SINR}_q(k) = \frac{\gamma_S^q(k)}{\gamma_N^q(k) + \gamma_I^q(k)}, \quad (3.15)$$

and the SER estimate of MPSK for the  $k$ th subcarrier can be obtained by [118]

$$\mathbb{P}_q(k) \approx 2\mathcal{Q}(\sqrt{2 \text{SINR}_q(k) \sin(\pi/M)}), \quad (3.16)$$

where  $\mathcal{Q}$  denotes the Q-function, which is  $\mathcal{Q}(a) = (2\pi)^{-1/2} \int_a^\infty e^{-f^2/2} df$  [118]. Corresponding to a particular pilot pattern matrix  $\mathbf{P}_q$ , the average SER estimates for the data subcarriers of the  $q$ th antenna can be represented as

$$\mathbb{P}_q(\mathbf{P}_q) \approx \frac{2}{N_d} \sum_{k=1}^{N_d} \mathcal{Q}(\sqrt{2 \text{SINR}_q(k) \sin(\pi/M)}), \quad (3.17)$$

where the quantity  $N_d$  denotes the number of data subcarriers. Hence, the optimum pilot allocation can be obtained by solving the following optimization problem:

$$\mathbf{P}_q^{\text{opt}} = \underset{\mathbf{P}_q \in \mathcal{P}}{\text{argmin}} \mathbb{P}_q(\mathbf{P}_q). \quad (3.18)$$

Note that the optimum pilot allocation for the transmit antennas would be obtained using an exhaustive joint search in the space and frequency domains, but this is impractical for any scenario.

### 3.4.2 Dynamic Pilot Allocation for ML Receivers

To simplify the matrix representation for ML receiver, the ML receiver is efficiently implemented subcarrier by subcarrier as described in (2.63). The SER estimates for ML receivers at the  $k$ th subcarrier can be approximated in a looser form as [1, 22, 119]

$$\mathbb{P}(k) \leq N_r(|\mathbb{C}| - 1) \mathcal{Q} \left( \sqrt{\frac{\frac{1}{N_t} d_{min}^2(\mathbf{H}(k))}{2\sigma_v^2}} \right), \quad (3.19)$$

where

$$d_{min}^2(\mathbf{H}(k)) = \underset{\substack{\mathbf{s}(k), \mathbf{s}'(k) \in \mathbb{C}^{N_t} \\ \mathbf{s}(k) \neq \mathbf{s}'(k)}}{\operatorname{argmin}} \frac{\|\mathbf{H}(k)(\mathbf{s}(k) - \mathbf{s}'(k))\|^2}{N_t}. \quad (3.20)$$

Note that the SER estimates for ML receiver cannot be easily approximated using SINR as linear and SIC receivers. In the following, a special MSE based SER approximation is used. where  $\mathbf{y}(k) = [y_1(k), \dots, y_j(k), \dots, y_{N_r}(k)]^T$  and  $\mathbf{s}(k) = [s_1(k), \dots, s_j(k), \dots, s_{N_r}(k)]^T$  denote the receive and transmit signal vectors corresponding to the  $k$ th subcarrier. The channel matrix for the  $k$ th subcarrier is defined as  $\mathbf{H}(k)$ , which is similar to the channel matrix  $\mathbf{H}$  defined in (2.51). Equation (3.19) has been verified as union bound in [1]. However, the complexity of the SER approximation is too high. An alternative method using a lower bound approximation (LBA) of (3.20) is considered in [119], but it suffers a performance loss. To obtain reliable SER estimates, the method proposed in [120], which reduce the complexity of searching  $d_{min}^2(\mathbf{H}(k))$ . Equation (3.6) cannot be simply substituted into (3.19), so it must be reformulated as

$$\mathbf{h}_q(k) = (\mathbf{I}_{N_t} + \sigma_v^2 \mathbf{\Xi}_q(k))^{-1} \hat{\mathbf{h}}_q(k) - \tilde{\boldsymbol{\omega}}_q(k). \quad (3.21)$$

where  $\mathbf{h}_q(k) = [h_{q1}(k), \dots, h_{qj}(k), \dots, h_{qN_r}(k)]^T$  denotes the  $q$ th column of  $\mathbf{H}(k)$ ,  $\tilde{\boldsymbol{\omega}}_q(k) = [\Omega_{q1}(k), \dots, \Omega_{qj}(k), \dots, \Omega_{qN_r}(k)]^T$  and  $\tilde{\Omega}_{qj}(k)$  denotes the  $k$ th diagonal element of  $\tilde{\boldsymbol{\Omega}}_{qj}$ , and  $\mathbf{\Xi}_q(k) = \operatorname{diag}(\Xi_{q1}(k), \dots, \Xi_{qj}(k), \dots, \Xi_{qN_r}(k))$  and  $\Xi_{qj}(k)$  denotes the  $k$ th diagonal element of  $\mathbf{\Xi}_{qj}$ . Substituting (3.21) into (3.19), we can obtain the SER approximation for the  $q$ th transmit antenna as

$$\mathbb{P}_q(k) \approx \sum_{k=1}^{N_s} N_r(M - 1) \mathcal{Q} \left( \sqrt{\frac{\frac{1}{N_t} d_{min}^2(\mathbf{H}(k))}{2\sigma_v^2}} \right), \quad (3.22)$$

Equation (3.22) is defined as the same as (3.16) for SER estimates. Hence, the optimization problem of ML receiver is identical to that of the linear and SIC receivers in (3.18). Note that the SER estimates of pilot and data subcarriers must be jointly optimized in order to obtain acceptable channel estimates.

### 3.4.3 Proposed MIMO Iterative Pilot Search

The MIPS algorithm proposes to reduce the complexity burden for optimum pilot allocation using an iterative search in the space-frequency domain. It is developed from the iterative pilot search for SISO-OFDM [53]. The main idea behind the iterative pilot search is to search for the optimum position for the  $p$ th pilot while fixing the other  $N_p - 1$  pilots on particular subcarriers. The MIPS follows the same pattern for a given transmit antenna  $q$ , but the pilot placement for other antennas must be considered. Furthermore, the first allocated antennas have more available subcarriers to insert pilots compared to the other antennas, so we perform the ordering with the aid of the SER estimates from the previous OFDM symbol period  $\mathbb{P}_i(n - 1)$ , which corresponds to the pilot allocation matrices  $\mathbf{P}_i^{\text{opt}}(n - 1)$ ,  $i = 1, \dots, N_t$ . Hence, the antenna with the highest SER estimates in the previous OFDM symbol is allocated first. In other words, it has more pilot allocation matrices to choose, so the SER performance has better chance to be improved. For SIC receiver, the ordering is determined by detection ordering as discussed in Subsection 2.6.4, because the performance of first detected antenna is worse than the later detected ones in most cases. The MIPS is performed as below:

Initialization: Set  $p = 1$ ,  $q = 1$ .

1. Allocate  $N_p$  pilots as the pilot pattern ( $\mathbf{P}_q(n - 1)$ ) to the  $q$ th transmit antenna, and keep the pilot positions already allocated to the first  $N_t - q$  antennas ( $\sum_{i=1}^{q-1} \mathbf{P}_i(n)$ ).
2. Calculate the expected error probability using (3.17) or (3.22) if the  $p$ th pilot is inserted in the  $k$ th unoccupied subcarrier while fixing the other  $N_p - 1$  pilots, until all available subcarriers have been tested successively, where  $\mathbf{I}_{N_s} - \sum_{i=1}^{q-1} \mathbf{P}_i(n)$  represents the remaining available subcarrier for the  $i$ th transmit antenna.
3. Select the position giving minimum error probability for the  $p$ th pilot, set  $p = p + 1$  and update  $\mathbf{P}_q(n)$ . Go back to step 2. If  $p = N_p$ , go to step 4.
4. The pilot allocation search for the  $q$ th antenna is complete; set  $q = q + 1$ , go back to step 1. If  $q = N_t$ , go to step 5.
5. Terminate, and return  $\mathbf{P}_q(n)$  and  $\mathbb{P}_q(n)$ .

Note that the covariance matrix of the noise  $\Xi_{i,i \neq q}$  associated with a particular pilot allocation must be used in step 2 for the calculation of the SER estimates. However the pilot allocation matrix  $\mathbf{P}_i, i = q + 1, \dots, N_t$ , are unknown. We assume that  $\Xi_i(n) \approx \Xi_i(n - 1), i = q + 1, \dots, N_t$ , in (3.15) and (3.21). The number of required trials for a conventional exhaustive search are given by

$$\prod_{i=1}^{N_t} \binom{N_s - (i-1)N_p}{N_p}, \quad (3.23)$$

but the MIPS can significantly decrease the number of trials to

$$\sum_{i=1}^{N_t} (N_s - iN_p + 1)N_p. \quad (3.24)$$

For example, a moderate size  $4 \times 4$  MIMO-OFDM system with  $N_s = 32$  and  $N_p = 4$  for each antenna requires approximately  $7 \times 10^5$  search trials for one OFDM symbol, which makes the exhaustive search impractical for the scenarios considered. However, the MIPS can find these optimum pilot patterns with 368 trials, which represents a significant complexity reduction, and no matrix inversion is involved. This is because all matrices are diagonal. In addition, most operations required in the search trials can be pre-computed accordingly to further save the computational efforts. The exact algorithm table is presented in Table 3.1.

### 3.5 Limited Feedback for Dynamic Pilot Allocation

Although the MIPS can reduce the complexity of finding an optimum pilot allocation, the feedback payload is still high, and so is the number of search trials. The total number of overhead bits is  $\sum_{i=0}^{N_t-1} \log_2 \binom{N_s - iN_p}{N_p}$ . For example, In a  $2 \times 2$  MIMO-OFDM system with  $N_s = 16$  and  $N_p = 4$  for each transmit antenna, the receiver relay back at least 18 bits per OFDM symbol. The amount of feedback can be reduced by treating each transmit antenna separately as in [52] (unstacked vector quantization), but this cause significant performance loss and does not reduce the number of feedback bits significantly. We therefore propose a stacked vector quantization (SVQ) technique (which can create a codebook for the pilot allocation of all transmit antenna) using the generalized Lloyd algorithm (GLA) for feedback, as well as reducing the number of search trials. GLA is a non-uniform

Table 3.1: MIPS for the  $q$ th transmit antenna

---

<b>Input:</b> $\mathbf{P}_i(n), i = 1, \dots, q - 1, N_s, N_p$
<b>Output:</b> $\mathbf{P}_q^{\text{opt}}$
1 $\mathbf{P}_q^{\text{opt}} \leftarrow \mathbf{P}_q(n - 1)$
$\mathbf{P}_i \leftarrow \mathbf{P}_i(n), i = 1, \dots, q - 1$
2 $\mathbb{P}_{\text{in}} \leftarrow 10^6$
3 $\text{idx} \leftarrow$ the indices of the diagonal elements of $\mathbf{P}_q(n - 1)$ that contain pilots
4 <b>repeat</b>
5 $\mathbb{P}_{\text{out}} \leftarrow \mathbb{P}_{\text{in}}$
6 <b>for</b> $p = 0$ <b>to</b> $N_p - 1$
7 $\mathbf{P}_q \leftarrow \mathbf{P}_q^{\text{opt}}$
8 $\mathbf{P}_q[\text{idx}[p]] \leftarrow 0$
9 $\mathbb{P}_{\text{in}} \leftarrow 1$
10 <b>for</b> $k \leftarrow 0$ <b>to</b> $N_s - 1$
11 $\mathbf{P}_q = \mathbf{P}_q + \sum_{i=1}^{q-1} \mathbf{P}_i$
12 <b>if</b> $\mathbf{P}_q[k] = 1$
13 $\mathbf{P}_q = \mathbf{P}_q - \sum_{i=1}^{q-1} \mathbf{P}_i$
14 <b>then</b> go back to 10
15 <b>else</b> $\mathbf{P}_q[k] \leftarrow 1$
16 $\mathbf{P}_q = \mathbf{P}_q - \sum_{i=1}^{q-1} \mathbf{P}_i$
17 $\mathbb{P}_{\text{out}} = \mathbb{P}_q$ given on $\mathbf{P}_q$ in (3.17) or (3.22)
18 <b>end</b>
19 <b>if</b> $\mathbb{P}_{\text{out}} < \mathbb{P}_{\text{in}}$ <b>then</b>
20 $\mathbb{P}_{\text{in}} \leftarrow \mathbb{P}_{\text{out}}$
21 $\mathbf{P}_q^{\text{opt}} \leftarrow \mathbf{P}_q$
22 $\text{idx}[p] \leftarrow k$
23 <b>end</b>
24 $\mathbf{P}_q[k] \leftarrow 0$
25 <b>end</b>
26 <b>end</b>
27 <b>until</b> $\mathbb{P}_{\text{in}} < \mathbb{P}_{\text{out}}$

---

quantization method that attain the optimum quantization after several iterations based on a pre-defined cost function [121, 122]. As stated earlier, the pilot allocation for all transmit antennas is correlated over time and frequency, so it is possible to compress the set of optimum pilot allocation into a codebook with a smaller size and fewer feedback bits than the unstacked vector quantization. Hence, DPA with SVQ can achieve a better performance and fewer feedback bits than the DPA with unstacked vector quantization [52]. Furthermore, the proposed SVQ can also be efficiently implemented using multi-stage vector quantization schemes and correlation between OFDM symbols can be exploited using predictive vector quantization schemes [123]. Furthermore, the SVQ jointly quantizes the optimum pilot allocation set. Thus the approximation  $\tilde{\Omega}_{i,i \neq q}(n) \approx \tilde{\Omega}_{i,i \neq q}(n-1)$  can be replaced by the actual  $\tilde{\Omega}_{i,i \neq q}(n)$  in the derivation of DPA, because the possible pilot patterns of all transmit antennas are already known. The procedures for generating a codebook for the transmit antennas can be summarised as follows.

1. Obtain the optimum pilot allocation set  $\mathcal{B} = \{\mathbf{x}^{opt}(1), \mathbf{x}^{opt}(2), \dots, \mathbf{x}^{opt}(n)\}$  for all transmit antennas from  $N$  different channel realizations, where  $\mathbf{x}^{opt}(n) = [\mathcal{D}(\mathbf{P}_1(n))^T, \mathcal{D}(\mathbf{P}_2(n))^T, \dots, \mathcal{D}(\mathbf{P}_{N_t}(n))^T]^T$ , and  $\mathcal{D}()$  is the column vector created from the diagonal elements of the matrix.
2. Randomly choose the initial codebook  $\mathcal{B}_0$  from the set  $\mathcal{B}$ , the size  $N_0$  of which is determined by the number of feedback bits.
3. The matrices of  $\mathcal{B}$  can be partitioned into different  $N_0$  different Voronoi regions according to the minimum distance criterion.
4. Create a new codebook by choosing the center of mass of the Voronoi region.
5. Repeat steps (3) and (4) as necessary
6. Due to the binary structure of the matrices, the matrices in  $\mathcal{B}_q$  may not be integer after the  $q$ th iteration. In this case, the  $N_p$  largest values will be set to one as pilot positions, while zeros are used for the rest of the diagonal entries.

Note that each pilot pattern in the codebook for the  $i$ th transmit antenna is unique, so the pilot positions cannot be occupied by those of other antennas. The proposed SVQ jointly quantizes the optimum pilot allocation for all transmit antennas, which exploits the

feedback bits better than the quantization based on separate transmit antennas, namely unstacked vector quantization (USVQ). Furthermore, the generation of codebooks by USVQ is not so straightforward. These pilot allocation of one transmit antenna cannot be reused for the other transmit antennas. In this case, the optimum pilot pattern set  $\mathcal{B}$  is required to exclude these pilot patterns occupying these tones, which makes it more complicated. The algorithm is provided in Table 3.2.

Table 3.2: SVQ for optimum pilot allocation

---

<b>Input:</b> $\mathcal{B}, Q$
<b>Output:</b> $\mathcal{B}_Q$
1 Choose initial codebook $\mathcal{B}_0$ from $\mathcal{B}$
2 <b>for</b> $q = 1:Q$
3 $\mathcal{B}_q = \mathcal{B}_{q-1}$
4 <b>for</b> $n = 1:N$
5 $n'_{\min} = \operatorname{argmin}_{\bar{\mathbf{x}}^{opt}(n') \in \mathcal{B}_q} \ \mathbf{x}^{opt}(n) - \bar{\mathbf{x}}^{opt}(n')\ _F^2$
6 $\mathcal{V}_{n'_{\min}} = \mathbf{x}^{opt}(n'_{\min}) + \mathcal{V}_{n'_{\min}}$ (the $n'_{\min}$ th column of $\mathcal{V}$ )
7 <b>end</b>
8 $\bar{\mathbf{x}}^{opt}(n') = \frac{1}{ \mathcal{V}_{n'} } \mathcal{V}_{n'}$
( $ \mathcal{V}_{n'} $ is the counter for $n'$ th column of $\mathcal{V}$ in step 6)
9     Put $\bar{\mathbf{x}}^{opt}[n']$ in corresponding column of $\mathcal{B}_q$
10 <b>end</b>
11 Map the $\mathcal{B}_Q$ to a binary structure antenna by antenna, and exclude the previous antenna's pilot tones.
12 Set the $N_p$ largest values to 1, and the rest to 0.

---

### 3.6 Simulation Results

In this section, the DPA and UPA with different receivers (linear, SIC, ML) based on MIMO-OFDM systems are compared via Monte Carlo simulations. A diversity gain can be observed from these simulation results. Note that the performance difference between ZF and MMSE receivers may be negligible. In this case, we use MMSE receivers as linear and MMSE-SIC receivers as SIC. We assume a scenario with the following settings: the carrier frequency  $f_c = 650\text{MHz}$ , the subcarrier spacing  $\Delta f = 976.5\text{Hz}$  and the

OFDM symbol duration  $T = 1/\Delta f \approx 1\text{ms}$ . The MIMO-OFDM system parameters are  $L = 4, N_s = 16, 32, N_p = 4, N_t = N_r = 2, 4$ . The transmit signals are modulated with BPSK. Extension to other modulations is straightforward, by modify (3.17) and (3.22) as appropriate. We expect the result to be similar for such modulation. The channel estimation and detection performances are measured via MSE and BER. The simulations are carried out over multipath channels with a uniform power delay profile and a normalized Doppler frequency  $f_d T_{OFDM} = 10^{-4}$  unless otherwise specified. In other words, the channel varies slowly between OFDM symbols. The feedback link is assumed to be perfect and instantaneous. With a limited feedback channel, the simulation is performed in a scenario where the receivers relay back the small number of codebook indices, which implies that the feedback link can only send several bits.

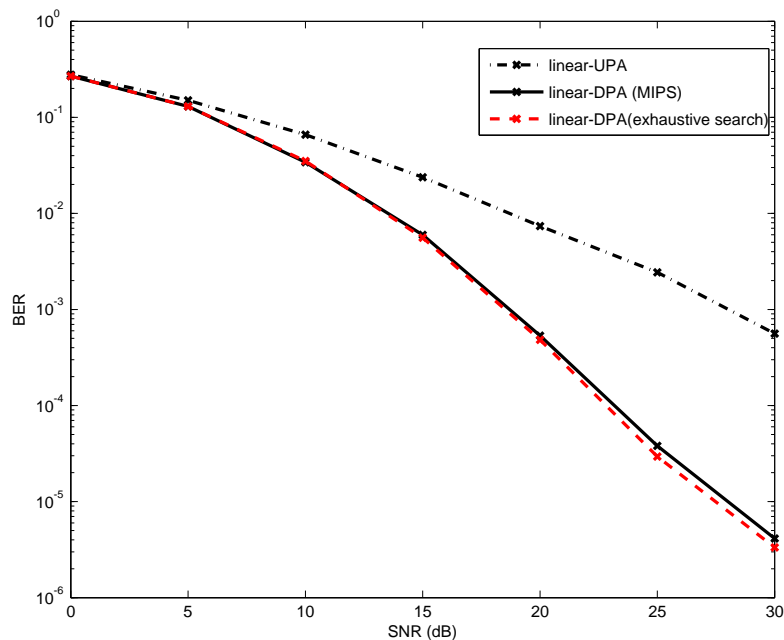
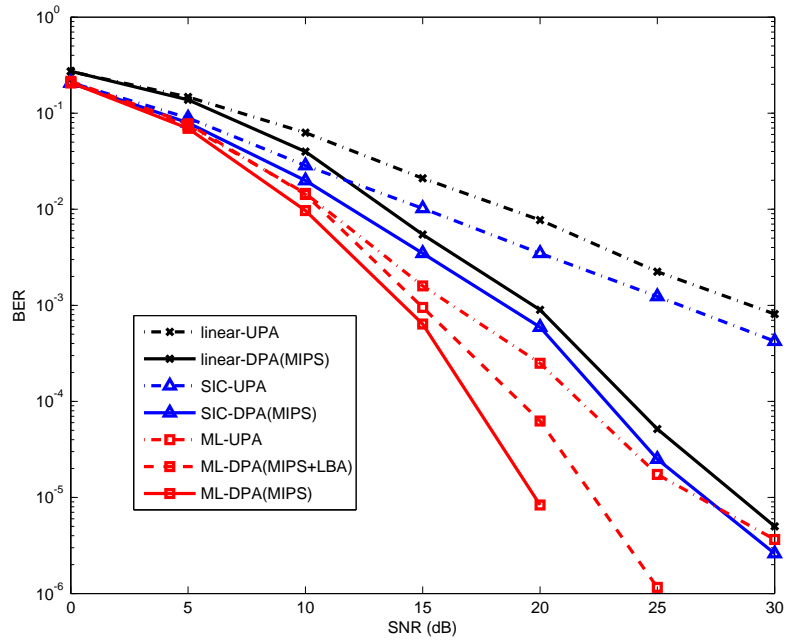


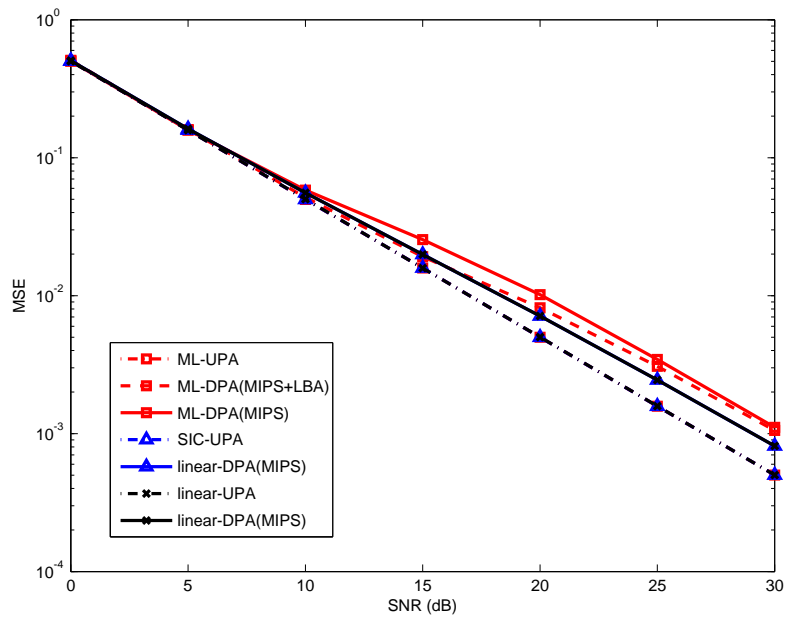
Figure 3.1: Comparison of BER between MIPS and exhaustive search of DPA for  $N_t = N_r = 2, N_s = 16, N_p = 4, L = 4$

In Fig. 3.1, we plot the BER of DPA with MIPS and the exhaustive search as described in [54]. The results show that the MIPS can perform equivalently to the exhaustive search in the BER performance. Hence, in what follows we do not employ DPA with the exhaustive search due to its prohibitive complexity, and focus on the MIPS algorithm.

Fig. 3.2 depicts the BER and MSE performances of different receivers with DPA or



(a) BER



(b) MSE

Figure 3.2: Comparison of BER and MSE between DPA and UPA for  $N_t = N_r = 2$ ,  $N_s = 16$ ,  $N_p = 4$ ,  $L = 4$

UPA in a MIMO-OFDM system with  $N_t = N_r = 2$ ,  $N_s = 16$ ,  $N_p = 4$  with BPSK. DPA with MIPS significantly outperforms the UPA in terms of BER around 10 dB at  $10^{-3}$ , but gives poorer MSE performance. In other words, the system can achieve better BER performance at the expense of MSE degradation.

The BER and MSE performances of DPA and UPA for ML receivers are also presented. From Fig. 3.2a, the DPA with lower bound approximation (LBA) of the SER estimates [119] performs worse than the DPA with the union bound in (3.19) even at low SNR values. 5 dB BER performance gain can be obtained by DPA at high SNR. We then plot the DPA in a moderate size system with  $N_t = N_r = 4$ ,  $N_s = 32$ ,  $N_p = 4$  modulated with BPSK in Fig. 3.3. The performance gains are still maintained for different receivers.

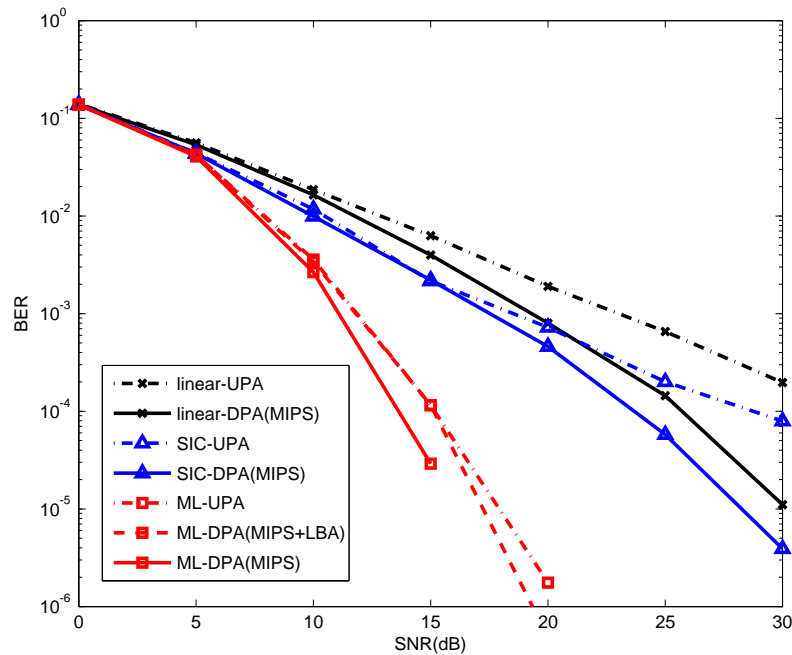


Figure 3.3: Comparison of BER between DPA and UPA for  $N_t = N_r = 4$ ,  $N_s = 32$ ,  $N_p = 4$ ,  $L = 4$

In Fig. 3.4, the curves of BER performance against the number of feedback bits at SNR= 15 dB are plotted to further illustrate the tradeoff between the number of feedback bits and the BER performance. Note that the complexity of DPA at the receiver is also reduced using a small number of feedback bits, which determines the number of search

trials. According to our observation in Fig. 3.4, an excellent tradeoff between complexity and performance gain can be achieved using 5 bits codebook. Hence, the feedback overhead is significantly reduced from 25 bits to several bits. The number of search trials is also reduced to a fixed number equal to  $2^5$ .

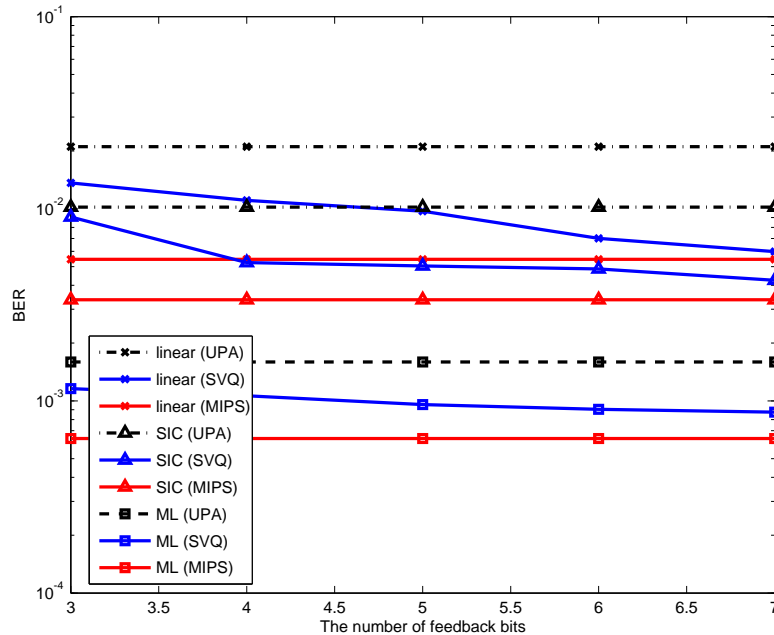


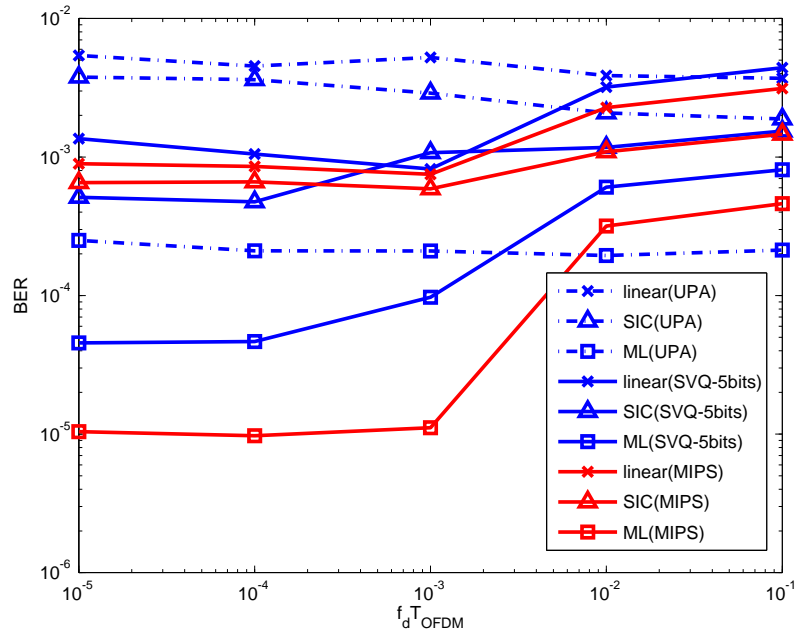
Figure 3.4: Comparison of BER between different feedback bits with SVQ for  $N_t = N_r = 2$ ,  $N_s = 16$ ,  $N_p = 4$ ,  $L = 4$  at 15 dB (The pilot positions for MIPS are perfectly known to the transmitter)

The delay of the feedback link is assumed to be 20 ms (equivalent to 20 OFDM symbols), which is twice the length of the normal WiMAX feedback delay [116]. Because of the delay in the feedback channel, the pilot allocation indices is not sent to the transmitter instantaneously, neither optimal. Here Fig. 3.5a details the BER performance of DPA over a range of  $f_d T_{\text{OFDM}}$  with a fixed delay at SNR= 20 dB. The performance of DPA is better than the UPA except for ML with SVQ-5 bits in a relatively slow varying channel with  $f_d T_{\text{OFDM}}$  values between  $f_d T_{\text{OFDM}} = 10^{-5}$  and  $f_d T_{\text{OFDM}} = 3 - 4 \times 10^{-3}$ . These are equivalent to a maximum relative velocity between the transmitter and receiver of around 3 – 4 mph, which is sufficient for the pedestrians in most scenarios. In other words, the effect of increasing the feedback channel delay is negligible in slowly varying channels. Fig. 3.5b shows that the BER performance of DPA employing SVQ (5 bits)

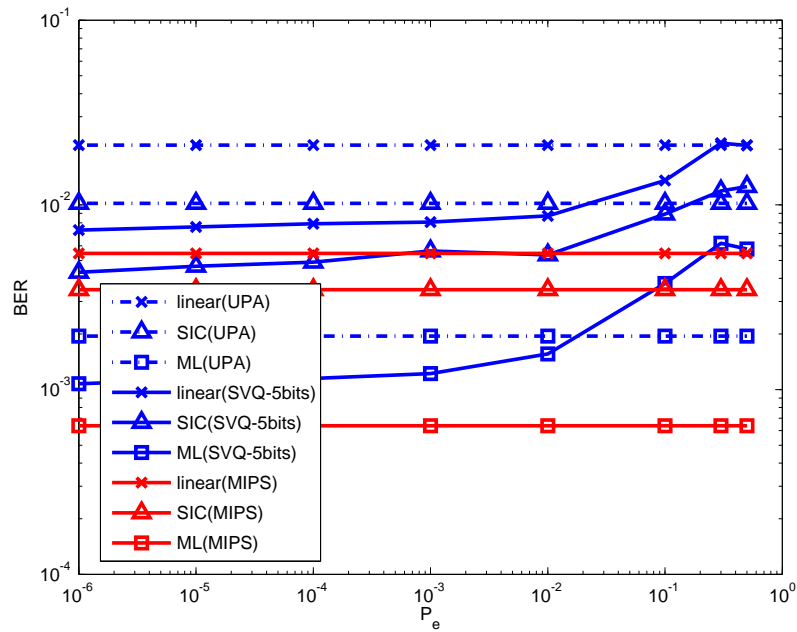
at SNR= 15 dB when the feedback channel operates over a binary symmetric channel (BSC) with different error probabilities  $P_e$ . The feedback indices may be impaired by the errors, which cause the indices mismatch with the channels at the transmitter side. The BER performance degrades with increasing error probability of the feedback link. Additionally, the linear and SIC receivers are more robust to the feedback channel errors at very high  $P_e = 10^{-3}$  than ML receivers similar to ML receivers in Fig. 3.5a. This is because the SER estimates of ML receivers for DPA significantly rely on minimum Euclidean distance estimates in (3.19) that are more sensitive to the channel estimation errors introduced by the pilot allocation. However, DPA still outperforms UPA within an acceptable level of  $P_e$ . From Fig. 3.5, It can be observed that if the channel is varying rapidly, the errors of the feedback channel must be reduced to maintain the reliability of the already delayed indices.

In Fig. 3.6, we present the BER performance of DPA using linear receivers with  $L = 4$ ,  $N_t = N_r = 2$  and  $N_s = 32$ ,  $N_p = 4, 6, 8, 10, 12, 14$  to illustrate the possible best diversity achieved by DPA. As shown above, the slopes of BER curves become steeper with the increasing number of pilots compared to UPA, because data avoid the faded subcarrier with DPA. DPA with perfect channel estimates can achieve a better performance. It may not only suggest that other receivers incorporating DPA can achieve a better performance, but also receivers with more advanced channel estimators will benefit from DPA much more than the channel estimators used above as similarly described in [53]. To further explain the performance improvement of DPA, we can introduce a simple diversity analysis. If the channels of subcarriers are uncorrelated, the upper bound of diversity order for linear receivers can be easily obtained as  $d = L(N_t - N_r + 1)$  [124] without transmit antenna selection, which normally is not achievable for DPA. In our case, the exact diversity analysis becomes intractable due to the correlation. For simplicity of analysis, the following assumptions are made as follows.

1. All pilots are optimally placed;
2. Channel estimates are perfect;
3.  $N_p \gg L$ ;
4. The entire OFDM symbol may be split into available  $N_b = \lceil \frac{N_s - N_t N_p}{N_s} L \rceil$  independent blocks which experience different fading.



(a) Normalized Doppler frequency, SNR= 20 dB



(b) Error probability of feedback channels  $f_d T_{\text{OFDM}} = 10^{-4}$ , SNR= 15 dB

Figure 3.5: Comparison of BER against  $f_d T_{\text{OFDM}}$  with a fixed feedback delay of 20 ms and  $P_e$  between DPA and UPA for  $N_t = N_r = 2$ ,  $N_s = 32$ ,  $N_p = 4$ ,  $L = 4$

Hence, we can assume that all data are transmitted over the available blocks with relatively high SINRs compared to the subcarriers occupied by pilots. According to the assumptions and simulation results above, the diversity of DPA is mainly affected by  $N_p$ , and DPA is prone to select  $N_b$  blocks out of  $L$ . So we can consider DPA as a special case of selection, but in the frequency domain rather than the space domain. Following similar rules in [124, Lemma 2], the achievable diversity equals  $d = (L - \lceil (\frac{N_s - N_t N_p}{N_s}) L \rceil + 1)(N_r - N_t + 1)$ , which approximately agrees with the red curve in Fig. 3.6. The conclusion can also be naturally extended to other receivers such as SIC or ML. In general, DPA exploits a selection diversity compared to UPA, the diversity of which can be further improved with the increase of  $N_p$  and more reliable channel estimates as in [53].

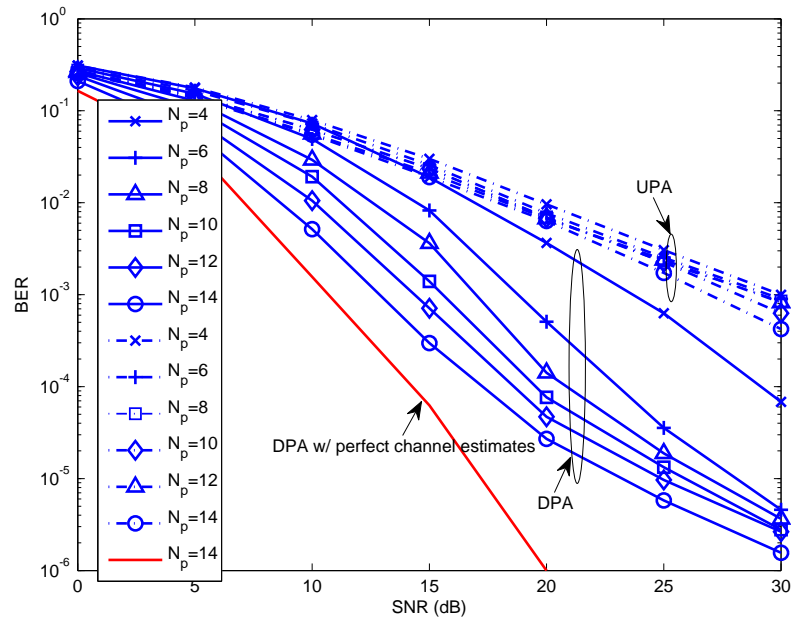


Figure 3.6: Comparison of BER between DPA and UPA with different  $N_p$  for  $N_t = N_r = 2$ ,  $N_s = 32$ ,  $L = 4$  with linear receivers

### 3.7 Summary

A low-complexity dynamic pilot allocation has been derived for MIMO-OFDM systems (linear, SIC, ML), which can improve the SER performance at the expense of MSE degradation. DPA over a limited feedback channel has also been investigated, and a stacked vector quantization (SVQ) scheme has been proposed to reduce the feedback bits and the

number of search trials for more practical scenarios. The gain of SER performance for DPA is promising over the limited feedback channels, and the time variation will not significantly affect the performance of DPA, if the channel is a slow time-varying channel. Finally, the achievable diversity of DPA with different receivers is discussed to further validate our simulation results.

# Chapter 4

## Sphere Decoding Algorithms for MIMO Detection and Bound Estimation

### Contents

---

4.1	Introduction . . . . .	94
4.2	System Model . . . . .	97
4.3	Complex Sphere Decoder with Successive Interference Cancellation based Tree Pruning . . . . .	98
4.4	Bound Estimation for Maximum Likelihood Detection . . . . .	102
4.5	List Soft Processing based Complex Sphere Decoder . . . . .	105
4.6	Simulation Results . . . . .	109
4.7	Summary . . . . .	120

---

### 4.1 Introduction

In this chapter, two different sphere decoding algorithms are proposed for MIMO detection and union bound estimation, respectively. Both algorithms are based on the tree structure to reduce the complexity of searching the minimum Euclidean distance in two different forms: (1) complex-valued system model and (2) real-valued system model. In what follows, a novel complex sphere decoder for MIMO detection will be presented

first, and then the low-complexity union bound estimation. To achieve a high spectral efficiency, maximum likelihood (ML) detection should be employed with high order constellations. However, “brute-force” ML detection is impractical even for a system with a small number of antennas. An alternative method is called the sphere decoder (SD), and this has attracted significant attention recently, due to the considerable complexity reduction it achieves [18, 101]. The key idea behind the SD is to find the lattice point closest to the received signals within a sphere radius. Although the computational complexity has been greatly reduced by Schnorr-Euchner enumeration (SE) [17, 19], sequential Fano decoders [91], and statistical pruning based algorithms [125–127], it is still very high for the systems with a large number of antennas and high order modulation compared to suboptimal methods, such as linear or DFE based techniques [5, 64].

In most applications, the complex-valued system is decoupled and reformulated as an equivalent real-valued system. Real-valued SDs can only process lattice based modulation schemes such as quadrature amplitude modulation (QAM) and pulse amplitude modulation (PAM), while other modulations such as phase shift keying (PSK) cannot be processed as efficiently, because some invalid lattice points are included in the search. Additionally, the depth of the expanded tree for real-valued SDs is twice of that for complex counterparts. Hence, the complex-valued SE-SD and a modified version of SE-SD were proposed in [28, 102]. The complex-valued SDs avoid the decoupling of the complex system and can be widely applied to different modulations without reaching invalid lattice points. Especially, the latter one has already achieved a very low complexity compared to other real-valued and complex-valued SDs [128]. However, the intricacy of complex SE enumeration is still a weak point that makes the real-valued SDs preferred for hardware implementation. Some novel low-complexity complex enumerators have been studied in [129–131], and these enumerators are interchangeable in most complex-valued SDs. However, the enumeration still must be employed in each detection layer, and performed for several times once new branches are accessed. In the rest of this chapter, the SDs we discuss are all based on complex-valued SE enumeration in [28, 102], namely computation of coordinate bound (CCB) enumeration.

Motivated by the description above and probabilistic tree pruning SD (PTP-SD) [126], we devise a novel complex-valued SD (CSD) with statistical pruning strategy (SPS), SIC aided modified probabilistic tree pruning (MPTP). There are three contributions in the

proposed method: (1) The use of MPTP to reduce the number of visited nodes by evaluating the partial path metrics (PPMs) of the next layer. If the PPM corresponding to the next layer's nulling-cancelling point exceeds the constraint of MPTP, the complex SE enumeration can be avoided. (Note that other novel enumeration schemes can also be exploited to replace the CCB [28, 102]). (2) For the SPS, the radius can be updated by the SPS at the bottom layer, if the first updated radius obtained by SIC is greater than the value given by SPS. Compared to the proposed algorithm, the inter-search radius control scheme (ISRC) works in a similar way [127], which further reduces the sphere radius after the search reach the bottom layer. But it must perform several Q-function and inverse Q-function calculations, and the parameters for ISRC are difficult to choose to maintain the tradeoff between complexity and performance. (3) Additional conditions for the CCB are specified to avoid missing candidates in each layer. Simulation results show that the proposed method can achieve a substantial complexity reduction as compared to existing CSD algorithms.

Besides hard decision type detection, soft processing for MIMO systems has been presented. In [28], the authors report a near-capacity MIMO detection using list-SD (LSD) with a relatively large candidate list. With a large list, the performance of the LSD will be very close to the MAP detector. The results in [129] illustrate the hardware implementation of LSD with 4 candidates, which may not be considered as a true implementation of LSD [132]. This is because the list size is too small to achieve near-capacity performance. Hence, it cannot be considered as an optimum detection technique. Additionally, the LLR clipping is also required for the LSD with a small list, because the  $+1$  or  $-1$  is missing in a particular bit LLR calculation based on the max-log MAP criterion. It can be fixed by setting a given magnitude of LLR as in [28], but the performance loss is unavoidable. Although the authors in [105, 106] have fixed this problem for non-iterative detection decoding scheme and non-coherent detection, these LLR clipping techniques are still relatively complicated in most cases. However, a large list will result in irreducible complexity to limit the applications of LSD in practice, because the candidate updates in the list is difficult in hardware implementation [103]. This may not be a desirable feature. If the list generation for LSD is simple, exact LLR clipping will not be required. In the following, we will discuss a simple list generation for the LSD given the proposed CSD.

Secondly, the union bound is usually considered as a useful analytical tool to estimate the union bound of ML detection. Because this bound only depends on the minimum Euclidean distance of receive constellations and the number of nearest neighbours. The union bound tightly approximates the exact probability of symbol error at SNR values [1]. Furthermore, the bound estimation can be applied in many works such as adaptive space-time modulation [119], dynamic pilot allocation for ML detection in the Chapter 3 and optimal minimum distance-based precoding [133]. However, the computational complexity of the union bound is impractical for MIMO systems, because the search is performed like the conventional ML detection. A sphere decoding based minimum Euclidean distance search algorithm has been reported in [120], which employs the symmetric properties to eliminate the symmetric symbol vectors. However, the removal of these symbol vectors has a limited impact on the complexity reduction. Hence, a novel depth-first search (DFS) based sphere decoding algorithm has been proposed to further reduce the search complexity. The initial radius of the search is also derived according to the statistical distribution of the channel matrix, because the initial radius determines the worst search complexity as discussed in [21]. In this context, we compare different sphere decoding algorithms for the search, and show that one can use this bound to estimate performance for ML receivers with a relatively lower complexity than the previous sphere decoding algorithms.

The rest of the chapter is organized as follows. Section 4.2 presents the system model and problem formulation. Section 4.3 describes the proposed complex sphere decoder and the algorithm table. The fundamentals of bound estimation is demonstrated in Section 4.4. The soft processing with LSD is also discussed in Section 4.5. In Section 4.6, the simulation results demonstrate the complexity and BER performance of CSD and LSD, respectively. Furthermore, the simulation results of bound estimation is also presented. A summary is drawn in Section 4.7.

## 4.2 System Model

MIMO systems and the system model after QR decomposition have been presented in Subsection 2.6.1, so the exact system model for CSD will not be detailed in this subsection. The transmit symbol vector  $\mathbf{s}$ , the received symbol vector  $\mathbf{y}$ , the channel matrix

$\mathbf{H}$ , and the noise vector  $\mathbf{v}$  are defined the same as (2.51) in the following. Note that we assume  $N_t \leq N_r$  throughout this chapter, because QR decomposition cannot yield a tree structure with overloaded MIMO systems. To clarify the Euclidean distance for one given layer, the full path metric (FPM) and partial path metric (PPM) are defined as

$$r_{\text{PPM}} = \sum_{i=1}^m \left| y_i - r_{i,i}s_i - \sum_{j=1}^{i-1} r_{i,j}s_j \right|^2 \quad (4.1)$$

Note that the quantity  $r_{\text{PPM}}$  denotes the full path metric when  $m = N_t$ , and it denotes the partial path metric when  $m < N_t$ .

### 4.3 Complex Sphere Decoder with Successive Interference Cancellation based Tree Pruning

In Subsection 2.6.7, the basic idea of CSD and computation of coordinate bound have been reviewed. The proposed CSD is based on the same enumeration scheme. Hence, the system model becomes (2.75). Furthermore, MMSE-SQRD, discussed in (2.73), is used as the processing technique in this chapter [101].

#### 4.3.1 Search Strategy and Successive Interference Cancellation Tree Pruning

In this subsection, we present three different techniques to reduce the complexity: (1) a novel search strategy with the aid of SIC; (2) the MPTP algorithm; (3) SPS.

##### Search Strategy

Compared to conventional SE-CSD, the novel search strategy first performs SIC to obtain the NC points and the full path metric (FPM) without calculating the partial path metrics (PPMs) of other constellation points and sorting for each layer, and the radius  $r_{\text{SD}}$  may be updated by FPM  $r_{\text{PPM}}, m = N_t$  or  $r'_{\text{SD}}$  obtained by SPS in Subsection 4.3.1 once the

search reaches the bottom layer. The rest of the search can be performed upwards starting from the NC point of the bottom layer rather than top layer as in conventional SE-CSD. Additionally, the span of tree can be further shrunk by MPTP. In (2.77), the candidates chosen by CCB can be determined by the new updated radius  $\rho_m$  in Subsection 4.3.1. Hence, the number of possible candidates for each layer can be significantly reduced. The details of the proposed algorithm are specified in Table 4.1.

### Statistical Pruning Strategy

The possible radius for SDs can be calculated as  $r'_{\text{SD}} = \sigma^2 \beta$  according to [21].

$$\begin{aligned} \Pr(x < r'_{\text{SD}}) &= \int_0^{r'_{\text{SD}}/\sigma_v^2} \frac{1}{2^{N_t} (\sigma_v^2/2)^{N_t} \Gamma(N_t)} x^{N_t-1} e^{-x/\sigma_v^2} dx \\ &= \int_0^\beta \frac{u^{N_t-1}}{\Gamma(N_t)} e^{-u} du, (x/\sigma_v^2 = u, \beta = T_s/\sigma_v^2) \\ &= 1 - \epsilon, \end{aligned} \quad (4.2)$$

where  $\epsilon$  is the threshold probability defined according to the empirical results with the size of the system, the modulation and the number of possible ML solutions [21], and the parameter  $\beta$  can be easily obtained by the inverse incomplete Gamma function. Once  $r_{\text{SD}} > r'_{\text{SD}}$ , the quantity  $r_{\text{SD}}$  will be replaced by  $r'_{\text{SD}}$  at the bottom layer.

### Modified Probabilistic Tree Pruning

Denoting the detected symbols as  $\hat{s}_j$ , the noise  $v_i$  can be used to model the branch metric weight as

$$B_i = |y_i - \sum_{j=1}^i r_{i,j} \hat{s}_j|^2 \leq |v_i|^2, i = 1, 2, \dots, N_t, \quad (4.3)$$

We assume the remaining  $N_t - m$  layers' symbols are perfectly detected in (4.3). Then, the branch metric weight is only affected by the noise. Hence, the current PPM  $P_m$  plus the norm of the remaining layers' noise  $\sum_{i=m+1}^{N_t} |v_i|^2$  must be smaller than the sphere radius in most cases. Hence, the possible full metric weight can be represented as

$$P_m + \sum_{i=m+1}^{N_t} |v_i|^2 \leq r_{\text{SD}}, \quad (4.4)$$

where  $P_m = \sum_{i=1}^m B_i$ . Since  $\sum_{i=m+1}^{N_t} |v_i|^2/\sigma_v^2 \sim \chi^2$  with  $2(N_t - m)$  degrees of freedom [21, 126]. After some manipulations, the noise term can be given by

$$\sum_{i=m+1}^{N_t} |v_i|^2/\sigma_v^2 \leq (r_{\text{SD}} - P_m)/\sigma_v^2 \quad (4.5)$$

Accordingly, the probability of  $\Pr(\sum_{i=m+1}^{N_t} |v_i|^2/\sigma_v^2 \leq (r_{\text{SD}} - P_m)/\sigma_v^2)$  is reasonably large. Because the sphere radius  $r_{\text{SD}}$  normally is very large to cover all possible combinations. As discussed above, the summation  $\sum_{i=m+1}^{N_t} |v_i|^2/\sigma_v^2$  follows Chi-square distribution, and the CDF is  $\Pr(\sum_{i=m+1}^{N_t} |v_i|^2/\sigma_v^2 \leq (r_{\text{SD}} - P_m)/\sigma_v^2)$ . Thus,

$$\Xi((r_{\text{SD}} - P_m)/\sigma_v^2; N_t - m) = \epsilon_v < \epsilon_p, \quad (4.6)$$

where  $\epsilon_v = \Pr(\sum_{i=m+1}^{N_t} |v_i|^2/\sigma_v^2 \leq (r_{\text{SD}} - P_m)/\sigma_v^2)$  and  $\Xi(x; a) = \int_0^x \frac{1}{\Gamma(a)} e^{-t} t^{a-1} dt$ .  $\epsilon_p$  denotes the pre-defined probability of occurrence for  $\sum_{i=m+1}^{N_t} |v_i|^2/\sigma_v^2 \leq (r_{\text{SD}} - P_m)/\sigma_v^2$ , which can be determined readily for complexity reduction. According to (4.6), the PPM  $P_m$  becomes

$$P_m \leq r_{\text{SD}} - \sigma_v^2 \Xi^{-1}(\epsilon_p; N_t - m), \quad (4.7)$$

where  $\Xi^{-1}(x; a)$  is the inverse of  $\Xi(x; a)$ . In other words, any PPM  $P_m$  larger than the LHS of (4.7) is unlikely to be the correct path for the ML solution, so these nodes with their child nodes are eliminated from the search tree. To avoid the CCB, we introduce the quantized NC point  $Q(\delta_m)$  obtained by SIC to calculate the minimum PPM for the  $m$ th layer as

$$P_m^\delta = \left| y_m - r_{m,m} Q(\delta_m) - \sum_{j=1}^{m-1} r_{i,j} \hat{s}_j \right|^2 + P_{m-1}, \quad (4.8)$$

and

$$P_m^\delta > \rho_m, \quad (4.9)$$

where  $\rho_m = r_{\text{SD}} - \sigma_v^2 \Xi^{-1}(\epsilon_p; N_t - m)$ , and  $Q(\delta_m)$  is a quantized symbol for the given  $m$ th layer. If the inequality in (4.9) is satisfied, the NC point and the remaining nodes with their child nodes are all pruned, and the CCB is not carried out. Otherwise, the quantity  $\mathfrak{P}_m^\delta$  is used in (2.77) to replace  $r_{\text{SD}}$  to further reduce the number of candidates. Note that the parameter  $\rho_m$  is pre-computed at the start of the transmission without any additional complexity.

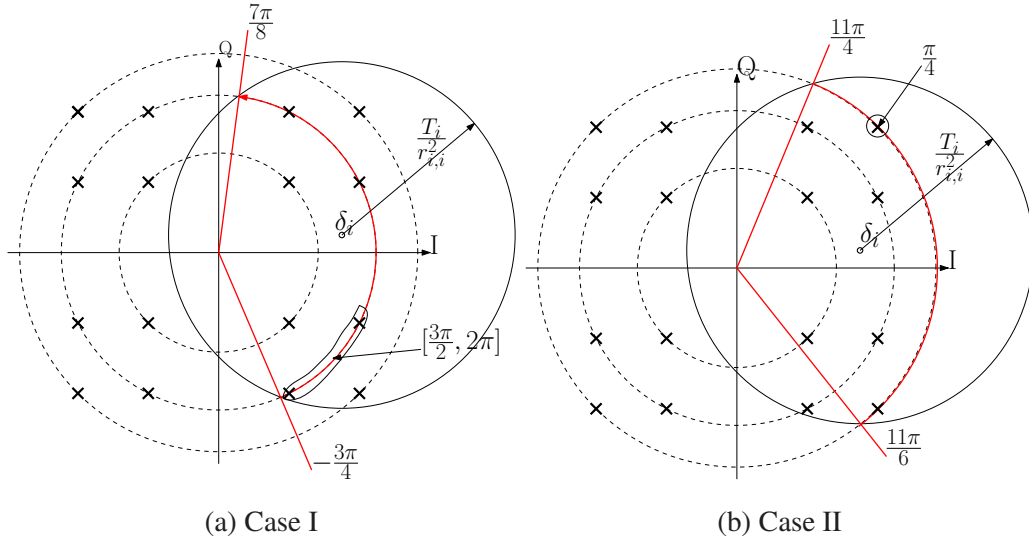


Figure 4.1: Two specific examples to exclude the constellation points erroneously: (a) In Case I, the phases are bounded by  $[\frac{7\pi}{8} - \frac{3\pi}{4}]$ , which is supposed to cover the constellation points between  $[\frac{3\pi}{2} 2\pi]$ . But these constellation points are excluded by the CCB, because they are not inside the bound. (b) Case II has the similar problem: the constellation point  $\frac{\pi}{4}$  is not in the bound  $[\frac{11\pi}{4} \frac{11\pi}{6}]$ .

### 4.3.2 Additional conditions for CCB

There are two additional conditions (AC) we should consider to avoid the performance loss, if we introduce  $T_i = \rho_i$  as the intra radius for CCB.

1. If  $\theta_{\delta_i} - \arccos(\psi) < 0$  and  $\theta_{\delta_i} + \arccos(\psi) > 0$ , set  $-\pi \leq \theta_k < \pi$ . If  $0 \leq \theta_k < 2\pi$ , some constellation points located in  $[\pi, 2\pi]$  will be eliminated erroneously.
2. If  $\theta_{\delta_i} + \arccos(\psi) > 2\pi$ , set  $\theta_{\delta_i} + \arccos(\psi) = \theta_{\delta_i} + \arccos(\psi) - 2\pi$ . If the upper bound of the phase is greater than  $2\pi$ , the constellation points in  $[0, \pi]$  will not be included.

In Fig. 4.1, we present two special cases that can be fixed by the conditions described above. The phase range between  $-\frac{3\pi}{4}$  and  $\frac{7\pi}{8}$  does not match to the above definition  $0 \leq \theta_k < 2\pi$ , so the two points between  $\frac{3\pi}{2}$  and  $2\pi$  will be pruned erroneously in Fig. 4.1a within the red circle. For Fig. 4.1b, the phase of the constellation point is  $\frac{\pi}{4}$ , which should be considered as a candidate based on the phase range. But the upper bound of

phase obtained by CCB is greater than  $2\pi$ , which will eliminate the candidate at  $\frac{\pi}{4}$ . Note that these additional conditions are not specified in previous works such as [28, 102], which employ extremely large initial radius instead. For PSK modulation and QAM, all constellation points are located on one ring, and the candidates can be obtained in one shot. For high order QAM, the CCB must be performed for different concentric rings.

## 4.4 Bound Estimation for Maximum Likelihood Detection

In this section, a novel union bound estimation technique using sphere decoding algorithm is proposed. The instantaneous SER performance of ML detection can be approximated by a looser bound (see [1], [22] and [119]).

### 4.4.1 System model

For the bound estimation of MIMO systems, the system model for the search is almost identical to (3.20) except that the real values are used in the model. Furthermore, the channel matrix  $\mathbf{H}$  will be decomposed into  $\mathbf{Q}$  and  $\mathbf{R}$  for the search as normal sphere decoders.

### 4.4.2 Channel-Statistics Based Initial Radius

As discussed above, the initial radius has a significant effect on the complexity of sphere decoding algorithms [21]. Hence, the initial radius is derived based on the channel statistics. A special matrix namely Wishart matrix is illustrated as follows. The Wishart matrix  $\mathbf{W}$  is a random and non-negative definite matrix with real, non-negative eigenvalues given by

$$\mathbf{W} = \begin{cases} \mathbf{H}^H \mathbf{H} & N_t > N_r \\ \mathbf{H} \mathbf{H}^H & N_t \leq N_r. \end{cases} \quad (4.10)$$

Table 4.1: Proposed complex sphere decoder with SIC based tree pruning

---

**Input:**  $r_{\text{SD}} = \infty$ ,  $\mathbf{R}$ ,  $\mathbf{v}$ ,  $\rho_i, i = 1, 2, \dots, N_t$ .

**Output:**  $\hat{\mathbf{s}}_{\text{ML}}$

- 1: Compute the NC points and obtain the full path metric and partial path metrics  $P_{1, \dots, N_t}^1$ , save  $s_{1, \dots, N_t}$ ,  $\hat{\mathbf{s}}_{\text{ML}} = \hat{\mathbf{s}}$ .
  - 2: **If**  $r'_{\text{SD}} < P_{N_t}$ ,  $P_{N_t} = T_s$ . **end**. Set  $r_{\text{SD}} = P_{N_t}$ . Perform step 6, and set  $k_i = 1, \forall i$ .
  - 3: Set  $i = N_t$ , go to 17.
  - 4: Compute the PPM  $P_i^\delta$  according to (2.76) and (4.8).
  - 5: **If**  $P_i^\delta > \rho_i$ , go to 17.
  - 6: **Else** obtain the sorted candidates  $s_i^{k_i} \in \mathbf{s}_i^{\text{cand}}, k_i = [1, 2, \dots, N_c^i]$  in (2.78) by the complex SE enumeration (CCB) with  $\rho_i$ , where  $N_c^i$  denotes the number of available branches at the  $i$ th layer.  
Set  $k_i = 0$ .
  - 7: **end**
  - 8:  $k_i = k_i + 1$ .
  - 9: **If**  $k_i \leq N_c^i$  or  $i = N_t$ , go to 12.
  - 10: **Else** go to 17.
  - 11: **end**
  - 12: Calculate the PPM for the  $k$ th candidate at the  $i$ th layer,  $P_i^{k_i} = B_i^{k_i} + P_{i-1}$ .
  - 13: **If**  $i = N_t$ ,  $P_{N_t} = P_i^{k_i}$ , go to 20. **end**
  - 14: **Else** go to 16.
  - 15: **end**
  - 16: **If**  $P_i^{k_i} < T_0$ ,  $i = i + 1$ ,  $P_{i-1} = P_i^{k_i-1}$ , save  $s_{i-1}$ , go to 4. **end**
  - 17:  $i = i - 1$ .
  - 18: **If**  $i = 0$ , output  $\hat{\mathbf{s}}_{\text{ML}}$  and terminate.
  - 19: **Else** go to 8.
  - 20: **end**
  - 21: **If**  $P_{N_t} < T_0$ .  $T_0 = P_{N_t}$ ,
  - 22: **If**  $r'_{\text{SD}} < r_{\text{SD}}$ ,  $r_{\text{SD}} = r'_{\text{SD}}$ . **end**
  - 23:  $\hat{\mathbf{s}}_{\text{ML}} = \hat{\mathbf{s}}$ , go to 17.
  - 24: **end**
-

After a simple transformation in (3.20), the minimum Euclidean distance for one channel use can be given by

$$d_{\min}^2(\mathbf{H}) = \underset{\substack{\mathbf{s}, \mathbf{s}' \in \mathbb{C}^{N_t} \\ \mathbf{s} \neq \mathbf{s}'}}{\operatorname{argmin}} \frac{\|\mathbf{H}\mathbf{e}\|^2}{N_t}, \quad (4.11)$$

where  $\mathbf{e} = \mathbf{s} - \mathbf{s}'$ . Additionally,  $\|\mathbf{H}\mathbf{e}\|^2 = \|\mathbf{R}\mathbf{e}\|^2$ . According to [134], the Rayleigh-Ritz theorem can be applied to the Wishart matrix as below

$$\|\mathbf{e}\|^2 \lambda_{\min}(\mathbf{W}) \leq \underset{\substack{\mathbf{s}, \mathbf{s}' \in \mathbb{C}^{N_t} \\ \mathbf{s} \neq \mathbf{s}'}}{\operatorname{argmin}} \|\mathbf{R}\mathbf{e}\|^2 \leq \lambda_{\max}(\mathbf{W}) \|\mathbf{e}\|^2, \quad (4.12)$$

where the symbols  $\lambda_{\max}$  and  $\lambda_{\min}$  denote the maximum and minimum eigenvalue of the Wishart matrix, respectively. For sphere decoding, the minimum eigenvalue of the Wishart matrix is not needed. Because the initial radius is only related to the maximum eigenvalue in this case. Let  $p \approx \lambda_{\max}(\mathbf{W})$ . Hence, the distribution of the initial radius  $p$ , defined similarly to  $r_{\text{SD}}$ , can be roughly approximated by the distribution of the maximum eigenvalue of the real Wishart matrix. Note that the quantity 0.99 used below implies that the initial radius obtained by (4.13) has 99% chance to be greater than the Euclidean distance  $\|\mathbf{H}\mathbf{e}\|^2$ . The CDF of the maximum eigenvalue of the real Wishart matrix can be expressed as [4]

$$\int_0^p \frac{1}{l_m} \sum_{i=1}^{l_m} \varphi_i(\lambda_1)^2 \lambda_1^{l_n - l_m} e^{-\lambda_1} d\lambda_1 = 0.99, \quad (4.13)$$

where  $\lambda_1 = \lambda_{\max}(\mathbf{W})$ ,  $l_m = \min(N_t, N_r)$ ,  $l_n = \max(N_t, N_r)$ . Additionally,

$$\varphi_{k+1}(\lambda_1) = \left( \frac{k!}{(k + l_n - l_m)} \right)^{1/2} L_k^{l_n - l_m}(\lambda_1), \quad k = 0, \dots, l_m - 1, \quad (4.14)$$

where  $L_k^{l_n - l_m}(\lambda_1) = \frac{1}{k!} e^{\lambda_1} \lambda_1^{l_m - l_n} \frac{d^k}{d\lambda_1^k} (e^{-\lambda_1} \lambda_1^{l_n - l_m + k})$  is the associated Laguerre polynomial. The MIMO channels can be decomposed into multiple virtual single-input and single-output (SISO) channel [4]. For a small number of transmit antennas, if one equivalent SISO channel experiences deep fading, the vector  $\mathbf{e} = [0, \dots, e_i, \dots, 0]^T$  may be the candidate to obtain the minimum Euclidean distance for the bound estimation. Hence, the initial radius  $p$  can be obtained by the Chi-square distribution as follows:

$$\int_0^{p\alpha} \frac{1}{\Gamma(N_t)} x^{t-1} e^{-x} dx = 0.99, \quad (4.15)$$

where  $\alpha$  denotes the average power of the candidate constellation. Hence, the rest steps is similar to the SPS in Subsection 4.3.1.

### 4.4.3 Modified Schnorr-Euchner Enumeration

We first define the PPM as normal sphere decoders, which are slightly different from the forms of the sphere decoders. In order to show the PPM, the branch metric weight for one given candidate  $\hat{e}_i$  at layer  $i$  can be evaluated by

$$B_i = |r_{i,i}\hat{e}_i + \sum_{j=1}^{i-1} r_{i,j}\hat{e}_j|^2, \quad (4.16)$$

where the quantity  $\hat{e}_j$  denotes the candidates at upper layers. Based on (4.16), the PPM for one given candidate  $\hat{e}_i$  at layer  $i$  can be given as

$$P_i = B_i + P_{i-1}, \quad (4.17)$$

where  $P_{i-1} = \sum_{m=1}^{i-1} B_m$ . The search strategy used in bound estimation is similar to that used in the complex sphere decoder, see Table 4.2. We therefore do not detail the search strategy further. The only difference is the way of acquiring the candidates at each layer. The bound of  $\hat{e}_i$  for layer  $i$  can be derived by [17, 19]

$$\underbrace{\left\lfloor \frac{-(p - P_{i-1})^{1/2} - \sum_{j=1}^{i-1} r_{i,j}\hat{e}_j}{r_{i,i}} \right\rfloor}_{c_{\min}} \leq \hat{e}_i \leq \underbrace{\left\lceil \frac{(p - P_{i-1})^{1/2} - \sum_{j=1}^{i-1} r_{i,j}\hat{e}_j}{r_{i,i}} \right\rceil}_{c_{\max}}. \quad (4.18)$$

where the notations  $\lfloor \cdot \rfloor$  and  $\lceil \cdot \rceil$  denote the floor and ceiling function, respectively. Note that the symmetric properties of e [120] can be used in the algorithm without any modifications.

## 4.5 List Soft Processing based Complex Sphere Decoder

As we discussed above, the conventional LSD has a variable complexity. In our case, we naturally extend our proposed CSD to the LSD with a simpler list generation. From the original idea of the LSD, a list of symbol candidates with the smallest FPM are required in the LLR calculation as (4.20). Furthermore, it may not be possible to construct a list with fixed complexity in terms of SE-SD, the complexity of which has been already reduced. In our case, the proposed CSD reaches the NC point first, and then starts the search from the bottom layer. Thus the number of visited nodes can be better controlled. The complexity

Table 4.2: Sphere Decoding Algorithm for Minimum Euclidean Distance Search

---

**Input:**  $p, \mathbf{R}, \mathbf{s} - \mathbf{s}' \in \mathbb{D}$ , where the quantity  $\mathbb{D}$  denotes the set of differences between  $\mathbf{s}$  and  $\mathbf{s}'$

**Output:**  $d_{min}^2$

- 1: Set  $i = 1, P_0 = 0$
  - 2: Compute the bounds  $(c_{min}, c_{max})$  of  $\hat{e}_i$  by (4.18) and sort them according to the distance from  $\lambda_i = -\sum_{j=1}^{i-1} r_{i,j}\hat{e}_j/r_{i,i}$ ,  $k \in [1, N_c^i]$ , where the quantity  $N_c^i$  denotes the number of candidates at layer  $i$ . Set  $k = 0$ .
  - 3:  $k = k + 1$ .
  - 4: **if**  $k > N_c^i$  **then**
  - 5:   go to 15.
  - 6: **else**
  - 7:   **if**  $\hat{e}_j = 0, j = 1, \dots, i - 1$  **or**  $i = 1$  **then**  $k = k + 1$ . go to 9.
  - 8:   **end if**
  - 9: Calculate the path metric for  $k$ th candidate node at  $i$ th level,  $P_i = B_i + P_{i-1}$ .
  - 10: **if**  $i = N_t$  **then**
  - 11:   go to 21.
  - 12: **else**
  - 13:   **if**  $P_i < p, i = i + 1$ , **then** go to 2. **end if**
  - 14: **end if**
  - 15:  $i = i - 1$ .
  - 16: **if**  $i = 0$  **then**
  - 17:   Output  $d_{min}^2(\mathbf{H}) = p$  and terminate.
  - 18: **else**
  - 19:   go to 3.
  - 20: **end if**
  - 21: **if**  $P_i < p$  **then**
  - 22:    $p = P_i$ , go to 15.
  - 23: **end if**
-

of list generation by the propose CSD is lower than the conventional LSD. Although its complexity is still not fixed, the number of updates and replacements in the list become more moderate compared to the conventional counterpart.

### 4.5.1 Extrinsic LLR Calculation of LSD

According to the MAP criterion in Subsection 2.6.8, the extrinsic LLR can be evaluated by

$$= \frac{1}{2} \sum_{\mathbf{b} \in \mathcal{B}_{k+}} \left\{ -\frac{1}{\sigma_v^2/2} \|\mathbf{y} - \mathbf{H}\mathbf{s}_{k+}\|^2 + \mathbf{b}_{\bar{k}}^T \cdot \mathbf{L}_{e2}(\mathbf{b}_{\bar{k}}) \right\} - \frac{1}{2} \sum_{\mathbf{b} \in \mathcal{B}_{k-}} \left\{ -\frac{1}{\sigma_v^2/2} \|\mathbf{y} - \mathbf{H}\mathbf{s}_{k-}\|^2 + \mathbf{b}_{\bar{k}}^T \cdot \mathbf{L}_{e2}(\mathbf{b}_{\bar{k}}) \right\}, \quad (4.19)$$

where the vector  $\mathbf{b}_{\bar{k}}$  denotes the bit vector omitting the  $k$ th bit, the a priori LLR  $\mathbf{L}_{e2}(\mathbf{b}_{\bar{k}})$  denotes the LLR from the channel decoder corresponding to the bits in  $\mathbf{b}_{\bar{k}}$ , and the quantity  $\mathcal{B}_{k\pm}$  denotes the list of bit vectors obtained by the LSD having  $\pm 1$  at the  $k$ th bit. The symbol vector  $\mathbf{s}_{k\pm}$  denotes the possible symbol combinations corresponding to the set  $\mathcal{B}_{k\pm}$ , and the corresponding  $k$ th bit of  $\mathbf{s}_{k\pm}$  equals  $\pm 1$ . Following the max-log approximation and the list obtained by the LSD [28] and the derivation in Subsection 2.6.8, equation (4.19) becomes:

$$L_{e1} \approx \frac{1}{2} \max_{\mathbf{b} \in \mathcal{B}_{k+}} \left\{ -\frac{1}{\sigma_v^2/2} \|\mathbf{y} - \mathbf{H}\mathbf{s}_{k+}\|^2 + \mathbf{b}_{\bar{k}}^T \cdot \mathbf{L}_{e2}(\mathbf{b}_{\bar{k}}) \right\} - \frac{1}{2} \max_{\mathbf{b} \in \mathcal{B}_{k-}} \left\{ -\frac{1}{\sigma_v^2/2} \|\mathbf{y} - \mathbf{H}\mathbf{s}_{k-}\|^2 + \mathbf{b}_{\bar{k}}^T \cdot \mathbf{L}_{e2}(\mathbf{b}_{\bar{k}}) \right\}. \quad (4.20)$$

The LLR  $L_{e1}$  for the  $k$ th bit in the transmit symbol vector is obtained for the channel decoder. Therefore, the extrinsic information  $L_{e1}$  from the LSD and  $L_{e2}$  from the channel decoder exchange between two decoding components.

### 4.5.2 Scatter List Generation

To build a list with simple implementation, a few modifications will be made to the proposed CSD: (1) Perform the proposed CSD to obtain the complete branches accessed in the search, and start several new sub-tree searches respectively given on each full branch obtained above until the list is filled. Note that the sub-tree search will be terminated once it reaches the starting point of the neighbouring sub-tree search. (2) Replace the radius

$r_{SD}$  by the largest FPM of the symbol vectors in the list. (3) MPTP will be carried out given the new radius  $r_{SD}$ . (4) The sphere radius  $r_{SD}$  may be updated in (4.2) with the new largest FPM in the list once a candidate with a smaller FPM is found. The search strategy described above splits the entire tree into different sub-trees and searches them independently. The flow chart has been presented in Fig. 4.2. Although the proposed CSD is needed to perform initially in the scatter list generation, its complexity has been significantly reduced, which is measured via the number of updates in the list generation.

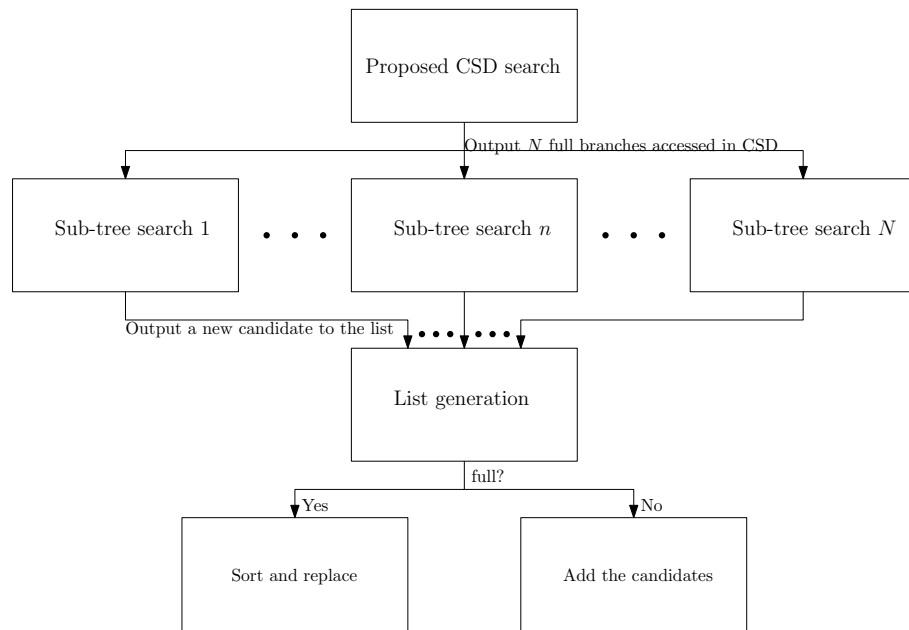


Figure 4.2: The flow chart of scatter list generation

### 4.5.3 ML based Ordering

The ML solution can be exploited to re-order the remaining branches for the list generation of the LSD. When the list is full, the search will go back to the upper layers and proceed down the tree. However, the unvisited nodes at the lower layers are unknown to this search, and these partial branches would be ordered according to SE enumeration. The basic idea of ML based ordering is to sort the remaining partial branches based on the ML solution in the lower layers rather than only computing their real PPM for a given layer. Additionally, a large proportion of the remaining branches may be discarded if the

distance ( $r_{SD}$ ) is much smaller than the distance of  $\mathbf{s}_r$ . In our case, the following equation can be used for ordering at the  $i$ th layer:

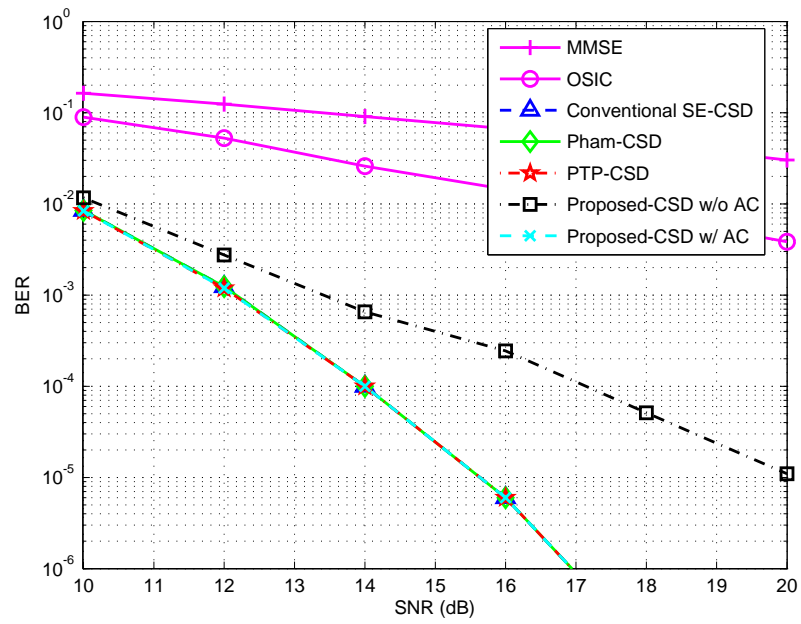
$$\kappa = \underset{\mathbf{s}_r \in \mathcal{R}}{\operatorname{argmin}} \|\mathbf{y} - \mathbf{R}\mathbf{s}_r\|^2, \quad (4.21)$$

where the vector  $\mathbf{s}_r = [s_{ML}^1, \dots, s_{ML}^{i-1}, s_r^i, \dots, s_r^{N_t}]^T$ , and the quantity  $\mathcal{R}$  denotes the set of available branches for the  $i$ th layers. The unvisited nodes in the lower layers are replaced by the ML solution ( $s_{ML}^i$ ). The calculation of ML based ordering is very moderate in (4.21), which only needs  $|\mathcal{R}|(i+1)$  multiplication for each layer.

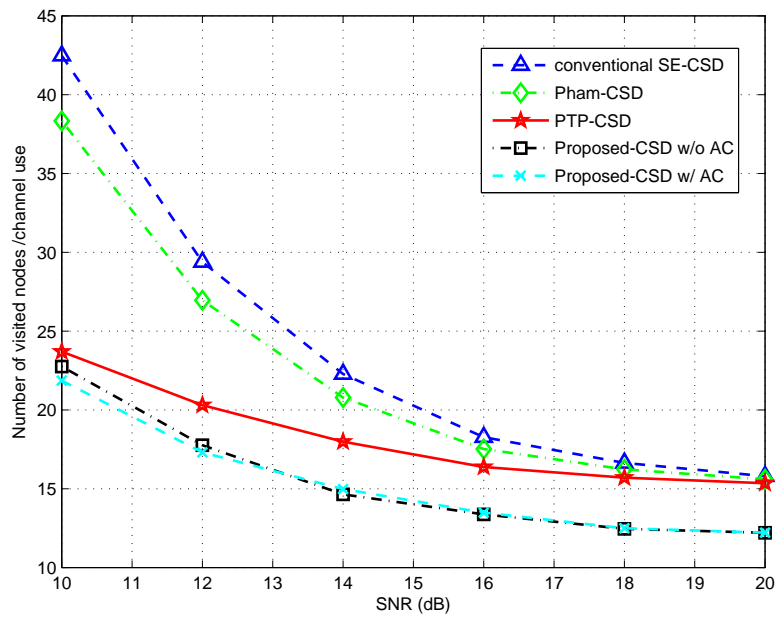
## 4.6 Simulation Results

In this section, we have discussed the proposed CSD in two different forms: (1) the hard output CSD, (2) the soft output CSD (LSD). For the hard output CSD, the performance and complexity of several CSDs are compared via BER and the number of visited nodes in a  $8 \times 8$ -MIMO system with 16QAM and 8PSK. An MPSK modulation in our simulation is defined as  $\gamma e^{(2n+1)\pi/M}$  :  $n = 0, 1, \dots, M-1$ . We consider the conventional SE-CSD, Pham-CSD [102], PTP-CSD [126], the proposed CSD with and without additional conditions for CCB, all of which are complex SE enumeration based CSD with  $r_{SD} = \infty$  at the beginning of the search. The PTP can be simply extended to Pham-CSD. The SNR is defined as  $\text{SNR}(\text{dB}) = 10 \log_{10} \left( \frac{E_s N_r}{\sigma^2} \right)$ . The probabilistic noise constraint is set to  $\epsilon_p = 0.2$ . The threshold  $\epsilon$  for SPS must be appropriately adjusted according to the dimensions and the modulation as stated earlier, and we set  $\epsilon = 0.001$ . The ISRC scheme [127] is not employed, because of the difficulty of choosing parameters for intra radius.

As shown in Figs. 4.4 and 4.3, the complexity of the proposed CSD improves upon the others in terms of visited nodes per channel use by 25% for 16QAM and more than 25% for 8PSK at high SNRs without any BER performance loss, even compared to conventional SE-CSD between the mid and high SNR regime. The performance loss of the proposed algorithm without additional conditions (AC) is significant at high SNRs. In other words, it is more sensitive to the missing candidates in low noise scenarios. However, the complexity reduction is not obvious at low SNR scenarios due to the CCB including

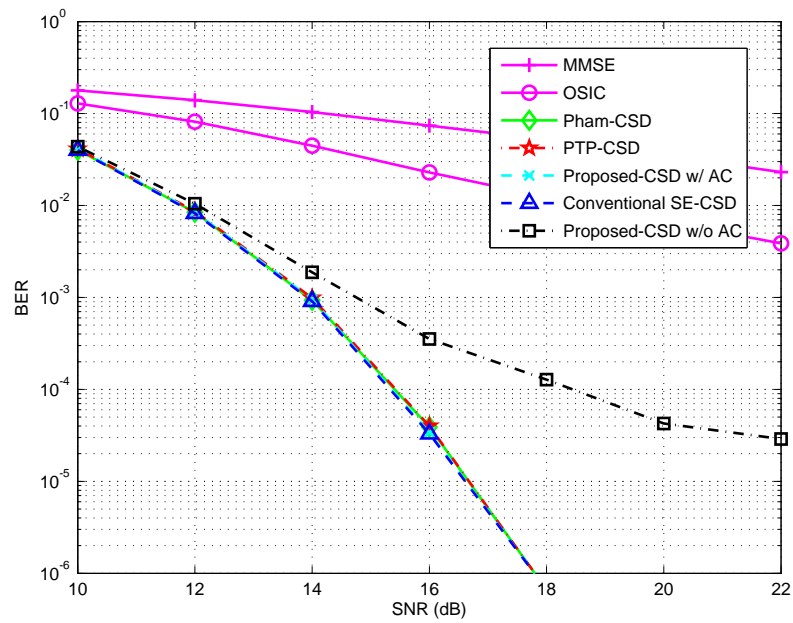


(a) BER

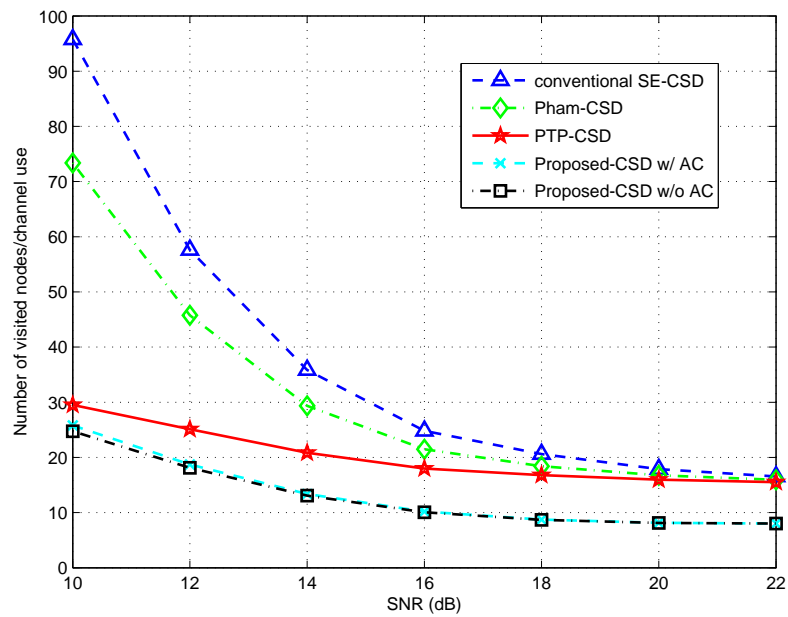


(b) Visited nodes

Figure 4.3: Comparison of BER and the number of visited nodes per channel use with perfect channel estimates between the proposed and other CSDs for  $N_t = N_r = 8$  with 8PSK. Note that the curves of Conventional SE-CSD, Pham-CSD, PTP-CSD and proposed-CSD w/ AC are superimposed in (a).



(a) BER



(b) Visited nodes

Figure 4.4: Comparison of BER and the number of visited nodes per channel use with perfect channel estimates between the proposed and other CSDs for  $N_t = N_r = 8$  with 16QAM. Note that the curves of Conventional SE-CSD, Pham-CSD, PTP-CSD and proposed-CSD w/ AC are superimposed in (a).

more unreliable constellation points. It can be observed that the curves of number of visited nodes for different SDs converge at very high SNR values, so the improvement of the proposed SD is reduced at high SNR, but is still very promising. To show the robustness to the channel estimation errors, the BER performance of CSDs for  $8 \times 8$  MIMO system with 8PSK and LS channel estimation [78] is plotted in Fig. 4.5. We can observe that the BER performance of the proposed CSD with imperfect channel estimates can still achieve the same performance as other existing CSDs. The BER performance of 16QAM is not shown here, because it has similar curves as in Fig. 4.5.

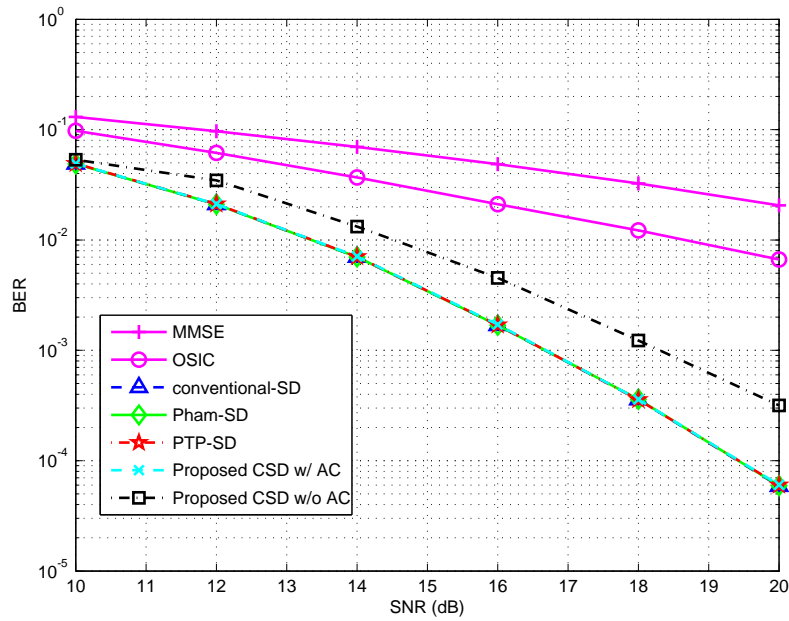


Figure 4.5: Comparison of BER with LS channel estimation between the proposed and other CSDs for for  $N_t = N_r = 8$  with 8PSK. Note that the curves of Conventional SE-CSD, Pham-CSD, PTP-CSD and proposed-CSD w/ AC are superimposed

The worst case complexity is measured by the 99% quantile of the total number of visited nodes per channel use ( $\Pr(\mathcal{C}_w > \mathcal{C}_{\text{any}}) = 0.99$ ) [135], where the quantity  $\mathcal{C}_w$  denotes the number of visited nodes accessed by the SDs in one particular channel use, and the quantity  $\mathcal{C}_{\text{any}}$  denotes the number of visited nodes accessed by the SDs in any channel use. The corresponding worst case complexity  $\mathcal{C}_w$  of CSDs are also plotted in Fig. 4.6, which implies that the number of visited nodes of the proposed CSD is tightly lower bounded by the complexity of SIC at high SNRs.

Additionally, the complexity of SDs increases exponentially with increasing dimen-

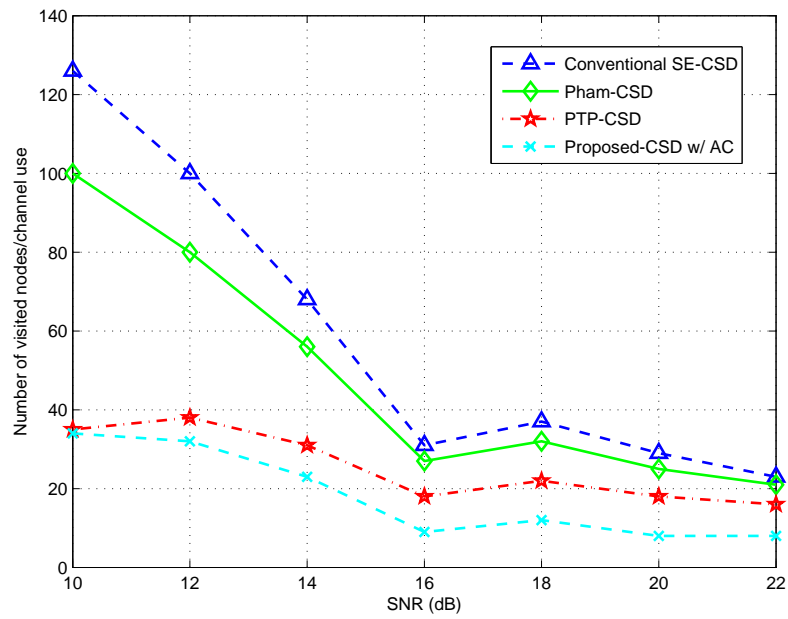


Figure 4.6: Worst case complexity of CSDs against SNR,  $N_t = N_r = 8$  with 16QAM

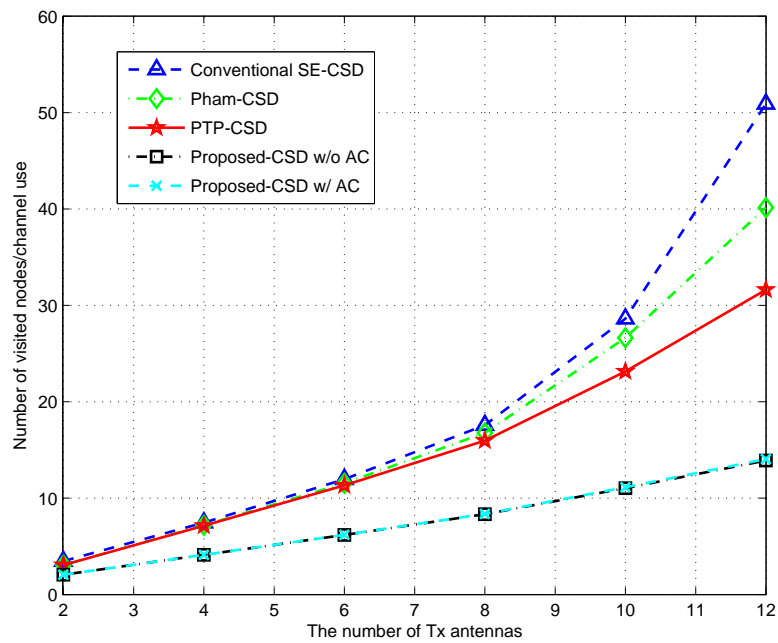
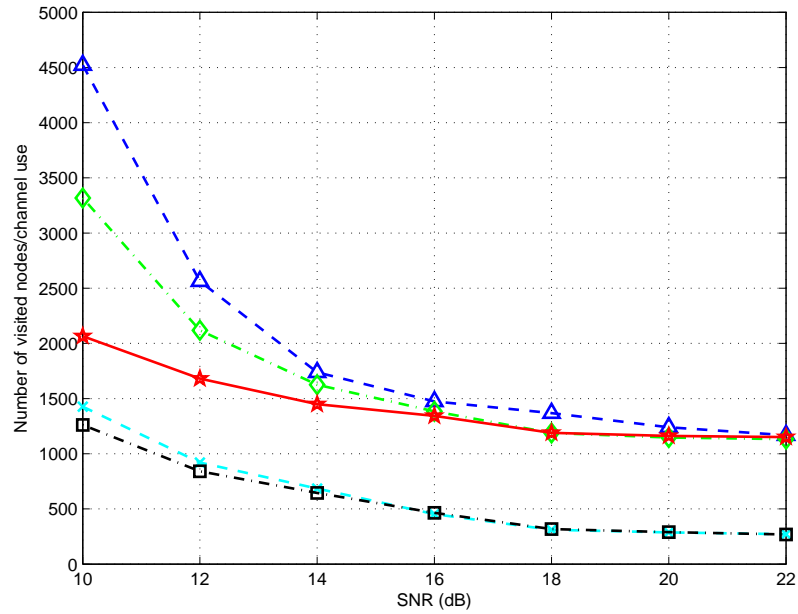


Figure 4.7: The number of visited nodes against increasing dimensions  $N_t = N_r$  with 16QAM at SNR= 20 dB

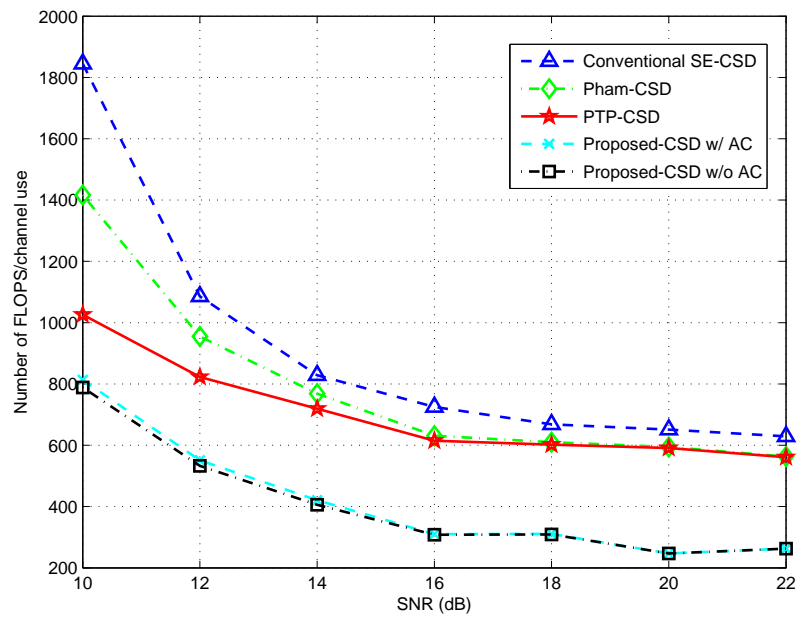
sion. We therefore plot the number of visited nodes against the dimensions ( $N_t = N_r$ ) at a high SNR value (20 dB) to show that the complexity is still reduced by our proposed algorithm in Fig. 4.7.

The complexity discussed so far is only based on the number of visited nodes. In order to show the advantages of complexity reduction of complex SE enumeration (CCB) and eliminating unnecessary candidates, the curves with the number of FLOPS are presented in Fig. 4.8. For the fair comparison, we assume that a complex addition requires 2 FLOPS, and a complex multiplication requires 16 FLOPS. The proposed algorithm still outperforms the other CSDs, because of fewer implementations of complex SE enumeration and the reduced number of candidates. The number of FLOPS of the detection ordering are not considered, because the CSDs are performed with the same preprocessing technique. Furthermore, the parameters for MPTP can be pre-computed before the start of the transmission.

For bound estimation of ML detection, the proposed sphere decoding algorithm for bound estimation, the conventional depth-first search (DFS) sphere decoding algorithm, [120] and the K best-first search (KBFS) sphere decoding algorithm are introduced. The complexity of the proposed and other algorithms are compared via Monte Carlo simulations in terms of floating-point operations (FLOPS). Note that the zeros in matrices or vectors do not count in FLOPS. The union bound and simulation performance of ML detection are measured via SER. The power of the transmit antennas is normalized to unity. The SNR is defined the same as above. Additionally, the root mean square error (RMSE) is defined as  $\text{RMSE} = \sqrt{E[|\hat{d}_{\min}^2 - d_{\min}^2|^2]}$ . The initial radius obtained in (4.13) is applied to the proposed and conventional DFS, and  $p = \infty$  in BFS. From Fig. 4.9a and 4.9b, the proposed sphere decoding algorithm and the method in [120] can precisely find the minimum Euclidean distance  $d_{\min}^2(\mathbf{H})$  (RMSE= 0) compared to other conventional algorithms such as DFS and KBFS, but the later one has higher complexity than the proposed search algorithm. The curves for the union bound and the simulation result approximately agree as shown in Fig. 4.10, so the proposed bound estimation technique is shown to be tight and requires lower complexity, and thus suits the instantaneous SER estimates. Note that the curves of union bound are slightly lower than the simulation results. This is because the scalar used in the (3.19)

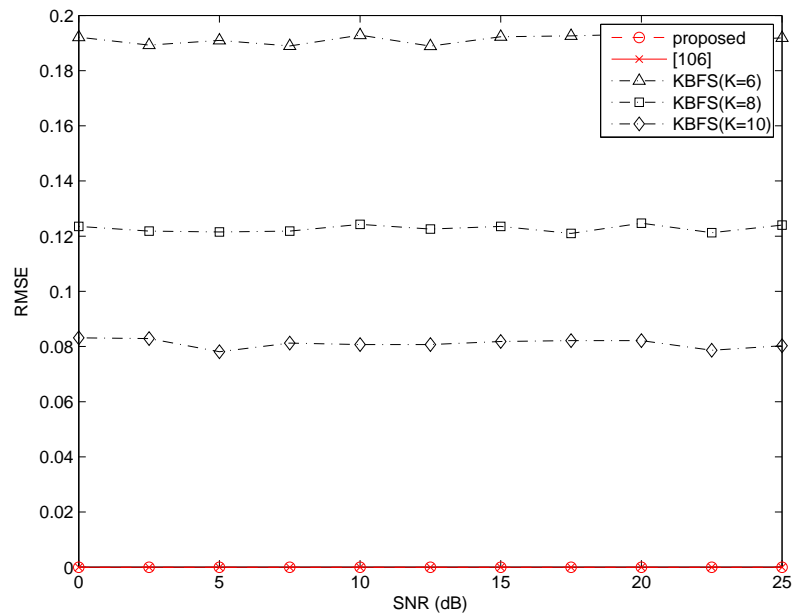


(a) 16QAM

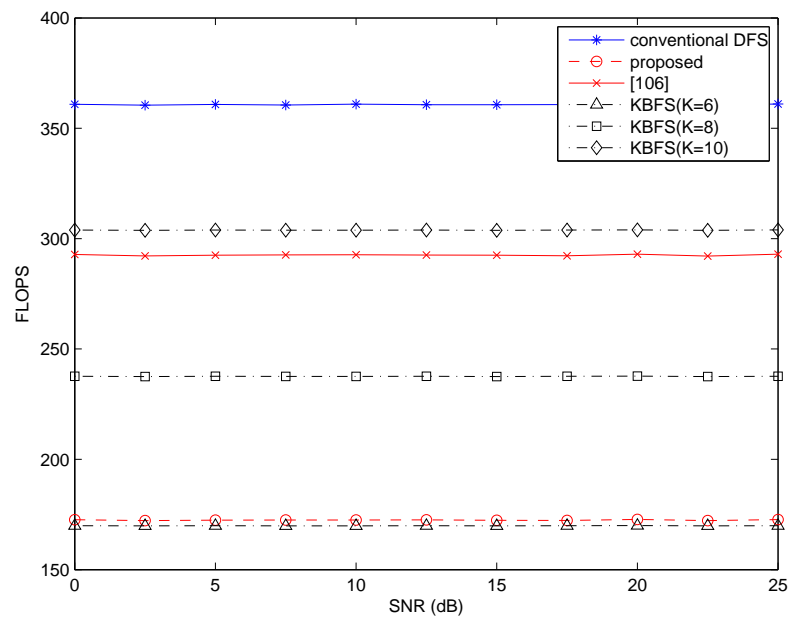


(b) 8PSK

Figure 4.8: Comparison of FLOPS between the proposed and other CSDs for  $N_t = N_r = 8$  with 16QAM and 8PSK



(a) RMSE



(b) FLOPS

Figure 4.9: Comparison of RMSE and FLOPS between the proposed and KBFS for  $N_t = N_r = 8$  with  $L = [-2, 0, 2]$  (4QAM case). The number of FLOPS of the exhaustive search is more than  $10^6$

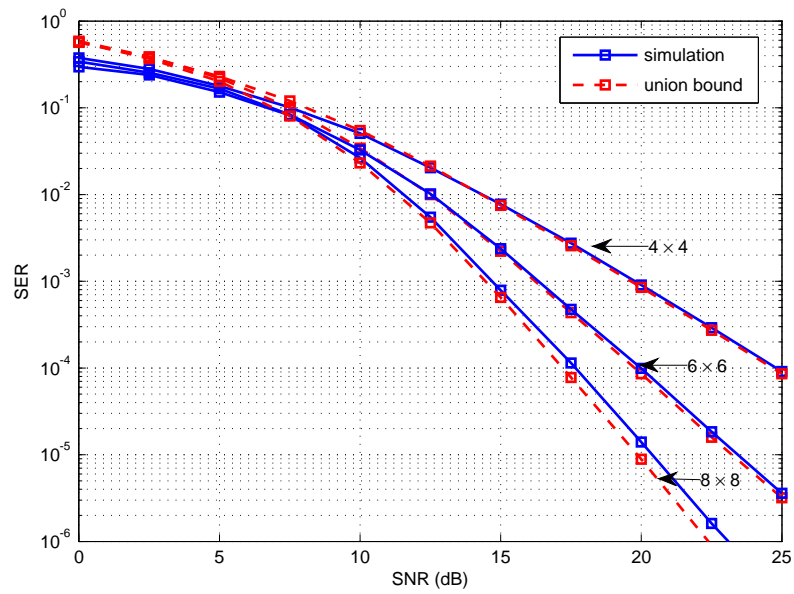


Figure 4.10: Comparison of SER performances of bound estimation (proposed) and simulation results for  $N_t = N_r = [4, 6, 8]$  with  $L = [-2, 0, 2]$  (QPSK case)

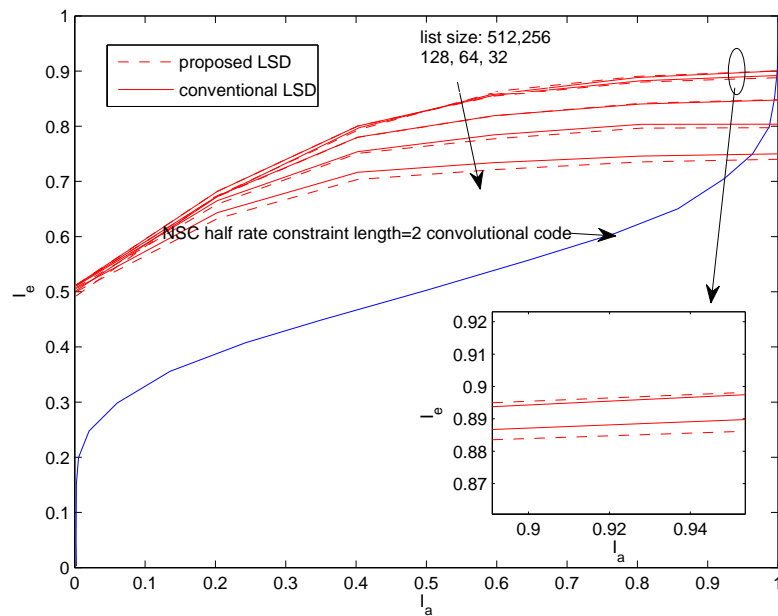


Figure 4.11: EXIT chart of conventional LSD and proposed LSD with different list size at 10 dB,  $N_t = N_r = 8$  with 16QAM

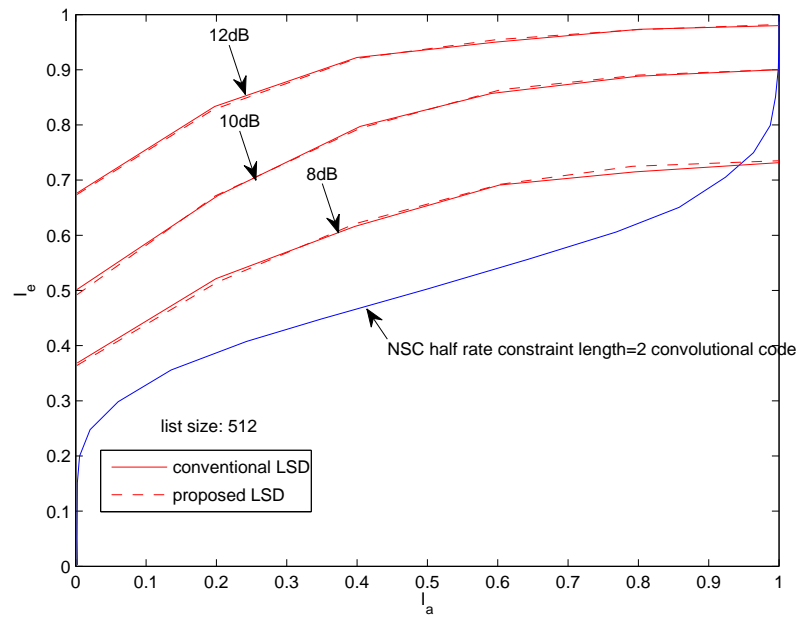


Figure 4.12: EXIT chart of conventional LSD and proposed LSD with  $L = 512$  in different SNR,  $N_t = N_r = 8$  with 16QAM

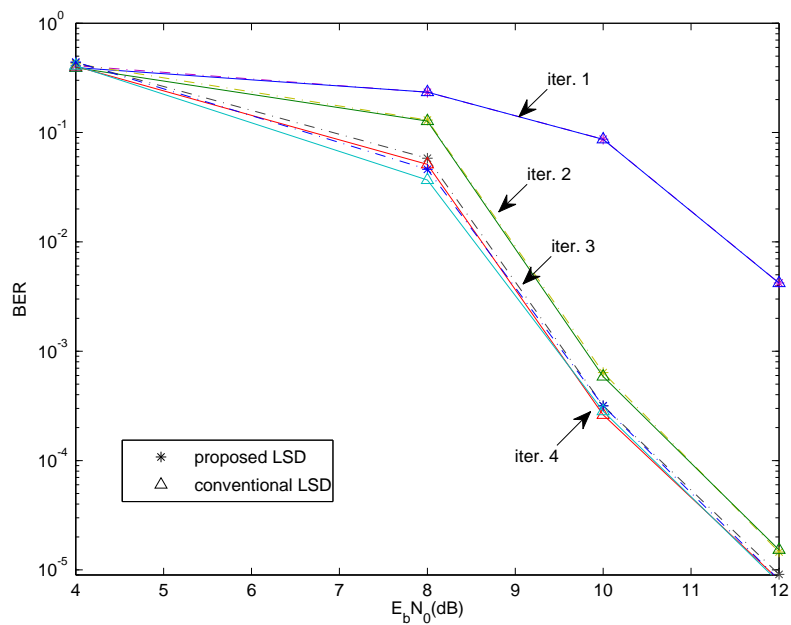


Figure 4.13: BER performance of conventional LSD and proposed LSD with different iterations,  $N_t = N_r = 8$  with 16QAM

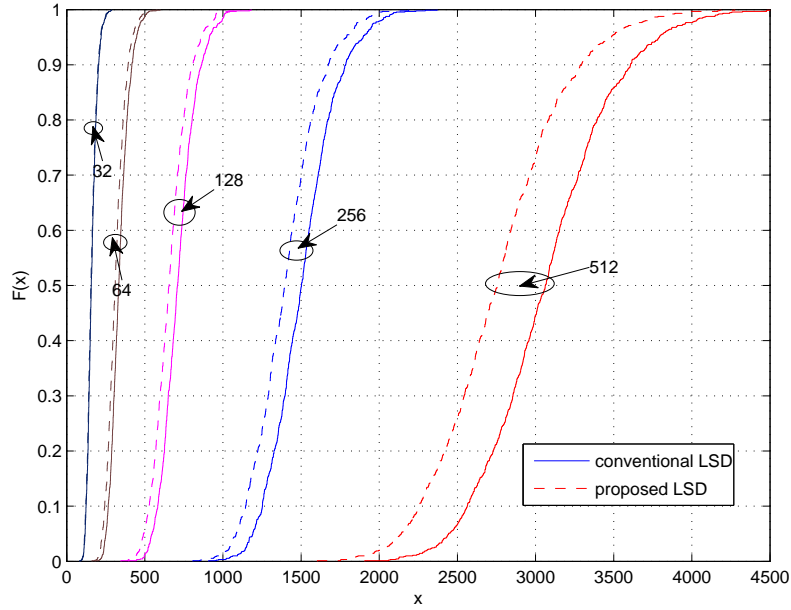


Figure 4.14: CDF of the number of visited nodes employing different list size at 12 dB,  $N_t = N_r = 8$  with 16QAM

For soft output CSD (LSD), we consider  $8 \times 8$ -16 QAM and a NSC half rate convolutional code with constraint length 3 for simplicity. In a coded system, the SNR has been re-defined:  $\frac{E_b}{N_0 \text{ dB}} = \text{SNR}_{\text{dB}} + 10 \log_{10} \frac{N_t}{RN_r M}$ , where  $R$  denotes the rate of the channel code. The performance and complexity of the proposed LSD has been evaluated by BER and the number of updates in the list. The EXIT chart has also been introduced to present the mutual information changes. Note that fixed value clipping has been adopted in our simulation, and the appropriate clipping values can be simply obtained by evaluating the mutual information  $I_e$  as [105]. In our case, the clipping value is set to  $\pm 12$ . In Fig. 4.11, the EXIT chart of conventional LSD [28] and the proposed LSD has been illustrated with different sizes of list. We can observe that both of them perform almost identically with different size of list, and the list size has a significant influence on the LSD performance. Additionally, the EXIT chart of LSD with the same list size in different SNR has also been plotted in Fig. 4.12. The SNR only moves the curves up and down without changing the shapes. Similarly, the BER performance of two LSD with  $L = 512$  agrees with the results in the EXIT chart, which has been presented in Fig. 4.13, and the performance improves with the increasing number of iterations. The complexity comparison made by CDF has been shown in Fig. 4.14, which implies that the number of updates in the list has been significantly reduced by the proposed LSD with large list size. Furthermore, the

search can be terminated early to suit the hardware implementation.

## 4.7 Summary

In this chapter, two novel sphere decoding algorithms for MIMO detection and bound estimation have been presented. The proposed CSD, incorporating the statistical tree pruning technique and SIC, first reaches the bottom layer, and eliminates the candidates for the lower layers before the search reaches them rather than eliminating these candidates at the lower layers. From the simulation results, it is seen that the proposed CSD can significantly save computational efforts compared to the conventional CSD. The search strategy is also applied to the bound estimation, but in a real-valued system model. Accordingly, we have defined how to choose the initial radius, and extended the SE enumeration to the search with the use of symmetric properties of symbol vectors. Furthermore, the proposed CSD has been naturally extended to the list SD (LSD) based on the scatter list generation. The proposed LSD makes better use of the ML solution to re-order the remaining branches. Hence, the list generation becomes simpler than that of the conventional LSD. The complexity of the proposed sphere decoding algorithms for MIMO detection and bound estimation are significantly reduced, which provides an attractive tradeoff between complexity and performance.

# Chapter 5

## Joint Iterative Receiver Design with Multi-Segmental Channel Estimation for OFDM Systems over Rapidly Varying Channels

### Contents

---

5.1	Introduction . . . . .	122
5.2	System model . . . . .	124
5.3	Matched Filter Parallel Interference Cancellation . . . . .	126
5.4	Proposed Multi-feedback Interference Cancellation . . . . .	127
5.5	Multi-Feedback Generation Mechanism . . . . .	130
5.6	SINR Ordering for MBMF-SIC . . . . .	137
5.7	Multi-Segmental Channel Estimation . . . . .	138
5.8	Complexity Requirements of MBMF-SIC and MSCE . . . . .	141
5.9	Simulation Results . . . . .	143
5.10	Summary . . . . .	150

---

## 5.1 Introduction

Due to their high spectral efficiency and simple equalization, OFDM have been widely adopted by many digital communication standards such as LTE, LTE-A, WiMAX. However, their performance suffers severely from inter-carrier interference (ICI) induced by rapid channel variations.

To eliminate the effects induced by ICI, several equalization techniques ranging from linear ones (ZF and MMSE) to non-linear ones (SIC and MAP) have been proposed. A simple frequency domain ZF equalizer using the banded channel structure has been proposed in [136]. A recursive MMSE filter with decision feedback equalization and matched filter bound (MFB) (perfect removal of ICI cancellation) [137] has been investigated, and can be considered as a performance benchmark for ICI cancellation. In [56, 57], the authors further enhanced the banded structure of the channel matrix in the frequency domain by a time-domain window, which maximizes the power inside the band, and designed the equalizers in serial and block form with ICI cancellation. Also, the authors in [58, 59] proposed two pre-equalizers to mitigate the effects of time variations, and obtain a diagonal channel matrix. One developed a partial FFT (PFFT) method to reduce the size of channel matrix for equalization, and the other has formulated the pre-equalizer by minimizing ICI power. In [60], ICI is modelled using derivatives of the channel amplitude, and an iterative decision feedback equalizer (DFE) was proposed to formulate a single tap equalizer in the frequency domain. A similar idea is implemented in [61] to obtain the diagonal matrix using mean values of transmit symbols based on LLR values from the channel decoder. Another method estimates the symbols using a sequential LSQR algorithm with selective parallel interference cancellation (PIC), which is also based on the banded structure of the modified channel matrix in the time or the frequency domain [63]. Some other iterative processing techniques employing a LLR criterion or different cancellation orders are presented in [64, 65]. Besides, a low-complexity sequential MAP detector using the Markov Chain Monte Carlo algorithm for mobile OFDM can be found in [66] with successively reduced search dimension using soft ICI cancellation, which is a variant of ICI cancellation with the aid of MAP detection. However, By introducing the Gibbs sampler, the

complexity of generating samples for MAP detection is almost the same as that of tens of sequential ICI cancellations with a relatively large channel matrix [66]. Due to the difficulty of estimating the rapidly varying channel, some joint receiver designs incorporating channel estimation have been proposed for OFDM systems in [62, 138, 139]. The authors of [62] propose a successive interference cancellation (SIC) scheme based on a group of subcarriers, namely MF-SIC, with iterative single-burst channel estimation (SBCE), but its working scenario is limited to relatively low normalized Doppler frequencies due to the channel estimation error and the residual ICI inside the band. The work presented in [139] is relatively robust to channel variation, but it requires a higher complexity than others. The recent work in [138] suggests an alternative way of estimating time varying channels in multi-segmental form with soft PIC, which can extend the operation of OFDM systems to higher Doppler frequencies. All these techniques discussed above consider only the dominant ICI terms inside the band, the rest of the ICI outside the band is treated as white noise. However, the ICI terms outside the band is not real noise. Hence, the autocorrelation function of the ICI outside the band has been discussed in [140] to design a pre-whitener to compensate ICI outside the band, the autocorrelation matrix of which can also be applied to the likelihood function for more accurate LLR computation. However, it will complicate the LLR computation, which is not a desirable feature for soft ICI cancellation. Furthermore, the error floor in the coded OFDM system is mainly caused by the ICI inside the band rather than the ICI outside the band.

In this chapter, we first discuss the matched filter based PIC with multi-segmental channel estimation (MSCE), and then we employ multi-feedback ICI cancellation matched filter in a sequential form (MBMF-SIC). The original idea is motivated by [95], which proposes multi-feedback cancellation for MIMO systems to approximate the ML solution by selecting one SIC solution out of multiple candidates. Unlike the work in [62, 66, 95], the proposed multi-feedback strategy has been employed to approximate the residual ICI induced by soft cancellation to obtain more reliable LLRs. We propose two generation mechanisms for the multi-feedback strategy: Gibbs sampling based generation (GSG) and tree search based generation (TSG). Note that the generation of feedback candidates by GSG is performed bit by bit independently unlike the recursive implementation described in [141, 142]. Furthermore, it does not require a burn-in period to reach its stationary distribution [66] and the removal of repetitions [143]. For TSG, it build up a tree structure like normal sphere decoders and search the most likely candidates given

the probability of bits, which is based on the conventional Bayesian framework. Hence, the contribution of this chapter can be summarized as: (1) two simple ICI cancellation algorithms (MF-PIC [138] and MBMF-SIC) have been proposed. (2) The MBMF-SIC using the reduced channel matrix for feedback candidates has been discussed, the effectiveness of which has been validated in terms of SINR. (3) The SINR ordering is also discussed to further remove the error floor induced by the ICI inside the band. (4) The proposed channel estimation (MSCE) has been presented, which estimates the time-varying channel several times in each OFDM symbol period. The proposed ICI cancellation algorithms also incorporates MSCE, which shows the robustness of the proposed MBMF-SIC to channel estimation errors, and a better performance than other cancellation techniques. Additionally, the lower bound MSE of MSCE has also been given.

The chapter is organized as follows. Section 5.2 states the system model and receiver structure. Section 5.3 discusses a parallel iterative interference cancellation (MF-PIC). Section 5.4 formulates the problem of MBMF-SIC and explains multi-feedback cancellation and the LLR computation. The multi-feedback generation mechanism is presented in Section 5.5 as well as SINR ordering for MBMF-SIC in Section 5.6. Followed by Section 5.6, the MSCE and the lower bound has been investigated. The simulation results has been illustrated in Section 5.9, and Section 5.10 draws the conclusion.

## 5.2 System model

We consider a coded OFDM system with  $N_s$  subcarriers and iterative processing as illustrated in Fig. 5.1. For a conventional SIC receiver, the number of feedback candidates is reduced to one in the multi-feedback generation block. The information bits are encoded as  $b_m$  by the channel encoder, and then interleaved as  $u_m$  through the random interleaver, where the subscript  $m$  denotes the  $m$ th bit in a bit sequence. Each group of  $c$  bits is modulated by the symbol mapper onto one symbol  $s_k$  on the  $k$ th subcarrier at the  $i$ th OFDM symbol, and then the IFFT is performed to obtain the serial data stream. The CP is inserted. Once the distorted transmitted signals reach the receiver, the CP is removed. The received signals are split into several segments, which go through the PFFT for the channel estimation (MSCE). The summation of the outputs of PFFT blocks is the same

as the conventional FFT. Thus the output is used for equalization (MBMF) as used in normal OFDM systems. The output of MBMF block is the output of equalization, which are the estimated symbols  $\hat{s}_k$ . The bit LLRs corresponding to these symbols can be obtained and deinterleaved for the channel decoder using BCJR algorithm [144]. The output of the channel decoder, after the interleaver, is also used for the interference cancellation. The interference is regenerated by the multi-feedback generation block. For the conventional SIC receiver, the number of feedback candidates is reduced to one in the output of multi-feedback generation block. Referring to (2.15) and (2.101), the system model can be represented as

$$\mathbf{y} = \mathbf{H}_{df}\mathbf{s} + \mathbf{v}. \quad (5.1)$$

In the following, the processing is based on the frequency domain unless otherwise specified.

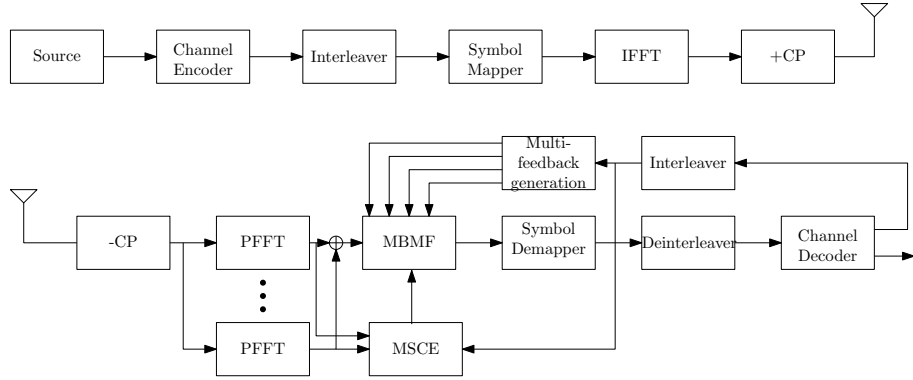


Figure 5.1: System Model of MBMF-SIC incorporating with MSCE

As discussed in Section 2.8, we employ a banded channel matrix  $\mathbf{H}_D$  for OFDM systems over doubly selective channels as shown in Fig. 5.2 and [56], so the truncated system model for  $k$ th subcarrier can be approximated as below:

$$\begin{aligned} \mathbf{y}_k &= \mathbf{H}_k \mathbf{s}_k + \mathbf{v}_k \\ &= \mathbf{h}_k s_k + \sum_{\bar{k}=k-Q, \bar{k} \neq k}^{k+Q} \mathbf{h}_{\bar{k}} s_{\bar{k}} + \sum_{\bar{k} \notin [k-Q, k+Q]} \mathbf{h}_{\bar{k}} s_{\bar{k}} + \mathbf{v}_k \end{aligned} \quad (5.2)$$

where the truncated received signals  $\mathbf{y}_k = [y_{k-D}, \dots, y_k, \dots, y_{k+D}]^T$ ,  $\mathbf{h}_k$  denotes the  $k$ th column vector of the truncated channel matrix, the truncated transmit symbol vector for

the  $k$ th subcarrier  $\mathbf{s}_k = [s_{k-2D}, \dots, s_k, \dots, s_{k+2D}]^T$ , the truncated noise vector  $\mathbf{v}_k = [v_{k-D}, \dots, v_k, \dots, v_{k+D}]$  and the truncated channel matrix with the size  $Q = 2D$

$$\mathbf{H}_k = \begin{bmatrix} h_{df}(k-D, k-2D) & \cdots & h_{df}(k-D, k) & \cdots & \mathbf{0} \\ \mathbf{0} & \ddots & \vdots & \ddots & \vdots \\ \cdots & \mathbf{0} & h_{df}(k+D, k) & \cdots & h_{df}(k+D, k+2D) \end{bmatrix}. \quad (5.3)$$

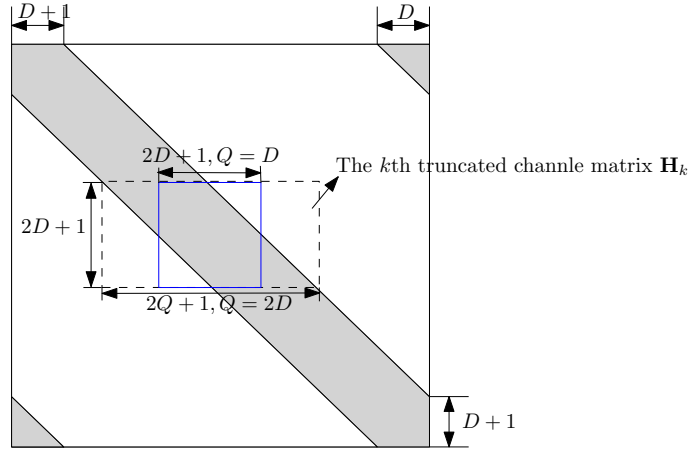


Figure 5.2: The matrix representations of the banded channel matrix  $\mathbf{H}_D$ , the  $k$ th truncated channel matrix  $\mathbf{H}_k$ , and the reduced channel matrix in blue square

### 5.3 Matched Filter Parallel Interference Cancellation

In this section, we present a MF-PIC approach to mitigate the ICI in OFDM systems. The banded structure is employed to reduce the complexity of MF-PIC in the matched filtering stage and the cancellation stage. This is because the elements of  $\mathbf{H}_D$  outside the shaded area are omitted for complexity reduction. The LLR calculation of MF-PIC is also discussed as follows. The ICI terms are mostly contributed from  $2Q$  adjacent subcarriers as illustrated in 5.2 and [56]. Hence, the residual ICI outside the band is considered as noise. Based on (2.101), the match filtered signals are expressed as follows:

$$\begin{aligned} \hat{\mathbf{y}} &= \mathbf{H}_D^H \mathbf{y} \\ &= \mathbf{H}_D^H \mathbf{H}_{df} \mathbf{s} + \mathbf{H}_D \mathbf{v} \\ &= \mathbf{R}_{Df} \mathbf{s} + \tilde{\mathbf{v}}, \end{aligned} \quad (5.4)$$

where the vector  $\hat{\mathbf{y}} = [\hat{y}_0, \dots, \hat{y}_k, \dots, \hat{y}_{N_s-1}]^T$  represents the MF outputs. In Subsection 2.6.8, the LLR computation for MIMO systems has been discussed in details for BPSK. We consider 4QAM here. Hence, the LLR values of  $s_k(i)$ ,  $i = 1, 2$  for the channel decoder and the soft symbol estimates for iterative interference cancellation can be computed as [62]

$$L(s_k(1)) = \ln \frac{\Pr(s_k(1) = +1|\hat{y}_k)}{\Pr(s_k(1) = -1|\hat{y}_k)} = \frac{4\Re(\hat{y}_k)}{\sigma_v^2} \quad (5.5)$$

Accordingly,  $L(s_k(1)) = \frac{4\Im(\hat{y}_k)}{\sigma_v^2}$ . where the quantity  $s_k(i)$  denotes the  $i$ th bit of the symbol  $s_k$  at the  $k$ th subcarrier, and  $i = 1, 2$ . Because 4QAM carries 2 information bits. Subsequently,  $L(s_k(i))$  from (5.5) is deinterleaved, and then fed to the channel decoder as the a priori LLRs. The extrinsic LLRs of  $L(s_k(i))$  can be obtained from the channel decoder, and then the soft symbol estimates  $\hat{s}_k$  is fed back for soft interference cancellation after the interleaver as given in (5.6). The received data vector after cancellation is given by

$$\bar{\mathbf{y}} = \hat{\mathbf{y}} - \tilde{\mathbf{R}}_{Df}\hat{\mathbf{s}}, \quad (5.6)$$

where  $\bar{\mathbf{y}} = [\bar{y}_0, \dots, \bar{y}_k, \dots, \bar{y}_{N_s-1}]^T$ ,  $\hat{\mathbf{s}} = [\hat{s}_0, \dots, \hat{s}_k, \dots, \hat{s}_{N_s-1}]^T$ ,  $\tilde{\mathbf{R}}_{Df}$  is the matrix  $\mathbf{R}_{Df}$  with zero diagonal elements, and the new LLR value  $L(s_k(i))$  can be re-computed in (5.5) to replace  $\hat{y}_k$  by  $\bar{y}_k$ . According to Bayes's theorem [78] and (5.5), the soft symbol estimate of the  $k$ th subcarrier for interference cancellation is given by

$$\hat{s}_k = \tanh(L(s_k(1))/2) + \tanh(L(s_k(2))/2)i, \quad (5.7)$$

where  $\sqrt{-1} = i$ . Therefore, the MF-PIC can cancel the ICI in one shot once the a priori LLR from the channel decoder is known, and then feed the new LLR after the ICI cancellation to the channel decoder.

## 5.4 Proposed Multi-feedback Interference Cancellation

In this section, we discuss the basic idea of multi-feedback interference cancellation, and compare it with the conventional soft interference cancellation and MAP detector via LLR representation. It can be verified that the proposed algorithm can be considered as a hybrid detection method performing MAP estimation in terms of multiple ICI suppression operations for the desired subcarrier.

### 5.4.1 Problem formulation and solution

The received signal in (5.2) after subtracting the soft symbol estimates is given by:

$$\tilde{\mathbf{y}}_k = \mathbf{h}_k s_k + \underbrace{\sum_{\bar{k}=k-Q, \bar{k} \neq k}^{k+Q} \mathbf{h}_{\bar{k}} (s_{\bar{k}} - \hat{s}_{\bar{k}})}_{\text{soft residual interference inside band}} + \underbrace{\sum_{\bar{k} \notin [k-Q, k+Q]} \mathbf{h}_{\bar{k}} s_{\bar{k}} + \mathbf{v}_k}_{\tilde{\mathbf{v}}}, \quad (5.8)$$

where  $\hat{\mathbf{s}}_{\bar{k}} = [s_{k-Q}, \dots, \hat{s}_{k-1}, \hat{s}_{k+1}, \dots, s_{k+Q}]^T$ ,  $\hat{s}_{\bar{k}} \in \hat{\mathbf{s}}_{\bar{k}}$  denotes the soft symbol vector omitting the desired symbol at the  $k$ th subcarrier  $\hat{s}_k$ , which are inside the band obtained by previously detected subcarriers or the LLR from the channel decoder. The vector  $\tilde{\mathbf{v}}$  denotes the interference outside the band plus noise. The residual interference inside the band can be approximated by the summation of received signals  $\tilde{\mathbf{y}}^{(b)}$ ,  $b = 1, 2, \dots, B$ , after subtracting multiple interference symbols  $\mathbf{s}_{\bar{k}}^{(b)}$  as follows:

$$\sum_{\bar{k}=k-Q, \bar{k} \neq k}^{k+Q} \mathbf{h}_{\bar{k}} (s_{\bar{k}} - \hat{s}_{\bar{k}}) \approx \sum_{b=1}^B (\tilde{\mathbf{y}}_k^{(b)} - \mathbf{h}_k s_k - \tilde{\mathbf{v}}) \Pr(\tilde{\mathbf{y}}_k^{(b)}), \quad (5.9)$$

where

$$\tilde{\mathbf{y}}_k^{(b)} = \mathbf{h}_k s_k + \underbrace{\sum_{\bar{k}=k-Q, \bar{k} \neq k}^{k+Q} \mathbf{h}_{\bar{k}} (s_{\bar{k}} - s_{\bar{k}}^{(b)})}_{\text{hard residual interference inside band}} + \tilde{\mathbf{v}}, \quad (5.10)$$

and  $\mathbf{s}_{\bar{k}}^{(b)} = [s_{k-Q}^{(b)}, \dots, s_{k-1}^{(b)}, s_{k+1}^{(b)}, \dots, s_{k+Q}^{(b)}]^T$ ,  $s_{\bar{k}}^{(b)} \in \mathbf{s}_{\bar{k}}^{(b)}$ . The quantity  $B$  denotes the number of feedback candidates. Substituting (5.9) into (5.8), it can be arranged as:

$$\mathbf{y}_k^* \approx \tilde{\mathbf{y}}_k - \sum_{b=1}^B (\tilde{\mathbf{y}}_k^{(b)} - \mathbf{h}_k s_k - \tilde{\mathbf{v}}) \Pr(\tilde{\mathbf{y}}_k^{(b)}) \approx \mathbf{h}_k s_k + \tilde{\mathbf{v}}, \quad (5.11)$$

where  $\mathbf{y}_k^*$  denotes the received signal if the residual interference inside the band is perfectly removed by (5.9), and the probability  $\Pr(\mathbf{y}_k^{(b)})$  denotes the a priori probability of received signals after interference cancellation, which are mainly determined by  $\Pr(\mathbf{s}_{\bar{k}}^{(b)})$ . Hence, the terms  $\Pr(\mathbf{y}_k^{(b)})$  and  $\Pr(\mathbf{s}_{\bar{k}}^{(b)})$  are interchangeable ( $\Pr(\tilde{\mathbf{y}}_k^{(b)}) \approx \Pr(\mathbf{s}_{\bar{k}}^{(b)})$ ). If we assume no residual interference inside the band Equation (5.11) after a rearrangement becomes:

$$\tilde{\mathbf{y}}_k - \sum_{b=1}^B \tilde{\mathbf{y}}_k^{(b)} \Pr(\tilde{\mathbf{y}}_k^{(b)}) = \mathbf{h}_k s_k + \tilde{\mathbf{v}} - \mathbf{h}_k s_k \sum_{b=1}^B \Pr(\tilde{\mathbf{y}}_k^{(b)}) - \tilde{\mathbf{v}} \sum_{b=1}^B \Pr(\tilde{\mathbf{y}}_k^{(b)}), \quad (5.12)$$

where  $\sum_{b=1}^B \Pr(\tilde{\mathbf{y}}_k^{(b)}) = \sum_{b=1}^B \Pr(\mathbf{s}_{\bar{k}}^{(b)}) \approx 1$ , if all possible combinations of symbol vectors  $\mathbf{s}_{\bar{k}}^{(b)}$  are considered in the summation. So  $\tilde{\mathbf{y}}_k - \sum_{b=1}^B \tilde{\mathbf{y}}_k^{(b)} \Pr(\tilde{\mathbf{y}}_k^{(b)}) \approx 0$ . Note that the conditional probability of  $\tilde{\mathbf{y}}_k^{(b)}$  given  $\mathbf{s}_{\bar{k}}^{(b)}$  and  $\tilde{\mathbf{y}}_k$  given  $\hat{\mathbf{s}}_{\bar{k}}$  in (5.12) will be mutually exclusive

and conditionally independent, if the residual interference term dominates. Hence, the likelihood functions of  $\tilde{\mathbf{y}}_k^{(b)}$  and  $\tilde{\mathbf{y}}_k$  given  $s_k$  can be separately evaluated by

$$\Pr(\tilde{\mathbf{y}}_k^{(b)} | s_k) \propto e^{-\frac{(\tilde{\mathbf{y}}_k^{(b)} - \mathbf{h}_k s_k)^H}{\sigma_v^2} (\tilde{\mathbf{y}}_k^{(b)} - \mathbf{h}_k s_k)} \quad (5.13)$$

For simplicity, we assume 4QAM is used as the previous subsection, so  $s_k(i) = \pm 1, i = 1, 2$ . Using (5.13), the LLR can be computed as

$$L(s_k^{(b)}(1)) = \ln \frac{\Pr(s_k(1) = +1 | \tilde{\mathbf{y}}_k^{(b)})}{\Pr(s_k(1) = -1 | \tilde{\mathbf{y}}_k^{(b)})} = \frac{4\Re(\mathbf{h}_k^H \tilde{\mathbf{y}}_k^{(b)})}{\sigma_v^2}, \quad (5.14)$$

and the conditional probability of  $s_k^{(b)}(1)$  given  $\tilde{\mathbf{y}}_k^{(b)}$  can be calculated by

$$\Pr(s_k^{(b)}(1) = +1 | \tilde{\mathbf{y}}_k^{(b)}) = \frac{1}{1 + e^{-L(s_k^{(b)}(1))}} \quad (5.15)$$

Accordingly,  $L(s_k^{(b)}(2)) = \frac{4\Im(\mathbf{h}_k^H \tilde{\mathbf{y}}_k^{(b)})}{\sigma_v^2}$ . From (5.15), multiple conditional probability  $\Pr(s_k^{(b)}(1) = +1 | \tilde{\mathbf{y}}_k^{(b)})$  and  $\Pr(s_k(1) = +1 | \tilde{\mathbf{y}}_k)$  can be obtained. Hence, the average conditional probability  $\Pr(s_k | \mathbf{y}_k^*)$  can be obtained by

$$\begin{aligned} \Pr(s_k(1) = +1 | \mathbf{y}_k^*) &= \sum_{b=1}^B \Pr(s_k^{(b)}(1) = +1 | \tilde{\mathbf{y}}_k^{(b)}) \Pr(\tilde{\mathbf{y}}_k^{(b)}) \\ &+ \Pr(s_k(1) = +1 | \tilde{\mathbf{y}}_k) \Pr(\tilde{\mathbf{y}}_k), \end{aligned} \quad (5.16)$$

As mentioned above,  $\Pr(\tilde{\mathbf{y}}_k^{(b)}) = \Pr(\mathbf{s}_k^{(b)})$ , which can be obtained by the LLR from the channel decoder. Equation (5.16) can be rewritten as

$$\begin{aligned} \Pr(s_k(1) = +1 | \mathbf{y}_k^*) &= \sum_{b=1}^B \Pr(s_k^{(b)}(1) = +1 | \tilde{\mathbf{y}}_k^{(b)}) \Pr(\mathbf{s}_k^{(b)}) \\ &+ \Pr(s_k(1) = +1 | \tilde{\mathbf{y}}_k) \Pr(\hat{\mathbf{s}}_k), \end{aligned} \quad (5.17)$$

The second term in (5.17) can also be evaluated according to (5.13). The LLR of  $s_k(1)$  for the channel decoder, with the use of (5.17), can be easily evaluated by

$$L(s_k(1)) = \ln \frac{\Pr(s_k(1) = +1 | \mathbf{y}_k^*)}{\Pr(s_k(1) = -1 | \mathbf{y}_k^*)}. \quad (5.18)$$

Hence, we have obtained the new LLR output by multi-feedback cancellation algorithm in this section, and further used in the channel decoder.

## 5.4.2 Comparison of soft interference cancellation and MAP detection

To show the differences between proposed MBMF-SIC and MAP and conventional soft ICI cancellation algorithm, the LLR of different methods are shown below. For the MAP detection algorithm, the LLR of the  $i$ th particular bit  $s_k(i)$  can be found as

$$L(s_k(i)) = \ln \frac{\sum_{\mathbf{s}_k \in \mathbb{S}_{i+}} \Pr(\mathbf{s}_k | \mathbf{y}_k)}{\sum_{\mathbf{s}_k \in \mathbb{S}_{i-}} \Pr(\mathbf{s}_k | \mathbf{y}_k)}, \quad (5.19)$$

where  $\mathbb{S}_{i\pm}$  denotes the set of different symbol vector combinations  $\mathbf{s}_k$  with  $s_k(i) = \pm 1$ . For soft interference cancellation based on (5.8), the LLR can be evaluated by

$$L(s_k(i)) = \ln \frac{\sum_{\mathbf{s}_k \in \mathbb{C}_{i+}} \Pr(s_k | \tilde{\mathbf{y}}_k)}{\sum_{\mathbf{s}_k \in \mathbb{C}_{i-}} \Pr(s_k | \tilde{\mathbf{y}}_k)}, \quad (5.20)$$

where  $\mathbb{C}_{i\pm}$  denotes the set of different symbol combinations  $s_k$  with  $s_k(i) = \pm 1$ . Given (5.19) and (5.20), equation (5.16) can be rewritten in the form of a LLR as

$$L(s_k(i)) \approx \ln \frac{\sum_{\mathbf{s}_{\bar{k}} \in \mathbb{S}_{\bar{k}}} \sum_{s_k \in \mathbb{C}_{i+}} \Pr(s_k | \tilde{\mathbf{y}}_k) \Pr(\tilde{\mathbf{y}}_k | \mathbf{s}_{\bar{k}}) \Pr(\mathbf{s}_{\bar{k}})}{\sum_{\mathbf{s}_{\bar{k}} \in \mathbb{S}_{\bar{k}}} \sum_{s_k \in \mathbb{C}_{i-}} \Pr(s_k | \tilde{\mathbf{y}}_k) \Pr(\tilde{\mathbf{y}}_k | \mathbf{s}_{\bar{k}}) \Pr(\mathbf{s}_{\bar{k}})}, \quad (5.21)$$

where  $\mathbb{S}_{\bar{k}}$  denotes the set of symbol vector combinations  $\mathbf{s}_k$  omitting the symbol  $s_k$ , the vector  $\tilde{\mathbf{y}}_k$  denotes the received signals suppressing the interference from  $\mathbf{s}_{\bar{k}}$ , and the vector  $\mathbf{y}_{\bar{k}}$  denotes the received signals cancelling the desired symbol  $s_k$ . Note that the quantity  $B$  actually constrains the set size of  $\mathbb{S}_{\bar{k}}$ . However, the probability  $\Pr(\tilde{\mathbf{y}}_k | \mathbf{s}_{\bar{k}})$  may not be tractable in the implementation, so  $\Pr(\mathbf{s}_{\bar{k}}) \approx \Pr(\tilde{\mathbf{y}}_k | \mathbf{s}_{\bar{k}}) \Pr(\mathbf{s}_{\bar{k}})$  is assumed. Hence, equation (5.21) can be considered as another way of implementing the conventional MAP detection in two steps. The first step performs MAP detection for the interference symbols  $\mathbf{s}_{\bar{k}}$ , and the last step performs interference cancellation for one particular bit  $s_k(i)$ .

## 5.5 Multi-Feedback Generation Mechanism

As mentioned above, the vectors  $\hat{\mathbf{s}}_{\bar{k}}$  in (5.8) and  $\mathbf{s}_{\bar{k}}^{(b)}$  in (5.10) denote the soft symbol vector and the  $b$ th feedback symbol vector, respectively. For soft symbol estimates, it can be obtained by

$$\hat{\mathbf{s}}_{\bar{k}} = \sum_{j=1}^{|\mathbb{C}|} \Pr(s_{\bar{k}} = C_j | \mathbf{y}_k^*) C_j, \quad (5.22)$$

where  $C_j$  denotes the  $j$ th symbol in the symbol alphabet  $\mathbb{C}$ . For the generation of  $s_k^{(b)}$ , there are two different generation methods described below: (1) Gibbs sampler based generation; (2) Tree search based generation. The algorithm procedure for 4QAM are also illustrated in Table 5.1. It can also be extended to other modulation schemes accordingly. However, it is unlikely that OFDM systems will operate with a high order modulation scheme in situations of very high mobility.

### 5.5.1 Gibbs sampling based generation (GSG)

The bit  $s_k^{(b)}(i)$  can be re-generated by the Gibbs sampler [142]:

$$s_k^{(b)}(i) = \begin{cases} +1 & \text{if } U(s_k^{(b)}(i)) \leq P(s_k^{(b)}(i)) \\ -1 & \text{otherwise} \end{cases}, \quad (5.23)$$

where  $P(s_k^{(b)}(i)) = \Pr(s_k(i) = +1 | \mathbf{y}_k^*)$  from the channel decoder, the notation  $U()$  denotes a random number generated based on a uniform distribution between  $[0, 1]$ . Hence, these bits can be re-mapped onto the symbols  $C_j$ . The probability  $\Pr(s_k^{(b)})$  is required for the computation of the average conditional probability in (5.17). However, the symbol vector  $\mathbf{s}_k^{(b)}$  is randomly generated by (5.23). Here, we assume an extreme case that the probability  $P(s_k^{(b)}(i)) = 1, \forall b, i$ , the symbol vectors  $\mathbf{s}_k^{(b)}, \forall b$  will be identical. In other words, the Gibbs sampler with reliable feedback from the channel decoder is prone to generate the similar symbol vectors, which have almost equal probability ( $\Pr(\mathbf{s}_k^{(1)}) \approx \dots \approx \Pr(\mathbf{s}_k^{(b)}) \approx \dots \approx \Pr(\mathbf{s}_k^{(B)}) \approx \Pr(\hat{\mathbf{s}}_k)$ ). The number of feedback candidates  $B$  can approaches  $\infty$  for GSG, so  $\tilde{\mathbf{y}}_k - \sum_{b=1}^B \tilde{\mathbf{y}}_k^{(b)} \Pr(\tilde{\mathbf{y}}_k^{(b)}) \approx 0$ . However, it is undesirable for the implementation to choose a very large  $B$ , so a pre-defined  $B$  would be possible to achieve an attractive tradeoff between complexity and performance.

### 5.5.2 Tree search based generation (TSG)

Compared to the Gibbs sampling based method, the feedback can also be generated given the probability of the symbol. For the case of 4QAM, the conditional probability can be

computed as

$$\begin{aligned}
 \Pr(s_{\bar{k}} = C_1 | \mathbf{y}_k^*) &= p_1 p_2 \\
 \Pr(s_{\bar{k}} = C_2 | \mathbf{y}_k^*) &= p_1 (1 - p_2) \\
 \Pr(s_{\bar{k}} = C_3 | \mathbf{y}_k^*) &= (1 - p_1) p_2 \\
 \Pr(s_{\bar{k}} = C_4 | \mathbf{y}_k^*) &= (1 - p_1) (1 - p_2)
 \end{aligned} \tag{5.24}$$

where  $p_i, i = 1, 2$  denotes the probability  $\Pr(s_{\bar{k}}(i) = +1)$  calculated by  $L(s_{\bar{k}}(i))$  from the channel decoder. Hence, the most likely symbol combinations can be obtained by calculating and sorting  $\Pr(\mathbf{s}_{\bar{k}}^{(b)})$ , the process of which is similar to the tree search problem in [93]. To further simplify the search process, the computation is performed in the logarithm domain. The search process is implemented as follows:

1. Initialization:  $P(C_1^{\bar{k}}) = -\log(p_1 p_2)$ ,  $P(C_2^{\bar{k}}) = -\log(p_1 (1 - p_2))$ ,  $P(C_3^{\bar{k}}) = -\log((1 - p_1) p_2)$ ,  $P(C_4^{\bar{k}}) = -\log((1 - p_1) (1 - p_2))$ ,  $\bar{k} = 1, 2, \dots, 2Q$ ,  $j = 1, 2, \dots, |\mathbb{C}|$ , and  $\Pr(\mathbf{s}_{\bar{k}}^{(b)}) = \sum_{\bar{k}=k-Q, \bar{k} \neq k}^{k+Q} P(C_j^{\bar{k}})$ , where the quantity  $C_j^{\bar{k}}$  denotes the probability of the  $j$ th symbol in the logarithm domain at the  $\bar{k}$ th subcarrier.
2. Solve  $\operatorname{argmin}_{\mathbf{s}_{\bar{k}}^{(b)} \in \mathbb{S}_{\bar{k}}} \Pr(\mathbf{s}_{\bar{k}}^{(b)})$ ,  $b = 1, 2, \dots, B$  using tree search algorithm in [93],
3. Output  $\mathbf{s}_{\bar{k}}^{(b)}$ ,  $b = 1, 2, \dots, B$  and the corresponding weight calculated in step 2.

The symbol vectors  $\mathbf{s}_{\bar{k}}^{(b)}$ ,  $b = 1, 2, \dots, B$  and the corresponding probability  $\Pr(\mathbf{s}_{\bar{k}}^{(b)})$ ,  $b = 1, 2, \dots, B$  can be obtained by the above search. For TSG, the probability  $\Pr(\hat{\mathbf{s}}_{\bar{k}})$  is unknown, so (5.17) cannot be derived. But the probability  $\Pr(\hat{\mathbf{s}}_{\bar{k}})$  can be assumed to be  $\frac{1}{B+1}$  as the assumption made in GSG, which is  $(\Pr(\mathbf{s}_{\bar{k}}^{(1)}) \approx \dots \approx \Pr(\mathbf{s}_{\bar{k}}^{(b)}) \approx \dots \Pr(\mathbf{s}_{\bar{k}}^{(B)}) \approx \Pr(\hat{\mathbf{s}}_{\bar{k}}))$ . Hence,  $\Pr(\mathbf{s}_{\bar{k}}^{(b)}) = \frac{1}{B+1} \Pr(\mathbf{s}_{\bar{k}}^{(b)})$  for TSG in (5.17). Thus, in this section, we have obtained two different multi-feedback generation schemes, which can provide the weighted feedback candidates generated by the a priori probability from the channel decoder.

### 5.5.3 Further discussion on generation mechanisms

From the above, the contribution of the second term in (5.16) will be reduced with the increasing number of feedback candidates for both generation mechanisms, and they will

Table 5.1: Proposed MBMF-SIC for 4QAM

---

**Input:**  $\tilde{\mathbf{y}}_k = \mathbf{y}_k, \mathbf{H}_k, \sigma_n^2, k = 0, 1, \dots, N_s - 1$

**Output:**  $L(s_k(1)), L(s_k(2)), k = 0, 1, \dots, N_s - 1$

- 1: **If** this is the initial iteration, go to step 2. **Else** go to step 9
- 2: **For**  $k = 0, 1, \dots, N_s - 1$
- 3: **For**  $\bar{k} = k - Q, \dots, k - 1, k + 1, \dots, k + Q$  inside the band
 
$$L(s_{\bar{k}}(1)) = \frac{\Re(\mathbf{h}_{\bar{k}}^H \tilde{\mathbf{y}}_{\bar{k}})}{\sigma_v^2}, L(s_{\bar{k}}(2)) = \frac{\Im(\mathbf{h}_{\bar{k}}^H \tilde{\mathbf{y}}_{\bar{k}})}{\sigma_v^2},$$
- End**
- 4: Generate feedback symbols  $\mathbf{s}_{\bar{k}}^b, b = 1, 2, \dots, B$  by GSG or TSG according to LLR obtained in step 3, and soft feedback symbols  $\hat{\mathbf{s}}_{\bar{k}}$  by (5.22).
- 5: Perform interference cancellation as (5.8) and (5.10) using  $\mathbf{s}_{\bar{k}}^b, b = 1, 2, \dots, B$  and  $\hat{\mathbf{s}}_{\bar{k}}$  to obtain  $\tilde{\mathbf{y}}_k^{(b)}$  and  $\tilde{\mathbf{y}}_k$ .
- 6: Calculate  $L(s_k^{(b)}(i))$  and  $L(\hat{s}_k(i))$  according to  $\tilde{\mathbf{y}}_k^{(b)}$  and  $\tilde{\mathbf{y}}_k$  respectively,  $i = 1, 2$ .
- 7: Calculate  $\Pr(s_k(1) = +1 | \mathbf{y}_k^*)$  and  $\Pr(s_k(2) = +1 | \mathbf{y}_k^*)$  as (5.16) and the corresponding LLR for the cancellation in (5.8) and the channel decoder.
- 8: **End**
- 9: **For**  $k = 0, 1, \dots, N_s - 1$
- 10: **For**  $\bar{k} = k - Q, \dots, k - 1, k + 1, \dots, k + Q$  inside the band
 
$$\text{Obtain } L(s_{\bar{k}}(i)), i = 1, 2 \text{ from the channel decoder.}$$
- End**
- 11: Generate feedback symbols  $\mathbf{s}_{\bar{k}}^b, b = 1, 2, \dots, B$  by GSG or TSG according to LLR obtained in step 10, and soft feedback symbols  $\hat{\mathbf{s}}_{\bar{k}}$  by (5.22).
- 12: Perform interference cancellation as (5.8) and (5.10) using  $\mathbf{s}_{\bar{k}}^b, b = 1, 2, \dots, B$  and  $\hat{\mathbf{s}}_{\bar{k}}$  to obtain  $\tilde{\mathbf{y}}_k^{(b)}$  and  $\tilde{\mathbf{y}}_k$ .
- 13: Calculate  $L(s_k^{(b)}(i))$  and  $L(\hat{s}_k(i))$  according to  $\tilde{\mathbf{y}}_k^{(b)}$  and  $\tilde{\mathbf{y}}_k$  respectively,  $i = 1, 2$ .
- 14: Calculate  $\Pr(s_k(1) = +1 | \mathbf{y}_k^*)$  and  $\Pr(s_k(2) = +1 | \mathbf{y}_k^*)$  as (5.16) and the corresponding LLR for the cancellation in (5.8) and the channel decoder.
- 15: **End**

---

converge to the MAP algorithm. However, it requires a larger channel matrix and more candidates as in [66]. The main difference between the Gibbs sampling based generation and the tree search based generation is the terms  $\Pr(\mathbf{s}_k^{(b)})$  and  $\Pr(\hat{\mathbf{s}}_k)$ . For TSG, the probability  $\Pr(\tilde{\mathbf{y}}_k^{(b)})$  is calculated with the LLR fed back from the channel decoder. On the other hand, each feedback in GSG is assumed to be equally probable. However, they perform almost identically in BER performance with the same number of feedback candidates. This is because TSG and GSG make use of the LLR from the channel decoder in different forms. The complexity of these two methods is not very intensive. The GSG employs one or multiple random number generators, which can be implemented efficiently without any multiply operations as stated in [132]. For TSG, the multipliers are also not required due to the use of logarithm domain computation. For example, the number of real additions required for TSG is around  $2QB|\mathbb{C}|$  at most.

#### 5.5.4 Reduced channel matrix for multi-feedback interference cancellation

Conventionally, the more interference is mitigated, the better SINR performance achieves. However, the output SINR of matched filter with a reduced size  $Q = D$  channel matrix may not suffer significant performance compared to that with a normal size  $Q = 2D$  channel matrix. According to the statements in [140], the channel matrix in (5.3) can also be reduced to (5.25) as shown in Fig. 5.2. The representation of the reduced channel matrix is illustrated in the blue square. It can be found that the elements in the upper-left corner and lower-right corner have been omitted. Hence, the normal size truncated channel matrix with  $Q = 2D$  in (5.3) is replaced by the following reduced size channel matrix:

$$\mathbf{H}_k = \begin{bmatrix} h_{df}(k-D, k-D) & \cdots & h_{df}(k-D, k) & \cdots & \mathbf{0} \\ \mathbf{0} & \ddots & \vdots & \ddots & \vdots \\ \cdots & \mathbf{0} & h_{df}(k+D, k) & \cdots & h_{df}(k+D, k+D) \end{bmatrix}. \quad (5.25)$$

To show the pre-processing SINR difference between the reduced size channel matrix  $Q = D$  and the normal size channel matrix  $Q = 2D$ , the pre-processing SINR obtained

by observing  $\tilde{\mathbf{y}}_k^{(b)}$  in (5.10) is

$$\begin{aligned} \text{SINR}_Q^{(b)} &\approx \frac{E_s \mathbb{E}\{\mathbf{h}_k^H \mathbf{h}_k\}}{\sum_{q=k-Q, q \neq k}^{k+Q} \mathbb{E}\{\mathbf{h}_{\bar{k}}^H \mathbf{h}_{\bar{k}}\} |s_{\bar{k}} - s_{\bar{k}}^{(b)}|^2 \bar{P}(s_{\bar{k}}^{(b)}) + \mathbb{E}\{\tilde{\mathbf{n}}_k^H \tilde{\mathbf{n}}_k\}} \\ &\approx \frac{\tilde{E}_s}{\sum_{\bar{k}=k-Q, \bar{k} \neq k}^{k+Q} \mathbb{E}\{\mathbf{h}_{\bar{k}}^H \mathbf{h}_{\bar{k}}\} |s_{\bar{k}} - s_{\bar{k}}^{(b)}|^2 \bar{P}(s_{\bar{k}}^{(b)}) + \mathbb{E}\{\tilde{\mathbf{n}}_k^H \tilde{\mathbf{n}}_k\}}, \end{aligned} \quad (5.26)$$

where  $\bar{P}(s_q^{(b)}) = \Pr(s_q \neq s_q^{(b)})$ , and the quantity  $E_s$  denotes the average transmit signal power. Note that the exact symbol error probability  $\bar{P}(s_q^{(b)})$  in a coded system cannot be easily obtained. The residual interference term inside the band is omitted for simplicity. Because the first term in the denominator of (5.26) will be significantly suppressed at high SNR by the MBMF-SIC. Hence, the entire ICI power  $\sigma_{c0}^2$  and ICI power  $\sigma_{cQ}^2$  outside  $Q$  central terms can be evaluated by an upper bound [140, 145] as

$$\begin{aligned} \sigma_{c0}^2 &\approx \frac{E_s}{12} (2\pi T_{sa} N_s)^2 \left( \sum_{l=0}^{L-1} \sigma_l^2 \sigma_{Dl}^2 \right) - \frac{E_s}{240} (2\pi T_{sa} N_s)^4 \left( \sum_{l=0}^{L-1} \sigma_l^2 \sigma_{Dl}^4 \right) \\ \sigma_{cQ}^2 &\approx \sigma_{c0}^2 \left( 1 - \frac{6}{\pi^2} \sum_{q=1}^{2D} \frac{1}{q^2} \right) \end{aligned} \quad (5.27)$$

where  $\sigma_l^2$  denotes the variance of the  $l$ th channel tap.  $\sigma_{Dl}^2 = \int_{-f_d}^{f_d} P_l(f) f^2 df$ , and  $P_l(f)$  is the Doppler power spectral density (PSD) of the  $l$ th path.  $\sigma_{Dl}^2 = f_d^2/2$ , and  $\tilde{E}_s = E_s - \sigma_{c2D}^2$  denotes the transmit signal power inside the band with a normal channel matrix  $Q = 2D$ . The quantity  $T_{sa} = \frac{T_{\text{OFDM}}}{N_s}$ . For  $Q = 2D$ , equation (5.26) can be rewritten as

$$\text{SINR}_Q^{(b)} \approx \frac{Q \tilde{E}_s}{\mathbb{E}\{\tilde{\mathbf{n}}_k^H \tilde{\mathbf{n}}_k\}} \quad (5.28)$$

Without the residual interference inside the band, the SINR for the  $b$ th feedback is mainly determined by the noise plus the ICI outside the band. Furthermore, the power of the signal  $\tilde{E}_s$  for  $Q = D$  will be identical to that for  $Q = 2D$ , because the power of the signal is derived from the same channel coefficients  $\mathbf{h}_k$  in (5.25) for  $Q = D$  or in (5.3) for  $Q = 2D$ . Similar to [140],  $\text{SINR}_{2D}^{(b)} > \text{SINR}_D^{(b)}$  if no pre-whitener is employed. However, the post-processing SINR of the matched filter  $\mathbf{h}_k^H$  will partially contradict the above discussion, which can be evaluated by

$$\text{PSINR}_Q^{(b)} \approx \frac{\tilde{E}_s^2 / E_s}{\text{tr}(\mathbb{E}\{\mathbf{h}_k \mathbf{h}_k^H\} \mathbb{E}\{\mathbf{c}_k \mathbf{c}_k^H\}) + \sigma_v^2} \quad (5.29)$$

where the vector  $\mathbf{c}_k = [c_{k-D,k} \ c_{k-D+1,k} \ \dots \ c_{k+D,k}]^T$  denotes the residual ICI outside the band for the  $k$ th subcarrier and  $c_k = \frac{1}{\sqrt{E_s}} \sum_{\bar{k} \notin [k-Q, k+Q]} H_{\bar{k},k}^H s_{\bar{k}}$ . The autocorrelation func-

tion of the channel coefficients  $\mathbf{h}_k$  can be derived by [140]

$$\mathbb{E}\{h_{df}(d, k)h_{df}^*(d+r, k)\} \approx 4\pi^2 T_{sa}^2 \left( \sum_{l=0}^{N_h-1} \sigma_l^2 \sigma_{Dl}^2 \right) \cdot \frac{1}{(1 - e^{-j2\pi d/N_s})(1 - e^{j2\pi(d+r)/N_s})} \quad (5.30)$$

where  $d \in [-D, D]$ . Note that there are singularity points when  $d = 0$  or  $d = -r$  in (5.30), and the autocorrelation function become unavailable. Let  $d = -d$  and  $r = -r$  to avoid the singularity point when  $d = -r$  and  $d \neq 0$ . For  $d = 0$ , thanks to the Hermitian symmetric property of the autocorrelation function, the value of the singularity point can be obtained by setting  $r = 0$  and  $d = r$ . For  $d = 0$  and  $r = 0$ ,  $\mathbb{E}\{h_f(0, k)h_f^*(0, k)\} = \frac{E_s - \sigma_{c0}^2}{E_s}$ . Additionally, the autocorrelation function of ICI can be obtained by [140]

$$\mathbb{E}\{c_{k+d}c_{k+d+r}^*\} \approx 4\pi^2 T_{sa}^2 \alpha_{d,r} \gamma(Q, r, N_s) \sum_{l=0}^{N_h-1} \sigma_l^2 \sigma_{Dl}^2 \quad (5.31)$$

where

$$\gamma(D, r, N_s) = \sum_{\substack{m \notin [-D, D] \\ \cup [-D-r, D-r]}} \frac{1}{(1 - e^{-j2\pi m/N_s})(1 - e^{j2\pi(m+r)/N_s})}. \quad (5.32)$$

and

$$\alpha_{d,r} = \begin{cases} e^{f_d T_{sa} N_s / 2 (|d| + |r|)} & d \neq 0, r \neq 0 \\ 1 & d = 0, r = 0 \end{cases} \quad (5.33)$$

Further simplification of (5.32) can be found in [140]. Note that for  $Q = D$  the autocorrelation of ICI in (5.32) is modified accordingly given the range of  $m$ . This is because the residual interference  $c_{k-D}, \dots, c_k, \dots, c_{k+D}$  outside the band in (5.25) is given by the different sets of  $m$ . The quantity  $\alpha_{d,r}$  in (5.33) will be used in this case, otherwise  $\alpha_{d,r} = 1, \forall d, r$ . Hence, the autocorrelation matrix  $\mathbb{E}\{\mathbf{h}_k \mathbf{h}_k^H\}$  and  $\mathbb{E}\{c_k c_k^H\}$  can be computed by (5.30) and (5.31), respectively. The analytical pre-processing SINR ( $\text{SINR}_Q^{(b)}$ ) and post-processing SINR after the matched filter ( $\text{PSINR}_Q^{(b)}$ ) can be calculated by (5.28) and (5.29).

In the following, we present some simple numerical results and analytical results of pre-processing SINR ( $\text{SINR}_Q^{(b)}$ ) and post-processing SINR ( $\text{PSINR}_Q^{(b)}$ ) in Fig. 5.3, and  $f_d T_{\text{OFDM}} = 0.65$ . We can observe that the post-processing SINR ( $\text{PSINR}_Q^{(b)}$ ), with the same size  $Q$ , can be improved by the matched filter compared to pre-processing SINR ( $\text{SINR}_Q^{(b)}$ ) at low SNR values. Furthermore, the post-processing SINR performance gap

between  $Q = D = 1$  and  $Q = 2D = 2$  is small (around 1 dB at 12 dB SNR). We can conjecture that the error probability of  $\Pr(s_k^{(b)} \neq s_k)$ , with  $Q = D$  in (5.8), will not be significantly degraded compared to that with  $Q = 2D$ . In other words, the multi-feedback cancellation with  $Q = D$  requires less complexity than that with  $Q = 2D$  in the cancellation stage, but achieves similar post-processing SINR performance.

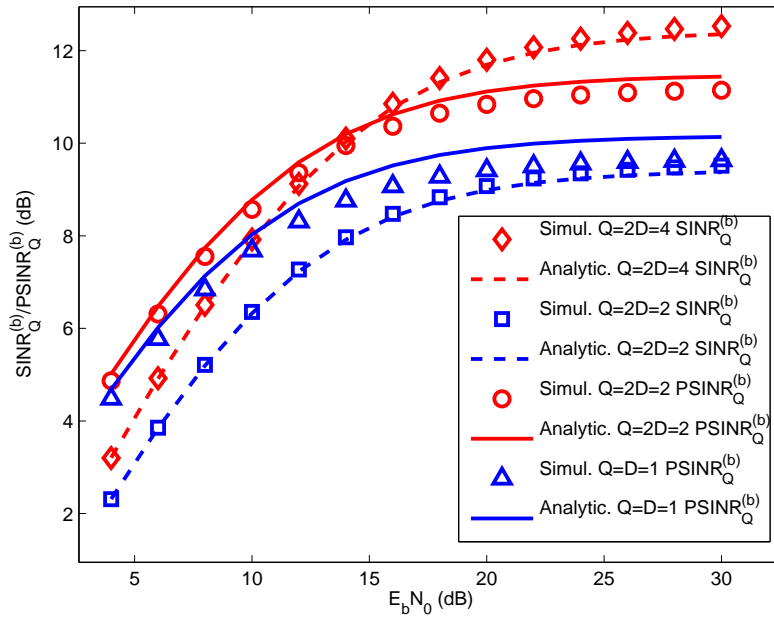


Figure 5.3: pre-processing and post-processing SINR comparison for the  $b$ th feedback with different  $Q$ .  $N_s = 128$ ,  $f_d T_{\text{OFDM}} = 0.65$

## 5.6 SINR Ordering for MBMF-SIC

For conventional sequential ICI cancellation for OFDM systems, the cancellation performs subcarrier by subcarrier, because the previous soft symbol estimates  $[\hat{s}_{k-2D}, \dots, \hat{s}_{k-1}]$  inside the band are needed in the cancellation for the desired subcarrier  $s_k$ . In this case, there is no significant benefit from the ordering, due to absence of previous soft symbol estimates. With the iterative ICI cancellation and the channel decoder, the soft symbol estimates  $[\hat{s}_{k-2D}, \dots, \hat{s}_{k-1}]$  are known beyond the initial iteration,

so any ordering can be performed. However, its performance improvement by ordering is very small. On the other hand, the sequential ICI cancellation will introduce the aggregation of residual interference. For MBMF-SIC, the interference is reconstructed by the multi-feedback symbols vectors  $[s_{k-2D}^b, \dots, s_{k-1}^b]$ ,  $b = 1, 2, \dots, B$ , so the aggregation of residual interference from previous soft symbols can be significantly removed. Furthermore, we assume that the conditional probability of  $\mathbf{y}_k^{(b)}$  given  $\mathbf{s}_{\bar{k}}^{(b)}$  and  $\tilde{\mathbf{y}}_k$  given  $\hat{\mathbf{s}}_{\bar{k}}$  are conditionally independent in (5.13). It will be true if the residual interference inside the band in (5.8) and (5.10) dominates. This assumption may be more reasonable by the ordering, which can reduce the coupling effects brought by the previous soft symbol estimates. Following (5.8) and (5.29), the SINR of the  $k$ th subcarrier for ordering can be evaluated as similar to the SINR ordering discussed in Subsection 2.6.4

$$\nu_k \approx \frac{(|\mathbf{h}_k^H \mathbf{h}_k|)^2 E_s}{E_s \text{tr}(\mathbb{E}\{\mathbf{h}_k \mathbf{h}_k^H\} \mathbb{E}\{\mathbf{c}_k \mathbf{c}_k^H\}) + \sigma_v^2 + \text{tr}(\sum_{\bar{k}=k-Q, q \neq k}^{k+Q} \mathbf{h}_{\bar{k}} \nu_k \mathbf{h}_{\bar{k}}^H)}, \quad (5.34)$$

where  $\nu_k = \mathbb{E}\{(s_q - \hat{s}_q)(s_q - \hat{s}_q)^*\}$ . In the remaining steps, the quantity  $\nu_k$  can be sorted for  $k = 1, \dots, N_s$ , and the detection ordering can be implemented accordingly. Other ordering methods can also be employed on the basis of error probability or LLRs, the calculation of which will introduce the channel matrix inversion, with complexity at least  $\mathcal{O}((2D+1)^2)$ . Hence, the complexity of LLR ordering in [146] will be more complicated than that of SINR ordering.

## 5.7 Multi-Segmental Channel Estimation

In this section, we discuss MSCE to estimate time-varying channels, and discuss the pilot symbol selection in each iteration. Additionally, the MSCE can be terminated in an early iteration by comparing with previous estimates.

### 5.7.1 Least-squares based MSCE

For MSCE, we split the received signal  $r(n)$ ,  $n = 0, 1, \dots, N_s - 1$  into  $T$  segments as in (2.109), and each segment has  $M = N_s/T$  samples. By defining  $\mathbf{y}_t = [y_t(0), \dots, y_t(N_s - 1)]^T$ ,  $\mathbf{h}_{df}(t) = [h_{df}(t, 0), \dots, h_{df}(t, N_s - 1)]^T$ ,  $\mathbf{h}_{tl}(t) =$

$[h_{tl}(t, 0), \dots, h_{tl}(t, l), \dots, h_{tl}(t, L - 1)]^T$ , and the term  $\delta_k(t)$  in (2.110) is reorganized in a matrix form as

$$\mathbf{\Delta}_t = \begin{bmatrix} \delta_0(t) & \dots & \delta_{N_s-1}(t) \\ \vdots & \ddots & \vdots \\ \delta_{1-N_s}(t) & \dots & \delta_0(t) \end{bmatrix}, \quad (5.35)$$

equation (2.111) for the  $t$ th segment can be rewritten in the following form:

$$\mathbf{y}_t = \underbrace{\sqrt{N_s} \mathbf{\Delta}_t \text{diag}(\mathbf{s}) \mathbf{F}_L}_{\mathbf{A}} \mathbf{h}_{tl}(t), \quad (5.36)$$

where  $\mathbf{h}_{df}(t) = \sqrt{N_s} \mathbf{F}_L \mathbf{h}_{tl}(t)$ . Using LS estimation in the time domain [78], the channel estimates in the  $t$ th segment can be obtained by

$$\hat{\mathbf{h}}_{tl}(t) = (\mathbf{A}^H \mathbf{A})^{-1} \mathbf{A}^H \mathbf{y}_t. \quad (5.37)$$

Note that there are  $N_p$  pilot symbols already known to the receiver, and the 0s can be set for the unreliable symbol estimates of  $\hat{\mathbf{s}}$  in each iteration, the reliability of which can be evaluated by LLRs from the channel decoder. In the following steps, we introduce the piece-wise linear model to approximate the channel impulse responses for the time-varying channels between the  $t$ th segment and  $(t + 1)$ th segment as in [147]. Hence, the channel estimates  $\hat{\mathbf{h}}_{tl}(n) = [\hat{h}_{tl}(n, 0), \dots, \hat{h}_{tl}(n, l), \dots, \hat{h}_{tl}(n, L - 1)]^T$  for different time indices can be obtained, and the corresponding channel frequency response  $\hat{h}_{df}(d, k)$  in (5.3) can be obtained. The matrix  $\mathbf{\Delta}_t$  can be pre-computed, once the number of segments  $T$  is determined. In addition, the differences of channel estimates between the  $(p - 1)$ th and  $p$ th iteration can be measured, which can help us to terminate the MSCE at an earlier iteration.

## 5.7.2 MSE lower bound analysis

In this subsection, we derive an overall MSE lower bound as a benchmark for the MSCE discussed above. As can be seen from above, the MSCE exploits the linear interpolation to approximate the channels between segments, that is, an approximation errors in the channel estimates rather the noise itself. Firstly, the channel estimates after the interpolation can be rewritten in another form as

$$\tilde{\mathbf{h}}_{tl} = \mathbf{\Phi} \hat{\mathbf{c}} \quad (5.38)$$

where

$$\begin{aligned}
 \tilde{\mathbf{h}}_{tl} &= [\tilde{\mathbf{h}}_{tl}^T(0), \dots, \tilde{\mathbf{h}}_{tl}^T(l), \dots, \tilde{\mathbf{h}}_{tl}^T(L-1)]^T \in \mathbb{C}^{N_s L \times 1}, \\
 \tilde{\mathbf{h}}_{ul}(l) &= [\tilde{h}_{ul}(0), \dots, \tilde{h}_{ul}(n), \dots, \tilde{h}_{ul}(N_s-1)]^T \in \mathbb{C}^{N_s \times 1}, \\
 \hat{\mathbf{c}} &= [\hat{\mathbf{h}}_{ul}^T(0), \dots, \hat{\mathbf{h}}_{ul}^T(l), \dots, \hat{\mathbf{h}}_{ul}^T(L-1)] \in \mathbb{C}^{TL \times 1} \\
 \hat{\mathbf{h}}_{ul}(l) &= [\hat{h}_{ul}(0, l), \dots, \hat{h}_{ul}(t, l), \dots, \hat{h}_{ul}(T-1, l)]^T,
 \end{aligned} \tag{5.39}$$

and

$$\begin{aligned}
 \Phi &= \mathbf{I}_L \otimes \Psi, \\
 \Psi &= [\psi(0), \dots, \psi(n), \dots, \psi(N_s-1)]^T \in \mathbb{R}^{N_s \times T} \\
 \psi(n) &= [\psi(n, 0), \dots, \psi(n, q), \dots, \psi(n, T-1)]^T
 \end{aligned} \tag{5.40}$$

where  $\psi(n, q)$  denotes the interpolation coefficients. Defining the noise term and the residual interference term in as  $\mathbf{z}_t$ , equation (5.36) can be rewritten in a compact matrix form:

$$\mathbf{y} = \underbrace{\begin{bmatrix} \Lambda_0 & & \\ & \ddots & \\ & & \Lambda_{T-1} \end{bmatrix}}_{\Theta \in TN_s \times TN_s} \underbrace{\begin{bmatrix} \mathbf{F}^H & & \\ & \ddots & \\ & & \mathbf{F}^H \end{bmatrix}}_{\mathbf{F}' \in TN_s \times TN_s} \underbrace{\begin{bmatrix} \text{diag}(\mathbf{s}) \\ \vdots \\ \text{diag}(\mathbf{s}) \end{bmatrix}}_{\mathbf{S} \in TN_s \times N_s} \mathbf{\Gamma} \Phi \mathbf{c} + \underbrace{\begin{bmatrix} \mathbf{z}_0 \\ \vdots \\ \mathbf{z}_{T-1} \end{bmatrix}}_{\mathbf{z} \in TN_s \times 1} \tag{5.41}$$

where

$$\begin{aligned}
 \mathbf{F} &= [\Lambda_0, \dots, \Lambda_t, \dots, \Lambda_{T-1}] \in \mathbb{C}^{N_s \times N_s} \\
 \mathbf{y} &= [\mathbf{y}_0^T, \dots, \mathbf{y}_t^T, \dots, \mathbf{y}_{T-1}^T]^T \in \mathbb{C}^{TN_s \times 1} \\
 \mathbf{\Gamma} &= [\gamma_0^T, \dots, \gamma_k^T, \dots, \gamma_{N_s-1}^T] \in \mathbb{C}^{N_s \times N_s L}
 \end{aligned} \tag{5.42}$$

and

$$\begin{aligned}
 \Lambda_t &\in \mathbb{C}^{N_s \times M}, \\
 \gamma_k &= \underbrace{[0, \dots, 0]_{k+1}}_{k+1} e^{-j\frac{2\pi}{N_s}k \cdot 0}, \underbrace{[0, \dots, 0]_{LN_s}}_{LN_s} e^{-j\frac{2\pi}{N_s}kl}, \underbrace{[0, \dots, 0]_{(L-l)N_s}}_{(L-l)N_s} e^{-j\frac{2\pi}{N_s}k(L-1)}, \underbrace{[0, \dots, 0]_{N_s-k+1}}_{N_s-k+1} ]^T \in \mathbb{C}^{LN_s \times 1},
 \end{aligned} \tag{5.43}$$

Hence, equation (5.41) can be represented as

$$\mathbf{y} = \underbrace{\Theta \mathbf{F}' \mathbf{S} \mathbf{\Gamma} \Phi}_{\mathbf{B}} \mathbf{c} + \mathbf{z}, \tag{5.44}$$

where the matrix  $\Theta$  denotes the partial FFT, and the matrix  $\mathbf{F}'$  denotes the normal IFFT. The channel estimates  $\hat{\mathbf{c}} = \hat{\mathbf{h}}_{tl}$  can be obtained by LS estimation accordingly. The overall MSE is based on the approximation errors of linear interpolation and the estimation error of  $\hat{\mathbf{c}}$ , namely  $\text{MSE}_{\text{appx}}$  and  $\text{MSE}_{\text{est}}$ , respectively. According to the derivation of [148], the overall MSE can be expressed as

$$\text{MSE}_{\text{overall}} = \text{MSE}_{\text{appx}} + \text{MSE}_{\text{est}}. \tag{5.45}$$

where

$$\begin{aligned} \text{MSE}_{appx} &= \frac{1}{N_s L} \text{tr}\{(\mathbf{I}_{N_s} - \Psi\Psi^H)\mathbf{R}\} \\ \text{MSE}_{est} &= \frac{1}{N_s L} \text{tr}\{\mathbb{E}\{(\mathbf{c} - \hat{\mathbf{c}})(\mathbf{c} - \hat{\mathbf{c}})^H\}\} \end{aligned} \quad (5.46)$$

Note that the unity power of the multipath channel is assumed, and the matrix  $\mathbf{R}$  represents the autocorrelation matrix, which is defined in (2.27). The autocorrelation matrix of  $\mathbb{E}\{(\mathbf{c} - \hat{\mathbf{c}})(\mathbf{c} - \hat{\mathbf{c}})^H\}$  can be given by

$$\mathbb{E}\{(\mathbf{c} - \hat{\mathbf{c}})(\mathbf{c} - \hat{\mathbf{c}})^H\} = \mathbb{E}\{\mathbf{z}\mathbf{z}^H\}\mathbb{E}\{\mathbf{B}\mathbf{B}^H\} \quad (5.47)$$

where the cross-correlation function of noise is  $\mathbb{E}\{z_t(d_1)z_t(d_2)\} = \frac{\sigma_n^2}{T} e^{-j\frac{\pi(d_1-d_2)(2t-1)}{T}} \text{sinc}\left(\frac{\pi(d_1-d_2)}{2T}\right)$ , and the notation sinc denotes the sinc function. Because we assume all data and pilot symbols for transmission are known to the channel estimator in the later iterations, so the matrix  $\mathbf{B}$  can be calculated and  $\mathbb{E}\{\mathbf{B}\mathbf{B}^H\}$  accordingly.

The overall MSE lower bound can be given by

$$\text{MSE}_{overall} = \frac{1}{N_s L} \text{tr}\{(\mathbf{I}_{N_s} - \Psi\Psi^H)\mathbf{R}\} + \frac{1}{N_s L} \text{tr}\{\mathbb{E}\{\mathbf{z}\mathbf{z}^H\}\mathbb{E}\{\mathbf{B}\mathbf{B}^H\}\} \quad (5.48)$$

Note that the prior assumption that channels are constant within the segment is not used in the MSE analysis, so the overall MSE is a lower bound for MSCE.

## 5.8 Complexity Requirements of MBMF-SIC and MSCE

The complexity of the MBMF-SIC discussed in this chapter is determined by the parameters: the number of multi-feedback candidates  $B$ , the reduced size truncated channel matrix  $Q = D$ , the number of subcarriers  $N_s$ , and the number of iterations for the cancellation  $P$ . Following the algorithm table in Table 5.1 with 4QAM, the computation of the algorithm for the initial iteration is slightly different from that for the later iterations. But the computational complexity of the initial iteration is almost identical to that of the later iterations. The computational complexity comes from two aspects: (1) the multi-feedback generation; (2) the multi-feedback cancellation. The computation of feedback symbols generation for  $k = 0, 1, \dots, N_s - 1$  in step 11 requires a maximum of  $8N_s B D$  complex additions (CAs) for GSG and TSG, and the computation of the cancellation in step 12 and 13 for  $k = 0, 1, \dots, N_s - 1$  requires  $N_s B(8D^2 + 6D + 1)$  complex multiplications (CMs) and  $N_s B(8D^2 + 6D + 2)$  CAs. In step 14, the computation of average

probability of  $\Pr(s_k(i) = +1 | \mathbf{y}_k^*), i = 1, 2$  and  $k = 0, 1, \dots, N_s - 1$  and the corresponding LLR leads to  $N_s B$  CAs. Hence, the total number of complex operations for one iteration required by the MFMB-SIC is  $N_s(16BD^2 + 20BD + 4B)$ , and the SINR ordering requires a total of  $\mathcal{O}(N_s \log N_s) + N_s$  complex operations [66]. The complexity comparison of ICI cancellation techniques has been made in Table 5.2. The complexity of MBMF-SIC and MF-PIC is moderate compared to MF-SIC, and much lower than that of conventional MMSE-SIC and banded MMSE-SIC.

Furthermore, the MSCE requires a maximum of  $\mathcal{O}(TL^2) + \mathcal{O}(2N_s L)$  complex operations for each OFDM symbol in the  $p$ th iteration. This is because the size of matrix inversion used in (5.37) is only related to the number of the channel paths  $L$ . The complexity comparison between different channel estimation techniques for rapidly time-varying channel is presented in Table 5.3. Note that pilot assisted-LS denotes the pilot assisted LS channel estimation, which uses the discrete Karhuen-Loève-basis expansion model (BEM) to approximate the time-varying channels with the limited number of expansion coefficients [149]. The number of expansion coefficients is lower bounded by  $2\lceil f_d T_{\text{OFDM}} \rceil + 1 = 2D - 1$  as described in [148]. The significant advantage of MSCE over the method in [149] is the use of linear interpolation to approximate the channels between two segments in the OFDM symbol. Hence, the MSCE can be considered as a special representation of BEM with 2 expansion coefficients. Compared to SBCE, the complexity of MSCE is a bit higher. Because the matrix inversion with the size  $L$  is required to estimate the channels in the mid-point of each segment.

Algorithm	Complex Operations
MMSE-SIC [150]	$\mathcal{O}(N_s^3) + \mathcal{O}(4N_s^2 D^2) + \mathcal{O}(N_s^2)$
banded MMSE-SIC [56]	$N_s(\frac{64}{3}D^3 + 80D^2 + \frac{104}{3}D + 4)$
MF-SIC [62]	$N_s(32D^2 + 16D + 3)$
MF-PIC [138]	$N_s(32D^2 + 22D + 1)$
MBMF-SIC	$N_s(16BD^2 + 20BD + 4B)$
MBMF-SIC+SINR ordering	$N_s(16BD^2 + 20BD + 4B) + \mathcal{O}(N_s \log N_s) + N_s$

Table 5.2: Complexity comparison between different interference cancellation techniques for the  $p$ th iteration

Algorithm	Complex Operations
SBCE [62]	$\mathcal{O}(N_s^2) + \mathcal{O}(2N_sL)$
PA-LS [149]	$\mathcal{O}((2D^2 - 1)L^3) + \mathcal{O}((4DN_s - 2)L^2)$
MSCE	$\mathcal{O}(TL^3) + \mathcal{O}(2N_sL)$

Table 5.3: Complexity comparison between different channel estimation techniques for the  $p$ th iteration

## 5.9 Simulation Results

In this section, the performance of the proposed methods (MF-PIC and MBMF-SIC) will be evaluated by BER in different scenarios. We assume a scenario with the following settings: the carrier frequency  $f_c = 650\text{MHz}$ , the subcarrier spacing  $\Delta f = 976.5\text{Hz}$ , and the OFDM symbol period is  $T_{\text{OFDM}} = 1/\Delta f \approx 1\text{ms}$ . The number of subcarriers is  $N_s = 128$ . The symbols are modulated by 4QAM, the extension of which to other modulation schemes is straightforward. In addition, a  $1/2$  rate convolutional code with generator polynomial  $(7, 5)$  is employed for the iterative interference cancellation, and the length of the code is 2560 bits. A wide-sense stationary uncorrelated scattering channel with a uniform power delay profile is simulated according to the Jakes model and the normalized Doppler frequency  $f_d T_{\text{OFDM}} = 0.65$ . The maximum delay of the channel is  $L = 8$ . In our setting, the normalized Doppler frequency corresponds to a speed of the transmitter relative to the receiver of 1000 km/h. Because of the band assumption, we assume  $D = \lceil f_d T_{\text{OFDM}} \rceil + 1$  as described in [56, 57] given the time-domain window. For MSCE, the number of segments ( $T = 2$ ) is used, and the number of pilots  $N_p = N_s/4$ . We also define an approximate matched filter bound (AMFB) as a benchmark for ICI cancellation, which implies that the ICI inside the band ( $Q = 2D$ ) is perfectly removed.

In Fig. 5.4, the BER performance of GSG based MBMF-SIC (GMBMF-SIC) and TSG based MBMF-SIC (TMBMF-SIC) with SINR ordering are quite close to the benchmark AMFB [137] with a fraction of one dB loss, and significantly remove the error floor compared to banded MMSE-SIC [56], MF-SIC [62] and MBMF-SIC without SINR ordering. It can be explained that the SINR ordering improves the reliability of detected symbols, and make the assumption for (5.12) more appropriate. For fair comparison, the SINR or-

dering is incorporated in other schemes in Subsection 5.6 in the later iterations except the 1st iteration. This is because serial ICI cancellation requires previous symbol estimates to improve the reliability of the remaining symbols. But the ordering for MBMF-SIC can be employed in the initial iteration due to the use of LLR to generate multi-feedback candidates in the step 3 and 4 of Table 5.1 . We can also observe that the BER performance between GMBMF-SIC and TMBMF-SIC is negligible, but TSG performs better than GSG. It also agrees with the statements in [132] that the tree search algorithm works better than the Gibbs sampler at high SNR. For simplicity, we only consider GMBMF-SIC and TMBMF-SIC with SINR ordering in the rest of the chapter, which will be referred to as OGMBMF-SIC and OTMBMF-SIC. Furthermore, the curves of OTMBMF-SIC may not be shown in some following figures, because there is almost no differences between OGMBMF-SIC and OTMBMF-SIC in the BER performance.

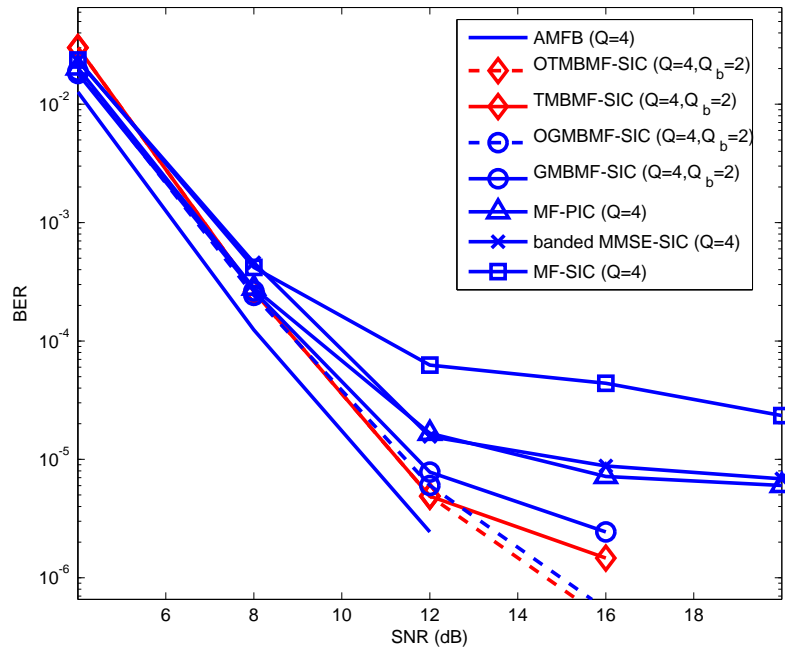


Figure 5.4: BER performance against SNR (dB) of MF-PIC, GMBMF-SIC, OGMBMF-SIC, TMBMF-SIC, OTMBMF-SIC ,MF-SIC, banded MMSE-SIC, and AMFB in the 4th iteration with  $f_d T_{\text{OFDM}} = 0.65$

In Fig. 5.5, the BER performance against the number of iterations of MF-PIC, GMBMF-SIC, OGMBMF-SIC and other soft ICI cancellation techniques (MF-SIC,

banded MMSE-SIC, AMFB) with 4QAM is shown. For MBMF-SIC, we can observe that its performance is closer to the banded MMSE-SIC in the 1st iteration at SNR= 12 dB than other matched filter based techniques, and it outperforms them significantly in the 4th iteration with ( $B = 5$ ) multi-feedback ( $Q_b = D$ ) and soft feedback ( $Q = 2D$ ). Unlike the BER performance of GMBMF-SIC and OGMBMF-SIC, the performance of MF-PIC is not promising in the 1st iteration, but it works almost identically to the banded MMSE-SIC in the 4th iteration.

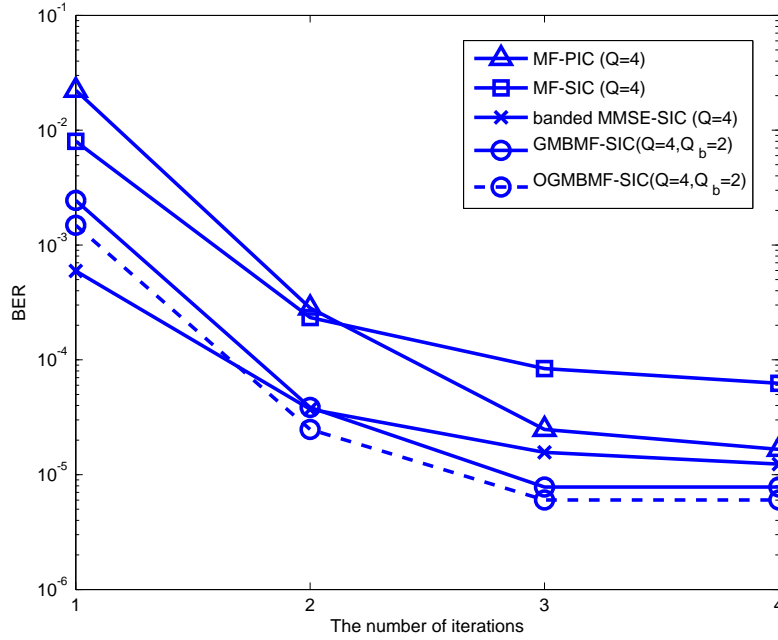


Figure 5.5: BER performance against the number of iterations of MF-PIC, GMBMF-SIC, OGMBMF-SIC, MF-SIC, banded MMSE-SIC, and AMFB with  $f_d T_{\text{OFDM}} = 0.65$  at SNR= 12 dB

The BER performance of the 1st iteration and the 4th iteration against normalized Doppler frequencies  $f_d T_{\text{OFDM}}$  from 0.25 to 0.65 has been illustrated in Figs. 5.6 and 5.7, which validates the statements that the proposed OGMBMF-SIC and OTMBMF-SIC can work in a wide range of high Doppler frequencies  $f_d T_{\text{OFDM}}$ . Fig. 5.6 shows that the BER performance in the 1st iteration of MF-SIC and MF-PIC is much poorer than that of banded MMSE-SIC at low normalized Doppler frequencies  $f_d T_{\text{OFDM}}$  from 0.25 to 0.35 except OGMBMF-SIC and OTMBMF-SIC, and the BER performance of OGMBMF-SIC and OTMBMF-SIC degrade slowly with an increasing normalized Doppler frequencies.

In Fig. 5.7, we can observe that the gain of BER performance obtained by OGMBMF-SIC and OTMBMF-SIC is not very significant in the 4th iteration at different normalized Doppler frequencies, because the power of ICI inside the band reduces. Hence, the MF-SIC and MF-PIC can be used in the low Doppler frequencies, and the determination of  $B$  can be adapted according to  $f_d T_{\text{OFDM}}$  to obtain a more attractive tradeoff between performance and complexity.

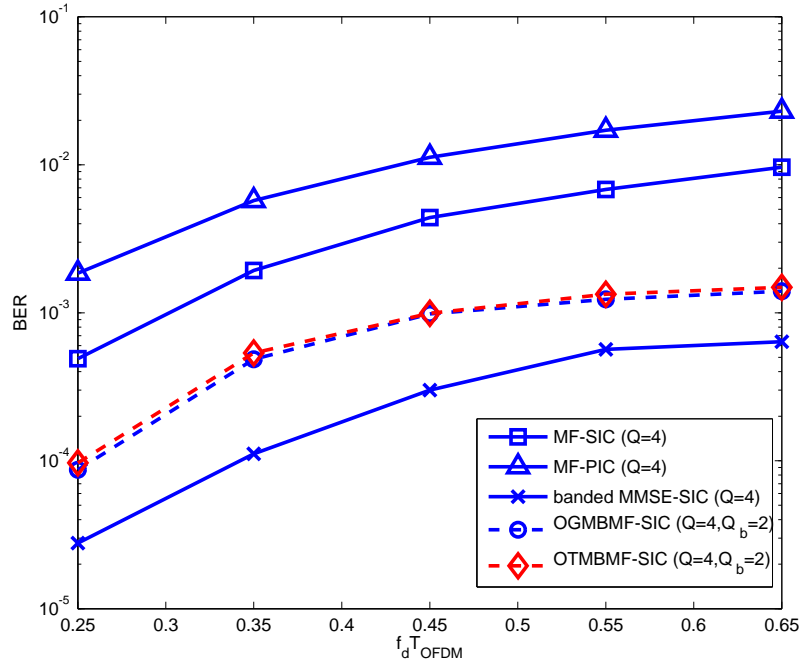


Figure 5.6: BER performance against  $f_d T_{\text{OFDM}}$  of MF-PIC, OGMBMF-SIC, OTMBMF-SIC, MF-SIC, and banded MMSE-SIC in the 1st iteration at SNR = 12 dB

Fig. 5.8 compares the BER performance against SNR (dB) with a normalized Doppler frequencies  $f_d T_{\text{OFDM}} = 0.65$  in the 4th iterations. The MSCE is iteratively performed in every iteration, once the new symbol estimates become available from the channel decoder. The BER performance of these receivers in the 1st iteration is very poor with  $f_d T_{\text{OFDM}} = 0.65$ , which may not be useful for comparison. Matched filter based receivers (MF-SIC, OGMBMF-SIC) are less sensitive to channel estimation errors, because they do not make use of channel coefficients as much as banded MMSE-SIC. For banded MMSE-SIC, the autocorrelation matrix must be used, which may amplify the channel estimation errors. In Fig. 5.4, the banded MMSE-SIC outperforms MF-SIC with perfect

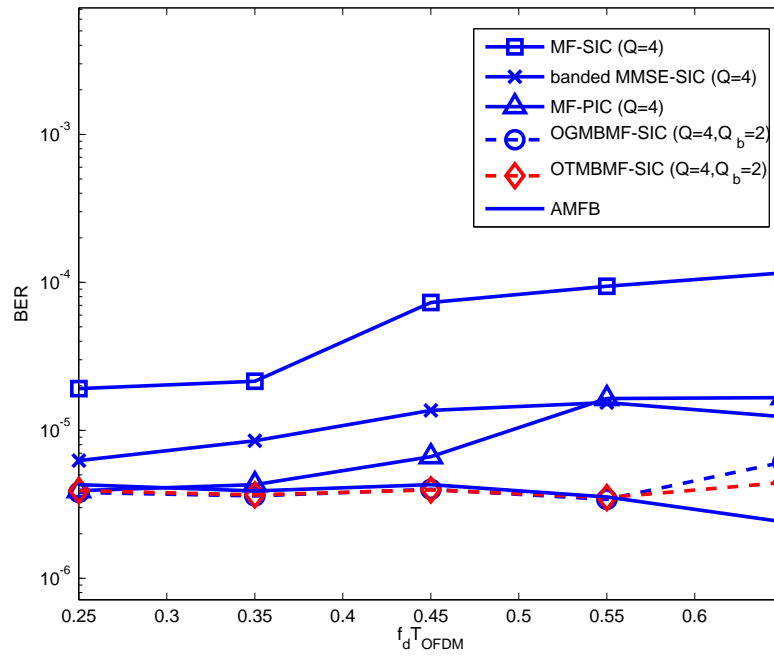


Figure 5.7: BER performance against  $f_d T_{\text{OFDM}}$  of MF-PIC, OGMBMF-SIC, OTMBMF-SIC, MF-SIC, and banded MMSE-SIC in the 4th iteration at SNR= 12 dB

channel knowledge in the BER performance. However, their performance at SNR= 20 dB has been degraded to the same level of BER (less than 1 dB performance loss) in the 4th iteration with MSCE. MF-PIC is not very close to banded MMSE-SIC with channel estimation, because the autocorrelation matrix is also required for MF-PIC for ICI cancellation. Intuitively, the proposed OGMBMF-SIC has the same advantages as MF-SIC. With MSCE, OGMBMF-SIC can still achieve an acceptable BER performance in such a high mobility scenario ( $f_d T_{\text{OFDM}} = 0.65$ ), which makes OGMBMF-SIC more practical.

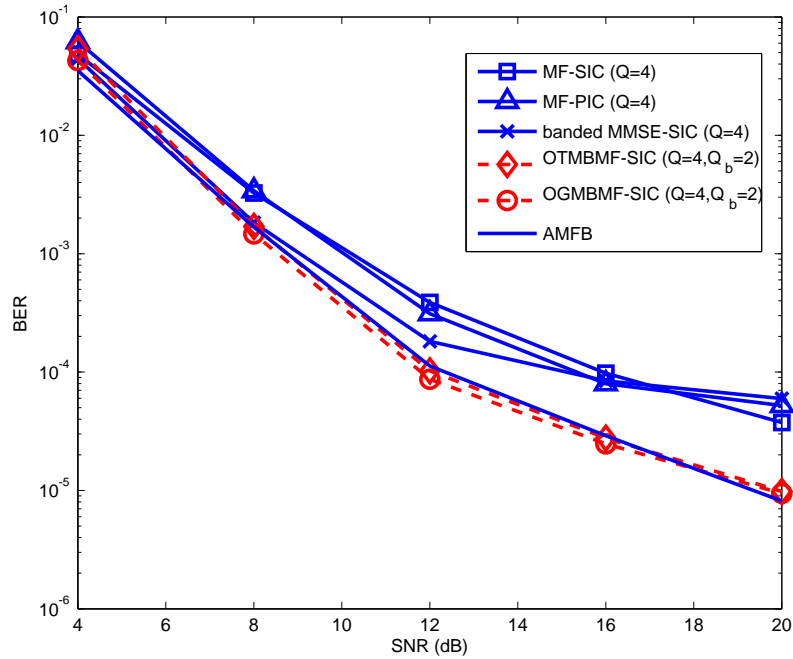


Figure 5.8: BER performance against SNR (dB) of MF-PIC, GMBMF-SIC, OGMBMF-SIC, MF-SIC, banded MMSE-SIC, and AMFB using MSCE in the 4th iteration with  $f_d T_{\text{OFDM}} = 0.65$

To show the robustness to the high normalized Doppler frequencies, we compared the SBCE, PA-LS and MSCE in terms of BER performance in the 4th iteration. In Fig 5.9, the MF-PIC and OGMBMF-SIC with SBCE cannot work at the normalized Doppler frequencies over 0.4. Additionally, the curves of MSCE is almost identical to that of PA-LS, only slightly poorer at high normalized Doppler frequencies, which implies that the MSCE performed in an iterative manner with the aid of data symbols can approach the performance of PA-LS, which uses the DKL-BEM to approximate the channels with 5

expansion coefficients.

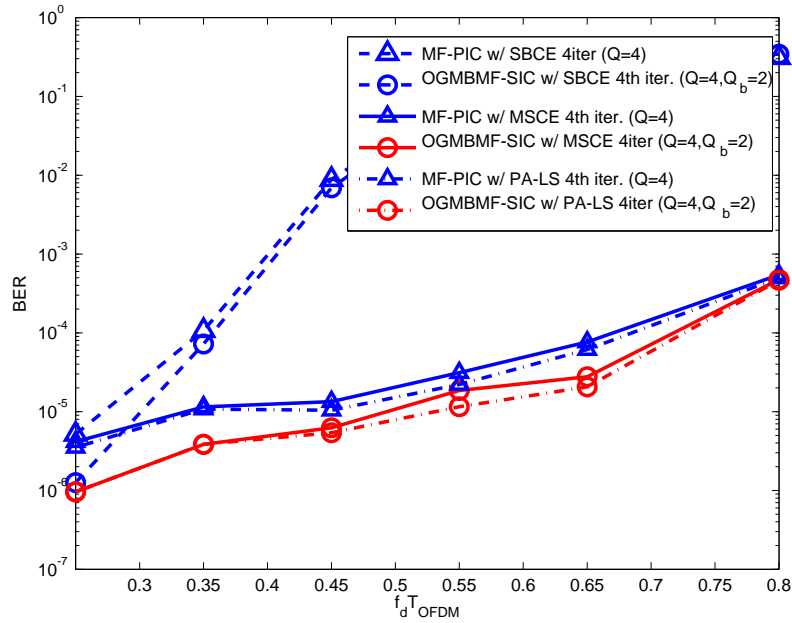


Figure 5.9: BER performance against  $f_d T_{\text{OFDM}}$  of OGMBMF-SIC and MF-PIC using MSCE and SBCE in the 4th iteration at SNR= 16 dB

To determine an appropriate number of multi-feedback candidates ( $B$ ) of MBMF-SIC for a given normalized Doppler frequency, the BER performance against the number of feedback elements has been plotted in Fig. 5.10 for OGMBMF-SIC and OTMBMF-SIC. The BER performance improves with an increasing number of feedback elements. We also observed that both of them reach the optimum BER performance around  $B = 7$  in the 4th iteration, which implies that both generation mechanisms can be considered as equivalent, if more iterations are performed by the receivers. Unlike the BER performance of OTMBMF-SIC, the BER performance of OGMBMF-SIC is poorer than that of OTMBMF-SIC in the first several iterations. This is because the feedback of OGMBMF-SIC is randomly generated given the a priori probability from the output of the channel decoder, and we assume each of them has equal probability, which may introduce instability into the LLR calculation with the increasing number of feedback elements. For OTMBMF-SIC, each feedback candidate has been weighted given the probability, so the feedback elements with low probability will not have a significant influence on the BER performance. In other words, it only takes the most significant feedback candidates into

account. Furthermore, MBMF-SIC is not equivalent to the MAP algorithm, and employs the reduced channel matrix in the multi-feedback cancellation. Thus a large  $B$  does not significantly improve the BER performance as compared to a small  $B$ .

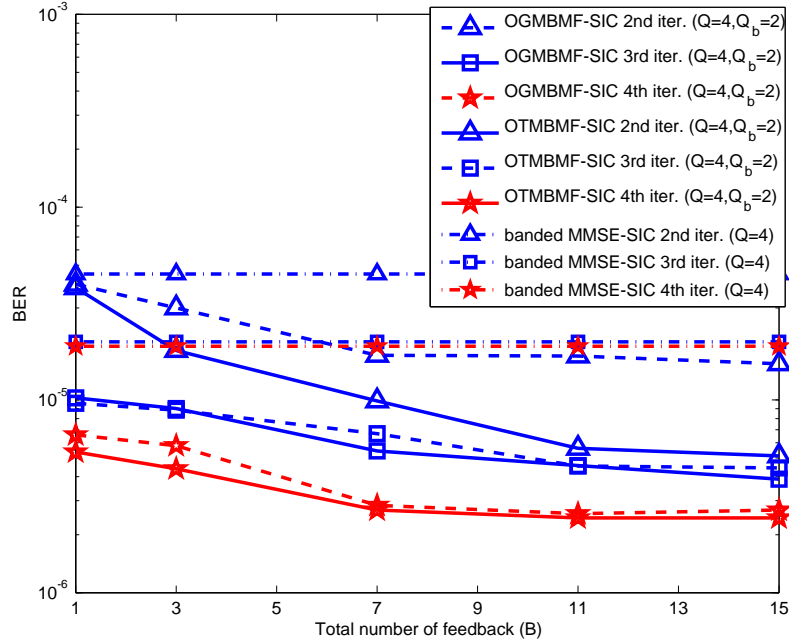


Figure 5.10: BER performance against the number of multi-feedback candidates  $B$  with  $f_d T_{\text{OFDM}} = 0.65$  at SNR= 12 dB

## 5.10 Summary

In this chapter, we have presented two low-complexity iterative receivers for coded OFDM systems. One is matched filter based parallel interference cancellation (MF-PIC), and the other is multi-feedback matched filter based sequential ICI cancellation (MBMF-SIC). For OFDM systems over the rapidly time-varying channel, the MF-PIC can be performed with low computational complexity, and achieve a satisfactory performance at the low normalized Doppler frequencies. The MBMF-SIC approximates the residual interference inside the band by multi-feedback candidates, and evaluate their log-likelihood function separately. It can be considered as an approximate MAP algo-

rithm and makes better use of a priori information from the channel decoder compared to the conventional soft ICI cancellation. Furthermore, two simple generation mechanisms for multi-feedback candidates have been investigated. The use of the reduced channel matrix for multi-feedback cancellation will not degrade the post-processing SINR significantly. Hence, the complexity of multi-feedback generation is further reduced compared to the use of the normal channel matrix. It can be found that the MBMF-SIC with SINR ordering can significantly remove the error floor induced by ICI inside the band. The simulation results demonstrate that the proposed MF-PIC can achieve a similar performance to banded MMSE-SIC and MF-SIC at low normalized Doppler frequencies, and the proposed MBMF-SIC outperforms other existing soft ICI cancellation techniques at the expense of a moderate complexity increase. With the use of MSCE, MBMF-SIC can still achieve an acceptable BER performance at high normalized Doppler frequencies. Thus MBMF-SIC provides an attractive tradeoff between the performance and complexity.

# Chapter 6

## Conclusions and Future Work

### 6.1 Conclusion

In the thesis, several channel estimation and detection techniques have been presented as follows:

1. For MIMO-OFDM system over the quasi-static channel, MIMO-OFDM can be considered as multiple parallel MIMO systems due to the diagonal channel matrix, the channels of which are highly correlated if the frequency selectivity is not very severe. In order to make better use of frequency selectivity, we have proposed dynamic pilot allocation (DPA) for MIMO-OFDM systems in Chapter 3. Firstly, the DPA algorithms, incorporating linear and SIC receivers, have been derived based on the SINR in the presence of channel estimation errors. The DPA algorithms allocate the pilots with the aid of SER estimates of different pilot patterns obtained by the SINR. Secondly, the instantaneous SER estimates of ML receivers cannot be easily obtained using the SINR. Hence, the SER estimates are approximated by the union bound instead. Using the union bound, the pilots can be assigned as similar to that of linear and SIC receivers. Thirdly, the stack vector quantization has also been discussed to reduce the overhead of the feedback link. The proposed DPA algorithms can also be used in an imperfect feedback link with delays and errors. Finally, the simulation results illustrate that the proposed DPA can significantly

improve the BER performance at the expense of MSE performance degradation. Furthermore, the pilot patterns generated by the DPA provide a higher diversity than the uniform pilot patterns.

2. In Chapter 4, two sphere decoding algorithms have been presented for MIMO detection and bound estimation. The basic principles of these two sphere decoding algorithms are very similar. To build a tree structure, the algorithms search across the tree and find the minimum Euclidean distance. The only difference between them is the system models. For MIMO detection, the complex-valued model is used. This is because the number of detection layers is only half of the real-valued system model. In the bound estimation method, we consider the real-valued model for the use of real-valued symmetric properties of the corresponding symbol vectors.

The proposed complex-valued sphere decoder for MIMO detection is an approximate detection method for MIMO systems. It incorporates the complex enumeration scheme namely computation of coordinate bound, which leads to the reduced number of candidates for each detection layer, because the constellation points outside the bound have been eliminated. In order to save the computational effort of computing coordinate bound, a successive interference cancellation is performed before the computation of coordinate bound. Thus the candidate corresponding to the minimum Euclidean distance for the current detection layer can be obtained. If the distance is smaller than the sphere radius derived by the probabilistic tree pruning, the algorithm will search down the branch. Otherwise, the search will return to the upper layer to access another branch. For iterative detection and decoding, we proposed a scatter list generation based on the proposed complex-valued sphere decoder. Hence, the list can be obtained with lower complexity compared to the conventional list generation. The idea of scatter list generation is to split the tree into different sub-trees with the aid of the ML solution obtained by the proposed complex-valued sphere decoder, so the search complexity of each sub-tree is very low. Furthermore, the ML solution can also be exploited for the branch ordering, namely ML based ordering, which inserts the symbols obtained by the ML solution in the lower detection layers. Hence, the full path metric can be derived accordingly for these remaining branches rather than the partial path metric, and these remaining branches can be ordered according to these full path metric. Therefore, the

search can first access these branches with smaller full path metric. The simulation results show that the proposed complex-valued sphere decoder and list sphere decoder can reduce the complexity with negligible BER performance loss compared to ML receivers and the conventional LSD.

A low complexity instantaneous bound estimation is proposed to obtain the union bound of ML receivers. The union bound is approximated by the minimum Euclidean distance of the receive constellation. Hence, the search can be performed similarly to the sphere decoder. We derive the initial radius for the search based on the channel statistics, and then extend the SE enumeration to the search strategy to bound the constellation points as discussed in the complex-valued sphere decoder. With the use of symmetric properties of constellation points, the number of constellation points accessed by the search is further reduced. The simulation results demonstrate that the proposed bound estimation technique can precisely find the minimum Euclidean distance, and the union bound obtained by the minimum Euclidean distance is very close to the SER performance for ML receivers obtained by simulation.

3. In Chapter 5, We have proposed two low complexity iterative ICI cancellation algorithms (MF-PIC and MBMF-SIC) for coded OFDM systems. The MF-PIC uses the output of matched filter, and then mitigates the ICI inside the band in a parallel form. The MBMF-SIC employs multi-feedback candidates to remove the residual interference inside the band in a serial form. The multi-feedback candidates can be generated based on Gibbs sampler or tree search algorithm with negligible complexity. Furthermore, the size of channel matrix used in the multi-feedback cancellation can be reduced with an acceptable post-processing SINR performance loss. In other words, the size of multi-feedback candidates does not affect the BER performance significantly. Additionally, we also propose multi-segmental channel estimation (MSCE) technique to estimate the time-varying channel several times rather than once in one OFDM symbol period. One can interpolate the time-varying channels with the channel estimates obtained by MSCE. Hence, the interpolated channels are estimated more accurate than that with single burst channel estimator, which estimates the time-varying channel once. The simulation results demonstrate that the BER performance of MF-PIC is close to that of the banded MMSE-SIC at the low normalized Doppler frequencies, and outperform the MF-SIC. On the other

hand, the MBMF-SIC can approach the BER performance of AMFB in a wide range of normalized Doppler frequencies. With the use of MSCE, the operational normalized Doppler frequencies can be extended compared to that with the single burst channel estimation. Furthermore, the proposed MBMF-SIC is less sensitive to the channel estimation errors, because no autocorrelation matrix calculation is required. Hence, the proposed MF-PIC is a good candidate to work at low normalized Doppler frequencies, and the MBMF-SIC provides excellent BER performance and manageable complexity for coded OFDM systems over rapidly time-varying channels.

## 6.2 Future Work

Some suggestions for future work based on this thesis are given below:

1. We have investigated dynamic pilot allocation for MIMO-OFDM systems with a small number of subcarriers. However, the complexity of searching the optimum pilot pattern for the large number of subcarriers is still very high. A lower complexity method is also required for WiMAX, LTE and LTE-A, which have hundreds of subcarriers in OFDM systems. Besides, the multi-user MIMO-OFDM systems have not been taken into account. This is because the channel estimation is more complicated. It is worth to study further on dynamic pilot allocation with other channel estimation techniques.
2. The enumeration schemes for complex sphere decoder are too complicate for the MIMO systems with a large number of transmit and receive antennas. It is useful to investigate enumeration schemes in complex plane and reduce the number of candidates found by the scheme at low SNR. Like the complex sphere decoder, the bound estimation for large MIMO systems is still a problem, which can be sorted out by reducing the search complexity as the sphere decoders do. However, it is valuable to avoid the search like the sphere decoders for large MIMO systems, and find the bound by a simple calculation.
3. Multi-segmental channel estimator estimates the time-varying channels twice,

which is sufficient for the simulation settings we use. However, it may not be sufficient for systems working at higher normalized Doppler frequencies. If the number of segments obtained by splitting the OFDM symbol is increasing, the noise will be enhanced for the channel estimation due to the less signal power left for each segment. It is useful to justify the maximum number of segments in one OFDM symbol. Additionally, the MF-PIC and the MBMF-SIC can be extended to MIMO-OFDM systems over rapidly time-varying channels. But the banded channel matrix for MIMO-OFDM may not exist. It is important to justify the multi-feedback cancellation with more interference from other transmit antennas or other users.

# Glossary

AC	<b>A</b> dditional <b>C</b> onditions
AMFB	<b>A</b> pproximate <b>M</b> atched <b>F</b> ilter <b>B</b> ound
AWGN	<b>A</b> dditional <b>W</b> hite <b>G</b> aussian <b>N</b> oise
BEM	<b>B</b> asis- <b>E</b> xpansion- <b>M</b> odel
BER	<b>B</b> it- <b>E</b> rror- <b>R</b> ate
BFS	<b>B</b> readth- <b>F</b> irst <b>S</b> earch
BLAST	<b>B</b> ell <b>L</b> Ab <b>S</b> pace <b>T</b> ime
BPSK	<b>B</b> inary <b>P</b> hase <b>S</b> hift <b>K</b> eying
CAs	<b>C</b> omplex <b>A</b> dditions
CCB	<b>C</b> omputation of <b>C</b> oordinate <b>B</b> ound
CDF	<b>C</b> umulative <b>D</b> istribution <b>F</b> unction
CDMA	<b>C</b> ode <b>D</b> ivision <b>M</b> ultiple <b>A</b> ccess
CSI	<b>C</b> hannel <b>S</b> tate <b>I</b> nformation
CMs	<b>C</b> omplex <b>M</b> ultiplications
CP	<b>C</b> yclic <b>P</b> refix
CSD	<b>C</b> omplex <b>S</b> phere <b>D</b> ecoder
dB	<b>D</b> ecibel
DF	<b>D</b> ecision <b>F</b> eedback
DF	<b>D</b> epth- <b>F</b> irst <b>S</b> earch
DFE	<b>D</b> ecision <b>F</b> eedback <b>E</b> qualizer
DFT	<b>D</b> iscrete <b>F</b> ourier <b>T</b> ransform
DKL	<b>D</b> iscrete <b>K</b> arhuen- <b>L</b> oève
DPA	<b>D</b> ynamic <b>P</b> ilot <b>A</b> llocation
DVB	<b>D</b> igital <b>V</b> ideo <b>B</b> roadcasting
EXIT	<b>E</b> Xtrinsic <b>I</b> nformation <b>T</b> ransfer
FFT	<b>F</b> ast <b>F</b> ourier <b>T</b> ransform
FLOPS	<b>F</b> loating point <b>O</b> peration <b>S</b>
FPM	<b>F</b> ull <b>P</b> ath <b>M</b> etric
GSG	<b>G</b> ibbs <b>S</b> ampling <b>G</b> eneration
Hz	<b>H</b> ertz

---

IAI	<b>I</b> nter <b>A</b> ntenna <b>I</b> nterference
ICI	<b>I</b> nter- <b>C</b> arrier <b>I</b> nterference
IDD	<b>I</b> terative <b>D</b> etection and <b>D</b> ecoding
IFFT	<b>I</b> nverse <b>F</b> ast <b>F</b> ourier <b>T</b> ransform
ISI	<b>I</b> nter- <b>S</b> ymbol <b>I</b> nterference
KBFS	<b>K</b> <b>B</b> est <b>F</b> irst <b>S</b> earch
LBA	<b>L</b> ower <b>B</b> ound <b>A</b> pproximation
LLR	<b>L</b> og- <b>L</b> ikelihood <b>R</b> atio
LS	<b>L</b> east <b>S</b> quares
LSD	<b>L</b> ist <b>S</b> phere <b>D</b> ecoder
LTE	<b>L</b> ong <b>T</b> erm <b>E</b> volution
MAP	<b>M</b> aximum <b>A</b> <b>P</b> osteriori probability
MBMF	<b>M</b> ulti-feed <b>B</b> ack <b>M</b> atched <b>F</b> ilter
MED	<b>M</b> inimum <b>E</b> uclidean <b>D</b> istance
MF	<b>M</b> atched <b>F</b> ilter
MIMO	<b>M</b> ultiple- <b>I</b> nput <b>M</b> ultiple- <b>O</b> utput
MISO	<b>M</b> ultiple- <b>I</b> nput <b>S</b> ingle- <b>O</b> utput
MIPS	<b>M</b> IMO <b>I</b> terative <b>P</b> ilot <b>S</b> earch
ML	<b>M</b> aximum <b>L</b> ikelihood
MPTP	<b>M</b> odified <b>P</b> robabilistic <b>T</b> ree <b>P</b> runing
MSCE	<b>M</b> ulti- <b>S</b> egmental <b>C</b> hannel <b>E</b> stimation
MMSE	<b>M</b> inimum <b>M</b> ean <b>S</b> quare <b>E</b> rror
MSE	<b>M</b> ean <b>S</b> quare <b>E</b> rror
NC	<b>N</b> ulling <b>C</b> ancelling
NP	<b>N</b> on-deterministic <b>P</b> olynomial-time
NSC	<b>N</b> on- <b>S</b> ystematic <b>C</b> onvolutional
OFDM	<b>O</b> rthogonal <b>F</b> requency <b>D</b> ivision <b>M</b> ultiplexing
OSIC	<b>O</b> rdered <b>S</b> IC
PA	<b>P</b> ilot <b>A</b> ssisted
PACE	<b>P</b> ilot-symbol- <b>A</b> ided <b>C</b> hannel <b>E</b> stimation
PDF	<b>P</b> robability <b>D</b> ensity <b>F</b> unction
PFFT	<b>P</b> artial <b>F</b> ast <b>F</b> ourier <b>T</b> ransform
PIC	<b>P</b> arallel <b>I</b> nterference <b>C</b> ancellation

---

---

PPM	<b>P</b> artial <b>P</b> ath <b>M</b> etric
PSK	<b>P</b> hase- <b>S</b> hift <b>K</b> eying
P/S	<b>P</b> arallel to <b>S</b> erial
QAM	<b>Q</b> uadrature <b>A</b> mplitude <b>M</b> odulation
RMSE	<b>R</b> oot <b>M</b> ean <b>S</b> quare <b>E</b> rror
S/P	<b>S</b> erial to <b>P</b> arallel
SBCE	<b>S</b> ingle <b>B</b> urst <b>C</b> hannel <b>E</b> stimation
SER	<b>S</b> ymbol <b>E</b> rror <b>R</b> ate
SC	<b>S</b> oft <b>C</b> ancellation
SD	<b>S</b> phere <b>D</b> ecoder
SE	<b>S</b> chnorr and <b>E</b> uchner
SIC	<b>S</b> uccessive <b>I</b> nterference <b>C</b> ancellation
SINR	<b>S</b> ignal to <b>I</b> nterference plus <b>N</b> oise <b>R</b> atio
SIR	<b>S</b> ignal to <b>I</b> nterference <b>R</b> atio
SISO	<b>S</b> oft- <b>I</b> nput <b>S</b> oft- <b>O</b> utput
SISO	<b>S</b> ingle- <b>I</b> nput <b>S</b> ingle- <b>O</b> utput
SNR	<b>S</b> ignal to <b>N</b> oise <b>R</b> atio
SPS	<b>S</b> tatistical <b>P</b> runing <b>S</b> trategy
SQRD	<b>S</b> orted <b>Q</b> R <b>D</b> ecomposition
STBC	<b>S</b> pace- <b>T</b> ime <b>B</b> lock <b>C</b> ode
SFBC	<b>S</b> pace- <b>F</b> requency <b>B</b> lock <b>C</b> ode
STC	<b>S</b> pace- <b>T</b> ime <b>C</b> oding
SVD	<b>S</b> ingular <b>V</b> alue <b>D</b> ecomposition
SVQ	<b>S</b> tacked <b>V</b> ector <b>Q</b> uantization
TSG	<b>T</b> ree <b>S</b> earch <b>G</b> eneration
UPA	<b>U</b> niform <b>P</b> ilot <b>A</b> llocation
USVQ	<b>U</b> nstacked <b>V</b> ector <b>Q</b> uantization
WiMAX	<b>W</b> orldwide <b>i</b> nteroperability for <b>M</b> icrowave <b>A</b> ccess
ZF	<b>Z</b> ero <b>F</b> orcing

# Bibliography

- [1] A. Goldsmith, *Wireless Communications*. New York, NY: Cambridge, 2005.
- [2] “IEEE standard for local and metropolitan area networks part 16: Air interface for broadband wireless access systems amendment 3: Advanced air interface,” IEEE Std 802.16m-2011 (Amendment to IEEE Std 802.16-2009), Tech. Rep., May 5 2011.
- [3] “Requirements for further advancement for evolved universal terrestrial radio access (E-UTRA) (LTE-Advanced),” 3GPP, Tech. Rep., 2008.
- [4] E. Telatar, “Capacity of multi-antenna Gaussian channels,” *Europe Trans. Telecomm.*, vol. 10, no. 6, pp. 585–595, Nov. - Dec. 1999.
- [5] G. J. Foschini, “Layered space-time architecture for wireless communication in a fading environment when using multiple antennas,” *Bell Labs Technical Journal*, vol. 1, no. 2, pp. 41–59, 1996.
- [6] P. W. Wolniansky, G. J. Foschini, G. D. Golden, and R. A. Valenzuela, “V-BLAST: an architecture for realizing very high data rates over the rich-scattering wireless channel,” in *URSI ISSSE’98*, Pisa, Italy, Oct. 1998, pp. 295–300.
- [7] V. Tarokh, N. Seshadri, and A. R. Calderbank, “Space-time codes for high data rate wireless communication: performance criterion and code construction,” *IEEE Trans. Inf. Theory*, vol. 44, no. 2, pp. 744–765, Mar. 1998.
- [8] S. M. Alamouti, “A simple transmit diversity technique for wireless communications,” *IEEE J. Sel. Areas Commun.*, vol. 16, no. 8, pp. 1451–1458, Oct. 1998.
- [9] S. Sanhdu and A. Paulraj, “Space-time block codes: a capacity perspective,” *IEEE Commun. Letters*, vol. 4, no. 12, pp. 384–386, Dec. 2000.

- [10] L. Zheng and D. N. C. Tse, "Diversity and multiplexing: A fundamental tradeoff in multiple-antenna channels," *IEEE Trans. Inf. Theory*, vol. 49, no. 5, pp. 1073–1096, Aug. 2003.
- [11] V. Tarokh, H. Jafarkhani, and A. R. Calderbank, "Space-time block coding for wireless communications: performance results," *IEEE J. Sel. Areas Commun.*, vol. 17, no. 3, pp. 451–460, Mar. 1999.
- [12] V. Tarokh, A. Naguib, N. Seshadri, and A. R. Calderbank, "Combined array processing and space-time coding," *IEEE Trans. Inf. Theory*, vol. 45, no. 4, pp. 1121–1128, May. 1999.
- [13] Z. Chen, J. Yuan, and B. Vucetic, "Improved space-time trellis coded modulation scheme on slow Rayleigh fading channels," *IEE Electron. Lett.*, vol. 37, no. 7, pp. 440–442, Mar. 2001.
- [14] W. Firmanto, B. Vucetic, and J. Yuan, "Space-time TCM with improved performance on fast fading channels," *IEEE Commun. Lett.*, vol. 5, no. 4, pp. 154–156, Apr. 2001.
- [15] H. Zhang, H. Dai, and B. L. Hughes, "On the diversity-multiplexing tradeoff for ordered SIC receivers over MIMO channels," in *Proc. IEEE Int. Conf. on Commun. (ICC) 2006*, Istanbul, Turkey, Jun. 2006.
- [16] N. Prasad and M. K. Varanasi, "Analysis of decision feedback detection for MIMO Rayleigh channels and optimization of power and rate allocations," *IEEE Trans. Inf. Theory*, vol. 50, no. 6, pp. 1009–1025, Jun. 2004.
- [17] C. P. Schnorr and M. Euchner, "Lattice basis reduction: Improved practical algorithms and solving subset sum problems," *Math. Program.*, vol. 66, pp. 181–191, 1994.
- [18] E. Viterbo and J. Boutros, "A universal lattice code decoder for fading channels," *IEEE Trans. Inf. Theory*, vol. 45, no. 1639-1642, p. 45, Jul. 1999.
- [19] E. Agrell, T. Eriksson, A. Vardy, and K. Zegar, "Closest point search in lattices," *IEEE Trans. Inf. Theory*, vol. 48, pp. 2201–2214, Aug. 2002.

- [20] L. Li, R. C. de Lamare, and A. G. Burr, "Complex sphere decoding with a modified tree pruning and successive interference cancellation," in *Proc. Int. Symp. on Wireless Commun. Syst. (ISWCS) 2012*, Paris, France, Aug. 2012.
- [21] B. Hassibi and H. Vikalo, "On the sphere-decoding algorithm I. Expected complexity," *IEEE Trans. Signal Process.*, vol. 53, pp. 2806–2818, Aug. 2005.
- [22] X. Zhu and R. D. Murch, "Performance analysis of maximum likelihood detection in a MIMO antenna system," *IEEE Trans. Commun.*, vol. 50, no. 2, pp. 187–191, Feb. 2002.
- [23] C. Berrou, A. Glavieux, and P. Thitimajshima, "Near shannon limit error-correcting coding and decoding: Turbo-codes. 1," in *IEEE Int. Conf. on Commun. (ICC) 1993*, Geneva, May 1993.
- [24] J. Hagenauer, E. Offer, and L. Papke, "Iterative decoding of binary and block convolutional codes," *IEEE Trans. Inf. Theory*, vol. 42, pp. 429–445, Mar. 1996.
- [25] S. ten Brink, J. Speidel, and R. Yan, "Iterative demapping and decoding for multi-level modulation," in *Proc. GLOBECOM 1998*, Nov. 1998, pp. 579–584.
- [26] X. Li and J. A. Ritcey, "Bit-interleaved coded modulation with iterative decoding," in *Proc. Int. Conf. on Commun. (ICC) 1999*, Jun. 1999, pp. 858–862.
- [27] J. Hagenauer, "The turbo principle: tutorial introduction and state of the art," in *Proc. 1st Int. Symp. Turbo Codes*, Sept. 1997, pp. 1–12.
- [28] B. Hochwald and S. ten Brink, "Achieving near-capacity on a multiple-antenna channel," *IEEE Trans. Commun.*, vol. 51, pp. 389–399, Mar. 2003.
- [29] "Digital Video Broadcasting (DVB): Framing structure, channel coding and modulation for digital terrestrial television," ETSI, Tech. Rep., 2004.
- [30] "Digital Video Broadcasting (DVB): Framing structure, channel coding and modulation for digital terrestrial television (DVB-T)," ETSI, Tech. Rep., 2009.
- [31] R. Chang and R. Gibby, "A theoretical study of performance of an orthogonal multiplexing data transmission scheme," *IEEE Trans. Commun.*, vol. COM-16, pp. 529–540, Aug. 1968.

- [32] S. Weinstein and P. Ebert, "Data transmission by frequency-division multiplexing using discrete Fourier transform," *IEEE Trans. Commun.*, vol. COM-19, pp. 628–634, Oct. 1971.
- [33] J. A. C. Bingham, "Multicarrier modulation for data transmission: An idea whose time has come," *IEEE Commun. Mag.*, vol. 28, no. 5, pp. 5–14, May 1990.
- [34] Y. Li, J. H. Winters, and N. R. Sollenberger, "MIMO-OFDM for wireless communications: signal detection with enhanced channel estimation," *IEEE Trans. Commun.*, vol. 50, no. 9, pp. 1471–1476, Sep. 2002.
- [35] M. Engels, *Wireless OFDM Systems: How To Make Them Work*. Kluwer Academic Publisher, 2002.
- [36] A. Peled and A. Ruiz, "Frequency domain data transmission using reduced computational complexity algorithms," in *in Proc. IEEE Int. Conf. Acoust., Speech, Signal Process. (ICASSP) 1980*, Denver, CO, 1980, pp. 964–967.
- [37] Y. Li, J. Cimini, and N. R. Sollenberger, "Robust channel estimation for OFDM systems with rapid dispersive fading channels," *IEEE Trans. Commun.*, vol. 46, no. 7, pp. 902–915, Jul. 1998.
- [38] T. Himsoon, W. Su, and K. J. R. Liu, "Single-block differential transmit scheme for broadband wireless MIMO-OFDM systems," *IEEE Trans. Signal Process.*, vol. 54, no. 9, pp. 3305–3314, Sep. 2006.
- [39] S. Coleri, M. Ergen, and A. Puri, "Channel estimation techniques based on pilot arrangement in OFDM systems," *IEEE Trans. Broadcast.*, vol. 48, no. 3, pp. 223–229, Sep. 2002.
- [40] J. K. Cavers, "An analysis of pilot-symbol-assisted modulation for Rayleigh fading channels," *IEEE Trans. Veh. Technol.*, vol. 40, no. 4, pp. 686–693, Nov. 1991.
- [41] O. Edfors, M. Sandell, J. van de Beek, S. K. Wilson, and P. O. Börjesson, "OFDM channel estimation by singular value decomposition," *IEEE Trans. Commun.*, vol. 46, no. 7, pp. 931–939, Jul. 1998.
- [42] D. Schafhuber, G. Matz, and F. Hlawatsch, "Adaptive Wiener filters for time-varying channel estimation in wireless OFDM systems," in *in Proc. IEEE Int. Conf.*

- Acoust., Speech, and Signal Process. (ICASSP) 2003*, vol. 4, Hong Kong, China, Apr. 2003, pp. 688–691.
- [43] P. J. Sartori, K. L. Baum, and F. W. Vook, “Impact of spatial correlation on the spectral efficiency of wireless OFDM systems using multiple antenna techniques,” in *in Proc. IEEE Veh. Technol. Conf. (VTC) 2002*, vol. 3, Birmingham, AL, US, May 2002, pp. 1150–54.
- [44] R. Chen and K. B. Letaief, “Channel estimation for space-time coded OFDM systems in non-sample-spaced multipath channels,” in *Proc. IEEE Wireless Commun. and Netw. Conf. (WCNC) 2002*, vol. 1, Orlando, FL, US, Mar. 2002, pp. 61–66.
- [45] H. Minn, D. I. Kim, and V. K. Bhargava, “A reduced complexity channel estimation for OFDM systems with transmit diversity in mobile wireless channels,” *IEEE Trans. Commun.*, vol. 50, no. 5, pp. 799–807, May 2002.
- [46] Y. Li, N. Seshadri, and S. Ariyavisitakul, “Channel estimation for OFDM systems with transmitter diversity in mobile wireless channels,” *IEEE J. Sel. Areas Commun.*, vol. 17, no. 3, pp. 461–471, Mar. 1999.
- [47] Y. Li, “Simplified channel estimation for OFDM systems with multiple transmit antennas,” *IEEE Trans. Wireless Commun.*, Jan. 2002.
- [48] A. Dowler, A. Doufexi, and A. Nix, “Performance evaluation of channel estimation techniques for a mobile fourth generation wide area OFDM systems,” in *in Proc. IEEE Veh. Technol. Conf. (VTC) 2002*, vol. 4, Vancouver, Canada, Sep. 2002, pp. 2036–2040.
- [49] M. X. Chang, “A new derivation of least-squares-fitting principle for OFDM channel estimation,” *IEEE Trans. Wireless Commun.*, vol. 5, no. 4, pp. 726–731, Apr. 2006.
- [50] M. Morelli and U. Mengali, “A comparison of pilot-aided channel estimation methods for OFDM systems,” *IEEE Trans. Signal Process.*, vol. 49, no. 12, pp. 3065–3073, Dec. 2001.
- [51] R. Negi and J. Cioffi, “Pilot tone selection for channel estimation in a mobile OFDM system,” *IEEE Trans. Consum. Electron.*, vol. 44, no. 3, pp. 1122–1128, Aug. 1998.

- [52] A. Y. Panah, R. G. Vaughan, and J. R. W. Heath, "Optimizing pilot locations using feedback in OFDM systems," *IEEE Trans. Veh. Technol.*, vol. 58, no. 6, pp. 2803–2814, Jul. 2009.
- [53] R. B. Moraes and R. Sampaio-Neto, "BER minimizing pilot symbol arrangement in closed-loop OFDM systems," *IET Commun.*, vol. 5, pp. 1999–2008, 2011.
- [54] L. Li, R. C. de Lamare, and A. G. Burr, "Low complexity dynamic pilot allocation for channel estimation in MIMO-OFDM systems with spatial multiplexing," in *Proc. European Wireless (EW) 2011*, Vienna, Austria, Apr. 2011.
- [55] ———, "Dynamic pilot allocation for channel estimation in MIMO-OFDM systems with spatial multiplexing," in *in Proc. Veh. Technol. Conf. (VTC) 2011 spring*, Budapest, Hungary, May. 2011.
- [56] P. Schniter, "Low-complexity equalization of OFDM in doubly selective channels," *IEEE Trans. Signal Process.*, vol. 52, no. 4, pp. 1002–1011, Apr. 2004.
- [57] L. Rugini, P. Banelli, and G. Leus, "Low-complexity banded equalizer for OFDM systems in Doppler spread channels," *EURASIP J. Adv. Signal Process.*, vol. 2006, no. 067404, pp. 1–13, Aug. 2006.
- [58] S. Yerramalli, M. Stojanovic, and U. Mitra, "Partial FFT demodulation: a detection method for highly Doppler distorted OFDM systems," *IEEE Trans. Signal Process.*, vol. 60, no. 11, pp. 5906–5918, Nov. 2012.
- [59] P. Baracca, S. Tomasin, L. Vangelist, N. Benvenuto, and A. Morello, "Per sub-block equalization of very long OFDM blocks in mobile communications," *IEEE Trans. Comm.*, vol. 59, no. 2, pp. 363–368, Feb. 2011.
- [60] S. Tomasin, A. Gorokhov, H. Yang, and J.-P. Linnartz, "Iterative interference cancellation and channel estimation for mobile OFDM," *IEEE Trans. Wireless Comm.*, vol. 4, no. 1, pp. 238–245, Jan. 2005.
- [61] S. U. Hwang, J. H. Lee, and J. Seo, "Low-complexity iterative ICI cancellation and equalization for OFDM systems over doubly selective channels," *IEEE Trans. Broadcast.*, vol. 55, no. 1, pp. 132–139, Mar. 2009.

- [62] V. Namboodiri, H. Liu, and P. Spasojević, “Low-complexity iterative receiver design for mobile OFDM systems,” *EURASIP J. Adv. in Signal Process.*, vol. 2012, no. 166, Aug. 2012.
- [63] G. Tauböck, M. Hampejs, P. Švač, G. Matz, F. Hlawatsch, and K. Gröchenig, “Low-complexity ICI/ISI equalization in doubly dispersive multicarrier systems using a decision-feedback LSQR algorithm,” *IEEE Trans. Signal Process.*, vol. 59, no. 5, pp. 2432–2436, May 2011.
- [64] R. C. de Lamare and R. Sampaio-Neto, “Minimum mean square error iterative successive parallel arbitrated decision feedback detectors for DS-CDMA systems,” *IEEE Trans. Commun.*, vol. 56, pp. 778–789, May 2008.
- [65] J. W. Choi, A. C. Singer, J. Lee, and N. I. Cho, “Improved linear soft-input soft-output detection via soft feedback successive interference cancellation,” *IEEE Trans. Comm.*, vol. 58, pp. 986–996, Mar. 2010.
- [66] E. Panayircı, H. Dogan, and H. V. Poor, “Low-complexity MAP-based successive data detection for coded OFDM systems over highly mobile wireless channels,” *IEEE Trans. Veh. Technol.*, vol. 60, no. 6, pp. 2849–2857, Jul. 2011.
- [67] W. C. Jakes, *Mobile Microwave Communication*. New York: Wiley, 1973.
- [68] R. H. Clarke, “A statistical theory of mobile-radio reception,” *Bell Syst. Tech. J.*, pp. 957–1000, July 1968.
- [69] P. Dent, G. E. Bottomley, and T. Croft, “Jakes fading model revisited,” *Electron. Lett.*, vol. 29, no. 13, pp. 1162–1163, Jun. 1993.
- [70] M. F. Pop and N. C. Beaulieu, “Limitations of sum-of-sinusoids fading channel simulators,” *IEEE Trans. Commun.*, vol. 49, no. 4, pp. 699–708, Apr. 2001.
- [71] Y. Li and X. Huang, “The simulation of independent Rayleigh faders,” *IEEE Trans. Commun.*, vol. 50, no. 9, pp. 1503–1514, Sept. 2002.
- [72] Y. Zheng and C. Xiao, “Simulation models with correct statistical properties for Rayleigh fading channels,” *IEEE Trans. Commun.*, vol. 51, pp. 920–928, Jun. 2003.

- [73] C. Xiao, Y. Zhang, and N. C. Beaulieu, "Second-order statistical properties of the WSS Jakes' fading channel simulator," *IEEE Trans. Commun.*, vol. 50, no. 6, pp. 888–891, Jun. 2002.
- [74] B. Muquet, Z. Wang, G. B. Giannakis, and M. de Courville *et al.*, "Cyclic prefixing or zero padding for wireless multicarrier transmissions," *IEEE Commun. Mag.*, vol. 50, no. 12, pp. 2136–2148, Dec. 2002.
- [75] M. Hsieh and C. Wei, "Channel estimation for ofdm systems based on comb-type pilot arrangement in frequency selective fading channels," *IEEE Trans. Consum. Electron.*, vol. 44, no. 1, pp. 217–228, Feb. 1998.
- [76] J. Heiskala and J. Terry, *OFDM Wireless LANs: A Theoretical and Practical Guide*. SAMS, 2002.
- [77] R. van Nee and R. Prasad, *OFDM for Wireless Multimedia Communications*. Artech House Publishers, 2000.
- [78] S. Kay, *Fundamentals of Statistical Signal Processing: Estimation Theory*. Upper Saddle River NJ: Prentice-Hall, 1993.
- [79] S. O. Haykin, *Adaptive Filter Theory*. Prentice-Hall 4th ed., 1993.
- [80] L. J. Cimini, "Analysis of simulation of a digital mobile channel using orthogonal frequency division multiplexing," *IEEE Trans. Commun.*, vol. 30, pp. 665–675, Jul. 2000.
- [81] Y. Li, J. Cimini, and N. R. Sollenberger, "Optimal training and pilot design for OFDM systems in Rayleigh fading," *IEEE Trans. Broadcast.*, vol. 52, no. 4, pp. 505–514, Dec. 2006.
- [82] J. J. Ran, R. Grunbeid, and H. R. *et al.*, "Decision-directed channel estimation method for OFDM systems with high velocities," in *in Proc. IEEE Veh. Technol. Conf. (VTC) 2003 spring*, vol. 4, Jeju, South Korea, Apr. 2003, pp. 2358–2361.
- [83] A. Y. Panah, B. Nosrat-Makouei, and R. G. Vaughan, "Non-uniform pilot-symbol allocation for closed-loop OFDM," *IEEE Trans. Wireless Commun.*, vol. 7, no. 7, pp. 2723–2731, Jul. 2008.

- [84] H. Minn and N. Al-Dhahir, "Optimal training signals for MIMO OFDM channel estimation," *IEEE Trans. Wireless Commun.*, vol. 5, no. 5, pp. 1158–1168, May 2006.
- [85] T.-L. Tuang, K. Yao, and R. E. Hudson, "Channel estimation and adaptive power allocation for performance and capacity improvement of multiple-antenna OFDM systems," in *Proc. IEEE Workshop on Signal Process. Adv. (SPAWC) 2001*, Taiwan, ROC, Mar. 2001, pp. 82–85.
- [86] I. Barhumi, G. Leus, and M. Moonen, "Optimal training design for MIMO OFDM systems in mobile wireless channel," *IEEE Trans. Signal Process.*, vol. 51, no. 6, pp. 1615–1624, Jun. 2003.
- [87] X. Wang and H. V. Poor, "Iterative (turbo) soft interference cancellation and decoding for coded CDMA," *IEEE Trans. Commun.*, vol. 47, no. 7, pp. 1046–1061, Jul. 1999.
- [88] M. Chiani, "Introducing erasures in decision-feedback equalization to reduce error propagation," *IEEE Trans. Commun.*, vol. 45, no. 7, pp. 757–760, Jul. 1997.
- [89] M. Reuter, J. C. Allen, J. R. Zeidler, and R. C. North, "Mitigating error propagation effects in a decision feedback equalizer," *IEEE Trans. Commun.*, vol. 49, no. 11, pp. 2028–2041, Nov. 2001.
- [90] S. Verdú, "Minimum probability of error for asynchronous Gaussian multiple-access channels," *IEEE Trans. Inf. Theory*, vol. 32, no. 1, pp. 85–96, Jan. 1986.
- [91] A. D. Murugan, H. E. Gamal, M. O. Damen, and G. Caire, "A unified framework for tree search decoding: rediscovering the sequential decoder," *IEEE Trans. Inf. Theory*, vol. 52, no. 3, pp. 933–953, Mar. 2006.
- [92] U. Fincke and M. Phost, "Improved methods for calculating vectors of short length in a lattice, including a complexity analysis," *Math. Comp.*, vol. 44, pp. 463–471, 1985.
- [93] T. M. Aulin, "Breadth-first maximum likelihood sequence detection: basics," *IEEE Trans. Commun.*, vol. 47, pp. 208–216, Feb. 1999.

- [94] L. G. Barbero and J. S. Thompson, "Fixing the complexity of the sphere decoder for mimo detection," *IEEE Trans. Wireless Commun.*, vol. 7, no. 6, pp. 2131–2142, Jun. 2008.
- [95] P. Li and R. C. de Lamare, "Multiple feedback successive interference cancellation detection for multiuser MIMO systems," *IEEE Trans. Wireless Commun.*, vol. 10, no. 8, pp. 2434–2439, Aug. 2011.
- [96] R. Dechter and J. Pearl, "Generalized best-first search strategies and the optimality of  $A^*$ ," *J. of ACM*, vol. 32, no. 3, pp. 505–536, Jan. 1985.
- [97] D. Seethaler, H. Artés, and F. Hlawatsch, "Dynamic nulling-and-cancelling for efficient near-ML decoding of MIMO systems," *IEEE. Trans. Signal Process.*, vol. 54, no. 12, pp. 4741–4752, Dec. 2006.
- [98] S. W. Kim and K. P. Kim, "Log-likelihood-ratio-based detection ordering in V-BLAST," *IEEE. Trans. Commun.*, vol. 54, no. 2, pp. 302–307, Feb. 2006.
- [99] A. Burg, M. Borgmann, M. Wenk, C. Studer, and H. Bölcskei, "Advanced receiver algorithms for MIMO wireless communications," in *Proc. of DATE*, vol. 1, Munich, Germany, Mar. 2006.
- [100] D. Wübben, J. Rinas, R. Böhnke, V. Kühn, and K. D. Kammeyer, "Efficient algorithm for detecting layered space-time codes," in *Proc. ITG Conference on Source and Channel Coding*, Berlin, Germany, Jan. 2002.
- [101] M. O. Damen, H. E. Gamal, and G. Caire, "On maximum-likelihood detection and the search for the closest lattice point," *IEEE Trans. Inf. Theory*, vol. 49, pp. 2389–2402, Oct. 2003.
- [102] D. Pham, K. R. Pattipati, P. K. Willett, and J. Luo, "An improved complex sphere decoder for V-BLAST systems," *IEEE Signal Process. Lett.*, vol. 11, pp. 748–751, Sep. 2004.
- [103] C. Studer, "Iterative MIMO decoding: Algorithms and VLSI implementation aspects," Ph.D. dissertation, Hartung-Gorre Verlag Konstanz, 2009.
- [104] M. Tüchler, A. C. Singer, and R. Kötter, "Minimum mean squared error equalization using a priori information," *IEEE. Trans. Signal Process.*, vol. 50, no. 3, pp. 673–683, 2002.

- [105] E. Zimmermann, D. L. Milliner, J. R. Barry, and G. Fettweis, "Optimal LLR clipping levels for mixed hard/soft output detection," in *Proc. IEEE GLOBECOM 2008*, New Orleans, LO, U.S., Nov. 2008, pp. 1–5.
- [106] R. H. Gohary and T. J. Willink, "On LLR clipping in BICM-ID non-coherent MIMO communications," *IEEE Commun. Lett.*, vol. 15, no. 6, pp. 650–652, Jun. 2011.
- [107] S. ten Brink, "Convergence behavior of iteratively decoded parallel concatenated codes," *IEEE Trans. Commun.*, vol. 49, no. 10, pp. 1727–1737, Oct. 2004.
- [108] J. Hagenauer, "The EXIT chart-Introduction to extrinsic information transfer in iterative processing," in *Proc. European Signal Process. Conf.*, Vienna, Austria, Sep. 2004, pp. 1541–1548.
- [109] S. ten Brink, G. Kramer, and A. Ashikhmin, "Design of low-density parity-check codes for modulation and detection," *IEEE Trans. Commun.*, vol. 52, no. 4, pp. 670–678, Apr. 2004.
- [110] Y. Wang, P. Li, L. Li, A. G. Burr, and R. C. de Lamare, "Irregular code-aided low-complexity three-stage turbo space time processing," in *IEEE Int. Symp. on Wireless Commun. Syst. (ISWCS) 2011*, Aachen, Germany, Nov. 2011, pp. 604–608.
- [111] G. H. Golub and C. F. V. Loan, *Matrix Computations*. Johns Hopkins 3rd ed., 1996.
- [112] L. Rugini, P. Banelli, and G. Leus, "Simple equalization of time-varying channels for OFDM," *IEEE Commun. Lett.*, vol. 9, no. 7, pp. 619–621, 2005.
- [113] C. C. Paige and M. A. Saunders, "LSQR: An algorithm for sparse linear equations and sparse least squares," *ACM Trans. Math. Software*, vol. 8, pp. 43–71, Mar. 1982.
- [114] T. Hrycak and G. Matz, "Low-complexity time-domain ICI equalization for ofdm communications over rapidly varying channels," in *Proc. Asilomar Conf. Signals, Syst., Comput.*, Pacific Grove, CA, Oct. 2006, pp. 1767–1771.

- [115] Y. Li, L. J. Cimini, and N. R. Sollenberger, "Robust channel estimation for OFDM systems with rapid dispersive fading channels," *IEEE Trans. Commun.*, vol. 46, no. 7, pp. 902–915, Jul. 1998.
- [116] K. Etemad and M.-Y. Lai, *WiMAX Technology and Network Evolution*. NY: Wiley-IEEE Press, 2011.
- [117] X. Cai and G. B. Giannakis, "Error probability minimizing pilots for OFDM with MPSK modulation over Rayleigh-fading channels," *IEEE Trans. Veh. Technol.*, vol. 53, no. 1, pp. 146–155, January 2004.
- [118] M. Simon and M. Alouini, *Digital Communication Over Fading Channels: A Unified Approach to Performance Analysis*. Hoboken, NJ: Wiley, 2000.
- [119] J. R. W. Heath and A. J. Paulraj, "Switching between diversity and multiplexing in MIMO systems," *IEEE Trans. Commun.*, vol. 53, no. 6, pp. 963–968, Jun. 2005.
- [120] M. Shin, J. Kang, B. Yoo, and C. Lee, "An efficient searching algorithm for receive minimum distance in MIMO systems with ML receiver," *IEICE Trans. Commun.*, vol. E92-B, no. 1, Jan. 2009.
- [121] A. Gersho and R. Gray, *Vector Quantization and Signal Compression*. Norwell, MA: Kluwer, 1992.
- [122] Y. Linde, A. Buzo, and R. Gray, "An algorithm for vector quantizer design," *IEEE Trans. Commun.*, vol. COM-28, no. 1, pp. 84–95, Jan. 1980.
- [123] R. C. de Lamare and A. Alcaim, "Strategies to improve the performance of very low bit rate speech coders and application to a variable rate 1.2 kb/s codec," *IEE Proc.- Vis. Image Signal Process.*, vol. 152, no. 1, pp. 74–86, Feb. 2005.
- [124] H. Zhang and R. U. Nabar, "Transmit antenna selection in MIMO-OFDM systems: Bulk versus per-tone selection," in *Proc. IEEE ICC*, Beijing, China, Apr. 2008.
- [125] R. Gowaikar and B. Hassibi, "Statistical pruning for near-Maximum likelihood decoding," *IEEE Trans. Signal Process.*, vol. 55, pp. 2661–2675, Jan 2007.
- [126] B. Shim and I. Kang, "Sphere decoding with a probabilistic tree pruning," *IEEE Trans. Signal Process.*, vol. 56, pp. 4867–4878, Oct. 2008.

- [127] ———, “On further reduction of complexity in tree pruning based sphere search,” *IEEE Trans. Commun.*, vol. 58, no. 2, pp. 417–422, Feb. 2010.
- [128] K.-C. Lai and L.-W. Lin, “Low-complexity adaptive tree search algorithm for MIMO detection,” *IEEE Trans. Wireless Commun.*, vol. 8, no. 7, pp. 3716–3726, Jul. 2009.
- [129] A. Burg, M. Borgmann, M. Wenk, M. Zellweger, W. Fichtner, and H. Bölcskei, “VLSI implementation of mimo detection using the sphere decoding algorithm,” *IEEE J. Solid-State Circuits*, vol. 40, pp. 1566–1577, 2005.
- [130] M. Shabany, K. Su, and P. Gulak, “A pipelined scalable high throughput implementation of a near-ML K-Best complex lattice decoder,” in *in Proc. IEEE Int. Conf. Acoust., Speech, Signal Process. (ICASSP) 2008*, 2008, pp. 3173–3176.
- [131] M. Barrenechea, M. Mendicute, I. Jimenez, and E. Arruti, “Implementation of complex enumeration for multiuser MIMO vector precoding,” in *19th European Signal Process. Conf. (EUSIPCO 2011)*, Barcelona, Spain, Sep. 2011, pp. 739–743.
- [132] S. A. Laraway and B. Farhang-Boroujeny, “Implementation of a Markov Chain Monte Carlo based multiuser/MIMO detection,” *IEEE Trans. Circuits Syst. I*, vol. 56, no. 1, pp. 246–255, 2009.
- [133] L. Collin, O. Berder, P. Rostaing, and G. Burel, “Optimal minimum distance-based precoder for MIMO spatial multiplexing systems,” *IEEE Trans. Signal Process.*, vol. 52, no. 3, pp. 617–627, Mar. 2004.
- [134] H. Lütkepohl, *Handbook of Matrices*. John Wiley & Son, 1996.
- [135] D. W. Waters and J. R. Barry, “The chase family of detection algorithms for multiple-input multiple-output channels,” *IEEE Trans. Signal Process.*, vol. 56, pp. 739–747, Feb. 2008.
- [136] W. G. Jeon, K. H. Chang, and Y. S. Cho, “An equalization technique for orthogonal frequency-division multiplexing systems in time-variant multipath channel,” *IEEE Trans. Commun.*, vol. 47, no. 1, pp. 27–32, Jan. 1999.

- [137] X. Cai and G. B. Giannakis, "Bounding performance and suppressing intercarrier interference in wireless mobile OFDM," *IEEE Trans. Commun.*, vol. 51, no. 12, pp. 2047–2056, Dec. 2003.
- [138] L. Li, A. G. Burr, and R. C. de Lamare, "Joint iterative receiver design and multi-segmental channel estimation for OFDM systems over rapidly time-varying channels," in *Proc. IEEE Veh. Technol. Conf. (VTC) 2013-spring*, Dresden, Germany, May 2013.
- [139] E. Panayırçı, H. Dogan, and H. V. Poor, "Joint channel estimation, equalization, and data detection for OFDM systems in the presence of very high mobility," *IEEE Trans. Sig. Process.*, vol. 58, no. 8, pp. 4225–4238, Aug. 2010.
- [140] H.-W. Wang, D. W. Lin, and T.-H. Sang, "OFDM signal detection in doubly selective channels with blockwise whitening of residual intercarrier interference and noise," *IEEE J. Select. Areas Commun.*, vol. 30, no. 4, pp. 684–694, May 2012.
- [141] S. Geman and D. Geman, "Stochastic relaxation, Gibbs distribution and the Bayesian restoration of images," *IEEE Trans. Pattern Anal. Machine Intell.*, vol. PAMI-6, pp. 721–741, 1984.
- [142] Y. Huang and P. M. Djurić, "Multiuser detection of synchronous code-division multiple access signals by perfect sampling," *IEEE Trans. Signal Process.*, vol. 50, no. 7, pp. 1724–1734, Jul. 2002.
- [143] B. Farhang-Boroujeny, H. Zhu, and Z. Shi, "Markov chain Monte Carlo algorithm for CDMA and MIMO communication systems," *IEEE Trans. Signal Process.*, vol. 54, no. 5, pp. 1896–1909, May 2006.
- [144] L. Bahl, J. Cocke, F. Jelinek, and J. Raviv, "Optimal decoding of linear codes for minimizing symbol error rate," *IEEE Trans. Inf. Theory*, vol. 20, no. 2, pp. 284–287, Mar. 1974.
- [145] Y. Li and J. L. J. Cimini, "Bounds on the interchannel interference of OFDM in time-varying impairments," *IEEE Trans. Commun.*, vol. 49, no. 3, pp. 401–404, Mar. 2001.

- [146] L.-L. Yang, "Receiver multiuser diversity aided multi-stage minimum mean-square error detection for heavily loaded DS-CDMA and SDMA systems," *IEEE Trans. Commun.*, vol. 58, no. 12, pp. 3397–3404, Dec. 2010.
- [147] Y. Mostofi and D. C. Cox, "ICI mitigation for pilot-aided OFDM mobile systems," *IEEE Trans. Wireless Comm.*, vol. 4, no. 2, pp. 765–774, Mar 2005.
- [148] H. Şenol, E. Panayırıcı, and H. V. Poor, "Nondata-aided joint channel estimation and equalization for OFDM systems in very rapidly varying mobile channels," *IEEE Trans. Signal Process.*, vol. 55, no. 5, pp. 2226–2238, May 2007.
- [149] Z. Tang, R. C. Cannizzaro, and G. Leus, "Pilot-assisted time-varying channel estimation for OFDM systems," *IEEE Trans. Signal Process.*, vol. 55, no. 5, pp. 2226–2238, May 2007.
- [150] Y.-S. Choi, P. J. Voltz, and F. A. Cassara, "On channel estimation and detection for multicarrier signals in fast and selective rayleigh fading channels," *IEEE Trans. Comm.*, vol. 49, no. 8, pp. 1375–1387, Aug. 2001.